Annealing twin formation mechanism

Yuan Jin

Ecole doctorale n° 364 : Sciences Fondamentales et Appliquées

Doctorat ParisTech

T H È S E

pour obtenir le grade de docteur

préparée dans le cadre d'une cotutelle entre

l'École nationale supérieure des mines de Paris

et Carnegie Mellon University

Spécialité "Science et Génie des Matériaux "

présentée et soutenue publiquement par

Yuan JIN

le 10 décembre 2014

Mécanismes de formation des macles thermiques

Annealing twin formation mechanisms

Directeurs de thèse : **Nathalie BOZZOLO et Anthony D. ROLLETT**
Co-encadrement de la thèse : **Marc BERNACKI**

Jury

M. Stefan ZAEFFERER PhD, Priv.-Doz. MPAD, Max-Planck-Institut	Rapporteur
M. Łukasz MADEJ, PhD, DSc. ISIM, AGH University of Science and Technology	Rapporteur
Mme. Dominique CHATAIN, Directrice de recherche CNRS, CiNaM, Aix Marseille Université	Examinateur
M. Anthony D. ROLLETT, Professeur, MSE, Carnegie Mellon University	Examinateur
Mme. Nathalie BOZZOLO, Professeur, CEMEF, Mines ParisTech	Examinateur
M. Marc BERNACKI, Chargé de recherche, HDR, CEMEF, Mines ParisTech	Examinateur

MINES ParisTech
Centre de Mise en Forme de Matériaux - CEMEF
1 rue Claude Daunesse –CS 10207
06904 Sophia Antipolis Cedex, France

T H E S E

Contents

GENERAL INTRODUCTION

MOTIVATION

Engineered metallic materials, which are used in a wide range of applications, are generally polycrystalline. The focus will be placed here on single-phase metals and alloys. Polycrystalline materials are composed of single crystal aggregates joined by a network of intergranular interfaces, also known as the grain boundary network (GBN). Mechanical and functional properties of polycrystalline metals are strongly dependent on the characteristics of GBN, e.g. the grain size. Two physical phenomena, taking place during the heating treatment following a prior deformation, mainly control the grain boundary network evolution i.e. recrystallization and grain growth.

Discontinuous primary recrystallization involves the formation of new strain-free grains in certain parts of the material and the subsequent growth of these to consume the deformed microstructure. It is thus convenient to divide the recrystallization process into two regimes: nucleation. which corresponds to the first appearance of new grains in the microstructure, and growth during which the new grains grow and consume the deformed materials. The recrystallization phenomenon is illustrated in Fig. 1. The main driving force for recrystallization is the internal energy difference between recrystallized grains and deformed matrix. Deformed grains have energy stored during plastic deformation (in the form of crystallographic defects, especially dislocations), recrystallized ones have a much lower defect density, so that they basically considered as being defect free.

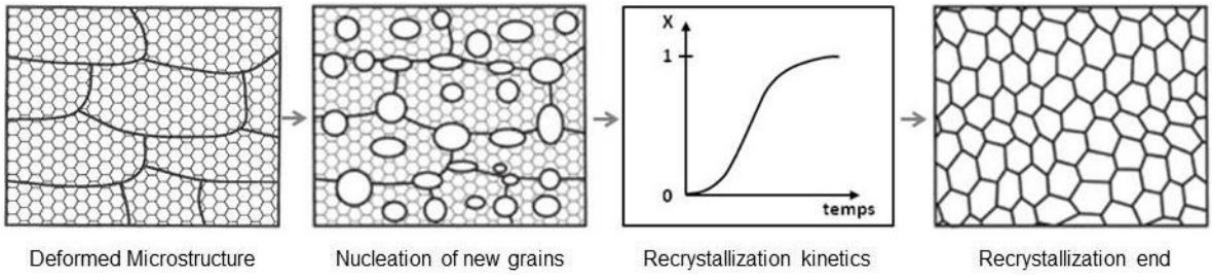

Fig. 1. Static recrystallization scheme; figure reproduced from reference [Humphreys 2004].

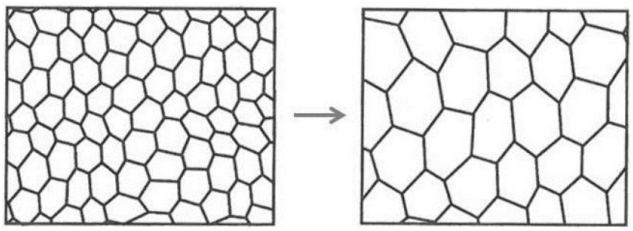

Fig. 2. Grain growth scheme; figure reproduced from reference [Humphreys 2004].

Grain growth is a phenomenon that increases the average grain size. Indeed the bigger grains grow at the expense of smaller ones which thus tend to disappear. This phenomenon takes place mainly after the primary recrystallization (illustrated in Fig. 2). The driving force for grain boundary migration is then the reduction of the material energy stored in the form of grain boundaries.

A physical phenomenon, known as annealing twinning, occurs during recrystallization and grain growth and gives rise to a crystallographic defect i.e. annealing twins, mainly in F.C.C. metals with low to medium stacking fault energy. However, these defects do not always have detrimental effect on the macroscopic material properties. Thanks to their special structure, annealing twin boundaries have lower interfacial energy compared to regular high-angle grain boundaries. When intercepting each other, they may also lead to the formation of other types of so-called special boundaries. Therefore, they are fundamental for the Grain Boundary Engineering (GBE), which was proposed by Watanabe [Watanabe 1984] in the 80's as a new route for improving the resistance to intergranular damages. An example of a grain boundary engineered material is given in Fig. 3.

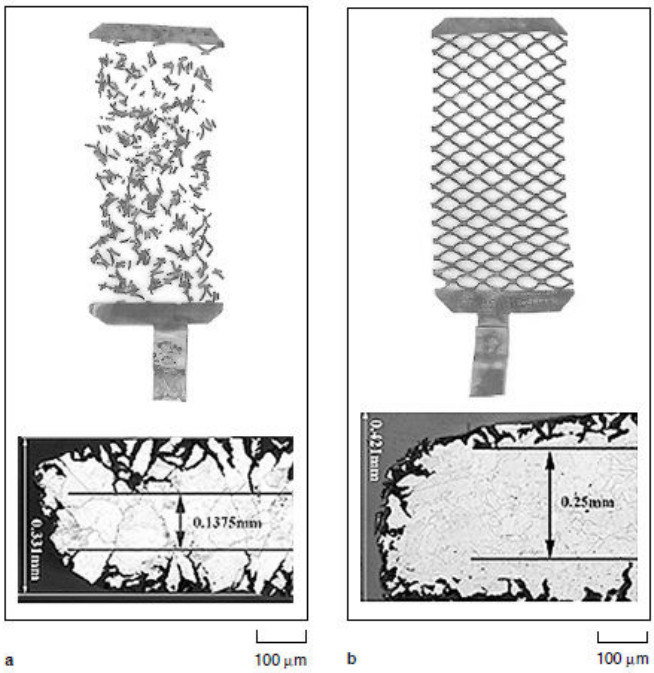

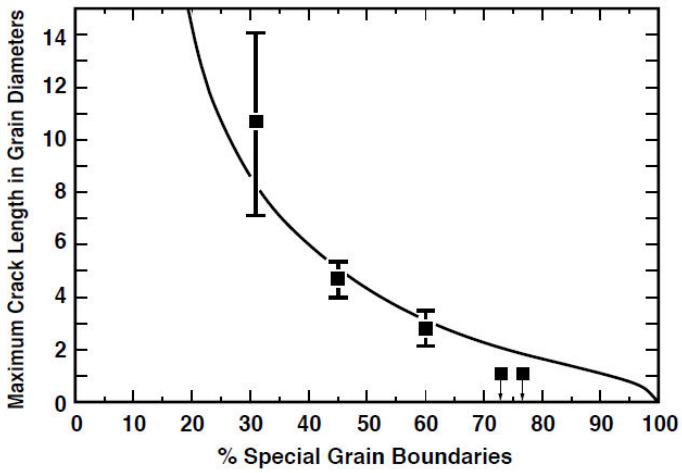

(c)

Fig. 3. (a) Intergranular corrosion and cracking in conventional lead-acid batteries having low (13%) population of special boundaries compared to (b) which exhibits relatively negligible cracking and has a high population (about 63%) of special boundaries introduced through GBE. (c) Maximum intergranular crack length and the fraction of special boundaries in a Ni-based alloy scale with each other. This figure was reproduced from reference [Palumbo 1998].

Thus, the understanding and modelling of annealing twin development during recrystallization and grain growth, which is the aim of the present PhD work, is of great importance especially for prediction of the material properties tightly related to GBN e.g. anti-corrosion and fatigue resistance. The objective of the experimental part of this work is to identify the general patterns of annealing twin development during recrystallization and grain growth and to determine the thermo-mechanical factors influencing this development. For this purpose, thermo-mechanical tests are carried out on different F.C.C. materials including 304L stainless steel, pure nickel and Inconel 718 superalloy. Moreover, electron back scatter diffraction (EBSD) were performed to investigate microstructural evolution.

In addition to the experimental work, a numerical study was also performed aiming at modelling annealing twin development counting for the mechanisms revealed by the experimental data. Thanks to the great progress of computational capacity in the last two decades, full field models are applied to simulate microstructure evolutions at the mesoscopic scale [Bernacki 2011] [Agnoli 2014] [Moelans 2009]. Two full field models i.e. phase field and level set methods that can implicitly describe interfaces are known for their capacity to model both recrystallization and grain growth phenomena. More precisely, in both approaches, fields are introduced for the purpose of avoiding explicit tracking interfaces. These two methods are largely applied on anisotropic grain growth simulations [Moelans 2009] [Elsey 2013]. However, due to their special interfacial properties, annealing twin boundaries have not been considered in these simulations. In the present PhD work, both methods are used.

Their performance to describe the strong anisotropy in grain boundary properties induced by annealing twin boundaries at the scale of a Representative Volume Element (RVE) is notably analyzed.

FRAMEWORK AND LAYOUT OF THIS THESIS

The present PhD work, conducted mainly at CEMEF (Centre de mise en forme des matériaux) Mines-ParisTech, was in cooperation with the material science and engineering department of Carnegie Mellon University (CMU). This cooperative project was supported by the French National Research Agency (ANR) (ANR project called FORMATING: ANR-11-NS09-001-01) and the Materials World Network of the US National Science Foundation under Grant number DMR-1107986. Within that frame, another PhD work (by Brian LIN) was conducted mainly at CMU, and focused on complementary aspects.

The present thesis is organized in two parts including seven chapters. The first part, including the first three chapters, lays down the experimental work of the PhD project concerning mainly the identification of annealing twin formation mechanisms. The second part presents the numerical tools developed and the related simulations performed in this work.

Chapter 1 introduces firstly annealing twins in general, including the concept of annealing twin and different annealing twin quantification methods. Secondly, a literature review on annealing twin formation mechanisms is presented. The two major analytical models used in literature for annealing twin density predictions are reviewed in details especially in terms of their theoretical bases.

In chapter 2, the experiments performed on three F.C.C. materials (commercially pure nickel, 304L stainless steel and nickel based superalloy Inconel 718) are presented. Based on these data, the general patterns of annealing twin development during recrystallization and grain growth are discussed and summarized.

In chapter 3, the effects of different thermo-mechanical parameters on annealing twin development during recrystallization are investigated. The results of different experiments performed on pure nickel are presented. Some new thoughts about annealing twin formation mechanisms are proposed.

Chapter 4 is the first chapter of the numerical part. In this chapter, a new mean field model is proposed to predict annealing twin density evolution during grain growth. The modelling result is compared with the experimental data of Inconel 718.

Chapter 5 presents a state-of-arts about full field modelling of anisotropic grain growth. Firstly, two phase field models are introduced. The difference in their formulations is

highlighted. Secondly, the theoretical basis of another implicit method i.e. the level set method is reviewed.

In chapter 6, the multi-phase-field and level set algorithms developed in our finite element code are firstly detailed. Then the performances of these approaches for anisotropic grain growth full field modeling are compared.

In chapter 7, different numerical tools that are essential for large-grain growth simulations are presented at first. Then two grain growth simulations with about 10000 grains and with respectively isotropic and anisotropic grain boundary energies, performed with the level set method, are compared. A new methodology based on the considered level set framework, with which we can insert annealing twin boundaries into synthetic microstructures and differentiate between coherent and incoherent twin boundaries, is proposed. The possibility to simulate annealing twin evolution during recrystallization and grain growth at the mesoscopic scale is discussed.

ORAL AND WRITTEN COMMUNICATIONS

The present PhD work has contributed to the following written communications:

- Y. Jin, M. Bernacki, G.S. Rohrer, A.D. Rollett, B. Lin, N. Bozzolo, 'Formation of annealing twins during recrystallization and grain growth in 304L austenitic stainless steel', Mater. Sci. Forum 753, 113-116 (2013).
- Y. Jin, B. Lin, M. Bernacki, G.S. Rohrer, A.D. Rollett, N. Bozzolo, 'Annealing twin development during recrystallization and grain growth in pure Nickel', Mater.Sci.Eng. A 597, 295-303 (2014).
- Y. Jin, M. Bernacki, A. Agnoli, G.S. Rohrer, A.D. Rollett, B. Lin, N. Bozzolo, ‘Evolution of the annealing twin density during grain growth’, to be submitted
- Y. Jin, B. Lin, M. Bernacki, G.S. Rohrer, A.D. Rollett, N. Bozzolo, ‘Thermo-mechanical factors influencing the annealing twin formation during recrystallization in pure nickel’, to be submitted.
- Y. Jin, M. Bernacki, A.D. Rollett, N. Bozzolo, ‘2D finite element modelling of anisotropic grain growth in polycrystalline materials: level set versus multi-phase-field method’, to be submitted.

- B. Lin, G.S. Rohrer, A.D. Rollett, Y. Jin, N. Bozzolo, M. Bernacki, Evolution of microstructure in pure nickel during processing for grain boundary engineering', Mater. Sci. Forum 753, 113-116 (2013).

and to the following oral communications:

- Y. Jin, M. Bernacki, G.S. Rohrer, A.D. Rollett, B. Lin, N. Bozzolo, 'Formation of annealing twins during recrystallization and grain growth in 304L austenitic stainless steel', Recrystallization and grain growth 2013, Sydney, Australia.
- Y. Jin, M. Bernacki, A. Agnoli, G.S. Rohrer, A.D. Rollett, B. Lin, N. Bozzolo, 'Evolution of the annealing twin density during grain growth in Inconel 718', Eurosuperalloy 2014, Giens, France.
- N. Bozzolo, M. Bernacki, Y. Jin, B. Lin, G.S. Rohrer, A.D. Rollett, 'Increasing twin density in polycrystalline nickel and nickel alloys by thermomechanical processing in view of grain boundary engineering', MS&T 2014, Pittsburgh, USA.
- B. Lin, Y. Jin, N. Bozzolo, M. Bernacki, C. Hefferan, R. Suter, A.D. Rollett, G.S. Rohrer, 'Interfaces, Grain Boundaries, and Surfaces from Atomistic and Macroscopic Approaches: Fundamental and Engineering Issues', MS&T 2014, Pittsburgh, USA.
- B. Lin, G.S. Rohrer, A.D. Rollett, Y. Jin, N. Bozzolo, M. Bernacki, Evolution of microstructure in pure nickel during processing for grain boundary engineering', Recrystallization and grain growth 2013, Sydney, Australia.
- B. Lin, Y. Jin, C. Hefferan, R. Suter, M. Bernacki, N. Bozzolo, A.D. Rollett, G.S. Rohrer, 'The role of texture and twin nucleation during grain growth in FCC nickel', ICOTOM 2014, Dresden, Germany.
- M. Bernacki, N. Bozzolo, R. Logé, B. Scholtes, Y. Jin, A. Agnoli, A.-L. Fabiano, K. Hitti, 'Advances in level set modeling of recrystallization at the mesoscopic scale', OptiMoM 2014, Oxford, UK.
- M. Bernacki, N. Bozzolo, R. Logé, Y. Jin, A. Agnoli, A.-L. Fabiano, A.D. Rollett, G.S. Rohrer, J.M. Franchet, J. Laigo, 'Full field modelling of recrystallization in superalloys thanks to level set method', Eurosuperalloy 2014, Giens, France.

1. A STATE OF ARTS ON ANNEALING TWIN DENSITY PREDICTION AND QUANTIFICATION

1.1. INTRODUCTION

In 1926, Carpenter and Tamura [Carpenter 1926] reported on annealing twin formation and annealing twins were already commonly mentioned in metallography articles before this [Edwards 1924]. Since then, annealing twins have been observed in almost all deformed and subsequently annealed F.C.C. metals with low to medium stacking fault energy (<0.15 J/m^2).

Grain boundary engineering, proposed by Watanabe in the 80's, was defined as the art of changing the grain boundary network in polycrystalline F.C.C. materials or alloys by sequential thermomechanical processing. Grain boundary engineering may improve macroscopic material properties such as intergranular stress corrosion cracking [Palumbo 1988] [Palumbo 1990] [Lin 1995], creep resistance [Don 1986] [Thaveeprungsriporn 1997] and fracture toughness and plasticity [Lim 1990] [Lehockey 1998] by means of increasing the amount of the so-called special boundaries. The term special boundary usually refers to low $\sum$ coincident site lattice (CSL) grain boundaries. CSL boundaries occur when the lattices of the adjacent crystals are misoriented in such a way that a large fraction of the lattice points of the two crystals overlap [Bollman 1970]. The "$\sum$" value of the boundary is the inverse of the fraction of overlapping lattice positions. For example, if two FCC crystals are separated by a twin boundary, then one third of the lattice sites coincide leading to a $\sum$ value equals to 3. Therefore, annealing twin boundaries are also referred to $\sum$3 boundaries.

Metallurgists still do not fully agree on the formation mechanism of annealing twins，despite the voluminous literature devoted to the topic. This chapter aims at summarizing the main exiting models of annealing twin formation. This chapter is composed of three main parts and a conclusion. In the first section, annealing twin concept will be introduced and the different twin quantification methods will be reviewed. In the second section, the two main annealing twin formation models i.e. the Gleiter's model and the Pande's model will be presented. In the third section, an ambiguity about one of the annealing twin quantification methods (the twin density) will be discussed.

1.1.1 Annealing twin concept

1.1.1.1 Grain boundary

Generally speaking, a grain boundary can be considered as an interface separating two regions with different crystallographic orientations. The overall geometry of a grain boundary such as that shown in Fig. 1.1(a) is defined by five macroscopic (or rotational) parameters. Among them, two describe the orientation of the boundary plane (inclination), and the other three define the rotation required to make the two separated crystals coincident (misorientation). Since the orientation of the grain boundary plane is difficult to be determined experimentally, the inclination is often ignored, and only the misorientation is used for grain boundary description [Humphrey 2004]. However, this ignorance can lead to misinterpretation of boundary behavior (especially for twin boundaries, see section 1.1.2). The relative orientation of two crystals is described by the rotation of one crystal, which brings it into the same orientation as the other crystal. This can be defined by a rotation matrix:

$$R = \begin{bmatrix} a_{11} & a_{12} & a_{13} \\ a_{21} & a_{22} & a_{23} \\ a_{31} & a_{32} & a_{33} \end{bmatrix}, \tag{1-1}$$

where $\left(a_{ij}\right)_{1\le j\le 3}$ are column vectors of direction cosines between the cartesian axes defined within the crystallographic frame. The rotation matrix can be expressed using Bunge Euler angles $\left(\varphi_1, \Phi, \varphi_2\right)$ as:

$$R = \begin{bmatrix} \cos\varphi_1\cos\varphi_2 - \sin\varphi_1\sin\varphi_2\cos\Phi & \sin\varphi_1\cos\varphi_2 + \cos\varphi_1\sin\varphi_2\cos\Phi & \sin\varphi_2\sin\Phi \\ -\cos\varphi_1\sin\varphi_2 - \sin\varphi_1\cos\varphi_2\cos\Phi & -\sin\varphi_1\sin\varphi_2 + \cos\varphi_1\cos\varphi_2\cos\Phi & \cos\varphi_2\sin\Phi \\ \sin\varphi_1\sin\Phi & -\cos\varphi_1\sin\Phi & \cos\Phi \end{bmatrix}. \tag{1-2}$$

The rotation angle is given by:

$$2\cos\theta + 1 = trace(R). \tag{1-3}$$

And the direction of the rotation axis $\vec{r}$ is:

$$\vec{r} = {}^{t}\left(a_{23} - a_{32}, a_{31} - a_{13}, a_{12} - a_{21}\right), \tag{1-4}$$

It is conventional to describe the rotation by the axis/angle associated with the smallest misorientation angle considering all the possible crystallographic symmetries (so called disorientation). Grain boundaries are generally divided into those whose misorientation is greater than a certain angle – the high angle grain boundaries (HAGB), and those whose misorientation is less than this angle – the low angle grain boundaries (LAGB). The transition is typically taken as between 10° and 15°. Compared to the complex structure of high angle grain boundaries, most of low angle grain boundaries can be represented by an array of dislocations. Depending on the characters of these dislocations, LAGB can be divided into tilt boundaries and twist boundaries.

1.1.1.2 Crystallographic description of a twin in FCC materials

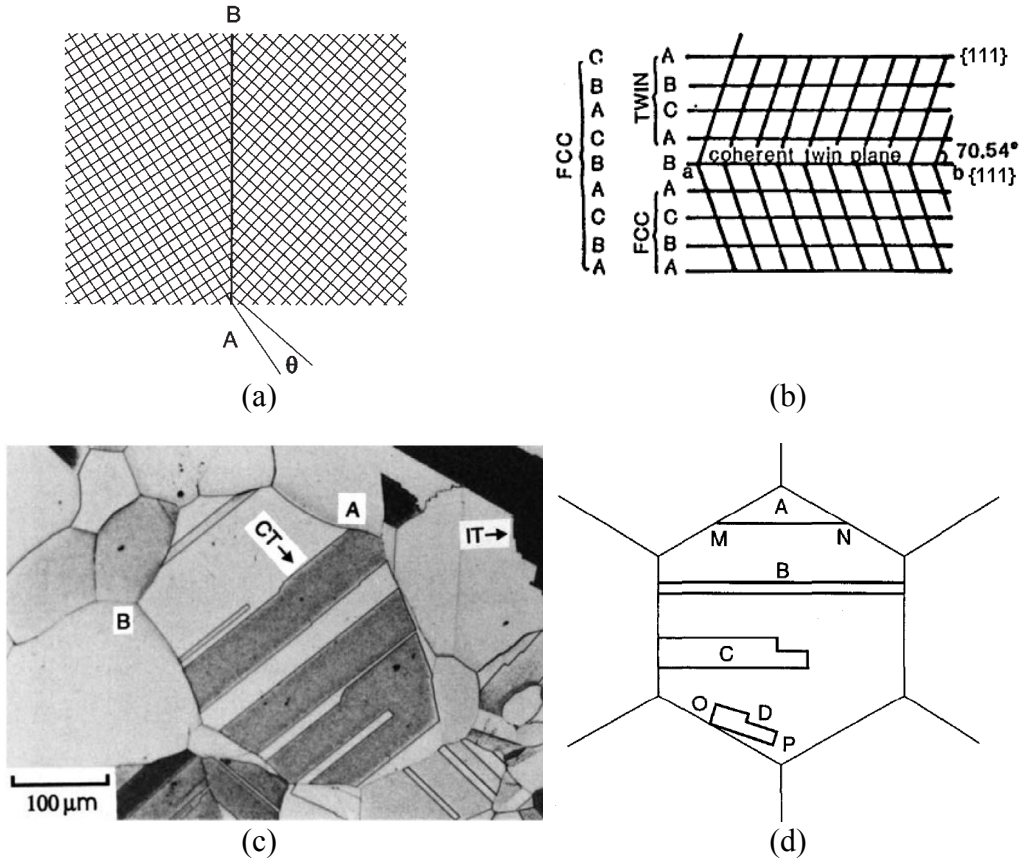

Fig. 1.1 (a) a grain boundary between two crystals misoriented by an angle θ about an axis normal to the page; (b) coherent twin structure in a F.C.C. material (this figure was reproduced from the reference [Humphrey 2004]); (c) annealing twins in an annealed 70:30 brass. Some coherent (CT) and incoherent (IT) twin boundaries are marked (this figure was reproduced from the reference [Humphrey 2004]); (d) schematics showing various two-dimensional morphologies of annealing twins observed in F.C.C. crystals (this figure was reproduced from the reference [Mahajan 1997]).

The relationship between the twin and the matrix grain is such that the stacking sequence of compact {111} planes in the FCC structure is changed. Fig. 1.1 (b) shows the stacking sequence of {111} planes on both sides of a coherent twin boundary plane. The stacking sequence is inverted from ABC to CBA at the twin plane, which thus behaves as a mirror plane. The three-plane layer (ABA), including the twin plane and the two adjacent planes has the characteristic of a hexagonal close-packed structure (H.C.P.). The interfacial energy of a coherent twin boundary can therefore be estimated as the difference between the free energy of a three-layer H.C.P. structure and the free energy of a F.C.C. structure. Note that a twin boundary is coherent if it lies in that {111} mirror plane (Fig. 1.1 (b)(c)), otherwise it is incoherent.

For the F.C.C. crystal structure, the twin boundary misorientation can also be obtained by rotating the orientation of the parent grain 60° about <111>. The coherent twin boundary plane is then the one perpendicular to that rotation axis.

1.1.1.3 Annealing twin morphologies

Annealing twins observed in metallographic sections of a variety of recrystallized F.C.C. metals and alloys exhibit four two-dimensional morphologies that are schematically shown in Fig. 1.1 (d) [Mahajan 1997]. A corner twin is labelled ‘A’ and its coherent twin boundary produces a trace MN in Fig. 1.1 (d). Twin B spans opposite sides of the grain, whereas twin C terminates within the grain. Finally, twin D is entirely embedded inside the grain. In addition, since there are four equivalent {111} planes, four variants of twins may exist in a given grain.

Mahajan et al [Mahajan 1997] proposed this classification for discussing twin formation. However, this classification is performed in a two dimensional (2D) context, which cannot describe the real three dimensional (3D) morphologies of annealing twins. By serial sectioning a $NiMn_2$ sample, Bystrzycki et al reconstructed 3D annealing twin shapes [Byzstrzycki 1993]. He pointed out that a given annealing twin can exhibit different types of two-dimensional morphologies (see Fig. 1.2(a)). Similarly to Fig. 1.1(d), totally four types of 2D twin morphologies are revealed. In addition, a serial sectioning experiment was done by manual polishing in the present PhD work. By performing EBSD measurements on each section, we confirmed the observation of Bystrzycki et al (Fig. 1.2(b)). For example, the twin in the black circle on the first layer (Fig. 1.2(b)) is a ‘B’ type twin. However, the same twin becomes a ‘C’ type twin on the eleventh layer. Thus, the explanation of annealing twin

formation based on their 2D morphologies is obviously misleading. This observation was also further confirmed by analyzing a 3D-XRD dataset of a pure nickel sample [Lin 2014].

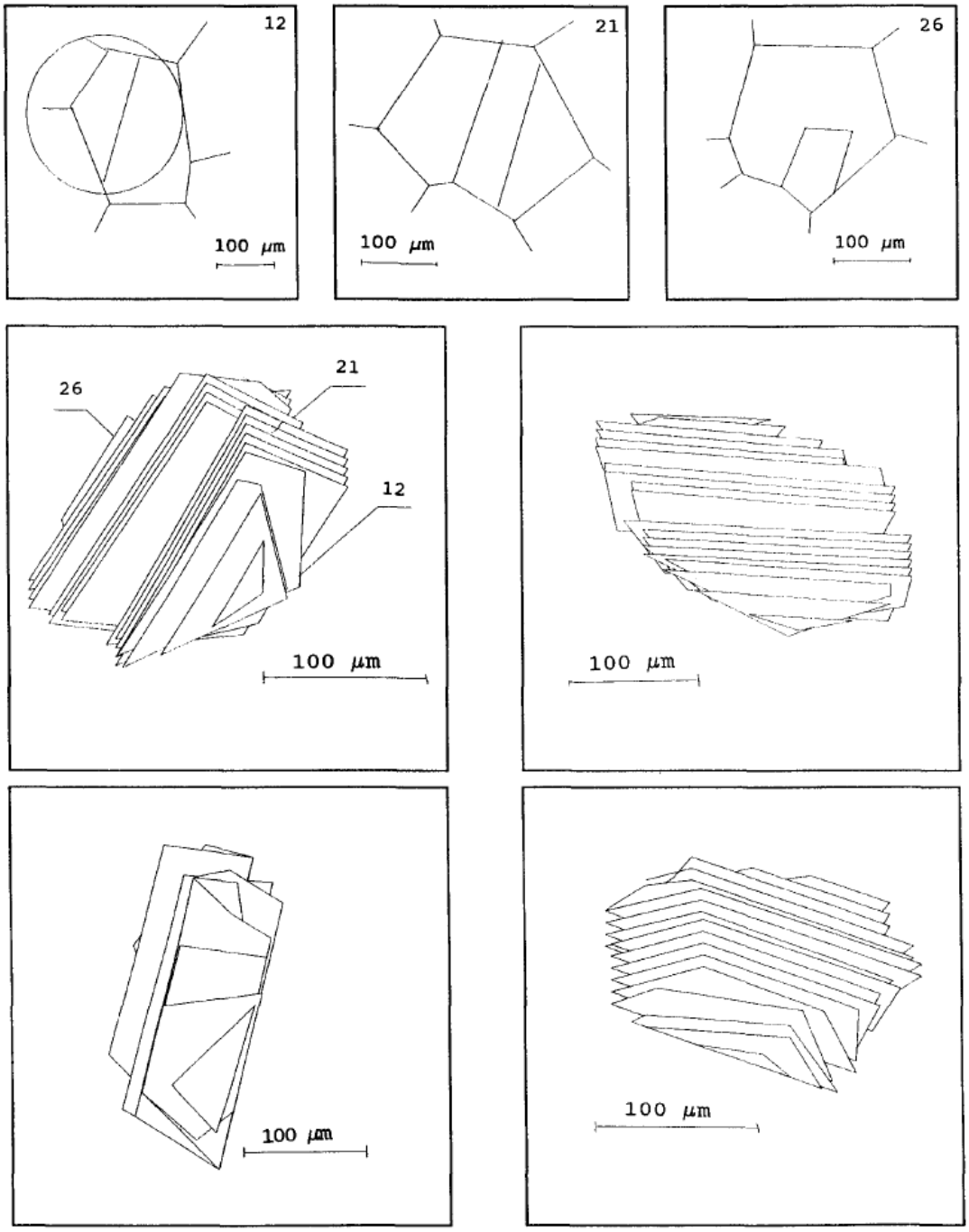

(a)

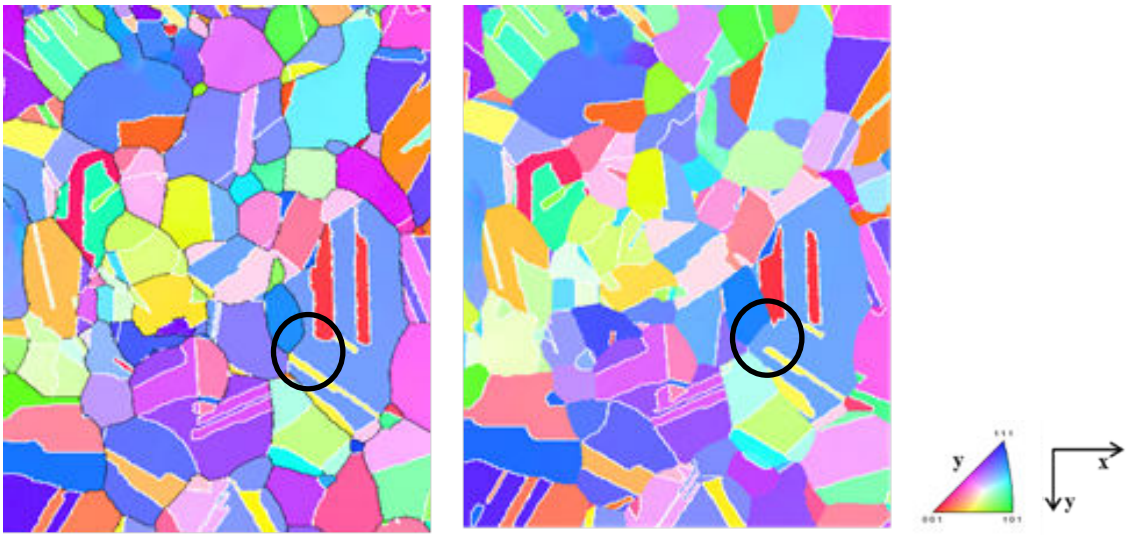

(b)

Figure 1.2. (a) Three-dimensional reconstruction of irregular twin (serial sections) [Byzstrzycki 1993]; (b) Serial sections of a fully recrystallized 304L stainless steel sample with an average grain size of 65µm (the vertical slice separation is between 1-2µm); the two EBSD maps correspond respectively the first and the eleventh layer shown by an orientation colour-coded scale (vertical direction of the map projected in the standard triangle).

1.1.1.4 Coincident Site Lattice

As mentioned previously, compared to LAGB, much less is known about the structure of high angle grain boundaries. Meanwhile, some high angle grain boundaries e.g. coherent twin boundaries and more generally low Σ boundaries may have relatively regular structures. Since LAGB and the grain boundaries with small Σ values (e.g. annealing twin boundaries (Σ3)) may confer some special interfacial structure and properties, they are called special boundaries. On the other hand, other high angle grain boundaries, and very high Σ values (typically bigger than 27) with no special properties, are called random or general boundaries. The misorientation angles and the corresponding rotation axes of some special boundaries are indicated in Table.1.1.

Σ	$\theta^{\circ}_{\min}$	Axis
1	0	Any
3	60	<111>
9	38.94	<110>
27a	31.58	<110>
27b	35.42	<210>

Table.1.1. Rotation axes and angles for coincidence site lattices (F.C.C. structure).

Due to the crystallographic nature of grain boundaries, misorientations must be conserved at each triple junction, so that a full circuit around the junction yields a net misorientation of zero. In the framework of the CSL model, this conservation law yields the 'the sigma combination rule': $\Sigma a \cdot \Sigma b = m^2 \cdot \Sigma c$, where $\Sigma a, \Sigma b, \text{and}\, \Sigma c$ are the Σ values of the three boundaries that meet at the triple junction. The scalar quantity *m* can be any common divisor of Σ*a* and Σ*b*.

For example, if two Σ3 boundaries meet at a triple junction, the third boundary linked to this junction is a Σ9 boundary, and the meet of a Σ3 and a Σ9 boundary can produce a Σ27 boundary as illustrated in Fig. 1.3.

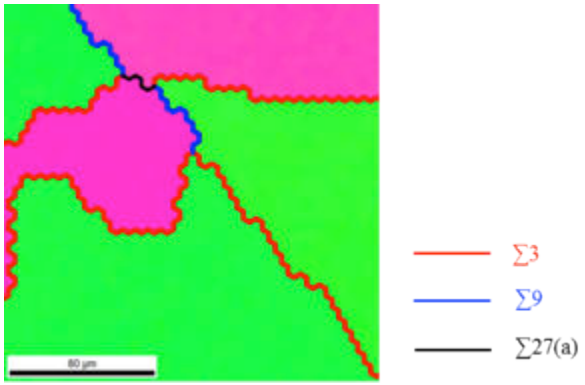

Figure 1.3. CSL boundary network (part of an EBSD map)

Brandon noted in [Brandon 1966] that the density of dislocations that can be introduced into a Σ boundary without destroying coincidence was limited by the density of coincident lattice at the boundary, which implies that the maximum permissible density of boundary dislocations should decrease with Σ value [Brandon 1966]. Based on this observation, Brandon assumed the maximum permissible deviation from coincidence to be given by an equation as follows:

$$\theta = \theta_0 (\Sigma)^{-\frac{1}{2}}, \tag{1-5}$$

where θ_0 is a constant ($\theta_0 \approx 15°$). Thus, for a Σ3 twin boundary, $\theta \approx 8.66°$.

1.1.2 Annealing twin quantification

- **GBCD and GBED**

As presented previously, a grain boundary is parameterized by five macroscopic degrees of freedom. The grain boundary character distribution (GBCD) is defined as the probability density or area fraction of a given grain boundary type (given misorientation and inclination) within the five parameter space. The discretization of the five parameter space is illustrated in Fig. 1.4.

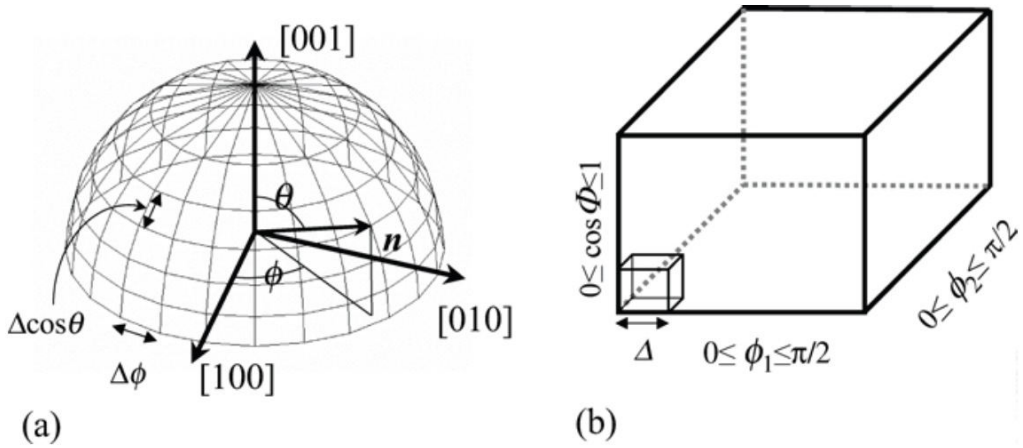

Fig. 1.4. The schematic diagram shows the discretization of five macroscopic degrees of freedom of (a) two boundary plane orientation parameters and (b) three lattice misorientation parameters. This figure was reproduced from the reference [Rohrer 2004].

Similarly to GBCD, grain boundary energy distribution (GBED) describes the energy of individual boundaries. These two distributions are essential for grain boundary network studies. Grain boundary energy was found to be inversely correlated with grain boundary population [Holm 2011] (Fig. 1.5(a)) and the GBED appeared to be correlated in different materials (Fig. 1.5(b)). Annealing twin boundaries, especially coherent twin boundaries have much lower interfacial energy than general high angle grain boundaries [Olmsted 2009] (about one twentieth), as illustrated in Fig. 1.5(c). Therefore, in FCC materials, especially those of low stacking fault energy, the GBCD is mainly dominated by $\sum 3$ boundaries [Kumar 2005]. It is worth highlighting the difficulty to determine experimentally the GBCD. The analysis of data from a single 2D section plane can be used to derive certain average properties of the grain boundary network, but not the actual three-dimensional network configuration. For example, the angle between the observation plane and the grain boundary plane is unknown from the information in a single section plane. It is possible to combine many observations from symmetrically indistinguishable bicrystals to determine the

probability that certain grain boundary planes appear in the microstructure. However, in this case, a large number of grain boundary traces needs to be characterized with respect to their lattice misorientation and orientation within the section plane [Saylor 2004]. Therefore, to fully describe GBCD, advanced 3D imaging techniques e.g. X-ray or serial sectioning [Rohrer 2004] must be used. An alternative method based on EBSD characterization of the commun edge of two orthogonal sections is used in the group of S. Zaefferer [Mandal 2014], but is better suited for individual boundary investigations than for the statistical description of GB populations.

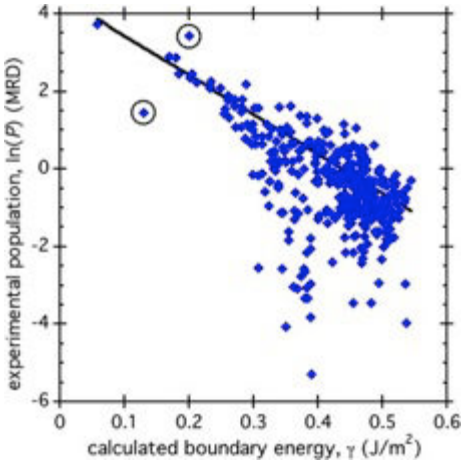

(a)

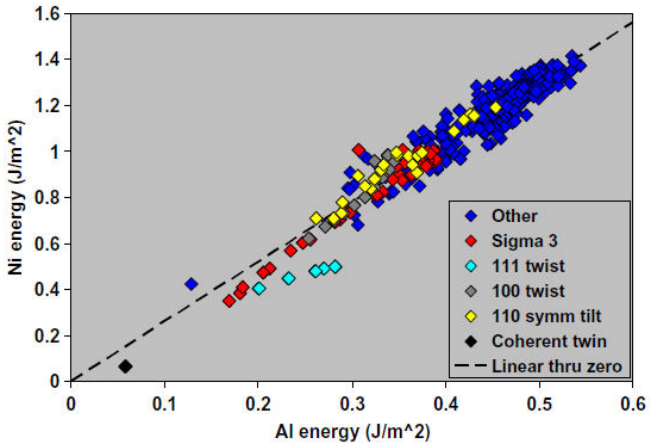

(b)

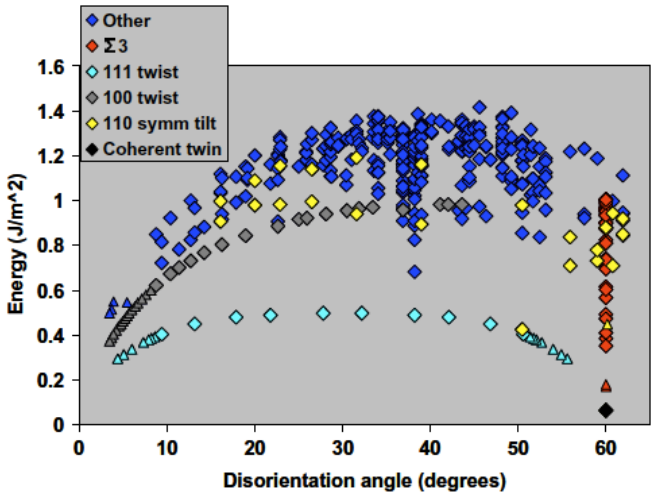

(c)

Fig. 1.5 (a) The relationship between experimental GBCD and calculated grain boundary energy for 388 grain boundaries in Al (this figure was reproduced from reference [Holms 2011]); (b) scatter plot of the computed grain boundary energies for Ni and Al. Each point represents the same macroscopic degrees of freedom; (c) calculated grain boundary energies of Ni as a function of misorientation angle; the red points correspond to Σ3 misorientations, the cyan points correspond to <111> twist grain boundaries, the grey symbols correspond to <100> twist grain boundaries, the yellow symbols correspond to <110> symmetric tilt grain

boundaries and dark blue symbols correspond to all other boundaries ((b) and (c) were reproduced from reference [Olmsted 2009]).

- **Quantification of annealing twin boundaries**

Several annealing twin quantification methods exist in the literature including twin boundary length fraction (f_L), twin boundary number fraction (f_N), twin density (N_L) and number of twin boundaries per grain (N_G). In this section, these quantification methods will be discussed in terms of their application fields and their equivalency. In addition, an example will be given to illustrate the differences that can be observed concerning 2D and 3D values of N_L, N_G and f_L.

1.1.2.1 Grain and twin boundary detection in EBSD maps

EBSD measurements are performed in the present study to analyze microstructural evolution and to quantify annealing twin quantity. The data set of an EBSD measurement stores a list of pixels composing the measured area. Each pixel has a crystallographic orientation determined by indexing the Kikuchi pattern of the probed volume at each pixel coordinates on the sample surface. The EBSD data sets are processed with the OIM^{TM} software from TSL. High angle grain boundaries are defined between two pixels having a misorientation angle higher than 15°. According to Brandon's criterion [Brandon 1966], the tolerance of misorientation angle for twin boundary detection is set to 8.66° for all the experimental data.

In the example shown on Fig. 1.6, three sets of pixels, having different orientations, are considered as three grains in the OIM^{TM} software, and all interfaces separating these three grains are HAGB (Fig. 1.6(a)). In OIM, the number of grain boundary segments is basically defined as the number of pixel edges composing the boundaries (the grain boundaries are totally composed by 161 hexagonal edges, each of which is 4.04 μm long). In practice, that pixelized description has many drawbacks, and should be replaced by the description of the reconstructed boundaries (shown on Fig. 1.6 (c)). For example, some of the grain boundary segments are in fact coherent or incoherent twin boundary segments (Fig. 1.6 (b) and (c)), which could hardly be distinguished within the pixel edge description.

As shown in Fig. 1.6(c), boundaries are reconstructed based on triple junctions. The characteristics of the reconstructed boundaries are indicated in Table 1.2. Coherent and incoherent twin boundaries can be distinguished by imposing a tolerance of the twin boundary plane deviation ϕ, which is defined in Fig 1.7.

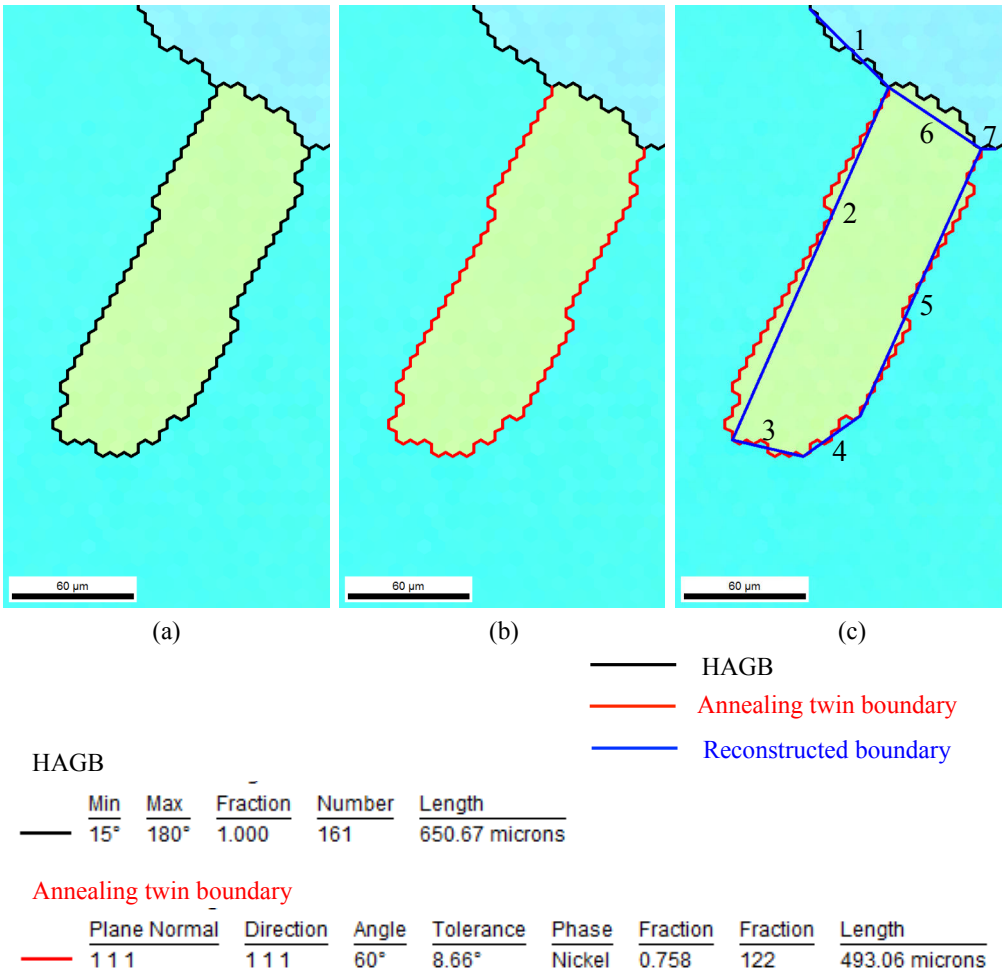

Fig. 1.6 Grain and twin boundary detection in EBSD maps (part of the EBSD map of the sample 60_R450_G650 that will be presented in the third chapter of the experimental part of the present thesis); (same orientation color code as in Fig. 1.2); (a) HAGB detection; (b) twin boundary detection; (c) detection of the coherent or incoherent character of the twin boundary (tolerance angle of twin boundary plane deviation (ϕ equals to 2°); details of grain and twin boundary length are indicated below the EBSD maps.

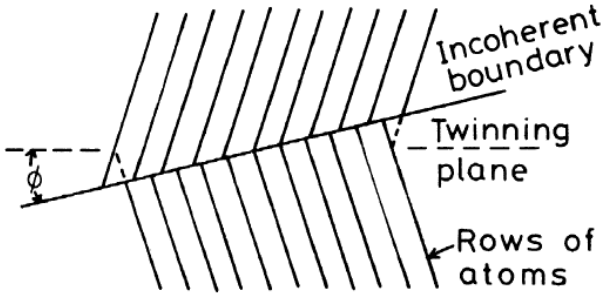

Fig. 1.7 Schematic of an incoherent twin boundary [Porter 1981].

Grain boundary	Twin boundary	Coherent twin boundary	Length (μm)
1			54.4
2	X	X	190.1
3	X		35.9
4	X		34.5
5	X	X	144.2
6			54.7
7			7.0

Table.1.2. Characteristics of the reconstructed grain boundaries

1.1.2.2 Twin boundary fraction by length and number

The length (f_L) and number (f_N) fractions are calculated by:

$$f_L = \frac{L_{TB}}{L_{HAB}}, \tag{1-6}$$

$$f_N = \frac{N_{TB}}{N_{HAB}}, \tag{1-7}$$

where L_{TB} and N_{TB} are, respectively, the length and the number of twin boundaries and L_{HAB} and N_{HAB} are, respectively, the length and the number of all the high angle grain boundaries. Neither of these two fractions indicates the absolute content of annealing twin boundaries. f_L and f_N reflect the proportion of twin boundaries in the grain boundary network. Thus, these two fractions have been used to rank materials in terms of their properties linked to grain boundary network e.g. corrosion resistance [Lin 1995].

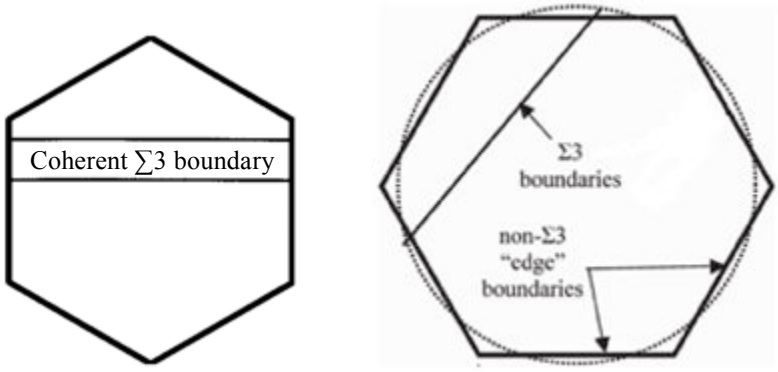

(a) (b)

Fig. 1.8 (a) Schematic illustration of one pair of lamellar twins delimiting one twin lamella in a six-sided, two dimensional grain (the length of each side of the hexagonal is *a*) [Randle 2002]; (b) a 2D regular hexagonal grain with its equivalent circular grain (dotted line); grain-spanning twin boundaries may lie on any chord of the equivalent circular grain [Kumar 2005].

In the literature, the length fraction of twin boundaries is reported to be higher than the number fraction in FCC materials [Kumar 2000] [Randle 2008]. This observation suggests that twin boundaries are longer on average than the general high-angle boundaries, which is consistent with their lower energy.

One version of the equivalency was proposed by Randle [Randle 2002] based on an idealised geometrical calculation. In a two-dimensional regular hexagonal grain as shown in Fig. 1.8(a), the two twin boundaries span the entire grain. Supposing the length of each side of the hexagonal is *a*, the length of all the boundaries (L_{HAG}) equals to 6.464*a* ($\frac{6a}{2} + 2a\sqrt{3} \approx 6.464a$) and the length of the twin boundaries (L_{TB}) equals to $2a\sqrt{3} \approx 3.464a$. The total number of interfaces is 5 and the number of twin boundaries is 2. It is worth mentioning in this study, the idealised grain is used to represent the overall microstructure. For example, for a 2D microstructure composed by *N* hexagonal idealised grains, the total regular high angle boundary length should be $\frac{6a \times N}{2}$ and the total number of these boundaries should be $\frac{6 \times N}{2}$, since each boundary is shared by two grains. Therefore, the total length of the regular high angle boundaries of one idealised grain (Fig. 1.8(a)) is equal to $\frac{6a}{2}$ and the total grain boundary number is equal to 3.

Using Eq.1-6 and Eq.1-7, f_N is 0.75 of the f_L. Accordingly, Randle deduced that the number fraction is 0.68, 0.75, 0.79 and 0.82 of the length fraction for 1, 2, 3 and 4 twin boundaries-per-grain respectively. Therefore, inversely one could deduce the average number of twin boundaries per grain by calculating the ratio between f_N and f_L.

However, in this model the ratio between the twin boundary (L_{TB}) and the grain boundary (*a*), which equals to $2\cos 30^\circ = 1.732$, is slightly beyond the range of experimental values in the literature (1.43-1.70) [Kumar 2000] [Gertsman 1994].

A modification was proposed by Kumar et al [Kumar 2005]. Fig. 1.8(b) shows a regular hexagonal grain edge length *a* and an equivalent circular grain of the same area with a radius of $r = \sqrt{\frac{3}{\pi}}a$. Considering the fact that twin boundaries that span the entire grain may lie on any chord of the equivalent circular grain, the average twin boundary length is given by:

$$L_{TB} = 2r\int_0^1 \sqrt{1-x^2}\,dx = 2\sqrt{\frac{3}{\pi}}a\frac{\pi}{4} \approx 1.53a, \qquad (1\text{-}8)$$

where x is an integration variable describing the perimeter of the circle. Consequently, the number fraction should be 0.84 but not 0.75 of the length fraction for 2 twins-per-grain.

Finally, in these two approaches, to quantify the equivalency between f_N and f_L, only coherent twin boundaries spanning opposite sides of the grain are taken into account for the sake of model simplification. However, as presented previously, an annealing twin can exhibit different 2D morphologies. The ignorance of other types of twin morphologies could introduce considerable deviation in the correlation between the number of twin boundaries per grain and the ratio between f_N and f_L. Besides, as presented in the previous subsection, the number of grain boundaries given in the OIM software can be the number of corresponding pixel edges. But the number of reconstructed grain boundary segments is much better suited to describe grain boundary number and to calculate f_N. Meanwhile, the dependence of the number of reconstructed boundaries on other parameters, notably the grain boundary curvature and the difference between the reconstructed boundary and the corresponding real grain boundary portion, could introduce deviation in f_N calculation. To summarize, f_N and f_L are suitable to indicate the proportion of $\sum 3$ boundaries. The ratio between f_N and f_L may be indicative but cannot describe quantitatively the number of twin boundaries per grain. In the present study, only f_L will be used to avoid the possible misinterpretation caused by f_N.

1.1.2.3 Twin density and number of twin boundaries per grain

The twin density (N_L) is defined as the number of twin boundary intercepts per unit length. Different from twin fractions, this quantity is an absolute indicator of the annealing twin content, which is independent of grain size, and commonly used in the literature for annealing twin quantification during microstructure evolution [Pande 1990][Cahoon 2009][Jin 2014]. Besides the direct measurement, the twin density can be calculated via the twin boundary length per unit area as expressed by the following equation [Underwood 1970] [Jin 2013]:

$$N_L = \frac{L_{TB}}{S}\frac{2}{\pi}, \tag{1-9}$$

where L_{TB} is the twin boundary length and S is the corresponding area.

The number of twin boundaries per grain (N_G) describes the twin content inside individual grains, and it is commonly used to illustrate annealing twin formation frequency in individual grains [Field 2007, Wang 2014]. N_G can easily be assessed from EBSD maps as follows:

$$N_G = \frac{N_2 - N_1}{N_1}, \tag{1-10}$$

where N_1 is the number of grains ignoring Σ3 boundaries in the grain detection procedure and N_2 is the number of grains by considering Σ3 boundaries as grain boundaries.

However, this quantity depending on the individual grain size should not be considered as an absolute indicator of annealing twin content in the overall microstructure. An example of this correlation will be given in the third chapter. Similar as the twin boundary fraction (both in number and length), it should only be used to compare this quantity in the microstructures having similar average grain sizes, or in individual grains having the same size.

Both of these two quantities N_L and N_G are used in the present study to quantify annealing twin evolution during recrystallization and grain growth.

1.1.2.4 2D versus 3D value of annealing twin content

For the sake of evaluating the difference in 2D and 3D values of f_L, N_L and N_G, a 3D microstructure obtained by serial sectioning combined with EBSD mapping is used. This microstructure of a nickel based superalloy sample, described in Fig. 1.9, was studied thanks to the open-source software Dream.3D which is developped with a great contribution of Carnegie Mellon University [Tucker 2012]. The microstructure is constructed using 117 2D EBSD maps. The vertical slice separation is 0.25 mm, while the step size of the EBSD scans is 0.25 µm. The 3D dataset contains about 5000 grains considering twins as grains.

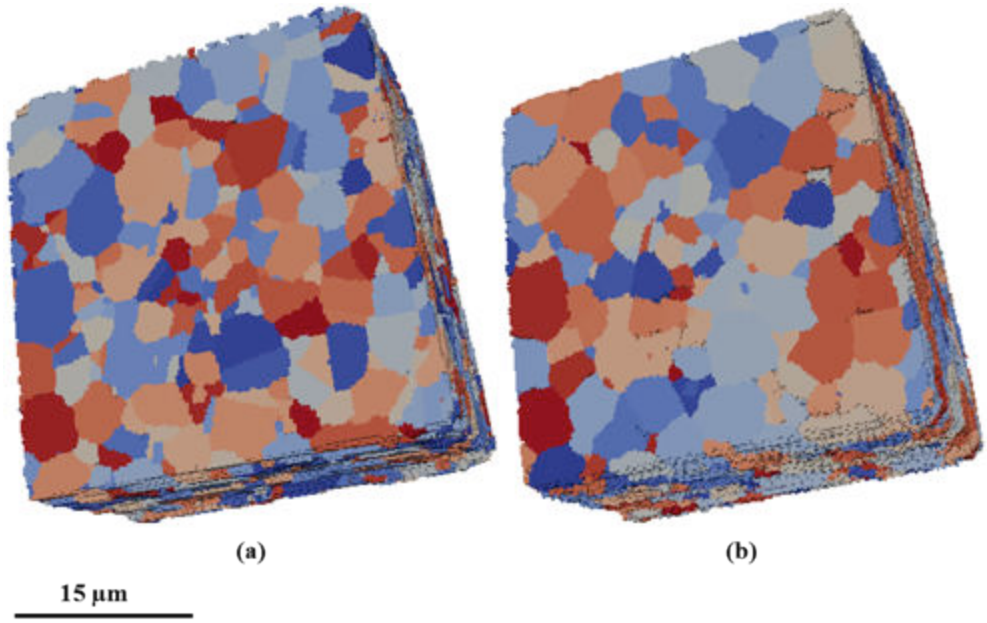

Fig. 1.9. 3D microstructure of a nickel based superalloy sample colored by grain id; (a) twins considered as grains; (b) twins not considered as grains.

	3D microstructure	1st layer	117th layer
N_L (mm^{-1})	75	60	70
N_G	0.88	0.5	0.53
f_L	0.203	0.18	0.22

Table. 1.3 Twin content in 2D and 3D.

The parameters N_L, N_G and f_L are calculated in the overall 3D microstructure and on the first and the 117th layer as shown in Table.1.3. In 3D, N_L is calculated via the total area of twin boundaries thanks to the following equation [Underwood 1970]:

$$N_L = \frac{1}{2}\frac{S_{twin}}{V}, \tag{1-11}$$

where S_{twin} is the area of annealing twin boundaries and V is the volume of the microstructure. In 3D, f_L is the area fraction of twin boundaries, which is generally considered as equivalent to length fraction in 2D [Underwood 1970]. For f_L and N_L , the 2D and 3D values are in the same range despite the limited statistical quantity of the dataset. However, since annealing twin chains exhibit complex 3D morphologies [Lin 2014], the number of twin boundaries calculated on a single section could under-estimate the real quantity in the 3D microstructure.

1.1.2.5 Conclusion

Several annealing twin quantification methods are analyzed in this section. Each method has advantages in its appropriate application field. To summarize, number and length fractions (f_N, f_L) of annealing twin boundaries are mainly suitable to quantify relative twin content in the grain boundary network but are highly sensitive to grain size. The twin density defined as the number of twin boundary intercepts per unit length and the number of twin boundaries per grain N_G can be used to describe annealing twin evolution, but N_G is also strongly correlated to the grain size. In the present PhD project, for the sake of pursuing the origin of annealing twin formation and following annealing twin evolution, the twin density and the number of twin boundaries per grain are mainly used for annealing twin quantification.

1.2. LITERATURE REVIEW ON ANNEALING TWIN FORMATION – THE GRAIN ACCIDENT MODEL: OVERVIEW AND NEW THOUGHTS

Four main schools-of-thought of annealing twin formation mechanisms and models exist in the literature. Table.1.4 summarizes the main contributions to the theoretical framework on the formation of annealing twins.

Growth accident
[Carpenter 1926], [Burke 1950], [Fullman 1951], [Gleiter 1969], [Mahajan 1997]
Grain encounter
[Burgers 1946], [Burgers 1949], [Nielsen 1967]
Stacking-Fault packets at migrating grain boundaries
[Dash 1963]
Grain boundary dissociation
[Meyers 1978], [Goodhew 1979]

Table. 1.4 Main twin formation mechanisms in the literature.

Among these models, the growth accident model is supported by a majority of recent experimental results [Song 2007] [Cahoon 2009] [Wang 2014]. Moreover, only the mathematical models based on the growth accident model, proposed by Gleiter and by Pande, provide a theoretical prediction of twin densities. In this section, we will recall at first the principle of the growth accident model. Then the Gleiter's model and Pande's model including both atomic model and mathematical formulation will be presented.

The growth accident model was first proposed by Carpenter *et al.* [Carpenter 1926] and emphasized again by Burke [Burke 1950] and Fullman and Fisher [Fullman 1951]. Gleiter [Gleiter 1969] presented an atomistic interpretation of this model and developed a predictive equation. Pande's group presented their own atomistic model in the 90s [Mahajan 1997] in order to support their mathematical model proposed earlier in 1990 [Pande 1990]. The principle of the original version of the growth accident model is shown in Fig. 1.10 [Meyers 1984]. Two grain boundaries are migrating to the right side in the Fig. 1.10. (A). The stacking error that occurs in (B) at the triple junction and remains stable under the condition that the formation event is energetically favorable:

$$\gamma_{tb}A_{12} + \gamma'_{ac}A_{13} + \gamma'_{bc}A_{23} < \gamma_{ac}A_{13} + \gamma_{bc}A_{23}\,, \tag{1-12}$$

where γ_{ij} corresponds to the interfacial energy between grain i and grain j, γ_{tb} is the interfacial energy of the twin boundary, A_{ij} is the surface of the boundary between the triple junction i and the triple junction j and the primes (') indicate the interfacial energies of the corresponding boundaries after the annealing twin formation event. The twinned area grows by grain boundary migration, but more precisely by the migration of the triple junction. If a second growth accident occurs (Fig. 1.10. (D)), then a lamellar twin spanning the entire grain will be formed.

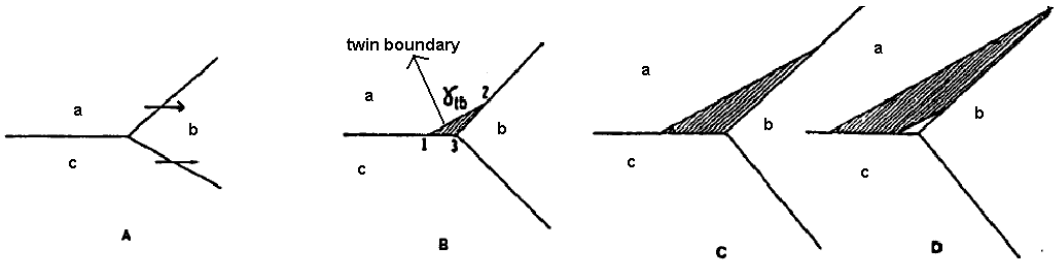

Fig. 1.10. Sequence leading to annealing twin formation in growth accident model; this figure was reproduced from reference [Meyers 1984].

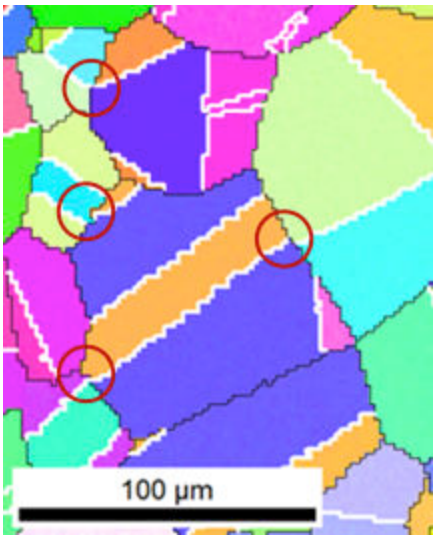

Fig. 1.11. Twin boundary network in fully recrystallized microstructure in Nickel based superalloy Inconel 718 (Same color-code as in Fig. 1.2).

Even if this was not pointed out in the literature, it is worth mentioning that for curvature driven grain growth, if the orientations of the adjacent grains do not change, the second formation event will increase the total interfacial energy compared to the first formation (detailed in section 1.2.1.1 and Fig 1.14). In this case, the second twin boundary is not stable. However, the orientation of the adjacent grains could also change due to another twin formation event. As illustrated in Fig. 1.11, in a two dimensional fully recrystallized

microstructure, twin boundaries inside different grains are indeed often found to be connected with each other (red circles). This coincidence is likely to provide orientation alternation, which could stabilize the formed twin boundaries. Under this circumstance, the formation of the second boundary of a lamellar twin can be understood as a result of the orientation change of the adjacent grain. In addition, if the adjacent grain is deformed (during recrystallization or Strain Induced Grain boundary Migration (SIBM)), first there might be an orientation gradient inside the neighbor grain and second the consumed stored energy has to be taken into account in the energy balance. These are two other reasons why the formation of the second twin boundary could be stable.

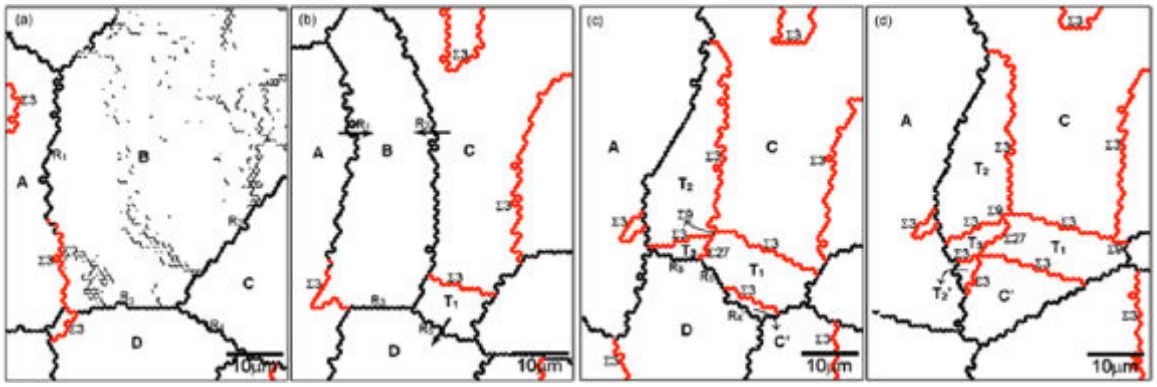

Fig. 1.12. Grain boundary maps of the same area at different annealing times showing generation and annihilation of annealing twins during the evolution of a microstructure [Song2007].

Some recent microscopic *in situ* observations support also the growth accident model [Song 2007] as illustrated in Fig. 1.12. A deformed Pb-base alloy was heated intermittently in order to sequentially follow the twin development during the annealing. As shown in the Fig. 1.12 a-d, annealing twin T1 was generated thanks to the movement of R4 at the expense of grain D, during which grain C was divided into C, T1 and C'. Here, the annealing twin formation results from the separation of a random high-angle boundary into a twin boundary Σ3 and another random boundary, which is consistent with the growth accident model. In addition, by analyzing an *in situ* 3D-XRD grain growth dataset of a pure nickel sample, Lin et al [Lin 2014] found that annealing twins could generate at triple junctions, which resulted in a net decrease in interfacial energy. Meanwhile, no lamellar twin is formed during grain growth in this 3D dataset.

Gleiter and Pande derived models, which are consistent with the growth accident model for twin density prediction, are detailed in the next sections.

1.2.1 The Gleiter's model

1.2.1.1 Atomistic model

Gleiter's atomistic model is based on microscopic observation of (static) grain boundaries, which have step-like structures. According to electron microscope observations, the steps are formed by the {111} planes in F.C.C crystals. It worth mentioning, these steps could dsappear at high temperature. The transition temperature is around $0.9T_m$ (the melting temperature) [Lee 2003]. The atoms deposit on the steps of a growing grain, and this deposition makes the steps sweep across the grain surface, which effectively moves the grain surface forward.

The Gleiter's model is derived from the assumption that '*the mechanisms generating the new lattice planes of a growing grain are also responsible for the generation of the twins'* [Gleiter 1969]. The observations by transmission electron microscopy suggest that the new {111} planes of the growing grain may be generated by two mechanisms:

1. Growth spirals [Burton 1949],
2. Two dimensional nucleation on close packed planes of the growing grain.

Other transmission electron microscopy observations, however, suggest that only the second mechanism is feasible for the creation of twins, since no lines having the form of a spiral were observed on coherent twin planes [Gleiter 1969].

In the two dimensional nucleation model, the generation of an annealing twin occurs at the boundary between a growing grain (grain II on Fig. 1.13) and a shrinking grain (grain I). The driving force of the atoms migrating from the shrinking grain to the growing grain can be the grain boundary curvature or the difference in dislocation density as implicitly considered in Fig. 1.13. However, in the mathematical formulation derived from this atomistic model, only the grain boundary curvature is considered as the driving force.

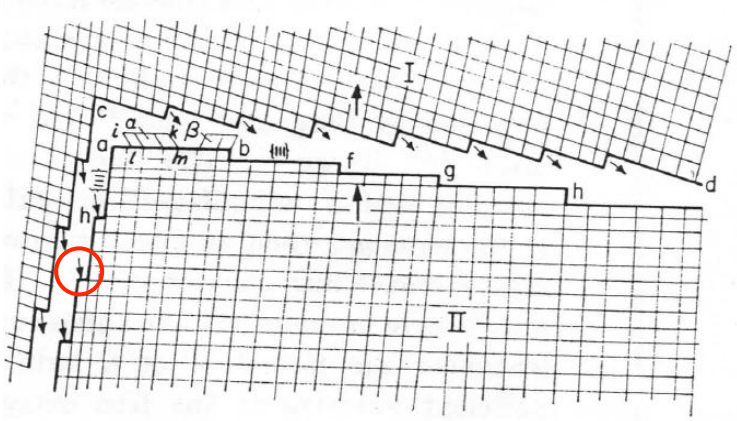

Fig .1.13. Formation of an annealing twin by the nucleation on a {111} facet (ab) from [Gleiter 1969].

The atoms impinge on the close packed plane facets (ab, bf, etc) of the growing grain (assumed to be grain II). For the F.C.C. material, if ab is supposed to be a B layer and the plane below is an A layer, as illustrated in Fig. 1.1 (b), this new-formed cluster has two possible atomic positions on the plane ab (C sites or A sites). These two correspond respectively to a continued F.C.C. stacking sequence or to the first layer of a twin structure (ABA sequence) as shown in Fig. 1.1 (b). Assuming that the atoms forming the new cluster are on A sites and that all the subsequent nuclei stack one on the other following the original stacking sequence of the F.C.C crystal, the {111} planes follow the following stacking sequence:

ABCABABCA…

which is typical of a stacking fault, not of a twin.

For a twin, the stacking sequence must be inverted:

ABCABACBA…

The twin grows until another growth accident occurs, and then the original stacking sequence of the F.C.C. crystal is retrieved.

ABCABACBA…CBACBCABC…

The B layers in red are the twin interfaces. In Fig. 1.13, if the two nuclei on the ab layer (α and β) both have the same twin orientation, then they will grow and coalesce to form a coherent twin boundary. Otherwise, the two clusters will expand by deposition of atoms at the edges, and the interface between these two clusters will be accommodated by a partial Shockley dislocation.

Assuming that the clusters are circular discs (radius r, height h), the interfacial energy change accompanying the formation of a twin can be analyzed as follows.

If the cluster and the growing grain have the same orientation, then the variation of the free energy by adding this cluster can be expressed as:

$$\Delta G = (\Delta G_v \times h + \gamma_{ik} - \gamma_{ab}) \times \pi r^2 + \varepsilon \times 2\pi r h \ , \qquad (1\text{-}13)$$

where ΔG_v corresponds to the variation of the Gibbs' free energy of the system (the bulk part) per volume of the atoms in the boundary, γ is the interfacial energy per unit area and ε is the energy of the step per unit area.

If the cluster is a twin nucleus, then the twin boundary energy γ_t must be taken into account:

$$\Delta G = (\Delta G_v \times h + \gamma_{ik}^t - \gamma_{ab} + \gamma_t) \times \pi r^2 + \varepsilon \times 2\pi r h \ . \qquad (1\text{-}14)$$

In order to guarantee that the nucleus will not vanish, ΔG should decrease with the growth of the nucleus once a critical value of the radius is reached. Thus, by taking into account the r-parabolic expression of ΔG, following relationships, used in the mathematical formulation of the Gleiter's model, are obtained:

$$\Delta G_v \times h + \gamma_{ik} - \gamma_{ab} < 0, \tag{1-15}$$

$$\Delta G_v \times h + \gamma_{ik}^t - \gamma_{ab} + \gamma_t < 0. \tag{1-16}$$

In order to validate his atomistic model, Gleiter used electron microscopy to observe a Ni-Al alloy sample (5 wt% Al), which was 99.9% cold-rolled and subsequently annealed for 20 min at 620°C. The results show that:

- Coherent twin boundaries that contain microscopic steps are found.
- Very thin twins are frequently observed.

As shown in Fig. 1.13, some nuclei may have the matrix orientation like β on the growing {111} plane. Growing together with α, these nuclei generate a step in the coherent twin plane. The same event occurs when the next few layers of the growing crystal are formed. Therefore, a coherent twin boundary can generate with small steps. However, as already pointed out, the formation of thin twins cannot be understood from a thermodynamic point of view.

It is worth mentioning that in the rationale, the formation of the second boundary of a lamellar twin is not independent of the formation of the first one. Fig. 1.14 illustrate respectively the formation of the first (*ab*) and second (a_1b_1) twin boundary of the lamellar twin A_t. The variation of the free energy associated to the formation of the second twin boundary of a parallel-sided twin $\Delta G_v^{'}$ can be expressed as:

$$\Delta G^{'} = (\Delta G_v^{'} \times h + \gamma_{i_1k_1}^t - \gamma_{a_1b_1} + \gamma_t) \times \pi r^2 + \varepsilon \times 2\pi r h. \tag{1-17}$$

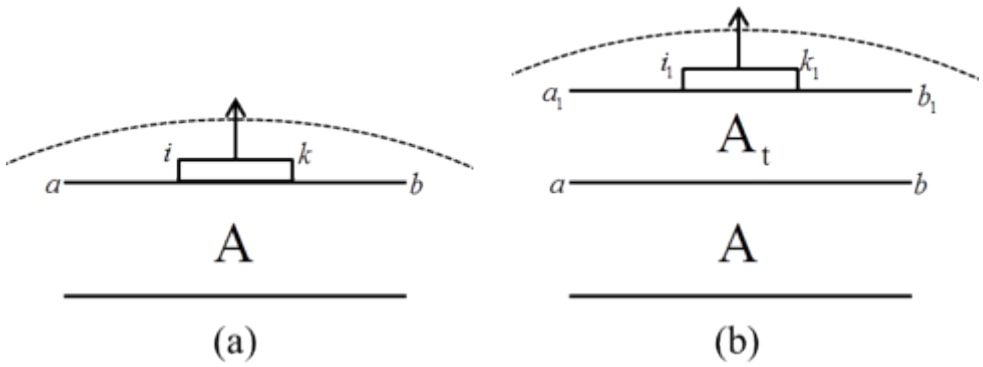

Fig. 1.14. (a) First twin boundary of a parallel sided twin Fig. 1.16. (b) Second twin boundary of a parallel sided twin.

The second nucleus should have the same orientation as the original matrix (A). Assuming that the orientation of the adjacent grain does not change, the following relationship is obtained:

$$\gamma_{a_1 b_1} = \gamma^t_{ik} \text{ and } \gamma^t_{i_1 k_1} = \gamma_{ab}. \tag{1-18}$$

This relationship leads to the instability of the second twin boundary, since $\Delta G_v \times h + \gamma^t_{i_1 k_1} - \gamma_{a_1 b_1} + \gamma_t = \Delta G_v \times h + \gamma_{ab} - \gamma^t_{ik} + \gamma_t$. This reasoning confirms our analysis of the growth accident model at the beginning of the section 2.1. During curvature driven grain growth, the formation of the second boundary of a lamellar twin is not energetically favorable if the orientation of the adjacent grain does not change.

Gleiter derived a mathematical formulation from his atomic model to predict annealing twin formation probability. This mathematical model is presented in the next section.

1.2.1.2 Mathematical formulation

The Gleiter's mathematical model closely follows the atomistic view of the process. Gleiter calculated the twin formation probability *P*, defined as the ratio between the fault nuclei (with twin orientation) and nuclei with the original matrix orientation, to quantify annealing twin formation. All the parameters used in the formulation are listed in Table 1.5. It is worth noticing that all these parameters have physical meanings. However, the determination of these parameters for certain materials is difficult, which mitigates the applicability of the Gleiter's model.

Math symbols	Physical meanings
ε	Energy of a step (surface *i_l* in Fig. 1.13.)
h	Height of a nucleus
R	Radius of a nucleus
k	Boltzmann's constant
n_0	Constant factor
γ_t	Surface energy of a coherent twin boundary (surface *l_m*)
γ_{ab}	Surface energy of the plane *a_b* (misorientation between the original matrix and the shrinking grain)
γ_{ik}	Surface energy of the plane *i_k* (misorientation between matrix-orientation nucleus and the shrinking grain)
γ_{ik}^{t}	Surface energy of the plane *i_k* (misorientation between twin-orientation nucleus and the shrinking grain)
ΔG°	Difference in the Gibbs' free energy between the growing and the shrinking grain
ΔG	Gibbs' free energy of formation of a nucleus
$\Delta G^{'}, (\overline{\Delta G^{'}})$	Gibbs' free energy of formation of a critical nucleus with matrix (twin orientation)
ΔG_v	Variation of the Gibbs' free energy of the bulk system per volume of the atoms on the boundary
Q	Activation enthalpy for grain boundary migration
T	Absolute temperature
T_m	Melting temperature
r_0	Grain radius
v	Migration rate of the grain boundary

Table. 1.5 Parameters in the mathematical formulation of the Gleiter's model.

The classical nucleation theory is applied to calculate the probability. The number of nuclei with the orientation of the matrix per unit time (n) is:

$$n = n_0 \times \exp\left\{\frac{-\Delta G^{'}}{kT}\right\}. \tag{1-19}$$

The necessary condition for a nucleus to have the critical formation Gibbs' free energy $\Delta G^{'}$ is that $\frac{\partial \Delta G}{\partial r} = 0$. From Eq. 1-13, $\frac{\partial \Delta G}{\partial r}$ can be expressed by

$$\frac{\partial \Delta G}{\partial r} = (\Delta G_v h + \gamma_{ik} - \gamma_{ab}) 2\pi r + 2\pi h \varepsilon. \tag{1-20}$$

The nucleus and the original matrix have the same orientation, thus, $\gamma_{ik} - \gamma_{ab} = 0$. Then the variation of the Gibbs free energy of the bulk system per volume of the atoms on the boundary (ΔG_v) can be expressed by

$$\Delta G_v = -\frac{\varepsilon}{r}. \tag{1-21}$$

Since

$$\Delta G^{'} = \pi h r \varepsilon = -\frac{\pi \varepsilon^2 h}{\Delta G_v}, \tag{1-22}$$

Eq. 1-19 can be rewritten as

$$n = n_0 \times \exp\left\{\frac{\pi \varepsilon^2 h}{\Delta G_v kT}\right\}. \tag{1-23}$$

Accordingly, the number of nuclei having twin orientation can be expressed by

$$\bar{n} = n_0 \times \exp\left\{\frac{-\overline{\Delta G^{'}}}{kT}\right\} = n_0 \times \exp\left\{\frac{\pi \varepsilon^2 h^2}{(\Delta G_v h + \gamma_t + \gamma_{ik}^{'} - \gamma_{ab}) kT}\right\}. \tag{1-24}$$

It is worth mentioning that since in this case the nucleus has different orientation from the matrix grain, $\gamma_{ik}^{'} - \gamma_{ab}$ cannot be ignored in Eq. 1-24.

Combining Eq. 1-23 and 1-24 and following Gleiter's rationale (by replacing ΔG_v by $\frac{\pi \varepsilon^2 h}{-Q + kT \ln \frac{\Delta G^{\circ}}{kT}}$), the twin formation probability P, defined as the ratio between n and $\bar{n}$, is expressed by the following equation [Gleiter 1969]:

$$P = \frac{\overline{n}}{n} = \exp\left\{\frac{-\overline{\Delta G'} + \Delta G'}{kT}\right\} = \exp\left\{\frac{\left(Q - kT\ln\frac{\Delta G^{\circ}}{kT}\right)(\gamma_t + \gamma'_{ik} - \gamma_{ab})}{(\gamma_t + \gamma'_{ik} - \gamma_{ab} + \frac{\pi\varepsilon^2 h^2}{-Q + kT\ln\frac{\Delta G^{\circ}}{kT}})kT}\right\}. \quad (1\text{-}25)$$

Assuming that $Q >> kT$ [Gleiter 1969], Gleiter reduced the mathematical model to Eq. 1-26. In this reduced version, the expression of the ratio is separated into two parts, which represent respectively the influence of the grain boundary mobility determined by the activation enthalpy (Q) and the influence of the driving force affected principally by the difference in Gibbs' free energy ($\Delta G°$). For curvature driven grain growth, the difference in Gibbs' free energy $\Delta G°$ can be replaced by $\frac{4\gamma_{gb}}{D}$, where γ_{gb} is the grain boundary energy and D is the equivalent grain diameter [Gleiter 1969].

$$P = \exp\left\{\frac{\left(Q - kT\ln\frac{\Delta G^{\circ}}{kT}\right)\gamma_t}{\left(\gamma_t + \frac{\pi\varepsilon^2 h^2}{-Q}\right)kT}\right\} = \exp\left\{\frac{-Q}{\left(\frac{\pi\varepsilon^2 h^2}{Q\gamma_t} - 1\right)kT}\right\}\exp\left\{\frac{\ln\frac{\Delta G^{\circ}}{kT}}{\left(\frac{\pi\varepsilon^2 h^2}{Q\gamma_t} - 1\right)}\right\}. \quad (1\text{-}26)$$

However, Li et al [Li 2006] pointed out that the hypothesis used by Gleiter ($Q >> kT$) is too strong and that the complete version of the Gleiter's model was better consistent with their own experimental data.

1.2.2 The Pande's model

Different from the Gleiter's model, the group of Pande proposed a mathematical model [Pande 1990] to predict annealing twin density evolution during grain growth and provided an atomistic model afterwards [Mahajan 1997] as a theoretical basis of their pseudo-empirical model. In the section, the presentation of the Pande's model is thus conducted according to the sequence of the publications.

1.2.2.1 Mathematical formulation

The Pande's model is based on the following experimental observations:

1. Annealing twin nucleation and growth occurs during the motion of grain boundaries.
2. The twin density is solely determined by grain size, which means that the dependence of twin density on temperature arises mostly through variations in grain size.

More precisely, Pande *et al.* [Pande 1990] assume that the increase in twin boundary number per grain (ΔN_G) is proportional to the driving force F and the increase in grain size ΔD.

$$\Delta N_G \propto \Delta D \times F . \tag{1-27}$$

Assuming $N_G = N_L \cdot D$ and considering that the driving force is only due to the grain boundary curvature, Pande *et al* [Pande 1990] obtained the following relationship:

$$N_L = \frac{1}{D} K \gamma_{gb} \ln \frac{D}{D_0} , \tag{1-28}$$

where γ_{gb} is the grain boundary energy, D_0 is the minimum grain size for annealing twin formation, and K is a constant.

Pande's model was shown to be consistent with several experimental data e.g. Baro and Gleiter [Gleiter 1969] (Cu – 3 wt pct Al), Hu and Smith [Hu 1957] (alpha brass 57.37 pct copper) and Charnock and Nutting [Charnock 1967] (80/20 brass) shown in Fig. 1.15, where the normalized grain size (D/D_0) is considered. However, it is worth mentioning that the difference between the experimental data and the Pande's model is graphically mitigated by the log scale.

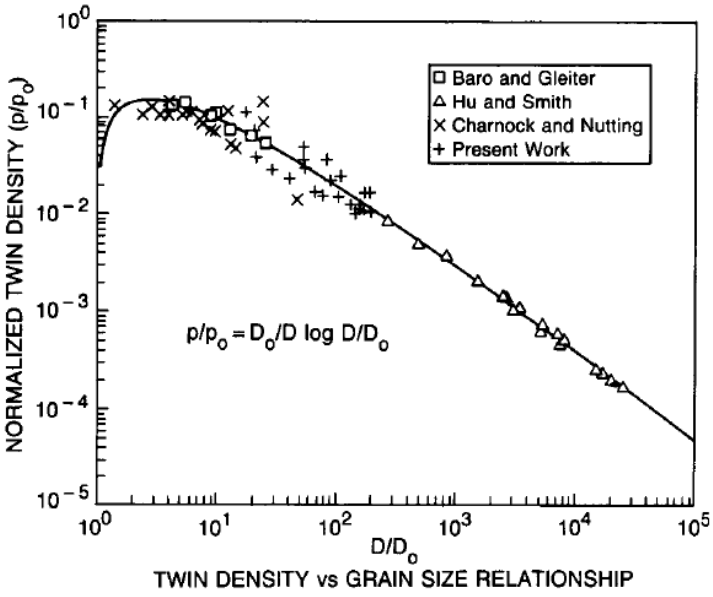

Fig. 1.15. C.S.Pande *et al* [Pande 1990] Relationship between twin density and grain size

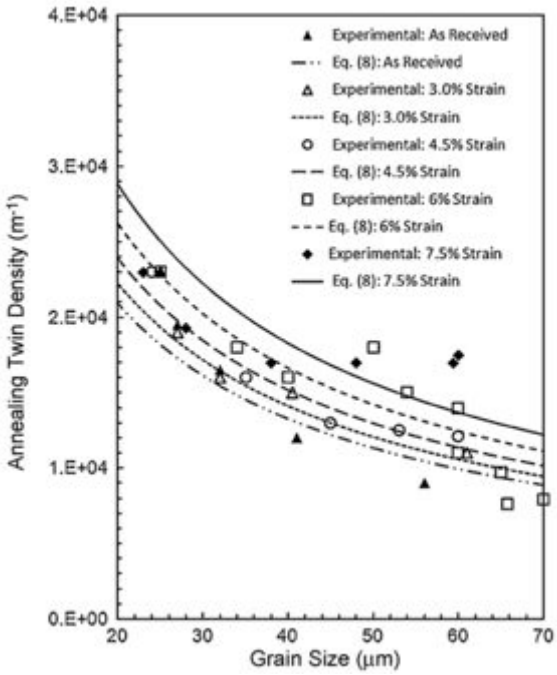

Fig. 1.16 Comparison of calculated annealing twin densities with experimental values for Ni cold rolled to various strains and then annealed at 800°C. Eq. (8) in the figure refers to Eq. 1-29 in the text; from [Cahoon 2009].

Cahoon *et al*. [Cahoon 2009] modified the Pande's model to take into account the effect of stored energy as an additional driving force for grain boundary migration:

$$N_L = \frac{C}{\gamma}\left(\frac{4\gamma_{gb}}{D}\left(1+As^2\right)\right)\ln\frac{D}{D_0}, \tag{1-29}$$

where C is a dimensionless constant, γ is the stacking fault energy, s is the plastic strain from cold working and A is a dimensionless material constant. The value s^2 is chosen become the amount of residual elastic string energy in a material is given by $Ee^2/2$ where e is the amount of residual elastic string and E is the elastic modulus. This relationship is compared with an experimental dataset of Strain Induced Grain Boundary Migration (SIBM) produced by the same research group [Cahoon 2009] (Fig. 1.16).

To summarize, the Pande's model is proven to be capable to reproduce annealing twin density evolution during grain growth (and SIBM). However, the fact that two parameters for grain growth (K and D_0) or three parameters for SIBM (by adding A) need to be identified in the mathematical formulation and that K and A do not have specific physical meaning makes the model less convincing. The validation of the Pande's model will be discussed in more detail in comparison with the experimental data obtained in the present PhD work in the following chapters.

1.2.2.2 Atomistic model

This atomistic model proposed by Pande's group has some similarities with the one proposed by Gleiter with regards to the following points:

1. The formation of annealing twins is due to grain boundary migration.
2. In both models, due to a stacking fault annealing twins are generated on the step-like structure of grain boundaries, which may very probably lie on a {111} plane in F.C.C. crystals.
3. The twin formation probability increases with an increase of grain boundary migration velocity.

As shown in Fig. 1.17 (a) [Mahajan 1997], the atoms on the hatched plane are in the B instead of the A positions. If growth accidents continue to occur during the migration of the grain boundary, annealing twins with various thicknesses can appear. The interface between the faulted area and the unfaulted area is delineated by Shockley partials.

Despite these similarities, a fundamental difference exists between the Pande's atomistic model and the Gleiter's model. In the Gleiter's model the nuclei deposit on the {111} facets of the moving grain boundary as described in Fig. 1.13. However, in Pande's model the twin nuclei form on the {111} steps, which are perpendicular to the facets as shown in Fig. 1.13 (the area circled in red). As illustrated in Fig. 1.17 (b), grain boundary PQRS moves towards the right by the movement of step MNRQ upwards, and the coherent twin boundary formed

on the {111} step will propagate towards the left, which is equivalent to the migration of the interface composed by the Shockley partials (1/6<112>). The difference between the Pande's atomistic model and the Gleiter's model is summarized in Fig. 1.17 (c).

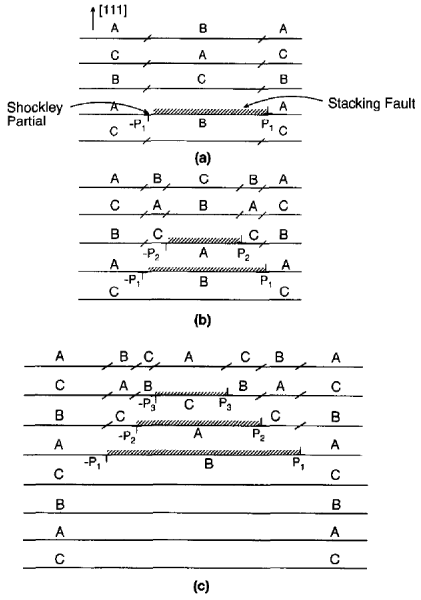

(a)

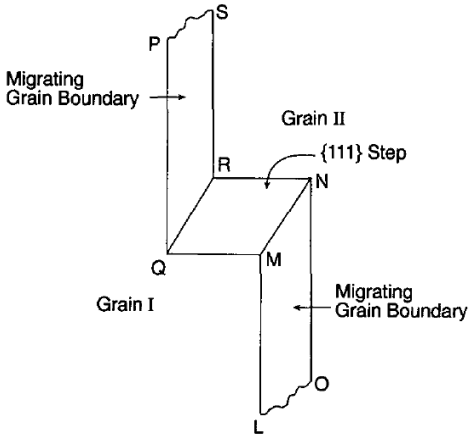

(b)

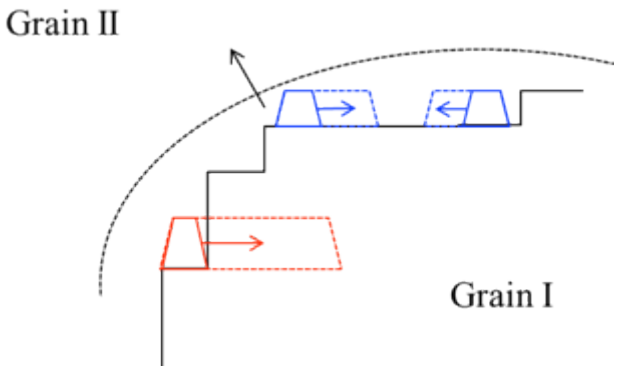

(c)

Fig. 1.17 Pande's atomistic model; (a) schematics showing the stacking arrangement of {111} planes within a one-, two-, and three-layer twin and a perfect crystal (partials P1, P2, P3 delineate the position of Shockley partials that separate the faulted and originally stacked regions); (b) schematic showing a {111} step, i.e. MNRQ, on a migrating boundary LMNO and PQRS. These figures were reproduced from reference [Mahajan 1997]; (c) annealing twin formation mechanism in the Pande's model (red) and in the Gleiter's model (blue).

Mahajan et al [Mahajan 1997] used this atomistic model to explain the formation of the different types of annealing twin morphologies illustrated in Fig. 1.1 (d). According to Mahajan et al, the driving force of an interface composed by Shockley partials is maximal when the Burgers vectors of these partials are identical. Since the Peierls stress is fairly low in F.C.C. materials, twins would tend to propagate to the other side of the grain, which corresponds to'A' and 'B' types of annealing twins in Fig. 1.1 (d). If the sum of the Burgers

vectors on the interface between the twin and the matrix grain is zero, which undermines the idea that the net associated Burgers vector is zero, then the driving force of the interface will be very small. This interface would thus be immobile and would become an incoherent twin boundary, which corresponds to the 'C' type annealing twin in Fig. 1.1. (d). However, as indicated in the previous section, one annealing twin can exhibit different types of two-dimensional morphologies. Therefore, Mahajan's explanation, which has not been demonstrated neither theoretically nor experimentally, seems to be incomplete. In addition, the nature of the drinving force for migration or expansion of a twinned volume into the bulk of a grain, thereby creating new grain boundary area, is not obvious.

In Pande's analysis, the change in free energy associated with the formation of a circular, one-layer twin of radius r was expressed as:

$$\Delta G = (\Delta G_v \times h + \gamma_{ik}^t - \gamma_{ab} + \gamma_t) \times \pi r^2 + \pi r G b^2, \tag{1-30}$$

where G is the shear module and b is the Burgers vector of the bounding Shockley partial. We can see that the only difference between Eq. 1-14 and Eq. 1-30 is that, in Eq. 1-30, the energy of the step per area ε is explicitly expressed. Therefore, same as the Gleiter's model, in Pande's reasoning, during curvature driven grain growth, the formation of the second boundary to form a lamellar twin is not energetically favorable if the orientation of the adjacent grain does not change.

The two statements, based on which the Pande's mathematical model was established, can be explained by the related atomistic model. First, with higher grain boundary migration rate, the probability of growth accident is higher and twins nucleate more frequently. Secondly, as the parameters in Eq.1-30 are weakly dependent on temperature, the dependence of twin nucleation on temperature is also weak.

Pande's atomistic model can explain the formation mechanism of annealing twins of different 2D morphologies. However, since an annealing twin can exhibit different 2D morphologies on different section planes, the explanations are less plausible. On the other hand, as noted above, the lateral propagation of the coherent twin boundary is based on the movement of the Shockley partials, but the driving force for this movement is not clear.

1.3. ON THE CALCULATION OF THE TWIN DENSITY

1.3.1 Twin density calculation

In the literature, the annealing twin formation probability P (ratio between the number of faulted nuclei with twin orientation and the number of nuclei with the original matrix orientation) is commonly considered to be proportional to the twin density N_L (number of twin boundary intercepts per unit length) [Gleiter 1969, Pande 1990, Li 2006, Cahoon 2009]:

$$N_L = \frac{P}{h}. \tag{1-31}$$

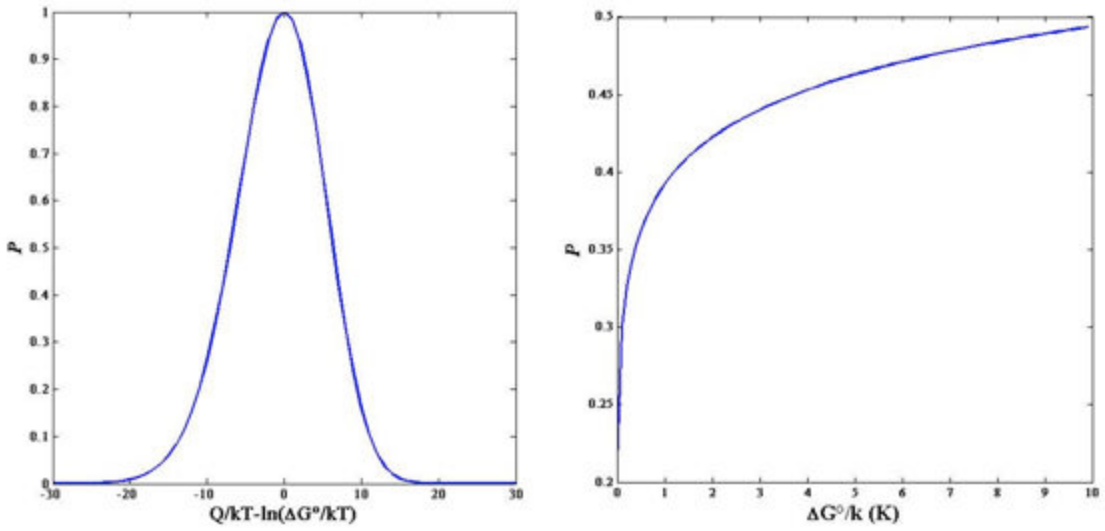

(a) (b)

Fig. 1.18 The twin formation probability P plotted as a function of (a) $\frac{Q}{kT} - \ln\left(\frac{\Delta G^{\circ}}{kT}\right)$, (b) $\frac{\Delta G^{\circ}}{k}$.

To plot Fig. 1.18, the values of the parameters of Eq. 1-25 are taken from the reference [Cahoon 2009] (Data for pure nickel). The values are given in Table.1.6.

Since h is the height of a nucleus on a {111} plane, $\frac{1}{h}$ can be understood as the number of {111} planes per unit length. In the Gleiter's model, P varies from 0 to 1 (see Fig. 1.18(a)). The twin formation probability P is expressed as a function of $\frac{\Delta G^{\circ}}{k}$ in Fig. 1.18 (b) according to Eq.1-25. This relationship indicates that P increases with ΔG°(difference in free energy between the growing and the shrinking grain). It is worth noticing that in the work of Cahoon

et al [Cahoon 2009], $\frac{\Delta G^{\circ}}{k} \approx 0.2K$ for grain growth in pure nickel ($D \approx 15\mu m$). The grain boundary migration driving force is about ten times higher during recrystallization than during grain growth (strain stored energy vs capillarity driving forces). Therefore $1K$ is a reasonable magnitude of $\frac{\Delta G^{\circ}}{k}$ during recrystallization. However, in Fig. 1.18(b), when $\frac{\Delta G^{\circ}}{k}$ equals to $1K$, P is close to 0.4. Accordingly, twin density calculated by Eq. 1-31 approximately equals to $2 \cdot 10^{9} m^{-1}$ ($2 \cdot 10^{3} \mu m^{-1}$). This value is not realistic at all for the twin density, which describes the absolute content of annealing twin boundaries. In fact, P describes the instantaneous annealing twin formation probability. Meanwhile, N_L is the cumulative content of annealing twin boundaries. Therefore, N_L can be considered as proportional to P only if P is a constant during microstructure evolution. However, as indicated by Eq. 1-25, during grain growth P is a function of the average grain size (implicitly considered in ΔG°) but not a constant.

Based on these considerations, we proposed a correction to calculate twin density from twin formation probability (P). Considering an idealized circular grain, the twin formation probability can be considered as a constant only in an increment of grain growth (dR). The increase in the number of twin boundaries inside this grain in this increment equals to $\frac{2P(R)}{h}dR$. Accordingly, the twin density in this grain could be expressed as

$$N_L = \frac{N_0 + \frac{2}{h}\int_{R_0}^{R} P(u)\,du}{2R_0 + 2\int_{R_0}^{R} du}, \tag{1-32}$$

where R_0 is a given grain radius and N_0 is the corresponding number of annealing twin boundaries. $N_0 + \frac{2}{h}\int_{R_0}^{R} P(u)\,du$ can be understood as the total number of annealing twin boundaries inside the grain of diameter $2R$. This rationale is now consistent with the calculation of annealing twin density in the Pande's model [Pande 1990]. In Eq. 1-32, when R equals to R_0, $N_L = \frac{N_0}{2R_0}$. When R is bigger than R_0, Eq. 1-32 is equivalent to Eq. 1-31 if the annealing twin formation probability P is a constant during microstructure evolution.

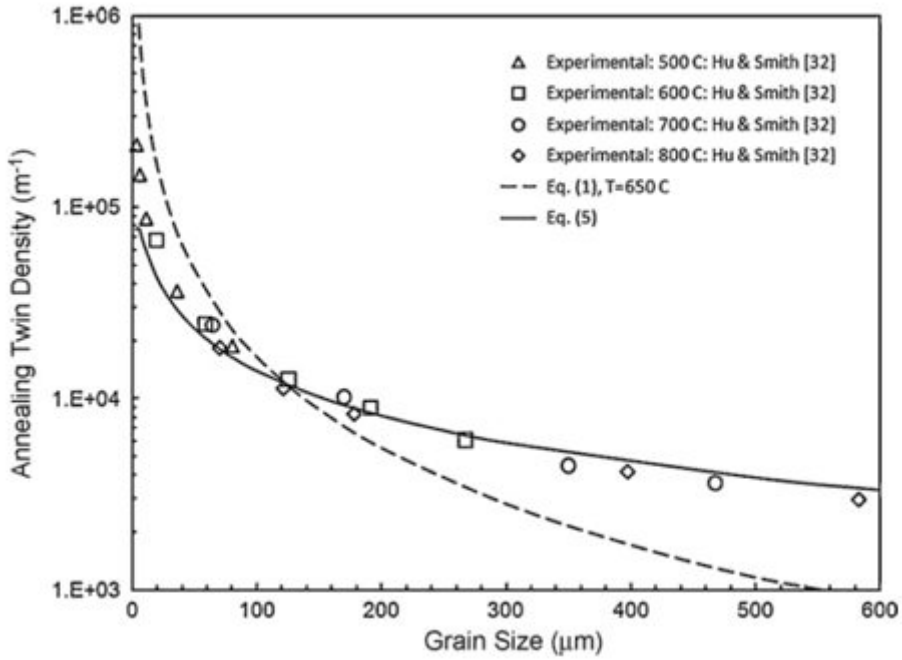

Fig. 1.19 Comparison of calculated values for annealing twin density with experimental values for Cu-32at% Zn brass annealed at various temperatures. Eq. (1) refers to Eq. 1-25 and Eq. (5) refers to Eq. 1-28; this figure was reproduced from reference [Cahoon 2009].

Cahoon et al [Cahoon 2009] compared the Gleiter's model with the experimental data produced by Hu & Smith [Hu 1956] using Eq. 1-31 for twin density calculation, as shown in Fig. 1.19. As explained previously, the twin density calculated by Eq. 1-31 is higher than the experimental data for small grain size. The twin formation probability obtained by Eq. 1-25 decreases rapidly as the grain size increases (Fig. 1.18(b)) ($\Delta G^{\circ} \propto \frac{1}{R}$ during grain growth). Consequently, the twin density calculated by Eq. 1-31, which uses the instantaneous twin formation probability to represent the average probability, becomes lower than the experimental data for large grain sizes.

The twin density calculated by Eq. 1-32 is shown in Fig. 1.20 (a). R_0 is chosen to be 10 μm, and the corresponding twin boundary number is 1.3 according to the experimental data of Hu & Smith [Hu 1956]. We use same values for the parameters in the Gleiter's formulation as in the work of Cahoon et al [Cahoon 2009] except the activation energy Q ($1.4\times10^{-19} J/atom$), which is slightly bigger than the value quoted by Cahonn et al ($1.27\times10^{-19} J/atom$) but still within the interval measured by Surholt and Herzig [Surholt 1997]. That value was adjusted to better fit the experimental data. The parameter values are given in Table 1.6 (Cu-32%Zn brass). Even it cannot perfectly reproduce them, the twin density calculated by Eq. 1-32 exhibits a better consistency with the experimental data as compared with Eq. 1-31.

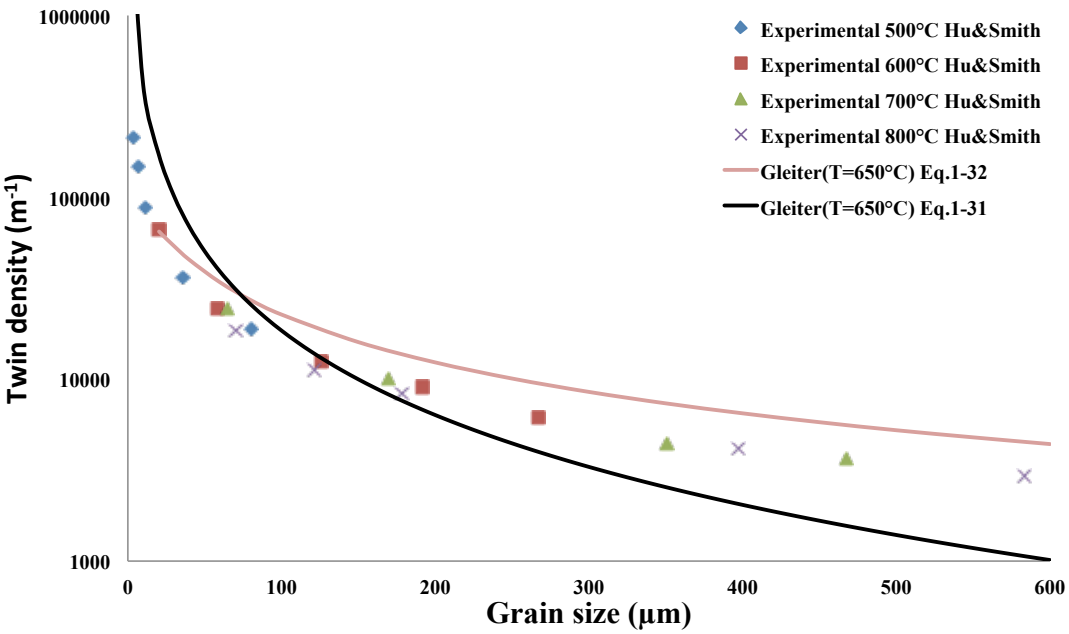

(a)

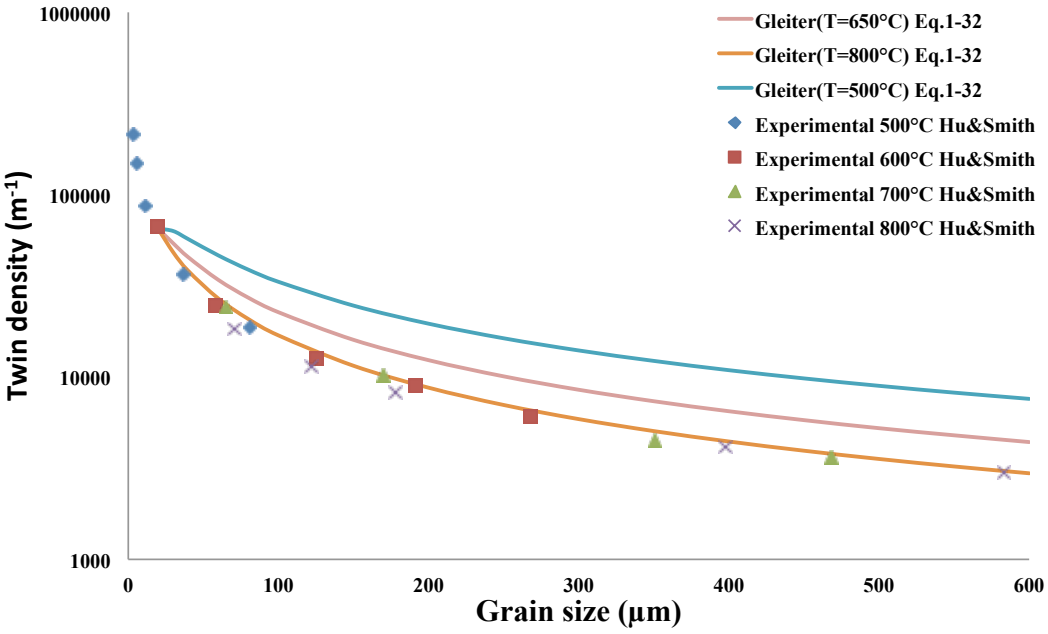

(b)

Fig. 1.20 Comparison of calculated values for annealing twin density with experimental values for Cu-32at% Zn brass annealed at various temperatures. (a) Twin densities calculated by Eq. 1-31 and Eq. 1-32; (b) twin densities calculated by Eq. 1-32 with different temperatures.

Variable	Nickel	Cu-33%atZn
$Q(J/atom)$	2×10^{-19}	1.4×10^{-19}
$\gamma_t\,(J/m^2)$	0.0336	0.0048
$\varepsilon\,(J/m^2)$	0.497	0.159
$h(m)$	2.0344×10^{-10}	2.1216×10^{-10}
$\gamma_{gb}\,(J/m^2)$	0.994	0.318

Table.1.6. Data for the calculation of annealing twin density

1.3.2 On the temperature dependence

However, this consistency with the experimental data cannot be regarded as a validation for the Gleiter's model. Hu & Smith [Hu 1956] performed four grain growth experiments at four different temperatures. They showed that i) the effect of annealing temperature on annealing twin density evolution during grain growth is not obvious and ii) the twin density is inversely correlated with the average grain size. In the work of Cahoon et al [Cahoon 2009] and for the calculation of twin density shown in Fig. 1.20(a), the mean temperature (650°C) of the range applied by Hu & Smith was used in the Gleiter's formulation. The twin densities calculated by the Gleiter's model (with Eq. 1-32) and with different temperatures are expressed as a function of the average grain size in Fig. 1.20(b). The twin density calculated by the Gleiter's model using 800°C as the annealing temperature is the most consistent with the experimental data. Meanwhile, different from this experimental data of Hu & Smith [Hu & Smith 1957] and other experimental data in the literature e.g. the data of Charnock & Nutting in Cu-19.54%Zn [Charnock 1967], Gleiter's model appears to be sensitive to the variation in annealing temperature. On the contrary, it is worth noticing that the Pande's model is not sensitive to the annealing temperature as indicated in Fig. 1.19. The reason why twin density evolution is not sensitive to annealing temperature will be explained in the third chapter based on experiments made with Inconel 718 and a mean field model will be proposed in the fourth chapter as an attempt to address the gap between the experimental data and the existing theoretical models.

1.4. CONCLUSION

In this chapter, after introducing the concept of annealing twin and its important role in physical metallurgy, especially GBE, we present the different annealing twin quantification methods used in the literature including length and number fraction of annealing twin boundaries, twin density and number of twin boundaries per grain. By comparing these methods, we have illustrated that each method has its appropriate application field. The annealing twin density, defined as the number of annealing twin boundary intercepts per unit length, will be mostly used in the present context, since it can be regarded as an absolute measure of the twin content, contrary to f_L, which is very sensitive to grain size.

The two main theoretical models of the literature i.e. the Pande's model and the Gleiter's model, including both the atomistic models and the corresponding mathematical formulations, are analyzed in this chapter. Several conclusions can be drawn based on this bibliographic study:

- Both models are consistent with the growth accident model, which asserts that a coherent twin boundary forms as a result of grain boundary migration due to a stacking fault on a {111} plane (facet or step of the moving boundary).
- Both models were initially proposed to predict twin density evolution during capilarity driven grain growth. The application of these two models within the recrystallization regime will be discussed in chapter 2.
- Adapting the classical nucleation theory, Gleiter developed a mathematical formulation to predict the annealing twin formation probability (P). However, in the literature this instantaneous probability seems to be not correctly converted into annealing twin density (N_L). A correction was proposed here.
- The Gleiter's model is shown to be sensitive to annealing temperature variation, which is not consistent with the experimental grain growth data found in the literature.
- The Pande's model is more consistent with the dependency of annealing twin density on average grain size during grain growth. However, the reason why annealing twin density would be solely determined by average grain size is not explained by this model.

Apart from those quantitative models, the analysis of the thermodynamical basis for explaining that a twin nucleus can be stable (interfacial energy balance) gave rise to two issues which are, to our knowledge, not addressed in literature:

- the formation of lamellar twin can not be explained following that rationale unless either the orientation of the neighbor grain is changing (because a grain has been consumed, or it had an orientation gradient), or another energy term must be introduced in the balance (e.g. stored energy).
- The former assumption of a necessary orientation change in the neighboring grain sounds consistent with the fact twins belonging to neighboring grains are quite often observed to be connected (Fig. 1.11).

To summarize, the understanding in the literature of annealing twin formation and its dependence on thermo-mechanical and microstructural factors is incomplete. The experimental work of the present PhD project will be conducted to explain these problems. In chapter 2, general patterns of annealing twin evolution during both recrystallization and grain growth are presented and discussed. The effects of temperature and stored energy on annealing twin evolution will be further analyzed in chapter 3.

Résumé en français

L'ingénierie de joints de grains, proposée par Watanabe dans les années quatre-vingt, vise à changer le réseau des joints de grains dans les matériaux polycristallins de type CFC via des procédés thermomécaniques séquentiels qui visent à augmenter la quantité des joints de grains spéciaux. Parmi ceux-ci, les joints de macles thermiques sont fondamentaux. L'ingénierie de joints de grains est une voie d'amélioration possible pour certaines propriétés macroscopiques comme la résistance à la fissuration intra-granulaire [Palumbo 1988] [Palumbo 1990] [Lin 1995] ou la tenue en fluage [Don 1986] [Thaveeprungsriporn 1997].

Malgré une importante littérature scientifique dédiée à ce sujet, les mécanismes de formation des macles thermiques ne sont pas totalement élucidés à ce jour. Le chapitre 1 présente les modèles existants dans la littérature pour la formation de macles thermiques. Il est composé par trois parties. Dans la première partie, après un bref rappel de ce que sont les macles thermiques, différentes méthodes pour les quantifier sont décrites et comparées. Dans la deuxième partie, les deux principaux modèles (i.e. le modèle de Pande et le modèle de Gleiter) décrivant la formation de macles thermiques au cours du phénomène de croissance de grains sont présentés. La troisième partie porte sur une ambiguité relevée dans l'une des méthodes pour permettant de quantifier les macles thermiques (calcul de la densité de macles).

Le modèle physique d'accident de croissance, qui suggère qu'un joint de macle cohérent se forme durant la migration d'un joint de grains en raison d'une erreur d'empilement, est

corroboré par la plupart des résultats expérimentaux [Song 2007] [Cahoon 2009] [Wang 2014]. La description analytique de la formation des macles thermiques par les modèles de Pande ou de Gleiter s'appuie sur ce modèle physique de l'accident de croissance. Néanmoins, l'un et l'autre de ces modèles analytiques sont incomplets, étant donné qu'ils ne considèrent que l'évolution des macles thermiques durant la croissance de grains sans considérer le cas de la recristallisation.

2. GENERAL PATTERNS OF ANNEALING TWIN DEVELOPMENT DURING RECRYSTALLIZATION AND GRAIN GROWTH

As explained in the first chapter, the growth accident model, which asserts that a coherent twin boundary forms at a migrating grain boundary because of a stacking error, is supported by a majority of recent experimental data [Song 2007] [Cahoon 2009] [Wang 2014]. However, by revising the two mathematical models i.e. the Pande's and the Gleiter's model that are consistent with the growth accident model, we found that these two models, which focus mainly on the average annealing twin evolution during grain growth, are not sufficient to explain annealing twin evolution mechanisms. This chapter aims thus at investigating general patterns of annealing twin development during recrystallization and grain growth. Three F.C.C. materials i.e. 99.995% (wt) pure nickel, the 304L stainless steel and a nickel based superalloy Inconel 718 are used for this investigation.

The most frequently used experimental techniques for studying recrystallization and related phenomena consist in considering a series of samples annealed at different temperatures and/or times, and result in average kinetics descriptions. Therefore, the local annealing twin evolution is difficult to obtain in these experiments. More accurate and detailed investigation of the twin evolution mechanism calls for more advanced characterization techniques. Developments in EBSD are enabling recrystallization and grain growth to be analyzed using an *in situ* annealing stage that can reach elevated temperatures [Kerisit 2013] [Bozzolo 2012][Humphrey 1996]. Such a technique was applied in the present study on pure nickel and 304L stainless steel.

By analyzing an *in situ* experimental data on pure nickel, we found that annealing twins are mainly formed during recrystallization and the existing twins essentially control annealing twin development during grain growth. Besides, by following annealing twin evolution in individual grains during recrystallization, different twin development mechanisms are revealed. Through another *in situ* experiments performed on 304L stainless steel, we confirmed the general trends of annealing twin evolution revealed in pure nickel. In addition to *in situ* experiments, grain growth experiments were performed on a nickel-based superalloy (Inconel718) at different temperatures making grain boundaries migrate at different rates. The number of twin boundaries per grain does not increase in the biggest grains, which control the overall microstructure evolution during grain growth. This statistical study is consistent with the twin evolutions revealed by *in situ* observations.

This chapter will be organized as follows. Firstly, the *in situ* technique used in the present work will be presented. Then the *in situ* experiments respectively on pure nickel and 304L stainless steel will be detailed successively. Finally the grain growth experiment perfomed on Inconel 718 will be discussed.

2.1. Experimental details

2.1.1 In situ heating experimental setup

By using a Scanning Electron Microscope (SEM) equipped with an *in situ* heating stage and the EBSD technique, the sample was annealed at desired temperature for a short time and was then cooled down to room temperature without removing the sample from the vacuum chamber. The area of interest was subsequently analyzed by EBSD at room temperature. By repeating this procedure, it is possible to follow the evolution of a given sample area. It provides thus a possibility to follow the annealing twin development during recrystallization and grain growth. Meanwhile, this technique remains limited to two-dimensional observations and has another main drawback, which is the possible interaction of the moving grain boundaries with the free surface.

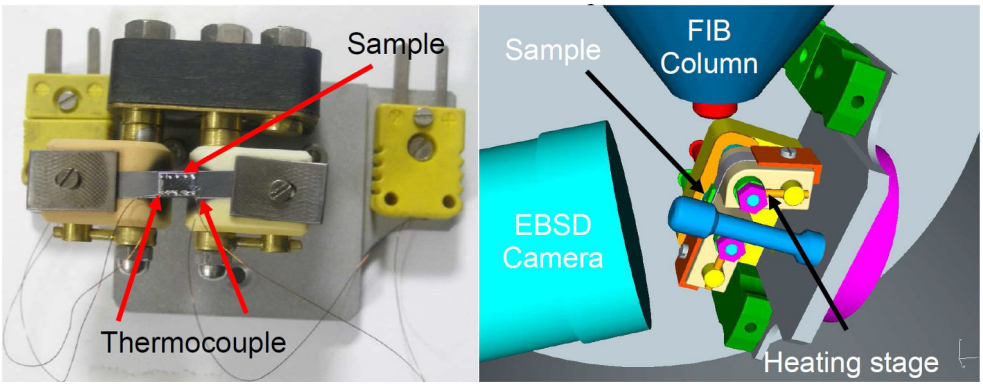

(a) (b)

Fig. 2.1 (a) Heating stage, (b) configuration of the heating stage inside the SEM chamber; the figure is reproduced from reference [Huang 2013].

In the *in situ* experiments performed in the present PhD work, a thin layer was extracted from the sample using a diamond saw and then prepared for EBSD measurements. The thin sample ($\sim 3mm \times 4mm \times 200\mu m$) was then welded on a tantalum ribbon which has a melting temperature higher than 3000°C. Two thermocouples are welded on the sample surface as illustrated in Fig. 2.1(a). One of the thermocouples is used in a feedback loop to set the input current to a specified temperature with a desired heating speed. The other thermocouple is used to record the temperature evolution. The sample is mainly heated by the tantalum sheet though heat conduction. The small size of all these system components allows for minimizing thermal inertia, and for achieving high heating rates (in the range of 100°C/s) with negligible temperature overshoot and also for naturally getting high cooling rates. Calibration runs showed that the temperature difference between the sample top surface and tantalum slice was

negligible thanks to the low thickness of the sample [Huang 2011]. Furthermore, the heating stage is compatible with the EBSD geometrical setup as illustrated in Fig. 2.1(b).

2.1.2 Annealing twin quantification in the recrystallization regime

In the present study, annealing twins, defined by a misorientation by 60° along the axis <111> with a tolerance of 8.66° according to the Brandon's criterion [Brandon 1966], are measured inside recrystallized grains all along the recrystallization regime. Following typical practice, the recrystallized grains were defined in the EBSD maps by a criterion that the Grain Orientation Spread (GOS) was less than 1° [Alvi 2008]. GOS is defined as the average of the misorientation angle between the orientation of each point inside a grain and the average orientation of that grain. In the analyses presented in this chapter, for grain detection, the minimum misorientation angle to define a grain boundary was set to 5° and twins were ignored.

As presented in the first chapter, annealing twin density defined as the number of annealing twin boundary intercepts per unit length is well suited to quantify twins during microstructural evolution. In practice, the length of twin boundaries detected inside the recrystallized grains and the recrystallized area provide the basis for the results reported here, and the twin density is obtained using Eq. 1-9. In addition, the number of twin boundaries per grain is also used in this study to determine whether new twins appeared in the developping grains. Those numbers are calculated using Eq. 1-10.

2.2. Annealing twin development during recrystallization and grain growth in pure nickel

The *in situ* experiment, presented in this section, was performed in cooperation with B. Lin from Carnegie Mellon University (CMU) to investigate in details the annealing twin development during recrystallization and grain growth. The experimental results were published in Materials Science and Engineering A [Jin 2014].

2.2.1. Experimental details

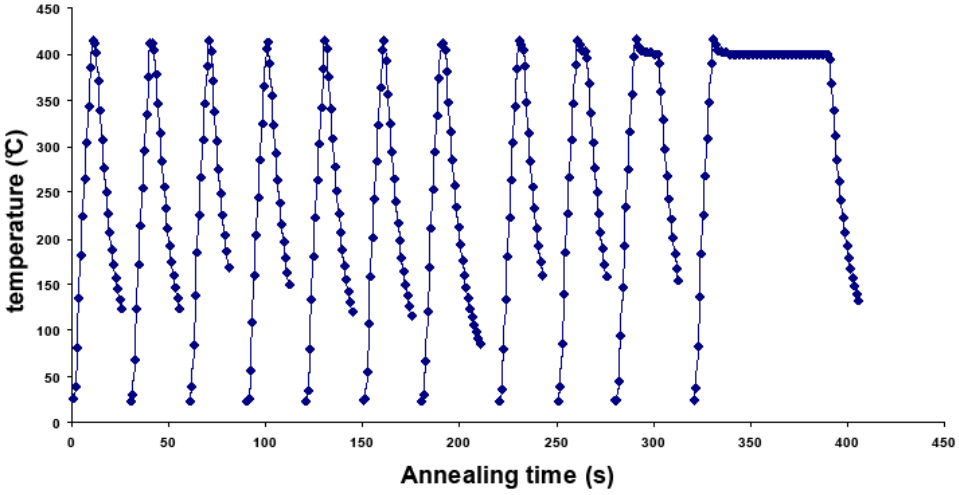

(a)

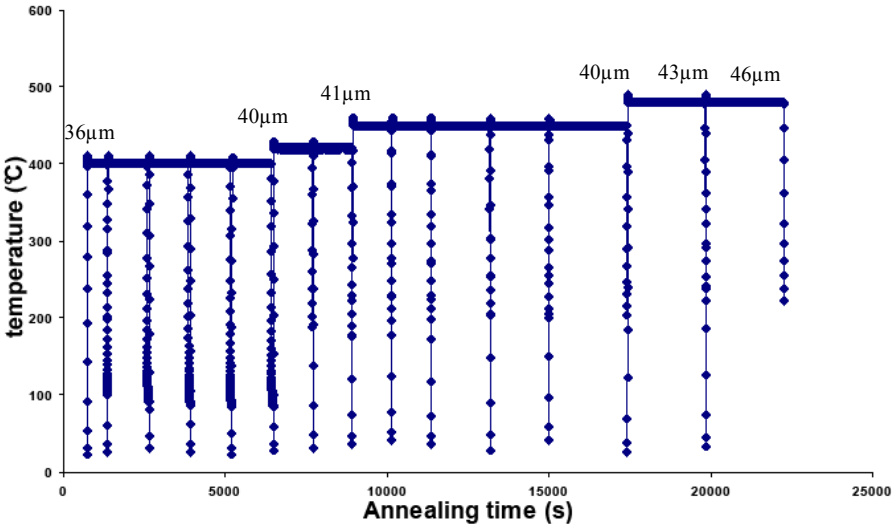

(b)

Fig. 2.2. *In situ* heat treatment sequence for the (a) recrystallization and (b) grain growth regimes. For the grain growth experiments, the area average grain sizes corresponding to the main annealing steps are indicated.

Commercially pure nickel (99.995 % wt) was used in this experiment. A cylindrical sample, 5 mm in diameter and 3 mm in height, was first compressed at room temperature to 25% height reduction. After deformation, a 200 µm thick slice parallel to the longitunal plane was extracted and metallographically prepared with a final mechanical polish using a 0.5 µm colloidal SiO_2 suspension.The sample was annealed *in situ* at 400°C in a FEI XL30 ESEM microscope equipped with a TSL EBSD system. EBSD orientation maps were recorded at the center of the sample with a 0.5 µm step size to compromise between spatial resolution and acquisition time. To capture the initial stages of the recrystallization regime, short annealing times (2s) were used at the start of the experiment. The heat treatment sequence is detailed in Fig. 2.2. Additionally, isolated pixels were not considered as grains in the following analyses.

2.2.2. Experimental results

2.2.2.1. Recrystallization

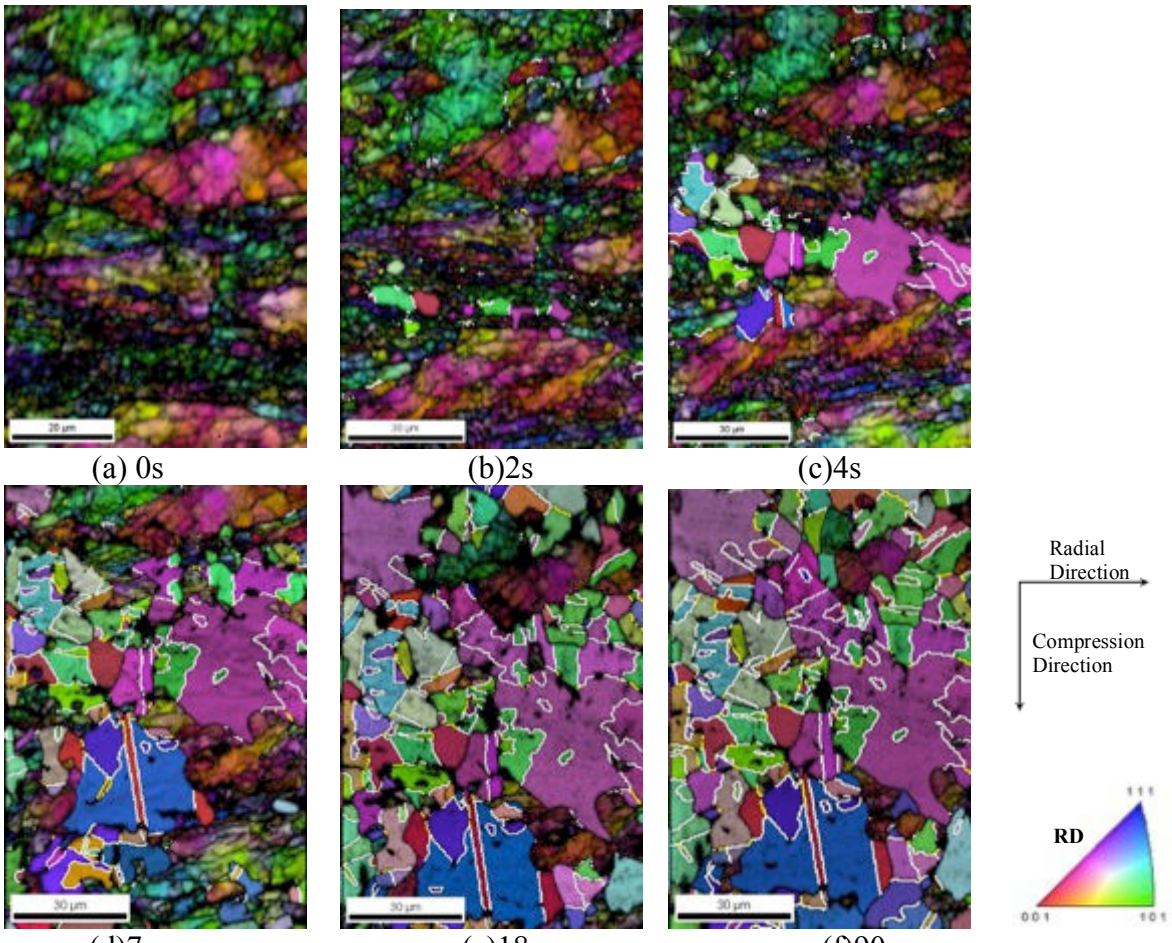

Fig. 2.3. *In situ* EBSD maps showing the progress of recrystallization. For each state, the microstructure is shown by combining an orientation colour-code (radial direction RD projected in the standard triangle) and a grey scale according to the Kikuchi pattern quality. The cumulated annealing time at 400°C is given below each map.

The series of EBSD maps in Fig. 2.3 describe the microstructural development during recrystallization. The white lines mark the annealing twin boundaries.

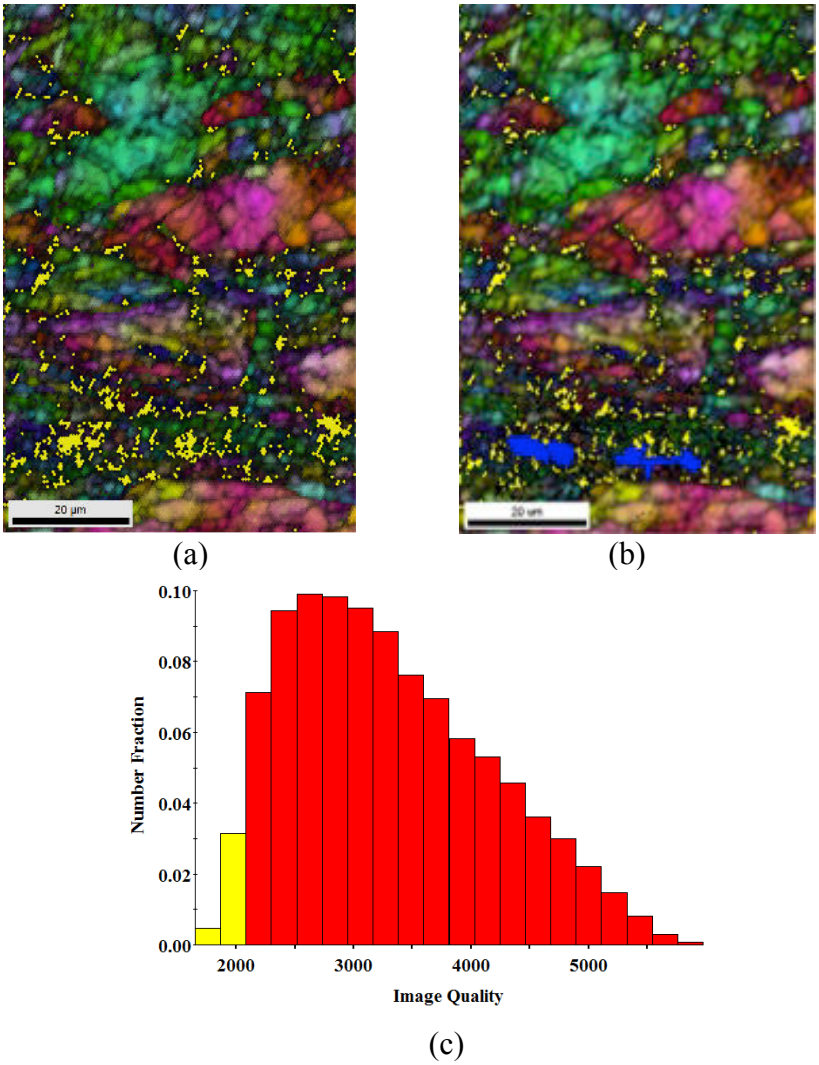

Fig. 2.4. (a) EBSD map of the initial state, the microstructure is shown by combining an orientation colour-code (same as in Fig. 2.3) and a grey scale according to the Kikuchi pattern quality. The yellow pixels belong to the first two bins in the corresponding image quality distribution. (b) Figure (a) overlapped with the two recrystallized grains that appeared after the first heat treatment (colored blue). (c) Image quality distribution.

The first map, recorded before the heat treatment, shows the heterogeneity of deformation. Recrystallizing grains first appeared in the most deformed areas where the quality of Kikuchi patterns was initially poor (Fig. 2.4) and the recrystallization front migrated very quickly into these areas. However, the spatial resolution of those EBSD maps prevents from analyzing the deformed matrix in detail. As recrystallization progressed, the first recrystallization nuclei grew together and formed clusters while new grains continued to appear in less deformed areas. The recrystallized grains began to impinge much before the end of recrystallization.

The overall recrystallization kinetics is illustrated in Fig. 2.5. In the early stages, the recrystallization nuclei grew independently and the recrystallization fraction increased rapidly. As impingement occurred after about 20s, the recrystallized grains forming clusters, the recrystallization fronts migrated at the rim of the clusters only, effectively reducing the transformation rate. The incubation time for recrystallization was negligible in this case.

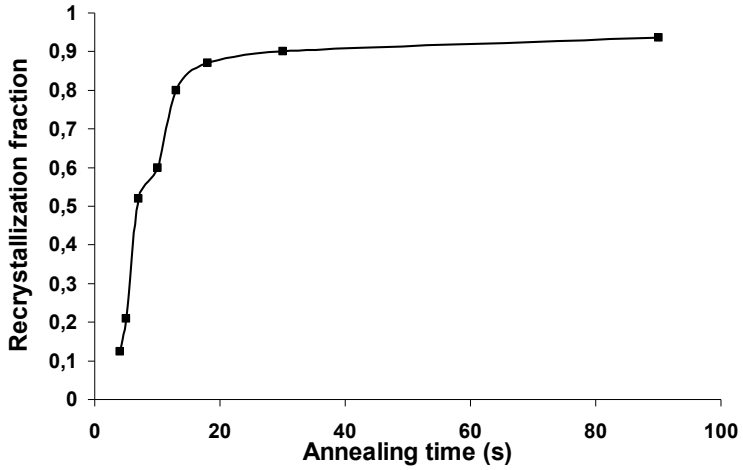

Fig. 2.5. Recrystallized fraction as a function of annealing time at 400°C.

- **Annealing twin density evolution in individual grains during recrystallization**

For the purpose of tracking the evolution of individual grains, four recrystallized grains (colored red in Fig. 2.6) were selected. Annealing twins were generated very early in the recrystallization process. As the recrystallized grains grew into the deformed matrix, more annealing twins were generated (see Fig. 2.6). However, after impingement of the recrystallized grains, fewer annealing twins were generated.

The change in size (equivalent circle diameter) of the four sampled grains with time is plotted in Fig. 2.7(a). Despite their different size range, the individual grains exhibit the same trend of first increasing in size and then stagnating before the end of recrystallization. The annealing twin density per grain was calculated with Eq. 1-9 with the twin boundary length in the grain and the area of the grain at each of the annealing steps (Fig. 2.7(b)).

The twin densities in the first three selected grains exhibit a non-linear relationship with the equivalent circle diameters (Fig. 2.7(c)). More precisely, the twin density increased most rapidly at the beginning of recrystallization and the rate of increase decreased monotonically with increasing recrystallized fraction. Meanwhile, the twin density in the fourth individual grain exhibited a different trend from the others. This grain was in contact with deformed areas until the end of recrystallization and new twins were generated continuously as it increased in size. More precisely the small grain in the yellow circle in Fig. 2.6 (Grain4 18s) was connected to the fourth grain at 90s forming new twin boundaries. The small grain in the

yellow is in fact a disjoint part of the fourth grain separated by the deformed matrix at 18s. The locally irregular shape of the fourth grain underneath the observed section plane accelerated the migration of the recrystallization front and consequently promoted annealing twin generation. Additionally, in the blue circle (Grain4 18s) the annealing twin boundaries that existed at 18s extended as the recrystallization front migrated into the deformed matrix.

Figure 2.8 describes the rate of increase of annealing twin density, i.e. the slope of Fig. 2.7(b), as a function of the growth rate of recrystallizing grains, i.e. the slope of Fig. 2.7(a). At the early stages of recrystallization, both the sizes of the recrystallized grains and the annealing twin densities increased at the highest rate. Later, the sizes of the recrystallized grains increased more slowly and fewer annealing twins were generated. This trend is easily understood because rapid changes occur during the initial unimpeded growth of recrystallizing grains into a deformed matrix, but the rate decreases once the recrystallized grains impinge.

In our *in situ* annealing series, three mechanisms appear to contribute to changes in the annealing twin density in individual grains. The first is that new annealing twins are generated as recrystallized grains increase in size. The second is that annealing twin boundaries intersecting migrating recrystallization fronts are extended in length as the recrystallization front advances. Both mechanisms are illustrated in Fig. 2.9(a). In addition, a third phenomenon that derives from the three-dimensional nature of the sample, contributes to an apparent increase in twin density. As shown in Fig. 2.9(b), in the yellow circle, the red grain and the green grain are twin related, even though they appear to be separated by the deformed matrix. They are actually two pieces of the same twinned grain that are connected below the section plane. The twinning event obviously occurred underneath the observed section plane. This phenomenon is actually another case of twin boundary extension mentioned above, but complicated by the irregular shape of the recrystallization front which results in disjoint parts of the twin-related grains reaching the observation surface at different times. Contrary to the mechanisms illustrated in the red circle of Fig. 2.9(a), this is more likely to happen during recrystallization than during grain growth. This is because local fluctuations in the stored energy can cause recrystallizing grains to develop convex shapes that are unlikely to occur during grain growth, i.e. a recrystallization front can migrate in the opposite direction to its center of curvature.

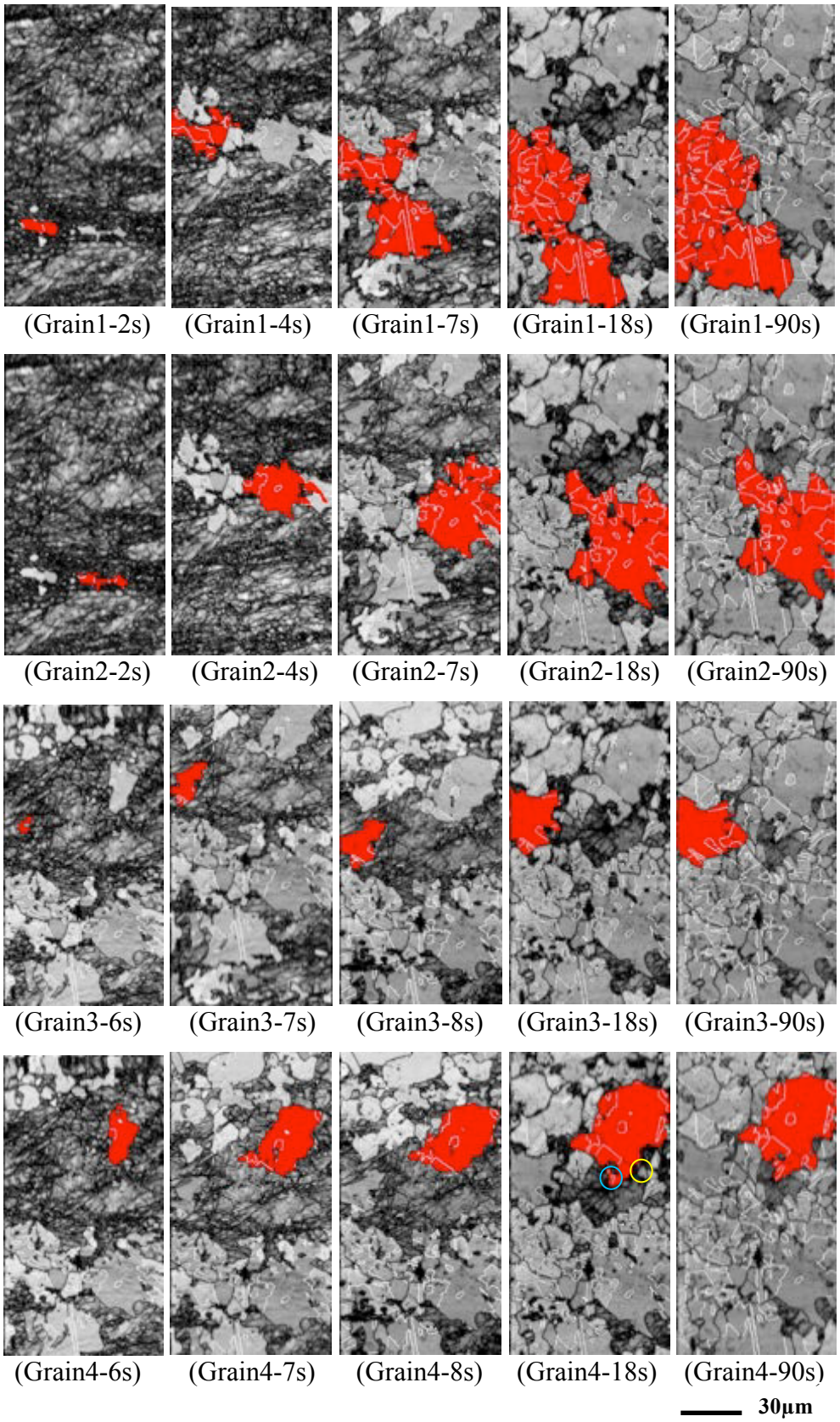

Fig. 2.6. Individual grain evolution. Selected grains (one per row) are colored red in the EBSD maps (grey scale shows the Kikuchi pattern quality). The accumulated annealing time is shown under each map. The thick white lines denote Σ3 boundaries. The blue circle and the

yellow circle in Figure (Grain4-18s) point out the two phenomena that contributed to the increase in annealing twin density in the fourth grain at the end of recrystallization.

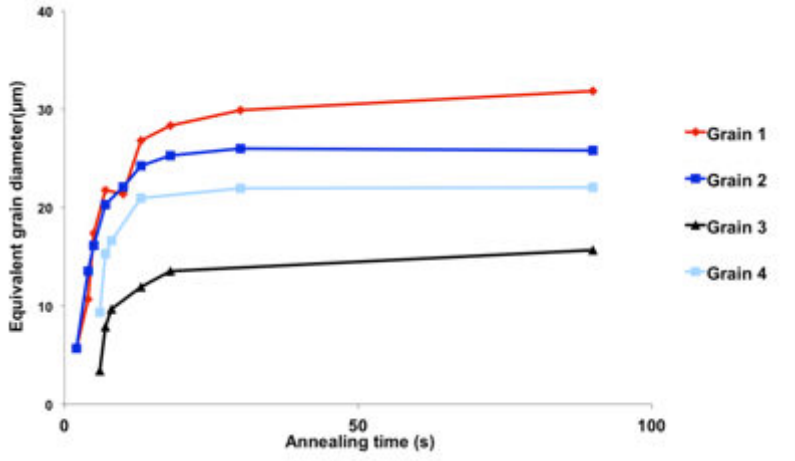

(a)

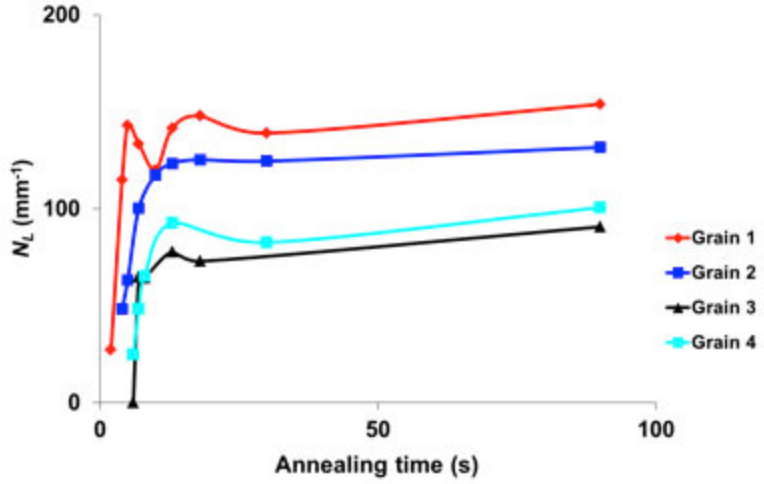

(b)

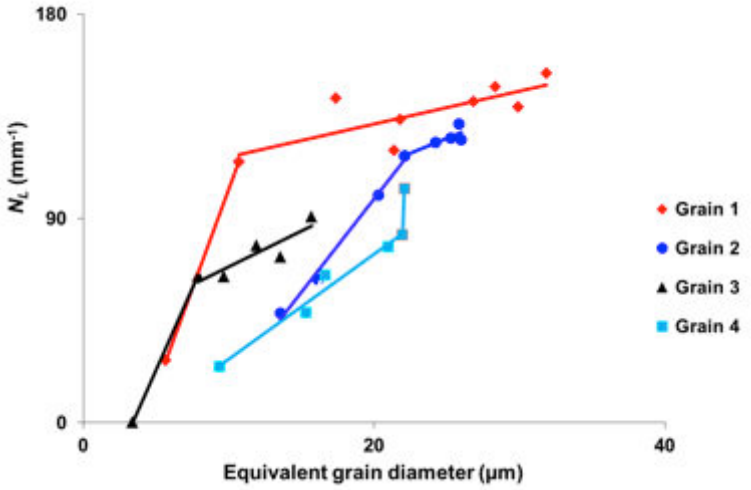

(c)

Fig. 2.7. Individual grain evolution: (a) grain size, (b) annealing twin density, (c) annealing twin density in individual grains as a function of equivalent circle grain diameter.

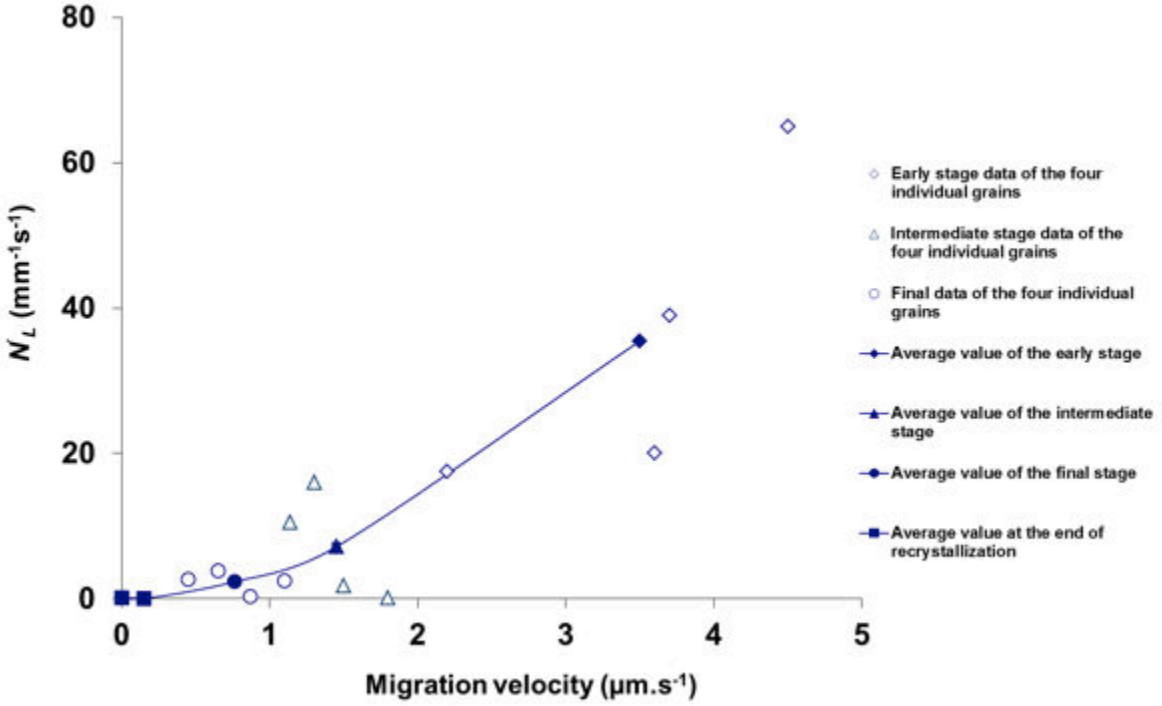

Fig. 2.8. Correlation of annealing twin density evolution rate with grain growth velocity.

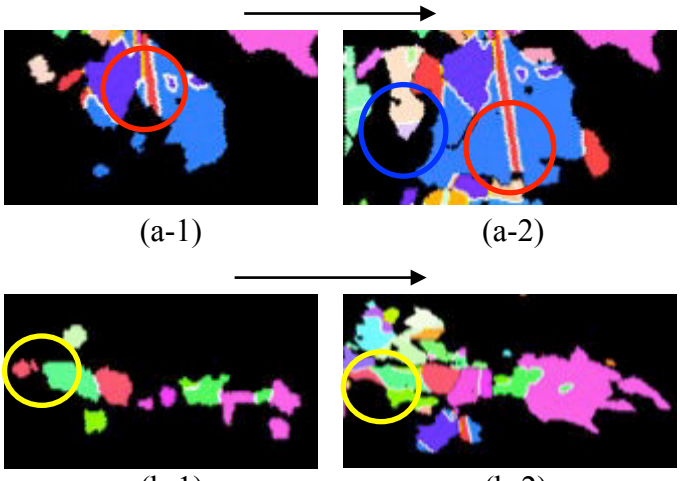

Fig. 2.9. Details of successive EBSD maps taken out of the *in situ* annealing series, showing different twin evolution mechanisms: extension of an existing twin in the section plane (red circle in (a)), generation (blue circle in (a)), propagation from below the analyzed section (yellow circle in (b)). Only recrystallized grains are shown (same orientation color code as in Fig. 2.10). The black part represents the deformed matrix. In (b-1) the misorientation between the two grains surrounded by the yellow circle is 59.5° <1 -1 1>.

To summarize, as recrystallization proceeds, the deformed matrix shrinks, the average stored energy level decreases and recrystallized grains impinge on each other forming clusters, thus slowing down their growth rate in both 2D and 3D. As the rate of the recrystallization front

slows down, fewer twin boundaries are created and the rate of extension of existing twins decreases. Additionally, fewer new annealing twin boundaries appear at the sample surface by the emergence of twin boundaries from below the section plane. Thus a correlation exist between recrystallization front migration rate and the rate of increase in annealing twin length.

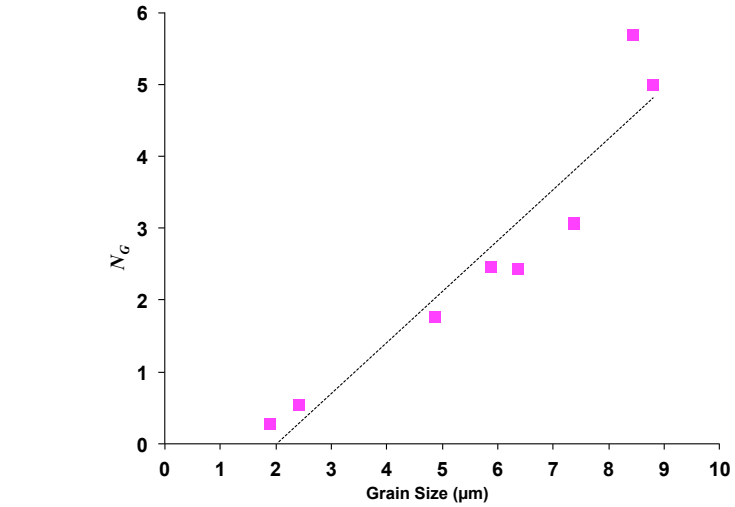

(a)

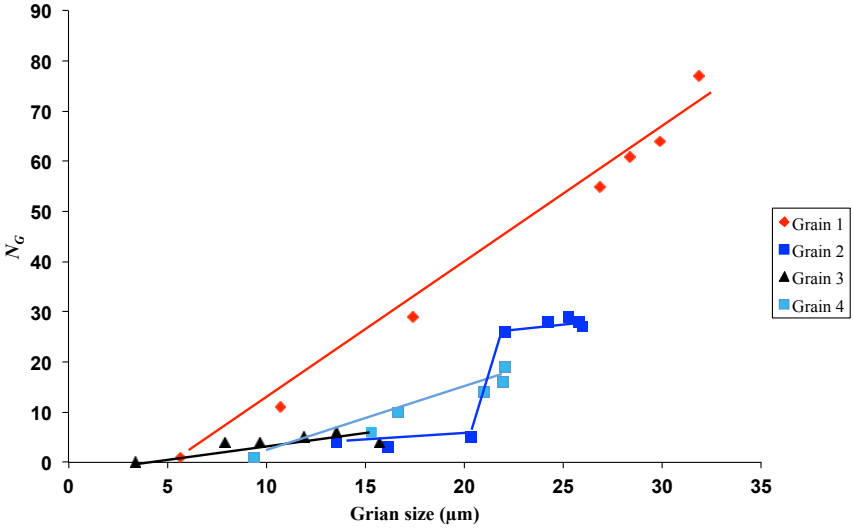

(b)

Fig. 2.10. Annealing twin density evolution (a) in the overall recrystallized microstructure; (b) in the selected individual grains.

In addition to the twin density, the number of twin boundaries per grain (N_G) was also measured (Fig. 2.10). The correlation between N_G and the average grain size also appears to be linear over the whole recrystallization process (Fig 2.10 (a)), which is consistent with the result in the literature [Field 2007, Wang 2014]. N_G in the individual grains also increases with the grain size measured as the equivalent circle diameter (Fig 2.10 (a)). In Grain 2 and 3,

the increase in N_G stagnated at the end of the recrystallization when the recrystallization front migration driving force mitigated. Similarly to the N_L parameter, N_G increased at the end of recrystallization in Grain 4. This increase can also be related to the local migration of the recrystallization front. As for the first grain, it impinged with other recrystallized grains with twin relationship with it, which suddenly increases the total number of twin boundaries.

- **Average annealing twin density evolution during recrystallization**

Fig. 2.11(a) illustrates the average recrystallized grain size evolution. The equivalent grain diameter is the *arithmetic mean* of the equivalent circle diameters of the recrystallized grains. The grain size evolution is consistent with the recrystallization kinetics. At the beginning of recrystallization, the recrystallized grains grew independently so that the average grain size increased rapidly. After impingement, the average grain size increased more slowly.

Here, using Eq. 1-9 with the twin boundary length in all the recrystallized grains and the entire recrystallized area, we calculated the annealing twin density in the recrystallized part. Fig. 2.11(b) shows that the average annealing twin density in the recrystallized grains increases linearly with the average recrystallized grain size. The rate of increase of the average annealing twin density is proportional to the average grain boundary migration rate, as illustrated in Fig. 2.11(c).

The correlation between the average twin density and the average grain size, Fig. 2.11(b), appears to be linear over the whole recrystallization process, contrary to the behavior of individual grains where two regimes could be depicted (Fig. 2.7). There are two factors that contribute to this difference. First, the continuous appearance of small recrystallized grains that nucleate or simply emerge from below the surface slows down the increase of the average recrystallized grain size. Second, as illustrated in Fig. 2.6, annealing twins are generated almost as soon as recrystallized grains appear on the observation surface. The annealing twin density in the recrystallized grains after the 2 s heat treatment is indeed higher than 60 mm^{-1}, which means that there were many annealing twins generated in the very early stages of recrystallization. Thus, the continual appearance of recrystallized grains effectively smoothes the rate of increase in annealing twin density.

To summarize, both the annealing twin density in the individual grains and the average twin density in the entire recrystallized domain increased during recrystallization. However, the creation of annealing twins in individual grains is clearly sensitive to the decrease in migration rate of the recrystallization front, which cannot be depicted as clearly from average microstructural quantities.

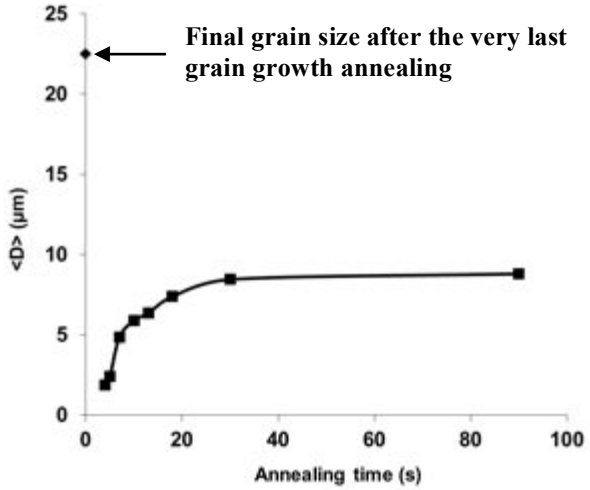

(a)

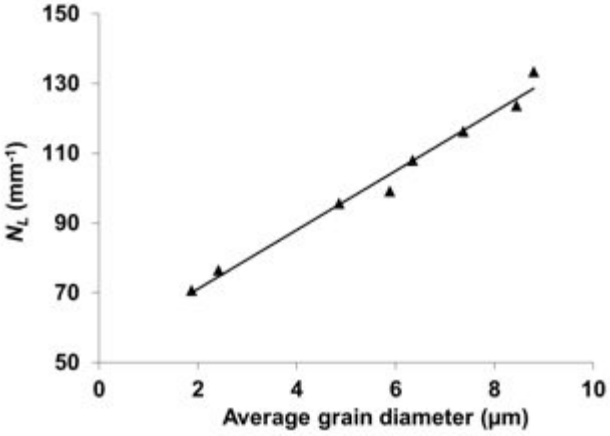

(b)

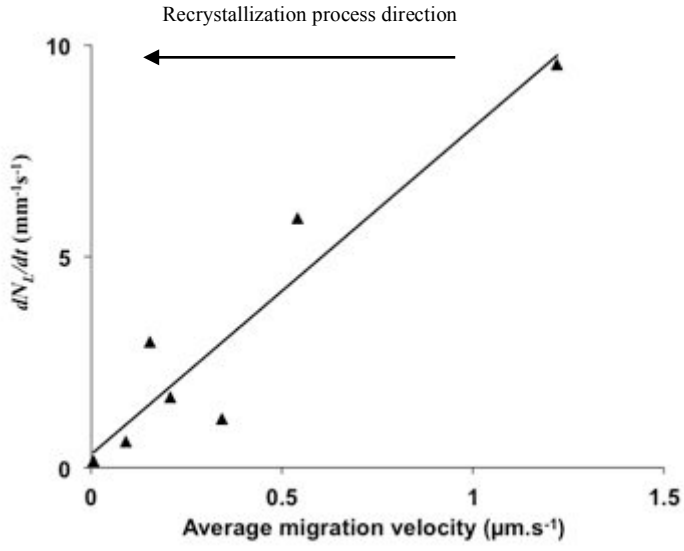

(c)

Fig. 2.11. (a) Average grain size evolution during recrystallization and after grain growth; (b) average annealing twin density during recrystallization as a function of average recrystallized grain size; (c) average annealing twin evolution rate as a function of average recrystallization front migration rate, showing that the twin generation rate is positively correlated with the migration rate.

2.2.2.2. Grain Growth

The *in situ* recrystallization experiment was performed at 400°C. However, because the driving force is much lower, grain growth is a much slower process. Therefore, the annealing temperature was increased gradually until grain growth could be detected, as shown in Fig. 2.2 (b). Because the temperature was adjusted in a relatively small range, the possible influence of annealing temperature on annealing twin fraction as reported by Randle [Randle 2008] and Brons [Brons 2013] will not be considered here.

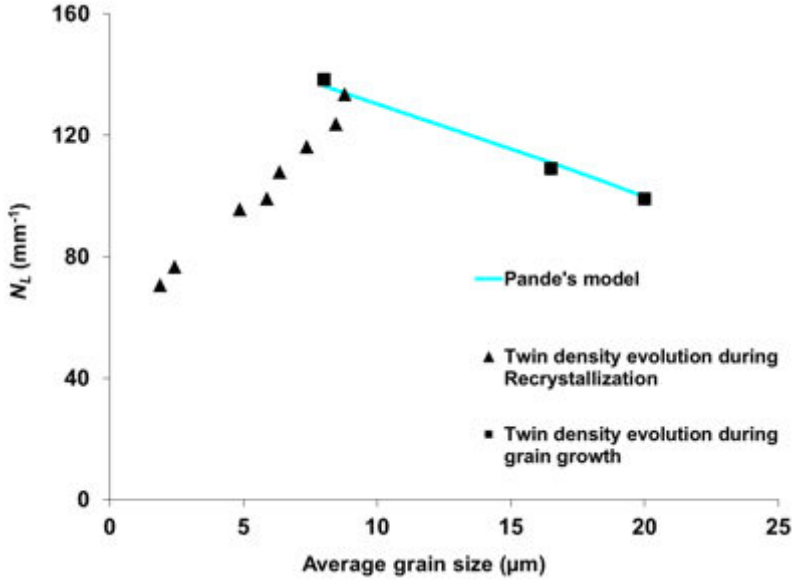

Fig. 2.12. Annealing twin density evolution in the grain growth regime (black squares) for three different annealing times in pure nickel (Fig. 2.2(b)) as a function of average grain size. The tendency is opposite to the dependence that applies during recrystallization (black triangles). The final arithmetic average grain size of the recrystallization regime is somewhat larger than the average grain size at the beginning of the grain growth regime because of a shift in the locations of the two considered areas.

The evolution of the average annealing twin density in the grain growth regime is presented in Fig. 2.12.

Here we used Eq. 1-9 with the twin boundary length in the entire analyzed domain and the area of the domain to calculate the average twin density. In contrast to the recrystallization regime, the twin density decreased continuously during grain growth. Despite the non-constant annealing temperature, it is still possible to fit the experimental data with the original version of Pande's model [Pande 1990] (Eq. 1-28). By using $\gamma_{gb} = 0.994\ J.m^{-2}$ [Murr 1972], parameters K and D_0 could be identified mathematically by an inverse method: $K = 0.94\ m^3.J^{-1}$ and $D_0 = 2.5\mu m$. These values are similar to those quoted by Cahoon

[Cahoon 2009] for pure nickel. The identified value of D_0 is in the right range of magnitude as compared to the smallest detectable grain size to trigger twin generation that was observed in the recrystallization regime.

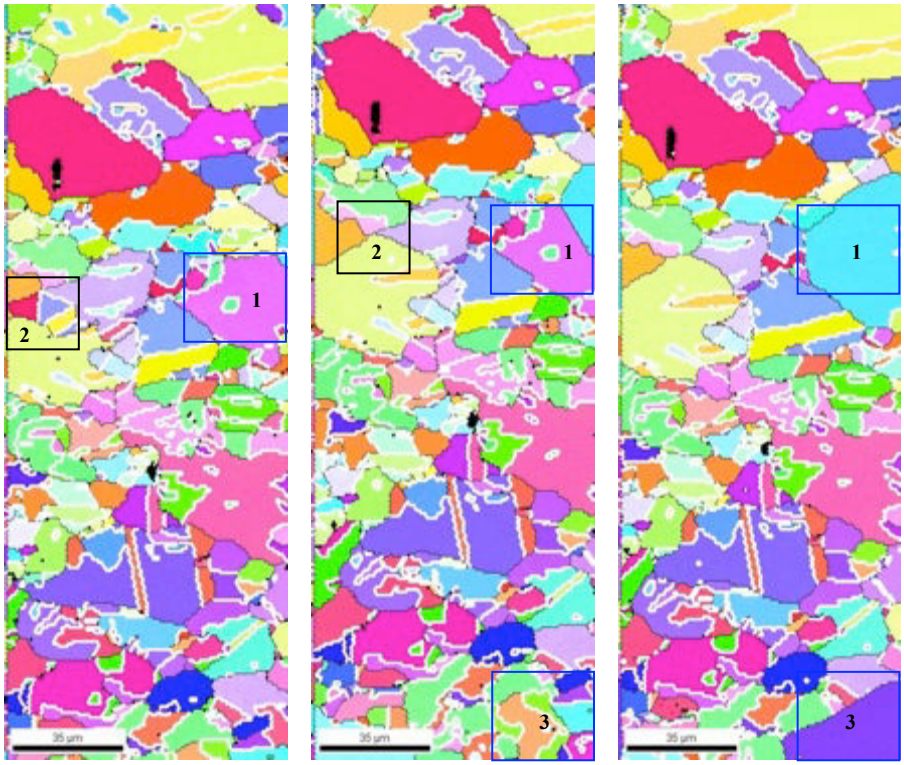

Fig. 2.13. *In situ* EBSD maps of the last three annealing steps in the grain growth regime. The black lines represent the general grain boundaries defined by a disorientation angle above 5°; the white lines denote the twin boundaries (same orientation color code as in Fig. 2.3. Note the (apparently) island grain (green) disappears as the pale blue grain grows in from the right.

The decrease in annealing twin density can be attributed to disappearance mechanisms shown in Fig. 2.13. In all three examples, small grains containing several twin boundaries were consumed by large grains, which grew without producing new twins. Such a microstructural evolution is of course energetically favorable. Meanwhile, this is not the only possible annealing twin evolution mechanism observed during grain growth. The shrinkage of twin lamellae caused especially by the migration of incoherent twin boundary segments was reported previously in a Pb-based alloy [Song 2007] and in 304L stainless steel [Jin 2013 and next section]. Besides, a few annealing twins are found formed at triple junctions during grain growth in a 3D-XRD dataset of a pure nickel sample [Lin 2014]. These creation events are obviously too rare to counterbalance those leading to twin disappearance, since the net balance is negative.

Certain formation mechanisms reported in the literature, like annealing twins formed on propagating {111} steps and then moving inside the grain as proposed by Mahajan *et al*. [Mahajan 1997], were not observed at all.

2.3. Annealing twin evolution during recrystallization and grain growth in the 304L stainless steel

This *in situ* experiment was performed by K. Huang in his PhD work dedicated to recrystallization phenomena in 304L stainless steel [Huang 2011]. We reanalyzed these *in situ* datasets for the purpose of following annealing twin evolution during recrystallization.

2.3.1 Material and thermo-mechanical treatments

Austenitic stainless steels, which do not undergo discernible phase transformation during hot-working over a wide temperature range, are ideal model alloys to investigate recrystallization. 304L austenitic stainless steel has a low stacking fault energy ($\approx 0.02 Jm^{-2}$) and so annealing twins are generated easily [Lehockey 1998]. That is why this alloy is also favorable for annealing twin formation observation. The melting temperature of 304L is 1400°C. The recrystallization phenomena of 304L were analyzed in detail in the PhD work of K. Huang [Huang 2011]. The chemical composition (weight percentage) of the material is given in Table 2.1. In the following, three such 304L samples which have been submitted to hot torsion tests are analyzed. The details of these tests are indicated in Table.2.2.

C	Mn	Si	P	S	Cr	Ni	N
<0.03	<2.00	<0.75	<0.045	0.03	8.0~12.0	8.0~112.0	<0.10

Table 2.1. Chemical composition of 304L (wt%, balance Fe).

	Deformation temperature (°C)	Strain rate (s^{-1})	Strain level
Sample 1	1000°C	0.01	0.3
Sample 2	1000°C	0.01	1.5
Sample 3	1000°C	0.1	0.4

Table 2.2. Thermo-mechanical history of the analyzed 304L samples.

After thermo-mechanical treatment, samples were water quenched to fix as much as possible the microstructure. After the quenching, the samples were annealed at 1000°C inside the SEM chamber using the *in situ* annealing technique presented in the section 2.1.1.

2.3.2. Experimental results

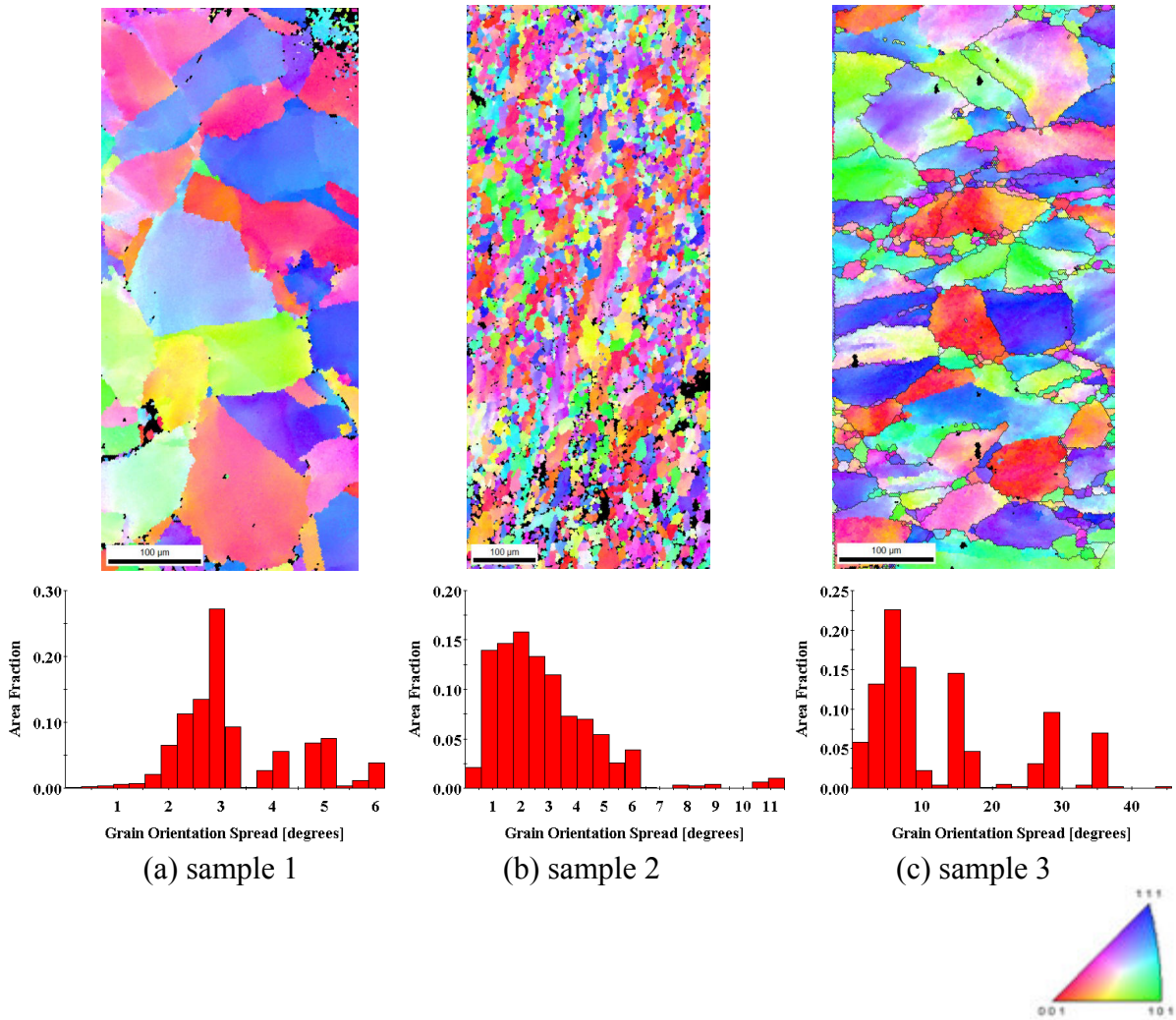

(a) sample 1 (b) sample 2 (c) sample 3

Fig. 2.14. The microstructures after the hot deformation of sample 1 (a), sample 2 (b), and sample 3 (c) shown as an orientation colour-coded EBSD map; The corresponding distributions of Grain Orientation Spread (GOS) are given below each microstructure.

The microstructures of the three samples after hot-torsion testing and quenching are illustrated in Fig. 2.14. The GOS distributions, which can be used to semi-quantify the stored energy level, are also given in Fig 2.14. Even though the maximal GOS value is higher in sample 2, the area fraction of grains with a GOS<2° is higher in sample 2 than in sample 1. In sample 2, grains are much smaller which is an obvious sign that dynamic recrystallization occurred. On the other hand, almost no recrystallization nuclei were found in sample 1. This difference leads to different microstructural evolution behaviors in these two samples during the subsequent heat treatment. In samples 1, static recrystallization occurred. Meanwhile, controlled by the growth of the recrystallization nuclei formed during the dynamic recrystallization, post-dynamic recrystallization also occurs in sample 2. Similar with sample 1, there are few recrystallization nuclei in sample 3. However, thanks to higher deformation

amount and deformation rate, the GOS value in sample 3 is much higher than in the sample 2, which leads to a faster recrystallization kinetics. In the dataset of sample 3, the recrystallization regime was so fast that it was barely captured. Therefore, in the present study, sample 1 and sample 2 will be used to study the recrystallization regime and sample 3 will be used to analyze annealing twin evolution during grain growth.

2.3.2.1. Annealing twin evolution during recrystallization

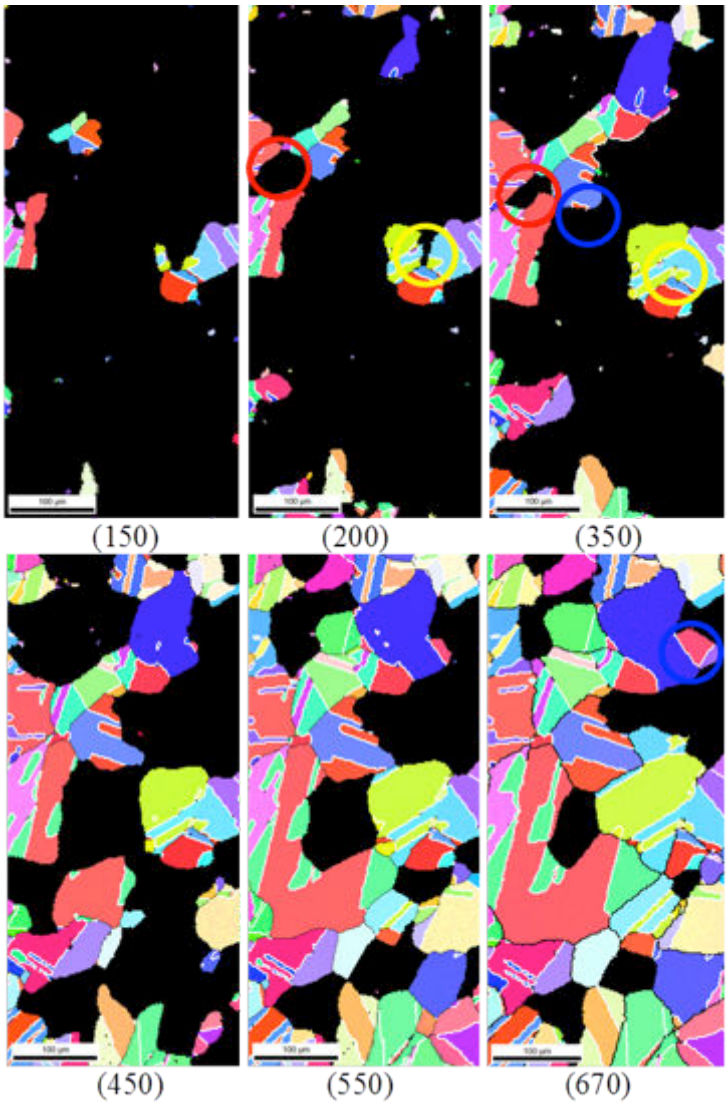

Fig. 2.15. Recrystallized grain evolution in sample 1; cumulative annealing time (s) are indicated below each map (same color code as in Fig. 2.14); white lines denote ∑3 boundaries; black lines denote high anlge boundaries defined by a disorientation angle above 5°.

The evolutions of the recrystallized grains in sample 1 and sample 2 are respectively shown in Fig. 2.15 and Fig. 2.16. In sample 1, since dynamic recrystallization was not triggered during hot deformation, the microstructural evolution was mainly controlled by the growth of nuclei

most probably formed during the heat treatment. Meanwhile, in sample 2, the recrystallization nuclei formed during the hot deformation continued to grow and consumed the deformed grains. The difference in nucleus number and in the stored energy level inside the deformed grains leads to different recrystallization kinetics shown in Fig. 2.17.

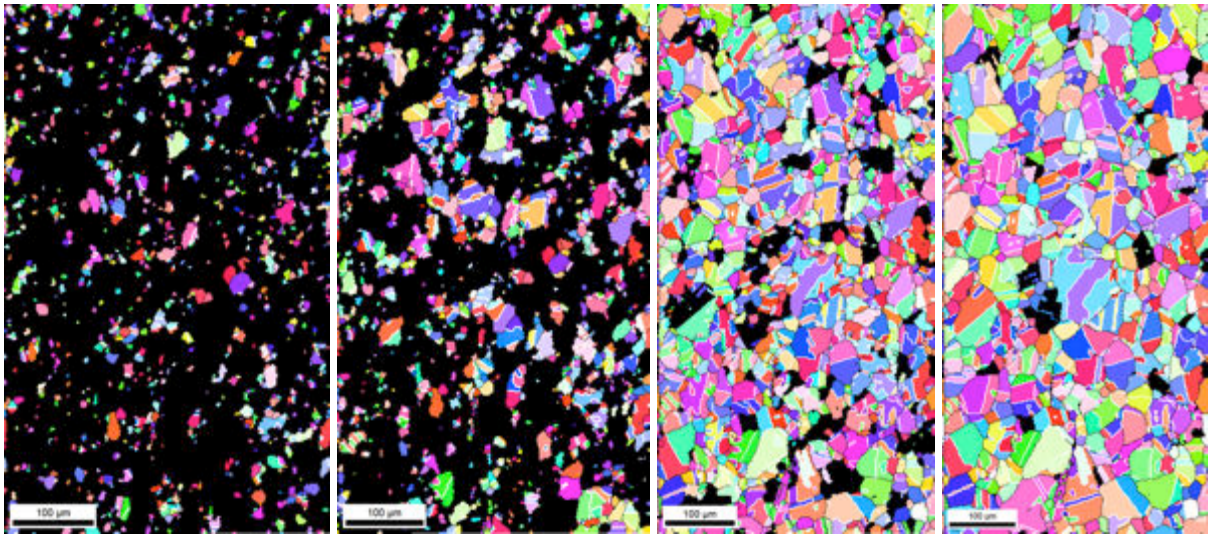

(20) (35) (50) (65)

Fig. 2.16. Recrystallized grain evolution in sample 2; same color-code as in Fig. 2.14; cumulative annealing time (s) are indicated below each map; white lines denote ∑3 boundaries.

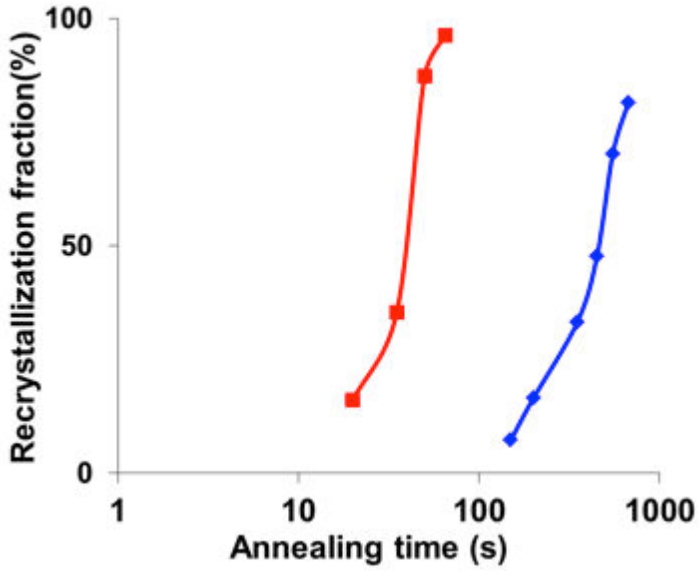

Fig. 2.17. Recrystallization kinetics in sample 1 (blue line) and sample 2 (red line).

The annealing twin density is expressed as a function of the recrystallization fraction in Fig. 2.18. Both the twin density at the end of recrystallization and the maximal value during recrystallization is higher in sample 2. As indicated by the recrystallization kinetics, and consistent with the initial GOS values, the stored energy level inside the deformed grains is

likely to be higher in sample 2 than in sample 1. Higher local stored energy level accelerates the recrystallization front migration. According to the growth accident model, the grain boundary migration velocity promotes annealing twin formation. Therefore, the difference in twin density in these samples is likely due to the apparent difference in stored energy level.

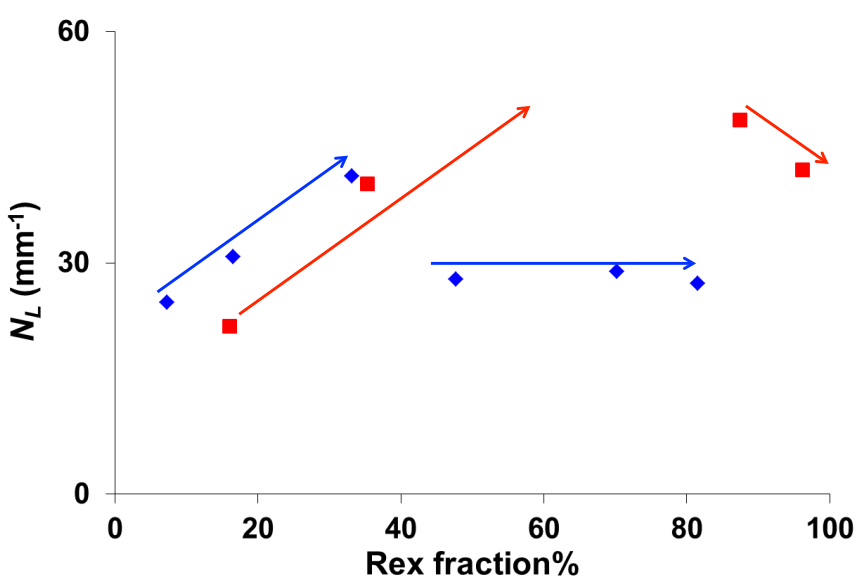

Fig. 2.18. Annealing twin density evolution during recrystallization in sample 1 (blue line) and sample 2 (red line).

The annealing twin density increased at the beginning of the recrystallization regime but decreased at the end in both samples. At the beginning of the recrystallization regime, driven by the important difference in stored energy level, recrystallized grains grow rapidly into the deformed matrix. However, as the recrystallization progressed, the recrystallized grains impinged with each other. This impingement decreases the average grain boundary migration driving force and this is accompanied by a decrease in twin formation events. As explained in the section 2.2, the recrystallization driving forces is a key factor for annealing twin formation. Therefore, the deceleration of the recrystallization migration likely leads to the decrease in twin density at the end of recrystallization. The relationship between the growth of recrystallized grains and the annealing twin development has been discussed in the section 2.2 by analyzing twin evolution in individual recrystallized grains. Similar annealing twin development mechanisms, including twin formation, twin boundary extension driven by recrystallization front migration and twin boundary extension from below the observed section, are revealed in the present dataset and highlighted by respectively blue, red and yellow circles in Fig. 2.15.

2.3.2.2 Annealing twin evolution during grain growth in 304L

The grain growth regime had not been followed in samples 1 and 2, but it was for sample 3; The microstructural evolution in sample 3 during grain growth is illustrated in Fig. 2.19. Different from the recrystallization regime, the twin density decreases during grain growth (Fig. 2.20), which is identical as what we observed in the pure nickel dataset. This decrease is mainly driven by two mechanisms revealed by the *in situ* annealing series. First, similar as in the pure nickel dataset shown in the section 2.2, small grains containing several twin boundaries are consumed by large grains (black circles in Fig. 2.19). Second, incoherent twin boundaries are found to migrate in the direction to reduce the total twin boundary length in the present dataset, illustrated by the red circle marked changes in Fig. 2.19. However, such transformation was not observed in the pure nickel dataset (Fig. 2.13) In addition to these disappearance mechanisms, a few annealing twins were found to appear on the observed 2D section during grain growth e.g. the formation event marked by the blue circle in Fig. 2.19. It is worth highlighting that these probable formation events only occurred at triple junctions, which is in agreement with the observations made in a 3D NF-HEDM dataset of a pure nickel sample [Lin 2014].

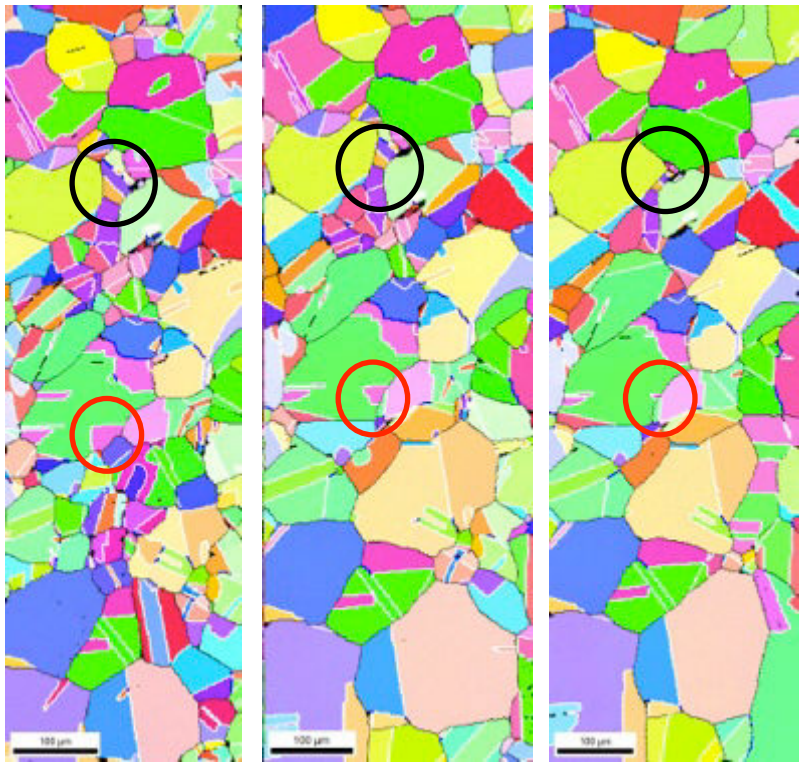

23s 43s 73s

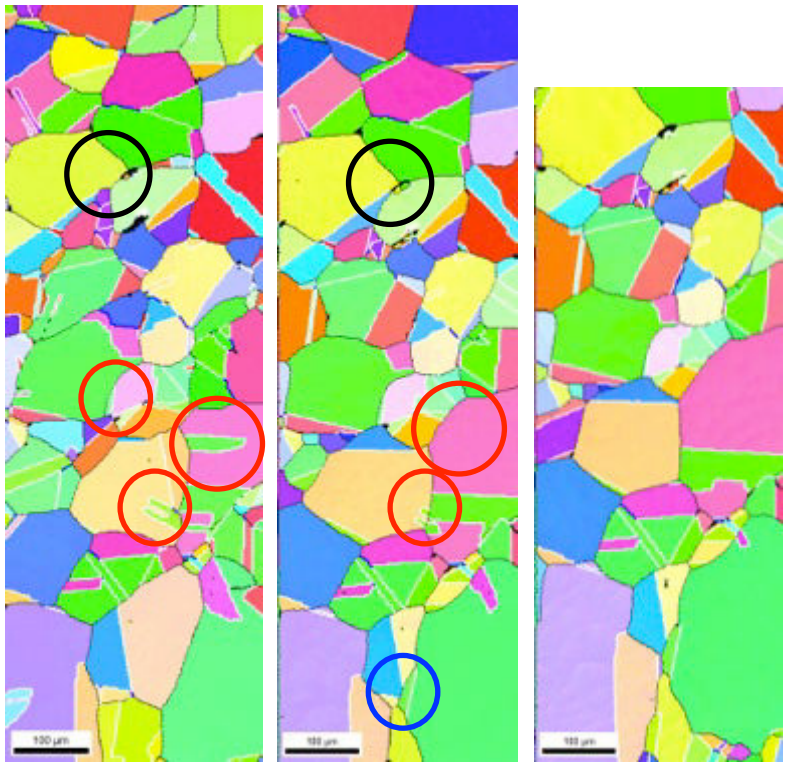

133s 253s 453s

Fig. 2.19, Microstructure evolution during grain growth in sample 3; same color-code as in Fig. 2.14 cumulative annealing time (s) are indicated below each map; white lines denote ∑3 boundaries. The black lines are grain boundaries with a disorientation higher than 5°.

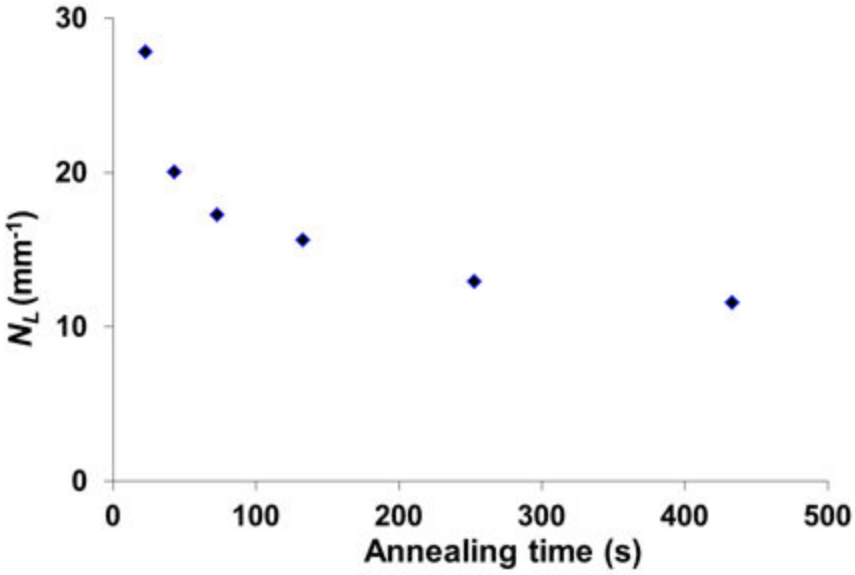

(a)

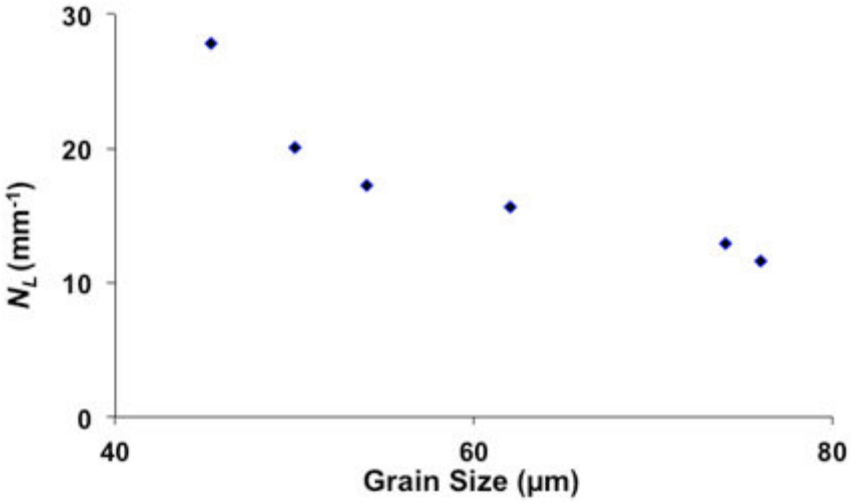

(b)

Fig. 2.20. Annealing twin density evolution during grain growth in sample 3 expressed as a function of (a) annealing time and (b) grain size.

2.4. Evolution of the annealing twin density during grain growth in the nickel based superalloy inconel 718

2.4.1 Experimental details

Grain growth experiments were performed on samples machined from an Inconel 718 billet at three different δ supersolvus temperatures and for different times (details given in Fig. 2.21). The samples had the same initial microstructure illustrated in Fig. 2.22. All the analysed samples were metallographically prepared with a final mechanical polishing using a 0.5µm colloidal SiO_2 suspension. The EBSD characterizations were performed using a ZEISS SUPRA 40 FEG SEM equipped with a Bruker CrystAlign EBSD system. The step size for EBSD map acquisition of the initial microstructure was 0.46 μm. However, as the average grain size in the annealed samples became larger, the step size was accordingly increased to 1.44 μm, in order to measure a sufficient number of grains and to complete each map acquisition within a reasonable time. The initial microstructure contains more than 5000 grains. The EBSD maps recorded during grain growth includes 150-800 grains (twins are excluded in grain counting). The OIM^{TM} software was used to analyse the EBSD data.

2.4.2 Experimental results

The initial microstructure (Fig. 2.22 (a)) is almost fully recrystallized (more than 93%) as indicated by the Grain Orientation Spread (GOS) value (Fig. 2.22 (b)). The recrystallized grains were identified in the EBSD maps using a criterion that the GOS is less than 1° [Alvi 2008]. Additionally, grains with an area smaller than 3 pixels were not considered in the present study. The number-weighted average grain diameter (D), defined as the arithmetic mean of the values of circle-equivalent diameter, was used to quantify average grain size in the following analyses. The average grain size of the recrystallized grains in the initial microstructure is 13 μm.

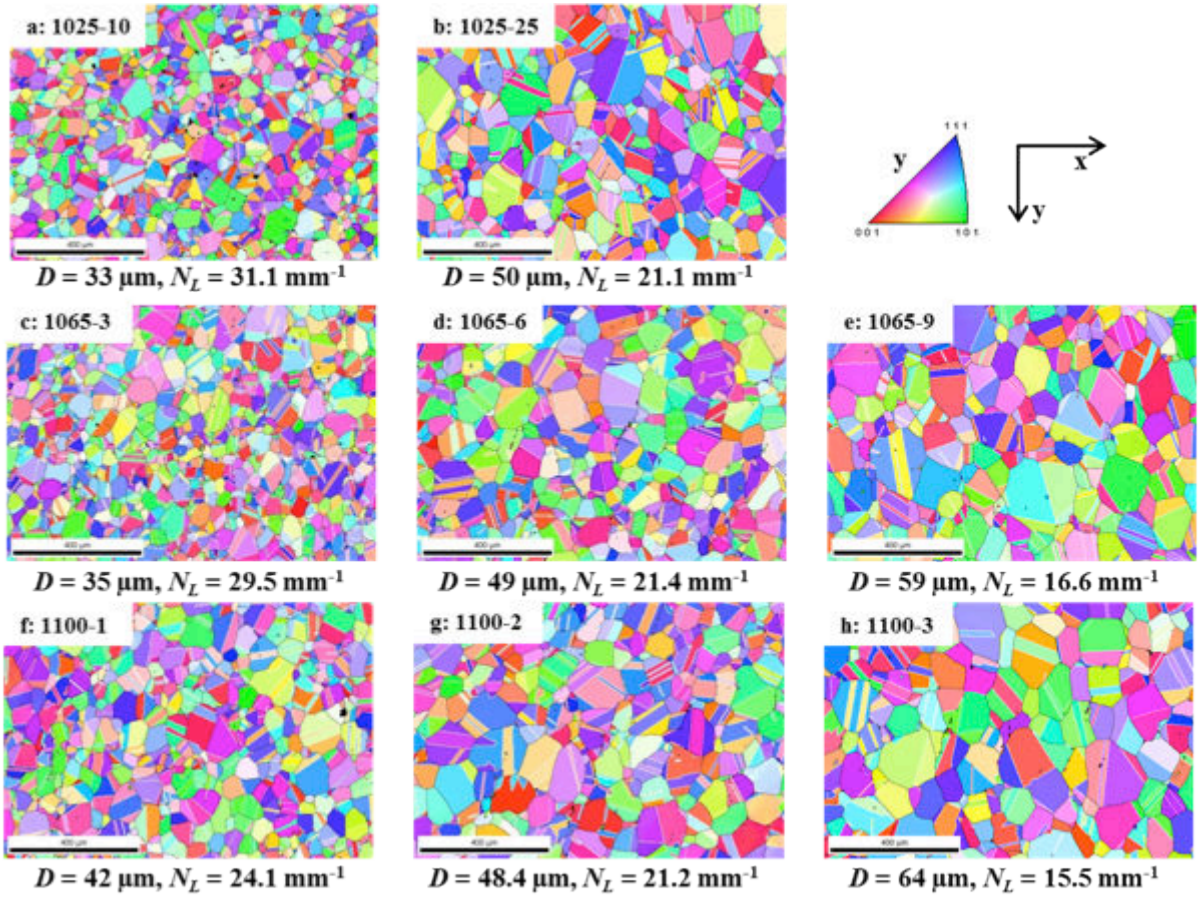

Fig. 2.21. Microstructure evolution at the three selected temperatures shown by an orientation color-coded scale (vertical direction of the map projected in the standard triangle) (1025-10: annealed at 1025°C for 10 minutes); the corresponding average grain size and the annealing twin density are specified under each map. The white lines denote ∑3 boundaries, the black lines are grain boundaries with a disorientation higher than 5°.

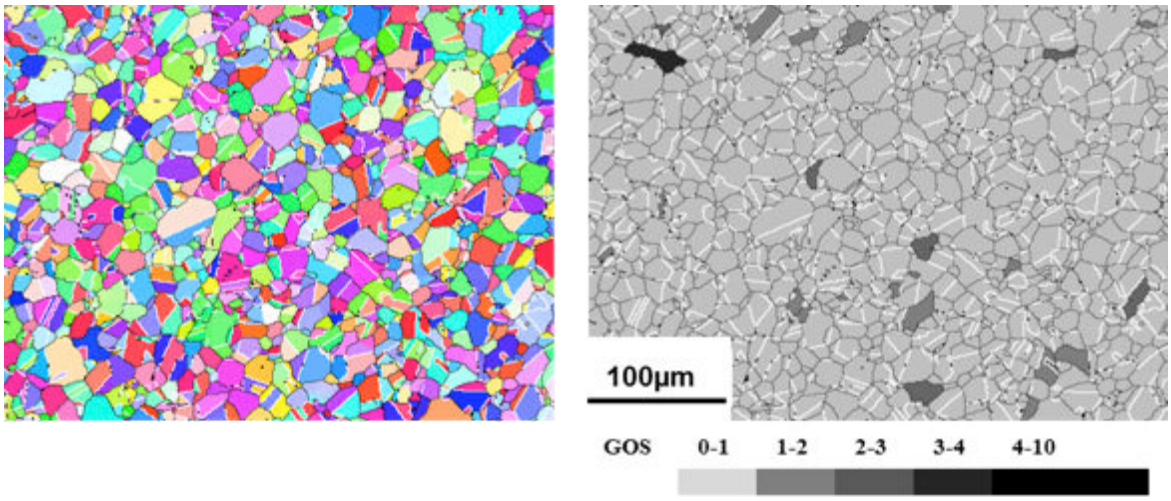

(a) (b)

Fig. 2.22. The initial microstructure: a) same colour code as in Fig. 2.21, b) the corresponding Grain Orientation Spread (GOS) map; Grain boundaries in black and twin boundaries ∑3 in white.

The microstructural evolution at the three annealing temperatures is shown in Fig. 2.21. The annealing times were adapted to result in similar grain sizes (in each column). The grain growth kinetics at the three temperatures is shown in Fig. 2.23. As expected, grain growth is faster at higher annealing temperature.

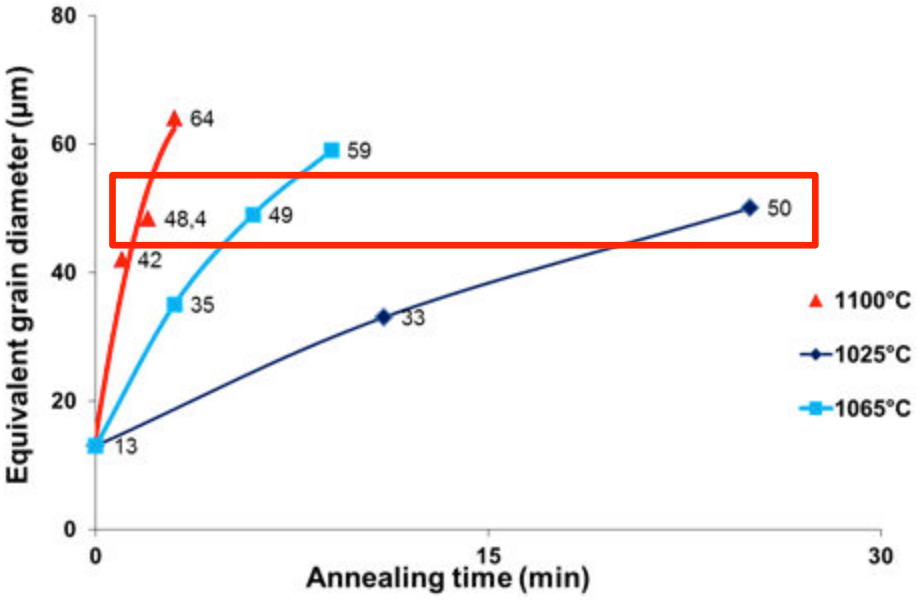

Fig. 2.23. Grain growth kinetics at different annealing temperatures.

The twin density is plotted as a function of the average grain size in the whole microstructure in Fig. 2.24. There is a strong inverse correlation of the twin density with the average grain size, which is same as in pure nickel and 304L stainless steel as presented in section 2.2 and 2.3. According to Pande [Pande 1990], the annealing twin evolution depends on the grain boundary migration driving force and on the grain boundary migration distance (therefore on grain size). In order to exclude the influence of grain size on annealing twin development, microstructures with an identical average grain size of about 50 μm but obtained at different annealing times and temperatures were compared (highlighted by the red rectangle on Fig. 2.23). Despite the difference in grain growth kinetics at the three temperatures, the twin densities for the same average grain size (50 μm) are very similar. Therefore, the twin density evolution is independent of grain growth kinetics within the present range. This observation is consistent with previous experimental data found in the literature [Hu 1956].

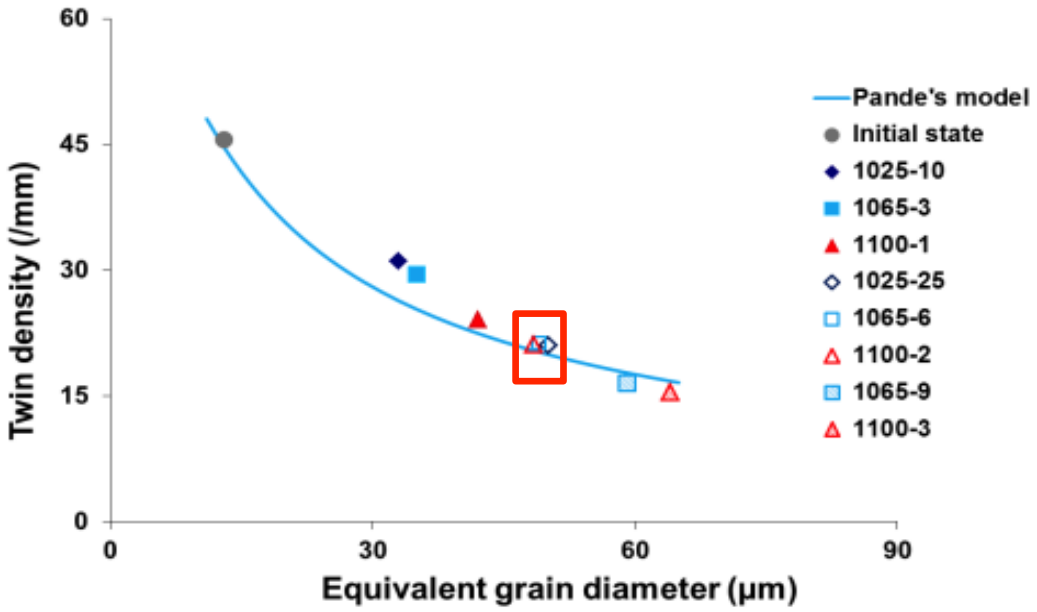

Fig. 2.24. Twin density evolution compared with Pande's model (best fit to Eq.1-28 with $\gamma_g \approx 1 J \cdot m^{-2}$).

In addition to the twin density, the number of annealing twin boundaries per grain (N_G) was also used for annealing twin quantification. During mean curvature driven grain growth, small grains are consumed by the bigger neighbouring grains. For studying the evolution of the number of twin boundaries in the growing grains, only the biggest grains (about 100 grains) in each analysed sample were considered. In the sample with the largest average grain size (1100-3), the 105 biggest grains occupy more than 95% of the EBSD acquisition area (Fig. 2.25). In addition, the number of twin boundaries per grain in the biggest grains does not increase with the corresponding average grain size (Fig. 2.26). This observation is consistent with the *in situ* observations reported in sections 2.2 and 2.3. Indeed, in the *in situ* observations, no or very few new twins were observed during grain growth. Small grains containing several twin boundaries were consumed by large grains, which grew producing rarely new twins. Incoherent twin boundaries may migrate in the direction to reduce twin length and total interfacial energy, but this is material-dependent. Therefore the fact that the twin evolution is independent of grain growth kinetics is consistent with those mechanisms where twin density evolution is mainly controlled by the extension of pre-existing twins (those formed during former recrystallization). How much twins extend depends on how much grains grow, but not on how fast they grow.

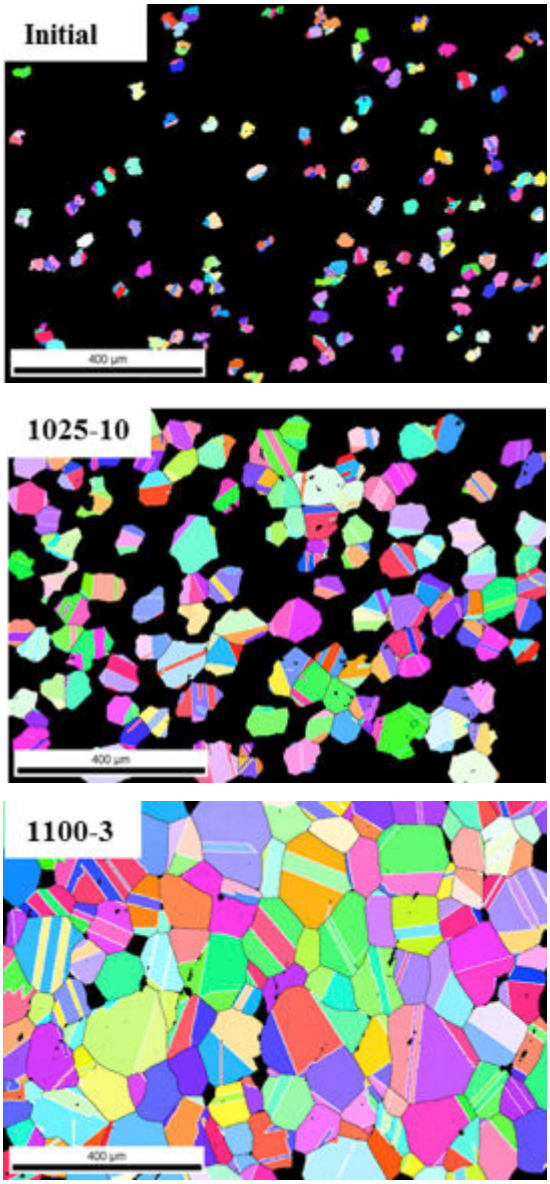

Fig. 2.25. The 100 biggest grains in the microstructures (same colour code as in Fig. 2.20).

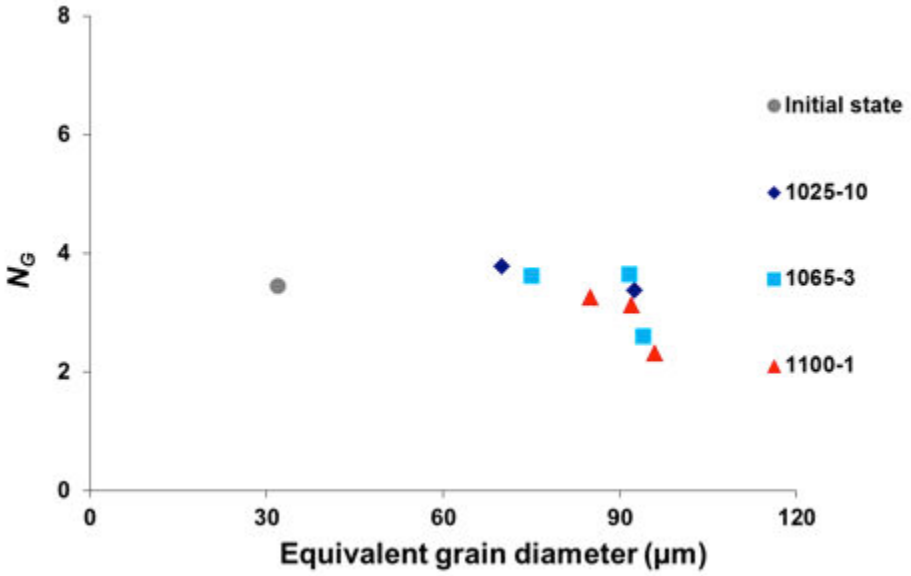

Fig. 2.26. Number of twin boundaries per grain in the 100 biggest grains expeessed as a function of the average grain size (considering the selected grains).

Pande's model is derived from the assumption that the increment of annealing twin boundary number per grain (ΔN_G) is proportional to the grain boundary migration driving force (F) and the increase in grain size (ΔD). Therefore, the model assumes that new twins are formed (N_G increasing) while grains grow (D increasing). This is not consistent with our observations presented previously.

The correlation between the annealing twin density and the average grain size can nevertheless be fitted accurately (see Fig. 2.24) by the formula derived from Pande's model (Eq.1-28). By using the grain boundary energy of pure nickel $\gamma_{gb} \approx 1\ J \cdot m^{-2}$ [Cahoon 2009] and assuming the mathematical form of Eq. 1-28, optimal parameters K and D_0 can be identified by an inverse method: $K \approx 0.3 m^3 \cdot J^{-1}$ and $D_0 \approx 2 \mu m$. Even though Pande's model can describe the correlation between the annealing twin density and the average grain size, it seems not consistent with the annealing twin evolution mechanism revealed by the experimental data. A mean field model will be proposed in the fourth chapter to address this gap.

2.5. Discussion

2.5.1. General patterns of annealing twin evolution during recrystallization

In both pure nickel and 304L stainless steel, the average annealing twin density in the overall microstructure, as measured in 2D sections, increases during recrystallization. Similar mechanisms observed in both dataset, including twin formation, twin boundary propagation driven by recrystallization front migration and twin boundary propagation from below the observed section, contribute to this increase.

In pure nickel, annealing twin evolution was analyzed in individual recrystallized grains. In the recrystallization regime, the correlation between the annealing twin density and the grain size in the overall microstructure differs from this correlation in individual grains. In individual grains, the twin density is more sensitive to the decrease in grain growth velocity. When the growth of the individual recrystallized grains decelerates, the creation of annealing twin density in these grains decelerates more sharply, notably because of:

i) reduced annealing twin boundary propagation,

ii) fewer annealing twin boundaries appearing by the propagation of twin boundary from below the observed section.

For 304L stainless steel, two hot deformed and quenched samples were subsequently annealed and analyzed for the recrystallization regime. It seems that higher stored energy promotes annealing twin formation especially at the beginning of the recrystallization regime. However, since dynamic recrystallization occurred in sample 2 during hot deformation and strongly affected grain sizes, the accurate stored energy level and its exact impact on twin formation during recrystallization are difficult to be determined in this case. Another experiment was performed in the present PhD work to study specifically the impact of the stored energy level on annealing twin development during recrystallization, which will be presented in chapter 3.

The growth accident model suggests that annealing twins are generated during grain boundary migration. The important factors that determine the annealing twin generation frequency are grain size, grain boundary migration velocity, grain boundary energy and twin boundary energy [Burgers 1949].

As presented in the first chapter, Gleiter [Gleiter 1969] and Pande [Pande 1990] independently established models consistent with this model to predict average annealing twin density in overall microstructures. However, both of these models are based on the annealing twin formation mechanism in an individual grain. Since during recrystallization, the

annealing twin evolution in the overall microstructure differs from their evolution in individual grains, the predictions of these models on average twin density could seem questionable. Moreover, the results presented here show that during recrystallization, twin boundary propagation from below the section plane contributes to the annealing twin density evolution in the 2D observed section while these models accounts neither for this mechanism nor for the possible annealing twin disappearance by incohent twin boundary migration. Therefore the physical basis of the existing models appears also to be somewhat questionable.

2.5.2. General patterns of annealing twin evolution during grain growth

As seen through the *in situ* experiments on pure nickel and 304L stainless steel presented in this chapter, during grain growth, the annealing twin development is mainly controlled by the evolution of the existing twins and only a few new twins are found formed at triple junctions. This result was confirmed by the 'conventional statistical approach' performed on nickel based superalloy Inconel 718. Therefore, annealing twin development mechanisms should definitely be differentiated between recrystallization and grain growth.

2.5.3. How to explain the difference in annealing twin evolution mechanisms during recrystallization and grain growth

We propose two factors as explanation. First, the lower driving forces in grain growth, compared to recrystallization, lead to much slower grain boundary migration. Li [Li 2009] and Bozzolo [Bozzolo 2012] mentioned that grain boundary migration velocity may promote annealing twin generation. The effect of grain boundary migration velocity is also implicit in Pande's and Gleiter's models through the effect of the driving force amplitude. This will be further investigated in chapter 3.

We propose here to consider a second factor linked to the grain boundary curvature (published in [Jin 2014]). As illustrated in Fig. 2.27, for a convex grain boundary (or a boundary moving in the direction opposite to its curvature center), once a coherent twin boundary forms on a {111} facet by a stacking error, it may propagate easily through the grain. However, for a concave boundary, Shockley partial dislocations must terminate the newly formed coherent twin boundary segment. These dislocations form incoherent twin boundaries. Energetically, this configuration is less favorable than the coherent twin boundary formed behind the convex boundary, incoherent twin boundaries have indeed much higher interfacial energy than coherent twin boundaries [Olmsted 2009]. As the growth of negative

curvature grain boundaries can only be observed in recrystallization regime (when the stored energy driving forces dominates the capillarity forces), it seems logical to estimate the recrystallization regime as energetically more favorable to annealing twin development. Following the same idea, during grain growth, only at triple junctions can coherent twin boundaries propagate through a grain, which explains why annealing twin boundaries are only found formed at triple junctions during grain growth. Grain boundary migration velocity and grain boundary curvature would have a synergistic effect on annealing twin generation. Finally, all rationales work in the same sens to explain why annealing twins are mostly generated during recrystallization.

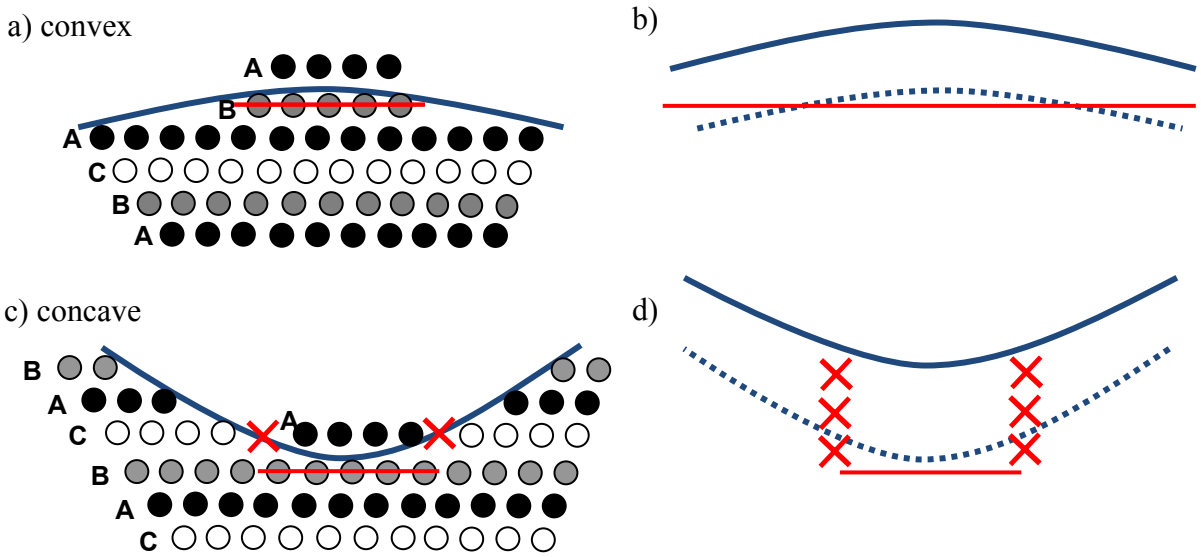

Fig. 2.27. Annealing twin formation at a convex or at concave migrating boundary moving from down to the top. The ABC stacking sequence of the compact planes is shown along a <110> direction, only for the growing crystal. The orientation of the counterpart (consumed crystal) can be considered to be random.
Following the growth accident model, the twin nucleation occurs by forming a cluster of atoms in the wrong position (A instead of C) on a {111} facet : a) on the convex boundary, c) on the concave boundary. Schemes b) and d) show how the twin segment evolves following the boundary migration. Thick red lines represent coherent twin boundaries. Red crosses in c) symbolize Shockley partial dislocations that are necessary in the case of the concave boundary, and that pile up to form incoherent twin segments after the boundary migrated further, in d).

2.5.4. Is annealing twin evolution material dependant?

Despite some similarities, in the *in situ* observations performed on pure nickel and 304L stainless steel, also revealed few differences in annealing twin evolution behaviors. The main one is that incoherent twin boundaries migrate in the direction to reduce the total interfacial energy was observed many times in 304L and almost never in pure nickel. This difference is likely related to the effect of annealing temperature on incoherent twin boundary mobility.

2.5.5. Is any of the existing models able to predict annealing twin density evolutions?

Curvature driven boundary migration by itself is not sufficient to generate annealing twins. Therefore twin formation mechanisms based solely on migration appear to be basically incorrect. Twin formation is most frequently observed for boundaries migrating into recrystallizing deformed regions. Therefore a model describing twin formation mechanisms need to account for this difference in the driving force nature, whether via the presence of dislocations or via inverse curvature.

In the present work, different annealing twin evolution mechanisms were observed during both recrystallization and grain growth. From a physical point of view, neither Gleiter's model nor Pande's model accounts for all of these mechanisms. In the numerical part of the present thesis, mean field and full field approaches will be presented as an attempt to draw bases for addressing the gap between the experimental data and the existing theoretical models.

2.6. Conclusion

In this chapter, three typical F.C.C. materials i.e. pure nickel, 304L stainless steel and nickel base superalloy Inconel 718 samples were used to study annealing twin development in both the recrystallization and grain growth regimes. The following conclusions could be drawn:

- the average annealing twin density, defined as the number of twin boundary intercepts per unit length measured in 2D sections, increased during recrystallization and decreased during grain growth.
- The number of annealing twin boundaries per grain in the overall recrystallized microstructure and in individual grains increased during recrystallization. Meanwhile, during grain growth, the number of twin boundaries per grain in the biggest grains, which control the overall microstructure evolution, did not increase with the

corresponding average grain size. Interpreted as directly linked with the number of twin formation events, the number of twins per growing grain shows (or confirms) that twins are mainly formed during recrystallization, and only very few during capillarity driven grain growth.

- In the recrystallization regime, the main mechanisms identified up to now as leading to an increase in annealing twin density are:
  i) annealing twin formation accompanied by recrystallization front migration,
  ii) annealing twin boundary propagation driven by recrystallization front migration either in the observed section or arising form below it.
- The mechanisms that decrease the annealing twin density in the grain growth regime are:
  i) in the grain growth regime, large grains consume small grains and their twins without producing new twin boundaries, or only very few ones,
  ii) incoherent twin boundaries may migrate in the direction to reduce the total interfacial energy (material dependant).
- Annealing twin development mechanisms should be differentiated between recrystallization and grain growth. If individual mechanisms may still be decribed in similar terms (e.g. "growth accident on a {111} facet" or "twin annihilation by the migration of an incoherent segment"), the overall twin density evolution behavior is clearly distinct in between the two regimes, because the relative contributions of the individual mechanisms are vey much different.
- The influence of the mean curvature sign of the migrating boundary was proposed as a new explanation consistent with all these results.

Résumé en français

Comme présenté dans le première chapitre, le modèle d'accident de croissance, qui suggère qu'un joint de macle cohérent se forme durant la migration d'un joint de grain à cause d'une erreur d'empilement, est supporté par la plupart des résultats expérimentaux [Song 2007] [Cahoon 2009] [Wang 2014]. Néanmoins, l'explication de la formation de macles thermiques avec les modèles de Pande et de Gleiter est incomplète Le chapitre 2 vise à établir les tendances générales du développement de macles thermiques durant la recristallisation et durant la croissance de grains. Trois matériaux de type C.F.C. i.e. le nickel pure, l'acier inoxydable 304L et le superalliage base nickel Inconel 718 sont utilisés pour cette étude.

Grâce à des expériences de traitement thermique *in situ* couplés à des cartographies d'orientation réalisées à différents stades d'avancement au cours d'un recuit post-déformation à froid, nous avons confirmé que la plupart des macles thermiques sont générées durant la recristallisation. En effet la densité de macles augmente nettement au cours de la recristallisation, le nombre de macles par grains également, tandis que pendant la croissance de grains, très peu de nouvelles macles ne semblent être génèrées.

Par conséquent, la recristallisation et la croissance de grains sont des régimes totalement distincts du point de vue de la de formation des macles thermiques, avec des mécanismes spécifiques, et doivent absolument être considérés et étudiés séparément.

CHAPTER 3 THERMO-MECHANICAL FACTORS INFLUENCING ANNEALING TWIN DEVELOPMENT DURING RECRYSTALLIZATION

3. THERMO-MECHANICAL FACTORS INFLUENCING ANNEALING TWIN DEVELOPMENT DURING RECRYSTALLIZATION

In the second chapter, we could confirm that annealing twins are mainly formed during recrystallization. In the present chapter, the influence of difference thermo-mechanical factors on annealing twin development during recrystallization is addressed.

This topic has been discussed recently in the literature. Cahoon et al [Cahoon 2009] found that the prior cold deformation level could increase the annealing twin density in commercially pure nickel. But due to the low deformation level (less than 7.5%) that they applied, their study was limited to the case of Strain Induced grain Boundary Migration (SIBM). Li et al [Li 2014] studied the role of deformation temperature and strain on grain boundary engineering of Inconel 600. Nevertheless, due to the complexity in terms of microstructural evolution during dynamic recrystallization, the precise roles of these parameters on annealing twin development were not determined. In addition, Bair et al [Bair 2014] found that the heating velocity could also influence annealing twin evolution during recrystallization. However, the actual values of the applied heating velocities were not given in his study. In the following experiments, we aim at properly establishing the influence of three thermo-mechanical processing factors i.e. the stored energy level, the annealing

temperature and the heating velocity on annealing twin formation during static recrystallization on commercially pure nickel. Different annealing twin quantification methods, including twin density, number of twin boundaries per grain and twin boundary length fraction, are used.

Two distinct experiment series were performed independently to analyze respectively the influences of prior deformation amount and annealing temperature on one hand and of heating velocity on the other hand. For that purpose, samples were submitted to compression tests at room temperature and subsequently annealed in a temperature range between 350°C to 550°C. The experiments and results will be presented in section 3.1. A discussion on the different phenomena revealed by the experimental results will be conducted in section 3.2.

3.1. Thermo-mechanical factors influencing annealing twin evolution during recrystallization

3.1.1. Influence of prior deformation level and annealing temperature

The experiment, presented in this subsection, was performed at Carnegie Mellon University (CMU) in cooperation with B. Lin.

3.1.1.1. Experimental details

Two cylindrical samples, 5 mm in diameter and 8 mm in height with a fully recrystallized microstructure (average GOS of 0.6°) and an average grain size (arithmetic mean) of 90 μm (Fig. 3.1 (a)) were compressed at room temperature to 30% or 60% height reduction. The corresponding true strains (ε) are indicated in Table 3.1. The compressed samples were then cut into semi-cylinder samples, which were then annealed at 350°C or 450°C to perform recrystallization. The microstructure *X*_R*Y* refers to the sample with *X*% deformation level and recrystallized at *Y*°C. The heating device was a Thermo Scientific™ Lindberg/Blue M™ MiniMite™ tube furnace. EBSD characterizations were performed in a FEI XL30 ESEM microscope equipped with a TSL EBSD system. EBSD orientation maps, which have the same size (800 μm × 800 μm), were recorded with a 1.2μm step size. At the end of recrystallization, EBSD maps contain about 100 to 500 recrystallized grains depending on the thermo-mechanical history (grains were detected with a threshold angle at 15°, twin boundaries being ignored and grains with equivalent diameter smaller than 3 μm not considered). It is worth mentioning that the average grain size calculated based on the EBSD maps with fewer grains (e.g. 100) could be poorly statistically representative.

As in the second chapter, the recrystallized grains were defined in the EBSD maps by a criterion that the Grain Orientation Spread (GOS) was less than 1° [Alvi 2008].

3.1.1.2. Experimental results

The EBSD maps in Fig. 3.1 illustrate the microstructure in the initial state and after 60% and 30% height reduction, observed in the longitudinal cross-section. The two deformation levels can be qualitatively distinguished by the gradient of the IPF colors. However, the resolution of the EBSD map does not allow for capturing the details of the microstructure of the 60% deformed sample. The overall recrystallization kinetics is illustrated in Fig. 3.2. Due to the fast recrystallization kinetics, the early recrystallization stage is not captured in the samples annealed at 450°C (60_R450 and 30R_R450). On the other hand at 350°C, for 60_R350, it

took 260 minutes to complete recrystallization and for 30_R350, recrystallization was still not completed after 460 minutes. The annealing temperature was then subsequently increased to 550°C for five minutes anneal to achieve full recrystallization in this sample.

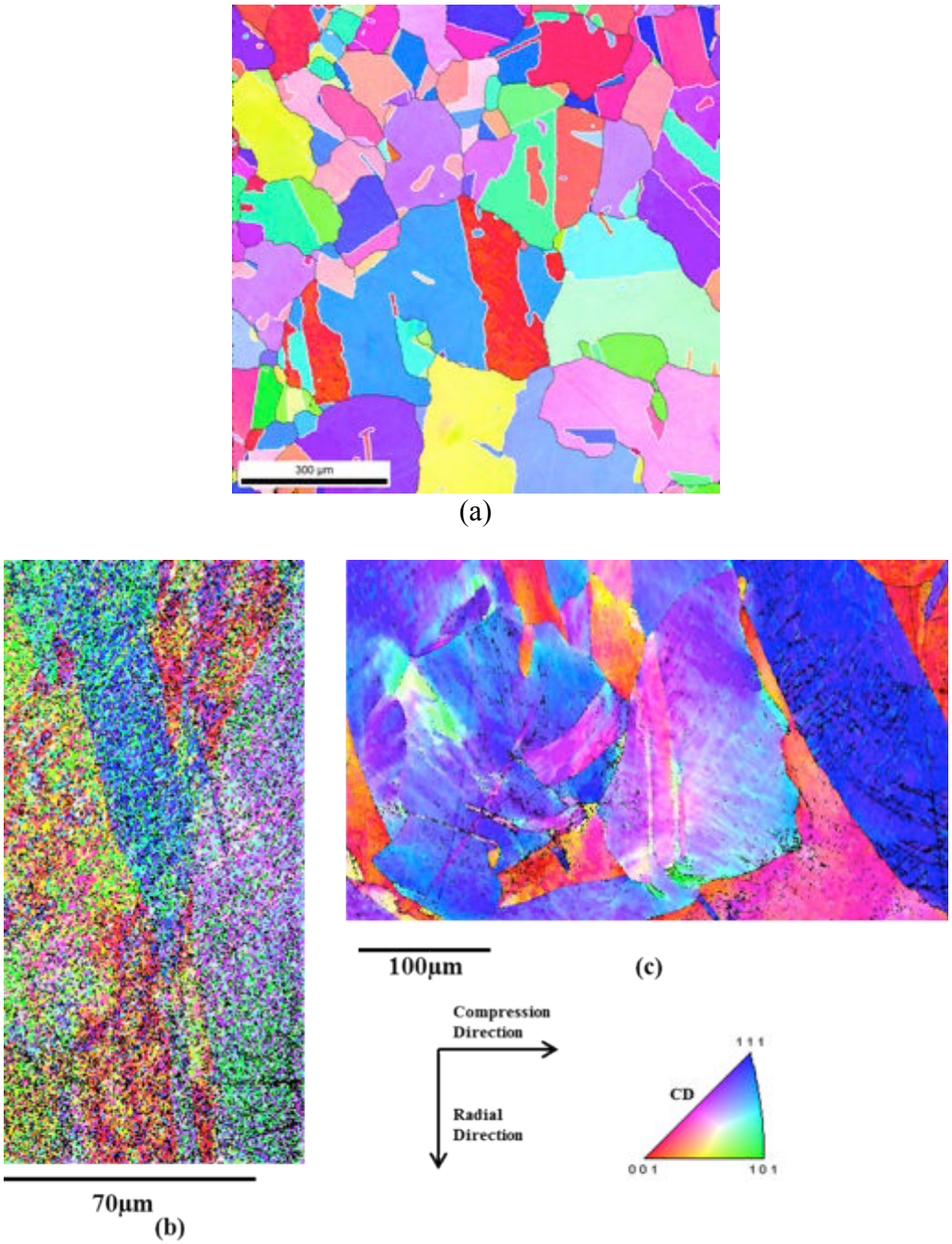

Fig. 3.1. EBSD map of the state of the material before (a) after respectively 60%(b) and 30%(c) height reduction by compression at room temperature, the microstructure is shown within an orientation colour-coded scale (Compression Direction CD) projected in the standard triangle); unreliable pixels are plotted black and will not be further considered.

	350°C	450°C
30%	**30_R350** ε = 0.36 $D = 60\mu m$ N_L=29 mm^{-1} N_G=10.6 f_L=0.64	**30_R450** ε = 0.36 $D = 65\mu m$ N_L=31 mm^{-1} N_G=10.5 f_L=0.66
60%	**60_R350** ε = 0.91 $D = 34\mu m$ N_L=46.4 mm^{-1} N_G=6.7 f_L=0.55	**60_R450** ε = 0.91 $D = 32\mu m$ N_L=44.8 mm^{-1} N_G=6 f_L=0.53

Table 3.1. Annealing twin quantification and grain size in the four samples after the completion of recrystallization.

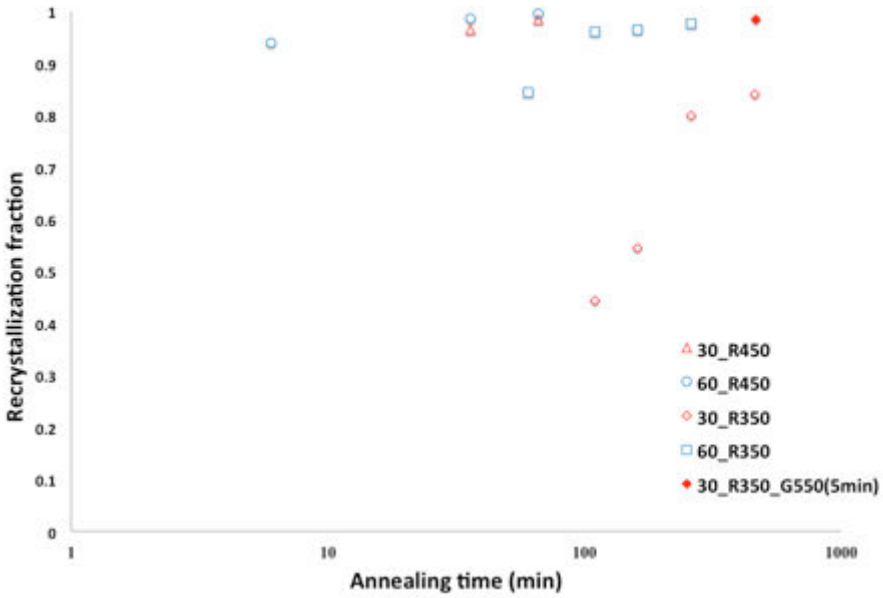

Fig. 3.2. Recrystallization kinetics at 350°C or 450°C after 30% or 60% height reduction by compression at room temperature.

The microstructure evolutions in the four samples during recrystallization are illustrated in Fig. 3.3. Despite the difference in recrystallization kinetics, the samples with the same deformation level but annealed at different temperatures (e.g. 60_R450 and 60_R350) have similar microstructures. The twin density evolutions in the four samples are expressed as a function of the recrystallization fraction in Fig. 3.4 (a) and the average recrystallized grain size in Fig. 3.4(b). With higher stored energy level, the twin density is higher at the end of recrystallization. This observation is consistent with other experimental results reported

previously in the literature in a nickel based superalloy [Wang 2014]. Meanwhile, the annealing temperature, in the present range, does not have an obvious effect on annealing twin development during recrystallization, which is consistent with another experimental result reported recently in nickel [Bair 2014], but contrary to the Gleiter's model, in which annealing temperature is supposed to influence twin density evolution [Gleiter 1969].

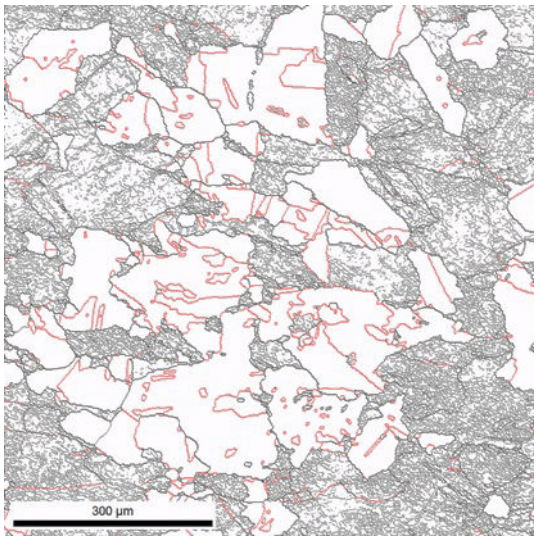

a) 30_R350 110min

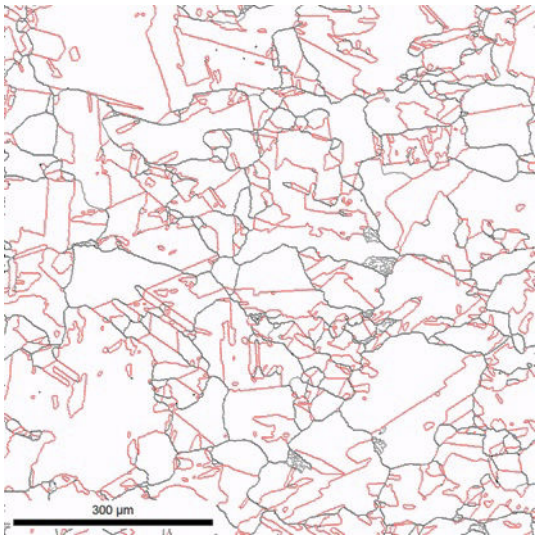

b) 30_R350_G550
460min at 350°C + 5min at 550°C

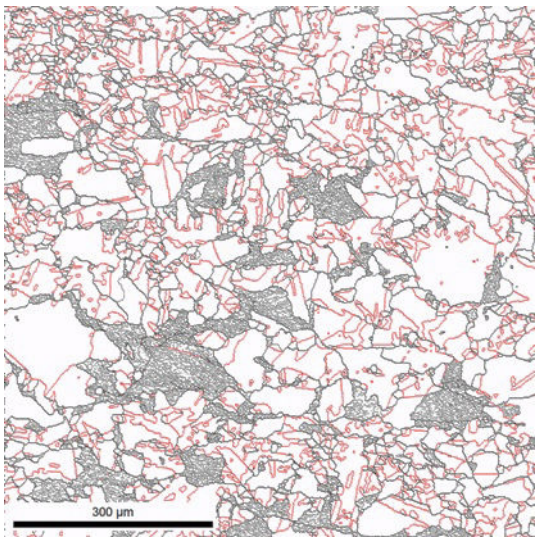

c) 60_R350 60min

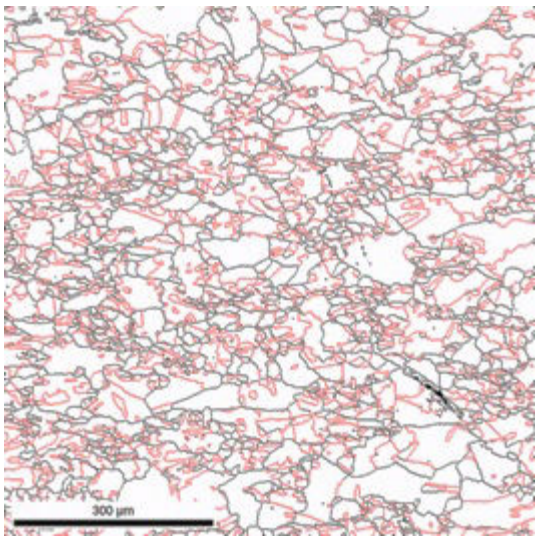

d) 60_R350_G550 260min

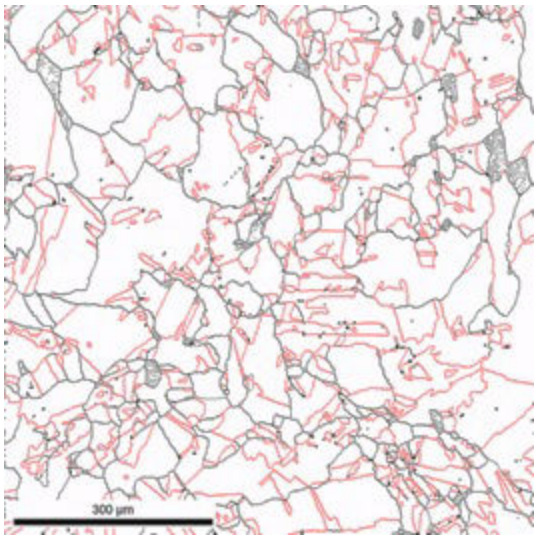

e) 30_R450 36min

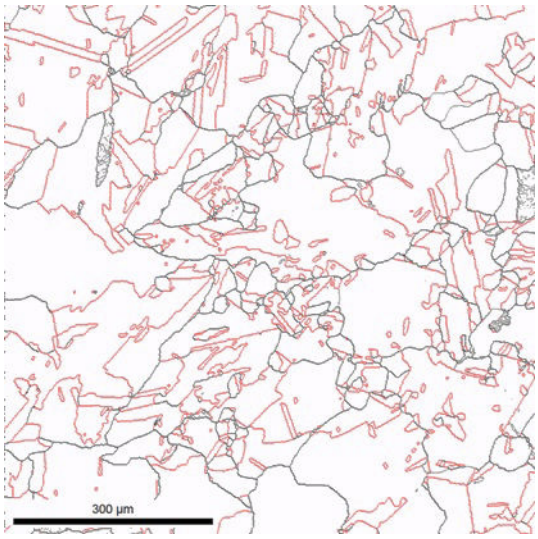

f) 30_R450 66min

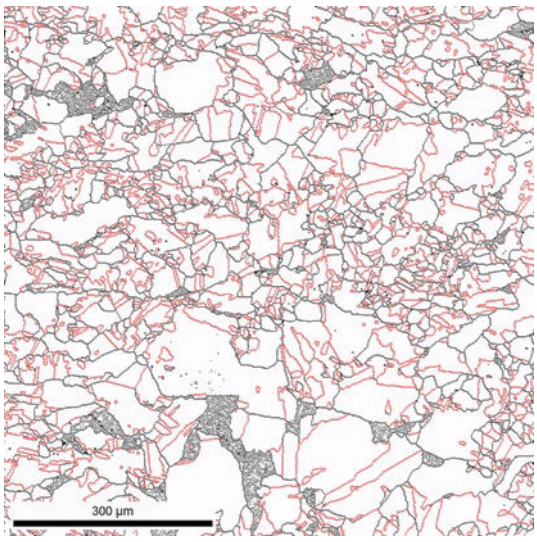

g) 60_R450 6min

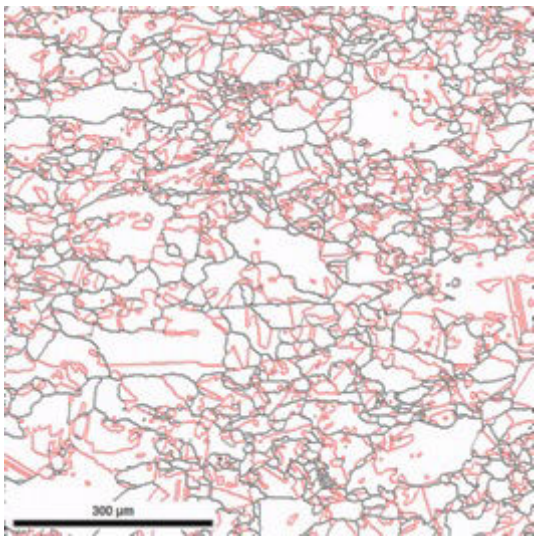

f) 60_R450 66min

Fig. 3.3. Microstructure evolution during recrystallization at 350 and 450°C after cold compression to 30 or 60%; Low angle grain boundaries (1-15°) are shown as grey thin lines with high angle boundaries shown as black lines; Twin boundaries within Brandon's tolerance criterion are plotted red; the sample reference and the corresponding cumulative annealing time are indicated under each map

The arithmetic average grain size (D) and the annealing twin content at the end of the recrystallization regime were primarily determined by the deformation level but not the annealing temperature, as indicated in Table 3.1 and visible on Fig. 3.4. Meanwhile, the number of twin boundaries per grain and the twin boundary length fraction exhibit an inverse trend from the twin density in those annealing twin quantifications. Indicated by Eq.1-9, the twin density is solely determined by the twin boundary length after the completion of recrystallization. On the other hand, the twin boundary length fraction (Eq.1-6) is inversely proportional to the total grain boundary length. Higher the deformation level is, smaller the

final recrystallized grain size is. And smaller recrystallized grain size leads to longer total grain boundary length. Therefore, different from the twin density the annealing twin length fraction decreases with higher deformation amount.

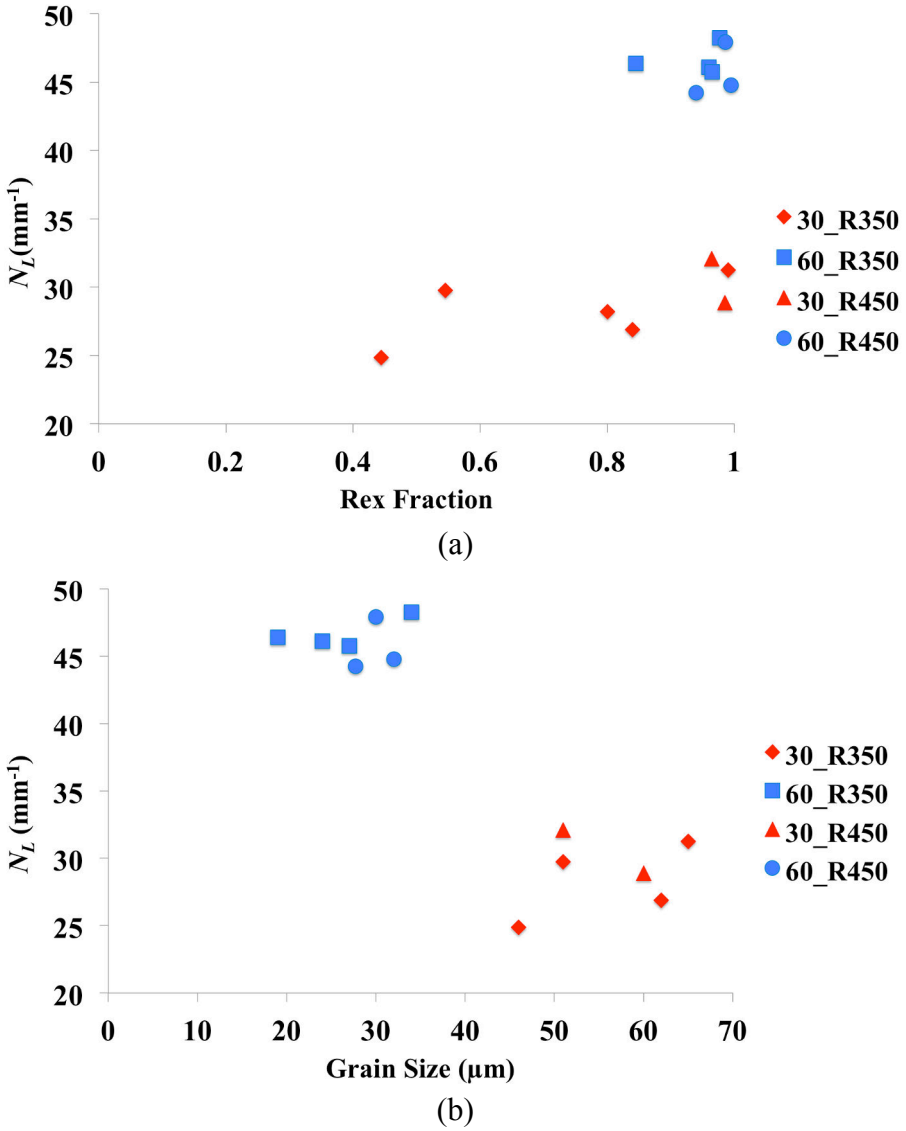

Fig. 3.4. Annealing twin density evolution during recrystallization, plotted as a function of (a) recrystallization fraction (b) average recrystallized grain size, at 350°C or 450°C after 30% or 60% height reduction by compression at room temperature.

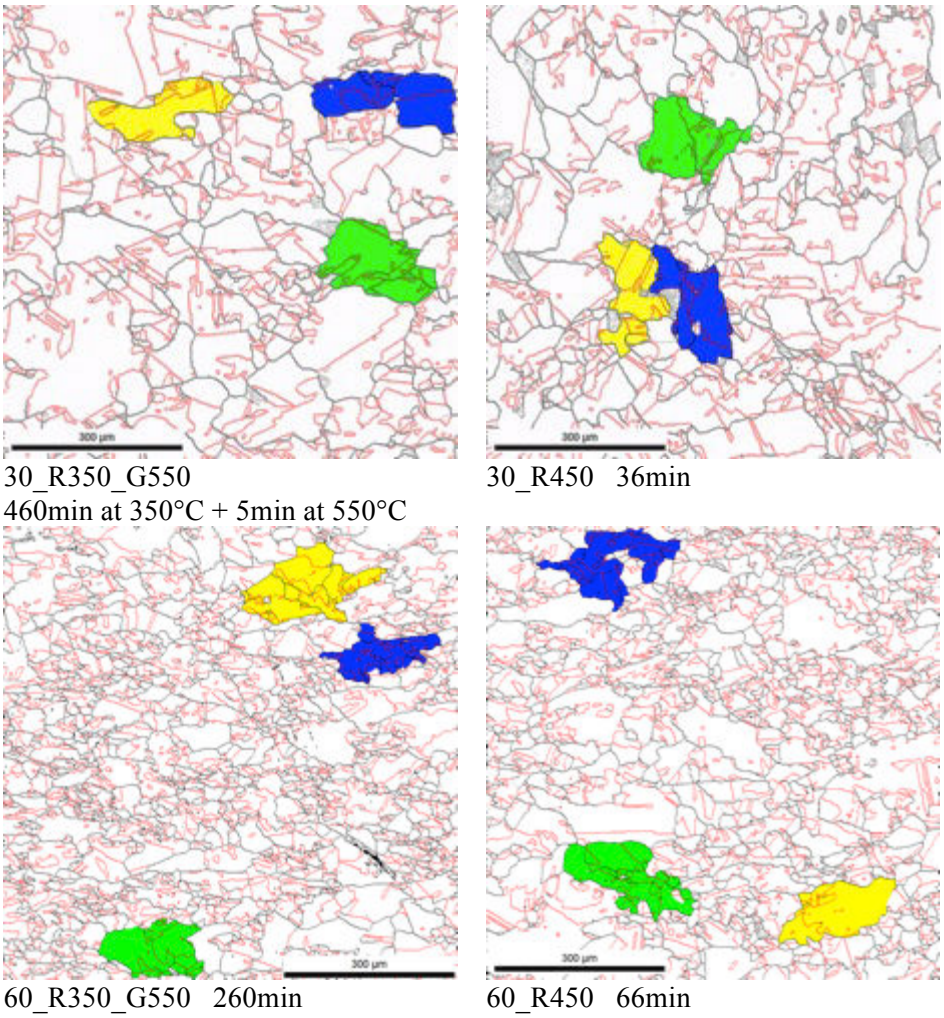

Fig. 3.5. The highlight of the grains selected to disconnect the effect of annealing temperature or prior strain and the influence of grain size during recrystallization at 350°C or 450°C after 30% or 60% height reduction by compression at room temperature; the annealing temperature and the corresponding cumulative annealing time are indicated under each map.

In the growth accident model, the grain boundary migration distance and the grain boundary migration driving force are considered as two key factors promoting the generation of annealing twins. During recrystallization, the recrystallization front migration driving force is dominated by the stored energy level, which is increasing with the prior cold deformation amount. Consistently, higher deformation level led to more twin boundaries per unit length, thus to higher twin density in the overall microstructure. Meanwhile, the number of twin boundaries per grain depends also on the grain boundary migration distance, which can be considered here to be half of the recrystallized grain size. In the samples with different average final recrystallized grain size, due to the difference in grain boundary migration distance, the average number of twin boundaries per grain cannot solely reflect the effect of grain boundary migration driving force.

	350°C	450°C
30%	**30_R350** $D = 150\mu m$ N_L=29 mm^{-1} N_G=22	**30_R450** $D = 143\mu m$ N_L=28.5 mm^{-1} N_G=19
60%	**60_R350** $D = 135\mu m$ N_L=46 mm^{-1} N_G=42	**60_R450** $D = 141\mu m$ N_L=41 mm^{-1} N_G=38

Table 3.2. Average annealing twin contents obtained thanks to different twin quantification methods and grain size of the three selected grains after recrystallization completion.

For the purpose of eliminating the effect of recrystallized grain size on annealing twin content interpretation, three grains having similar sizes (equivalent circle grain diameter of about 140μm) were selected in each of the four samples at the end of recrystallization (colored in Fig. 3.5), and twin contents inside these grains were compared. Relatively big grains were selected, as small grains in the observed 2D section can be large ones in 3D. Those three grains account for about 27 to 33% surface fraction of the EBSD maps of each state. In addition, the grains were selected in such a way that they were not in contact with the borders of the EBSD acquisition area to correctly calculate the number of twin boundaries per grain and the equivalent grain size. The number of twin boundaries per grain and twin density confirm the conclusions drawn from the overall average values (Table 3.2): higher stored energy level promotes annealing twin formation during recrystallization and the effect of annealing temperature on annealing twin formation is not obvious in the actual range.
In addition, it is worth emphasizing again that different final recrystallized grain size may lead to different twin content interpretations in the overall microstructure depending on the used quantification methods.

3.1.1.3. Discussion

As expected, the recrystallization kinetics was accelerated by higher prior cold deformation amount and higher annealing temperature. During recrystallization, the driving force for recrystallization front migration depends mainly on the stored energy level, which increases with the cold deformation amount. Besides, the grain boundary mobility generally increases with temperature [Maksimova 1989]. Thus, the recrystallization front migration velocity increases with both of the deformation amount and the annealing temperature through their

effects respectively on driving force and mobility, which both increase the migration velocty. An issue still requiring clarification is why annealing twin formation is promoted by the grain boundary migration velocity. From an atomistic point of view, two types of atomic motions can be depicted during grain boundary migration in molecular dynamic simulations [Zhang 2006] [Yan 2010]:

Type 1: string-like cooperative motions parallel to the grain boundary plane;

Type 2: single-atom jumps across the grain boundary plane.

Type 2 controls the rate of boundary migration and is necessary to redistribute the free volume to allow for Type1 motion [Zhang 2006]. With higher driving force and higher annealing temperature, the characteristic times associated with both types decrease [Zhang 2006] [Zhang 2009]. These two types of motions, that cause the grain to change from one orientation to another, are very likely to be related to the formation of annealing twins, especially Type1 which controls the position of the latest added atoms on the underlying atomic plane. However, the exact role of atomic movement inside grain boundaries on annealing twin formation is not clear, especially due to the complex structure of high angle boundaries [Zhang 2009]. The explanation of annealing twin formation at an atomistic scale requires thus a more detailed and targeted study.

3.1.2. Influence of heating velocity

3.1.2.1. Experimental details

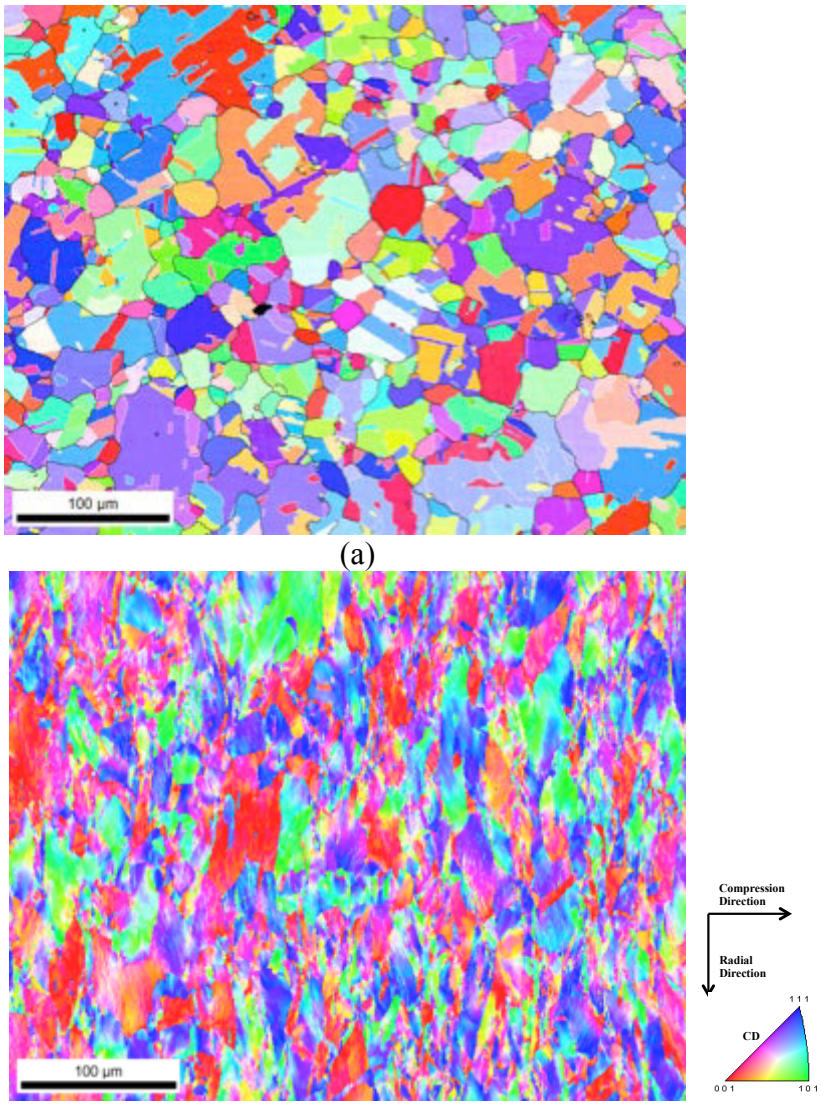

Fig. 3.6. EBSD map of the state of the material before (a) and after (b) 50% height reduction by compression at room temperature.

A cylindrical sample, 5 *mm* in diameter and 8 *mm* in height, was used. The initial microstructure fully recrystallized (average GOS equals to 0.6°) with an average grain size (arithmetic mean) equal to 16 µm is shown in Fig. 3.6(a). The sample was then compressed at room temperature to 50% height reduction, and the resulting microstructure is shown in Fig. 3.6 (b). The compressed sample was cut into two semi-cylinder samples. These two samples referred to as V500 and V5 were then heated up to 350°*C* at 500°*C/min* and 5°*C/min* respectively to perform recrystallization. Several annealing steps were performed on the same samples till the end of recrystallization. The cooling velocity, which was identical for the two

samples, was about 200°*C/min*. The EBSD characterizations were performed in a ZEISS SUPRA 40 FEG SEM equipped with a Bruker CrystAlign EBSD system. The step size for EBSD map acquisition is 0.46 μm. Grains were detected with a threshold angle at 15°, twin boundaries being ignored. The grains with an equivalent circle diameter smaller than 1 μm will not be considered in the coming analysis. As in the second chapter, the recrystallized grains were defined in the EBSD maps by a criterion that the Grain Orientation Spread (GOS) was less than 1° [Alvi 2008].

3.1.2.2. Experimental results

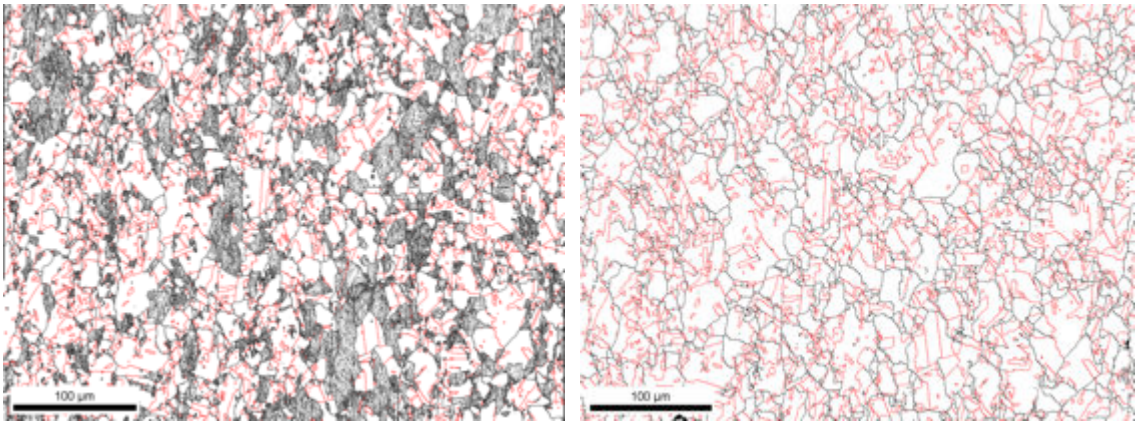

a) V5_0min b) V5_16min

Rex fraction: 68% 93%

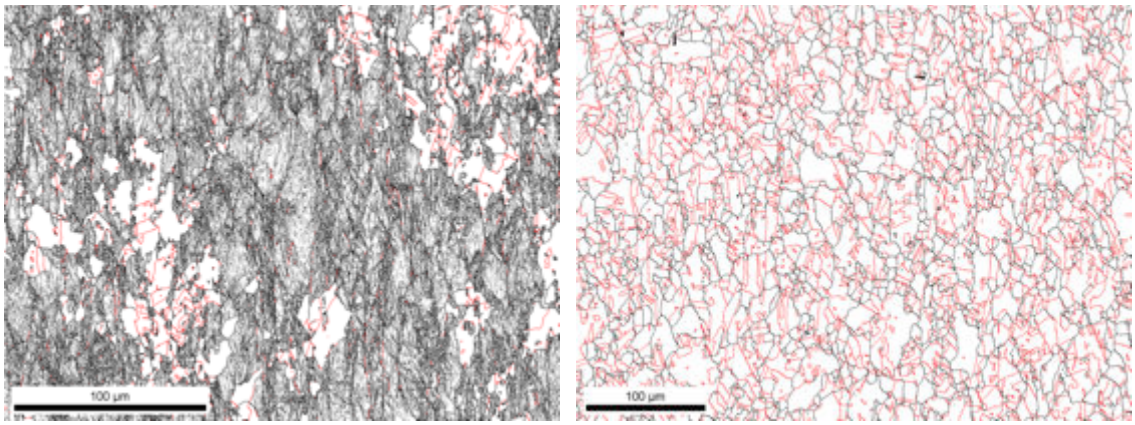

c) V500_1min d) V500_128min

Rex fraction: 22% 93%

Fig. 3.7. Microstructure evolution during annealing at 350°C after heating at either 5°C/min (samples labeled V5_Xmin) or 500°*C/min* (V500_Xmin); The annealing time and the corresponding recrystallization fraction are given below each map. The microstructure V5_0min (a) was obtained by heating the sample up to 350°*C* at 5°*C/min* and cooling down immediately. Low angle grain boundaries (1-15°) are shown as grey thin lines with high angle boundaries shown as black thick lines; the red lines denote ∑3 boundaries.

The microstructure evolutions in both samples during recrystallization are illustrated in Fig. 3.7. In each sample, an almost fully recrystallized microstructure (about 94%) was obtained at the end of the heat treatment series. The cumulative annealing time at 350°*C* is much shorter for V5 than for V500. This phenomenon is consistent with another study recently published by Bair et al [Bair 2014] from D.P. Field's group. As indicated in Fig. 3.7, about 70% of the microstructure was recrystallized in V5 at the moment when the annealing temperature was reached. Meanwhile, in V500, the recrystallization fraction was only 22% after 1 minute anneal at 350°*C*. Therefore, different from the almost instantaneous heat up in V500, the recrystallization was triggered during heating in V5, which decreased the annealing time to complete recrystallization at 350°*C*.

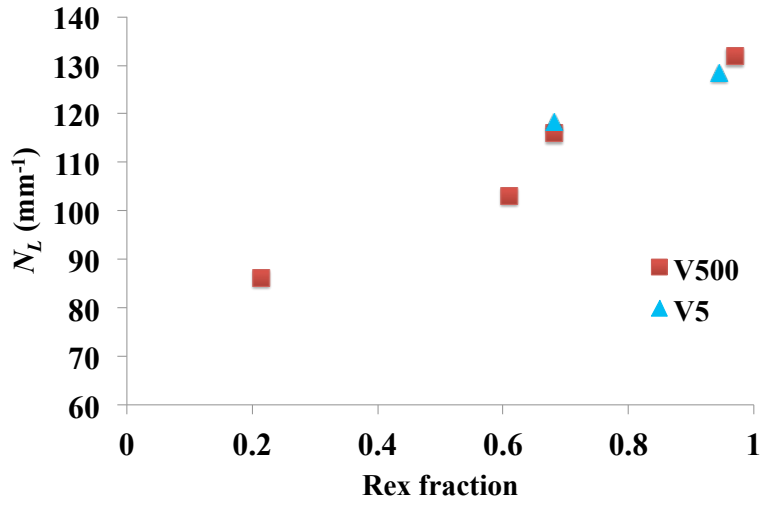

(a)

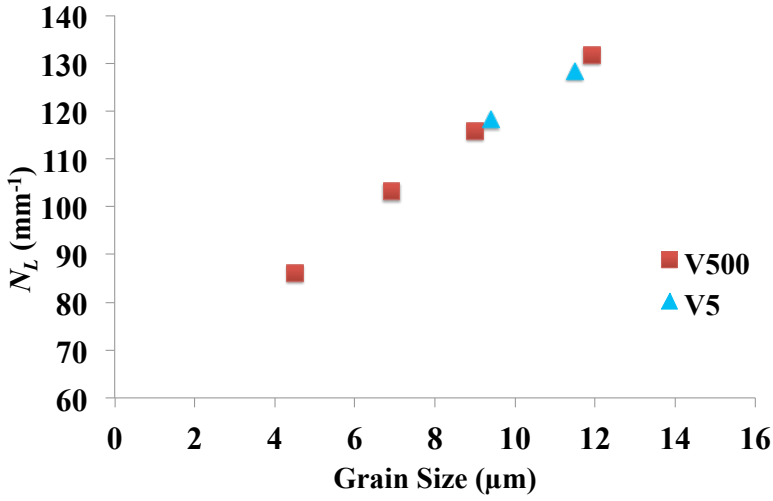

(b)

Fig. 3.8. Annealing twin density evolution in the two samples during recrystallization (at 350°C) plotted as a function of (a) recrystallization fraction (b) recrystallized grain size.

The twin densities in both samples are expressed as a function of the recrystallization fraction (Fig. 3.8(a)) and the average recrystallized grain size (Fig. 3.8(b)). Despite the difference in recrystallization kinetics, for the same recrystallization fraction, the twin densities in the two samples are almost identical. In addition to the twin density, the length fraction of annealing twin boundaries and the number of twin boundaries per grain in the overall microstructure at the end of the recrystallization regime were calculated for both samples (Table 3.3).

Ref	Grain size (μm)	N_L (mm^{-1})	f_L	N_G
V5	11	128.5	0.56	3.1
V500	11.5	131	0.55	3.4

Table 3.3. Annealing twin quantification and grain size in the two samples after the completion of recrystallization.

At near-complete recrystallization, the average grain sizes (arithmetic mean) and the twin contents including N_L, N_G and f_L are very close in V5 and V500. This observation indicates that the heating velocity within the present range does not influence the grain size nor the twin content at the end of the recrystallization regime.

3.1.2.3. Discussion

From our results, the heating rate does not seem to have any significant effect on annealing twin development during recrystallization. However, in the work reported recently by Bair et al [Bair 2014] about twin formation during recrystallization, also in nickel, the twin boundary fraction (f_L) increased with a decrease in heating velocity. In their work, the thermo-mechanical path has some differences with the one we designed for our experiments, e.g. the annealing temperature is higher (600°C-750°C). In addition, the difference in the applied heating velocity is not given. Details are missing in the paper to allow for an attempt of explaining why conclusions may differ from ours.

In this experiment, which evaluates the impact of the heating velocity, the height reduction of the sample was 50%. But the twin density at the end of the recrystallization regime is much higher in this experiment compared to the samples with 60% height reduction in the previous series. The initial grain size before deformation was 90 µm in the 60% compressed sample (Fig. 3.1 (a)) but only 16µm for the 50% compressed samples Fig. 3.6 (a). This difference is likely to be responsible for the difference in twin density. A fine-grained initial microstructure leads to a more random distribution of recrystallization nucleation sites [Humphreys 2004]. Randomly distributed recrystallization nuclei can grow independently at the early stage of recrystallization before impinge with other nuclei. In chapter 2, annealing twins are reported

to be formed mostly before the impingement of recrystallized grains, since the impingement decelerates the growth of individual recrystallized grains. Therefore, as illustrated in Fig. 3.8, after 1 minute anneal (about 20% recrystallized), the twin density in the recrystallized part of sample V500 (higher than 80 mm^{-1}) is much higher than in the initially coarse-grained samples. Since the annealing twin formation decelerated after the impingement of recrystallized grains in both initialy fine-grained and coarse-grained sample, this difference created at the beginning of recrystallization could result in a different in annealing twin density at the end of recrystallization.

3.2. Discussion

In the present study, the microstructure evolution of a small area in sample 60_R450 and sample V5 was followed in more details (Fig. 3.9). Several incoherent twin boundary migration events, though limited, were found in 60_450 (circles in Fig. 3.9 (a)(b)). Meanwhile, almost no incoherent twin boundary migrates at 350°C in V5 (Fig. 3.39 (c)(d)), which is identical to the *in situ* observation in pure nickel at 400°C (section 2.2.2.2). The coherent twin boundary has very low mobility, but the incoherent twin boundary can be much more mobile [Olmsted 2009]. At higher annealing temperature, the mobility of incoherent twin boundaries increases, which leads to more twin boundary migration events. This result suggests that the annealing temperature may influence the evolution of the existing annealing twin boundaries, especially the incoherent twin boundaries. In addition, the incoherent twin boundary migration events are reported in other materials annealed at different temperatures (304L stainless steel at 1000°C [Jin 2013] and Pb alloy at 280°C [Song 2007]). These observations indicate that annealing twin boundary migration behaviors could be material dependant, it could also be a question of temperature (T/T_m). This point needs to be further investigated.

In the experiment aiming at testing the impact of prior deformation level and annealing temperature, only the deformation level but not the annealing temperature promoted the annealing twin formation within the present range. This result suggests that the grain boundary migration velocity influences annealing twin formation only through the effect of the migration driving force, which is consistent with the Pande's model [Pande 1990].

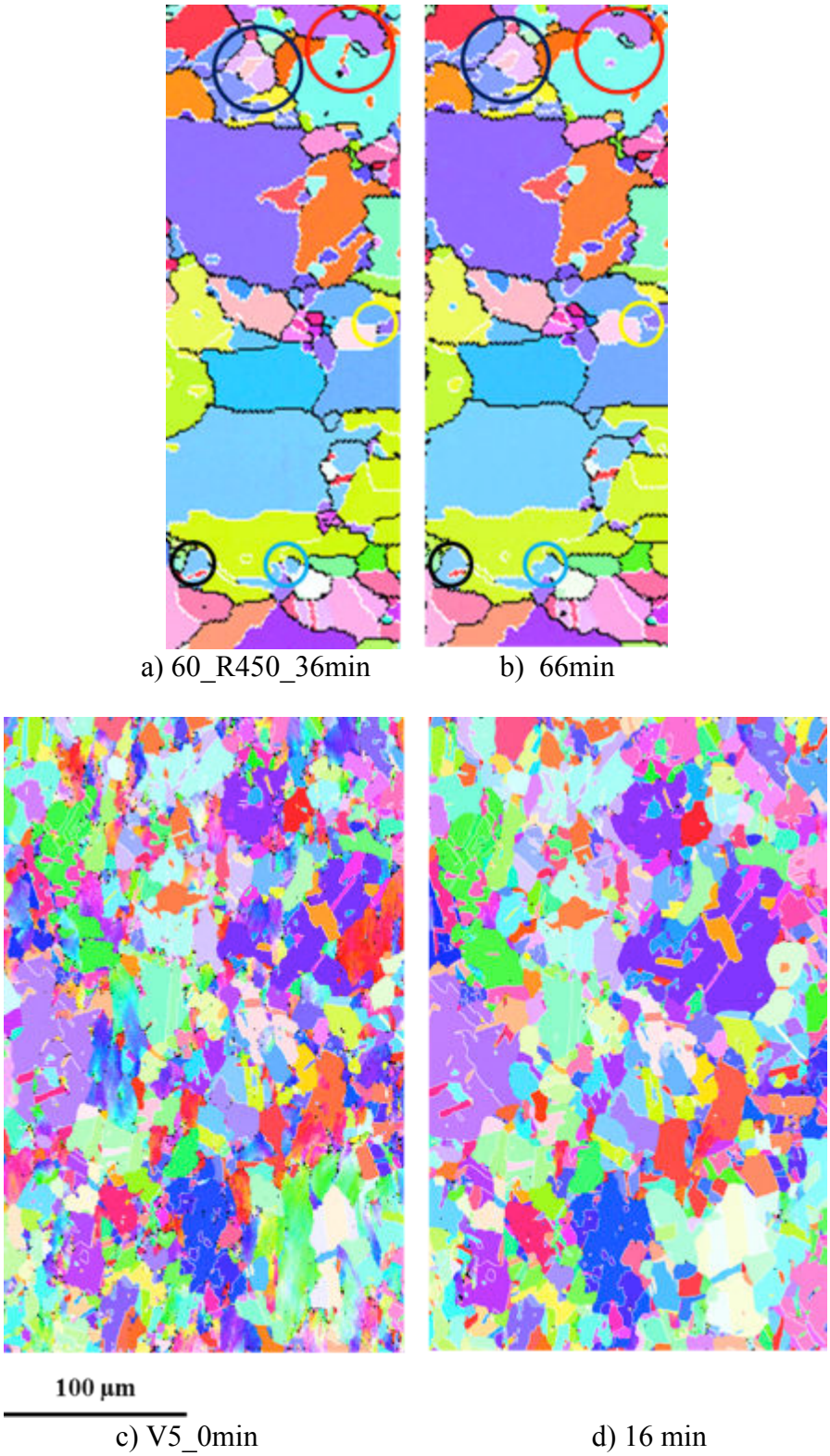

a) 60_R450_36min b) 66min

c) V5_0min d) 16 min

Fig. 3.9. Incoherent twin boundary migration in the recrystallized grains during recrystallization in the sample 60_R450 and V5 (same orientation color code as in Fig. 1); the cumulative annealing times are indicated under each EBSD map.

The numbers of annealing twin boundaries per grain N_G in the six analyzed samples in this chapter are plotted as a function of the average grain size in Fig. 3.10. Same as in the *in situ* dataset of pure nickel (section 2.2.2.1), the average N_G in the overall recrystallized microstructure increased continuously during recrystallization. Meanwhile, the correlation between N_G and the average grain size depends on the thermo-mechanical history of the sample e.g. the deformation amount and the initial grain size before deformation. (N_G was also calculated in the five biggest grains in each microstructure. The evolution of N_G in the biggest grains is very similar to the evolution of the average value in the overall recrystallized microstructure). As mentioned, in the Pande's model, the grain boundary migration driving force and the grain boundary migration distance are supposedly the only two factors influencing annealing twin formation. However, in the present study, the initial grain size before deformation, which could not influence significantly the average recrystallization front migration driving force, influences considerably the annealing twin development during recrystallization. Therefore, new considerations should be introduced to better explain annealing twin formation mechanisms.

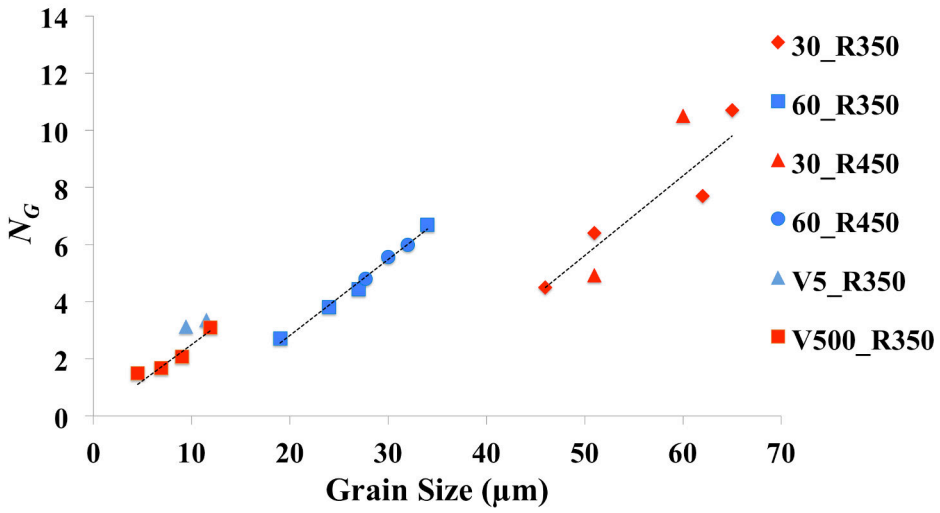

Fig. 3.10. The average number of annealing twin boundaries per grain in the overall recrystallized microstructure plotted as a function of the average recrystallized grain size in the six analyzed samples.

In the second chapter, a semi-atomistic model was proposed to explain the relationship between annealing twin formation and grain boundary curvature (see Fig. 2.27). According to this model, annealing twins are more likely to be formed behind convex grain boundary portions. In fact, annealing twins are mostly generated during recrystallization and behind the migrating recrystallization front(s). Following the growth accident model, a twin is more likely to form if the recrystallization front, or at least a portion of it, has {111} facets. Those

facets are wider if the considered portion is close to be parallel to {111} (at the mesoscopic scale). As schematized on Fig. 3.11 (a), the more tortuous the recrystallization front is, the higher is the probability to find portions of it parallel to any kind of plane and especially to {111} (arrowed on Fig. 3.11(a)). Among those {111} portions, those moving opposite to their curvature (double arrows) are more likely to form coherent twins according to the principle described on Fig. 2.27.

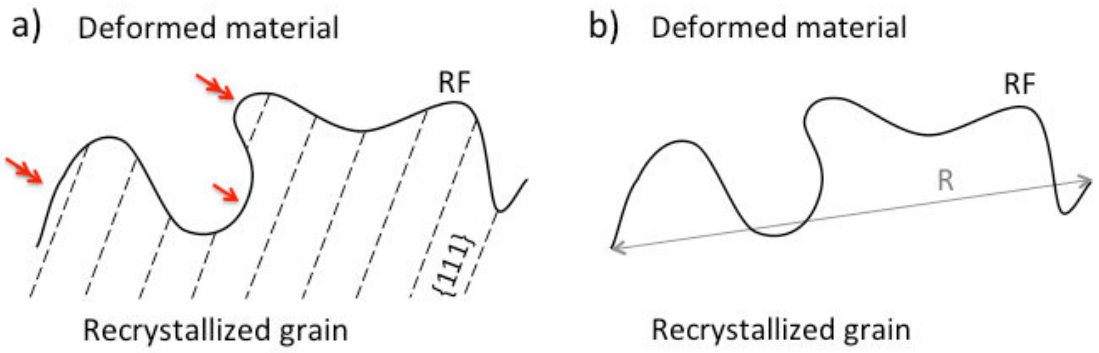

Fig. 3.11. a) Schematic of a recrystallization front (RF) with portions close to be parallel to {111} (arrowed). Following the principle proposed on Fig. 2.27, the convex ones, moving opposite to their curvature (double arrows), are potential sites for perfect coherent twins; the concave ones moving towards their curvature center (simple arrow) can only lead to coherent segments associated with incoherent ones which may further migrate and make the new twin annihilate. b) Same recrystallization front (RF) and its end-to-end length (R).

For a rough recrystallization front, the variations in local curvature should therefore lead to more potential sites for annealing twin generation. Overall, this implies that the recrystallization front tortuosity could also influence annealing twin formation during recrystallization. Therefore, we quantified the recrystallization front tortuosity within our EBSD maps (i.e. at the mesoscopic scale).

According to Epstein [Epstein 1989], the tortuosity of the recrystallization front (τ) can be calculated by a simple relationship:

$$\tau = \frac{L_{\mathrm{RF}}}{R}, \tag{3-1}$$

where L_{RF} is the length of the recrystallization front (geodesic length) and R is the end-to-end length of the recrystallization front (Euclidean length). Following that and as illustrated in Fig. 3.11, the average tortuosity of the recrystallization front in the overall microstructure has been calculated by following steps within the OIM software:

1. reconstruct the high-angle grain boundaries (twin boundaries excluded) in the overall microstructure based on the triple junctions (blue segments on Fig. 3.12 (a)). The maximum deviation between reconstructed boundary and corresponding boundary segments is 30 times the EBSD acquisition step sizes (e.g. 36μm for the EBSD maps shown in Fig. 3.3). It is worth mentioning that the applied deviation (30 pixels) is the maximum value allowed in the OIM software. For the considered EBSD maps, with this value, nearly all of the high-angle grain boundaries defined between two triple junctions can be reconstructed by a single straight line.
2. Calculate the total length of high-angle grain boundaries in the overall microstructure ($L_{\mathrm{GB}}^{\mathrm{O}}$) (twin boundaries are excluded) and the total length of the corresponding reconstructed boundaries (R^{O}).
3. Repeat step 1 and step 2 inside the deformed matrix only and the recrystallized part only as indicated respectively in Fig. 3.12 (b) (c). $L_{\mathrm{GB}}^{\mathrm{Rex}}$, $L_{\mathrm{GB}}^{\mathrm{Def}}$, R^{Rex} and R^{Def} denote respectively the length of high-angle grain boundaries inside all the recrystallized grains and the deformed matrix, the length of reconstructed boundaries inside all the recrystallized grains and the deformed matrix. Those values do not include the recrystallization front lengths.
4. The length of the recrystallization front and of the corresponding reconstructed boundaries can be calculated by the following equations:

$$L_{\mathrm{RF}} = L_{\mathrm{GB}}^{\mathrm{O}} - \left(L_{\mathrm{GB}}^{\mathrm{Rex}} + L_{\mathrm{GB}}^{\mathrm{Def}}\right), \tag{3-2}$$

$$R = R^{\mathrm{O}} - \left(R^{\mathrm{Rex}} + R^{\mathrm{Def}}\right). \tag{3-3}$$

The tortuosity of the recrystallization front was calculated in the EBSD map 30_350_110min, 60_350_60min, and V5_0min where the recrystallization is in progress and recrystallized grains impinge on each other forming clusters. As the deviation between reconstructed boundary and the corresponding boundary segments is defined by the EBSD acquisition step size, for the sake of consistency, the step size of the EBSD map of V5_0min was converted from 0.46 μm to 1.38 μm, which is close to the step size used the experiment aiming at testing the impact of prior deformation level and annealing temperature (1.2 μm), before applying the above procedure. As indicated in Table 3.4 and in Fig. 3.13, the recrystallization front tortuosity during recrystallization is positively correlated with the annealing twin density at the end of recrystallization.

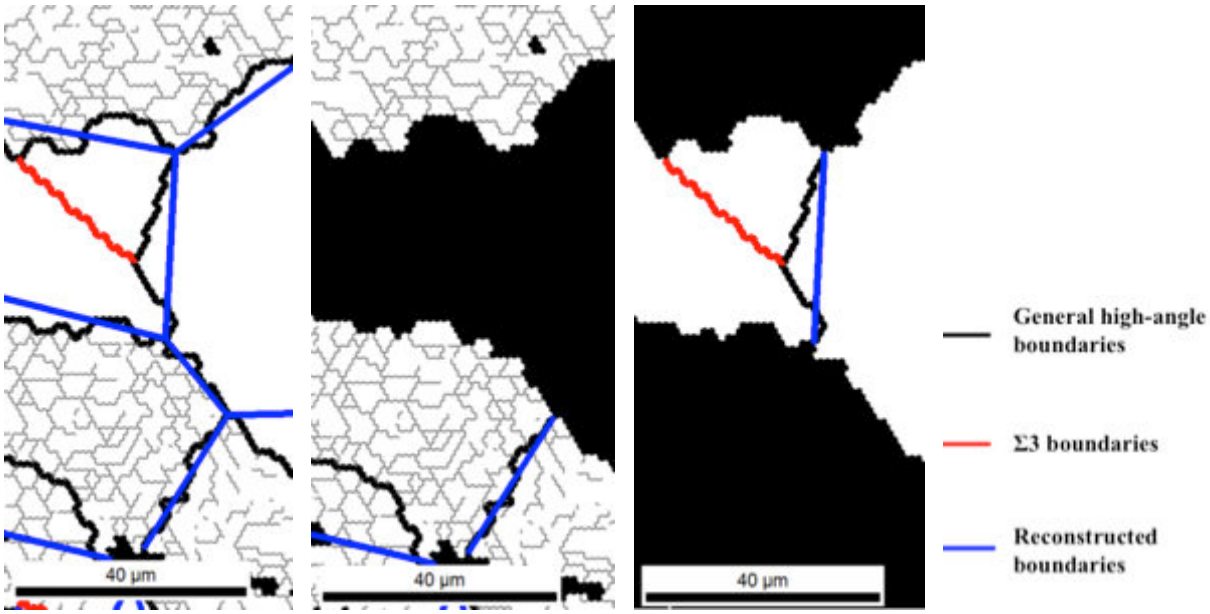

Fig. 3.12. Schematic of recrystallization front tortuosity calculation procedure; (a) the overall microstructure; (b) the non-recrystallized part; (c) the recrystallized part. Low angle grain boundaries (1-15°) are shown as grey thin lines, black lines are the general boundaries with a disorientation higher than 15°, red lines are Σ3 boundaries (within the Brandon's criterion), and blue lines are the reconstructed grain boundary segments (with a parameter for the allowed distance to the boundary of 30 pixels).

This observation is consistent with our idea that the variation in local curvature of the recrystallization front could promote annealing twin formation by providing more potential nucleation sites. The tortuosity of a migrating recrystallization front is found to arise when the stored energy level in the adjacent deformed matrix is non-uniform [Martorano 2006]. Indeed the stored energy level determines the driving force for recrystallization migration. Thus, the local fluctuation in stored energy level introduces local variation in recrystallization front migration velocity, which changes the local morphology of the front. This rationale may also explain the effect of deformation amount and the initial grain size before deformation on annealing twin formation observed in the present study through their influence on the fluctuations in the stored energy field. It is unclear whether increasing strain tends to homogenize or on the contrary to make the strain field more heterogeneous, considerations which are in addition very much scale dependent. There could be different answers depending on the strain range, on the material plasticity anisotropy, on its crystallographic texture, and many other microstructure properties. A dedicated study must be performed to answer such questions. On the other hand, prior grain boundaries give rise for sure to locally large orientation gradient due to strain incompatibility between the neighboring grains

[Humphyreys 2004]. Therefore, a fine-grain initial microstructure could also promote the heterogeneity in the stored energy field with shorter characteristic distances, and therefore higher tortuosity of the recrystallization front, and thus lead to higher twin densities.

Ref	L_{RF} (mm)	R (mm)	τ	Rex Fraction	N_L (mm^{-1}) at the end of Rex
30_R350_110min	13.1	7.9	1.79	0.46	29
60_R350_60min	15.2	7.6	2	0.84	46
V5_0min	17.3	6.9	2.5	0.61	128.5

Table 3.4. Recrystallization front tortuosity calculated in samples 30_R350, 60_R350 and V5.

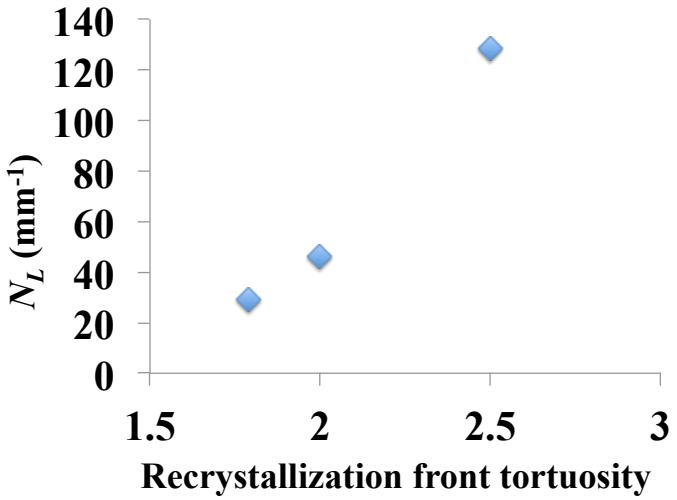

Fig. 3.13 Annealing twin density at the end of recrystallization as a function of recrystallization front tortuosity.

3.3. Conclusion

Two recrystallization experiment series were performed separately to analyze the influence of three thermo-mechanical processing parameters on annealing twin formation i.e. the stored energy level and annealing temperature on one hand and the heating velocity on the other hand, leading to the following conclusions:

- for a given initial grain size, annealing twin density in the overall microstructure after the completion of recrystallization appears to be primarily influenced by the deformation level.
- For a given strain level, smaller initial grain size leads to higher twin density.
- Different annealing twin quantification methods, including twin density, number of twin boundaries per grain and twin boundary fraction, can lead to different twin content interpretation depending on whether the average grain size is constant or not.
- The annealing twin content, measured as the twin density or the number of twin boundaries per grain in grains with similar sizes, is higher in samples with higher deformation level. Therefore the prior deformation level is confirmed to be a promoting factor for annealing twin formation during recrystallization.
- The annealing temperature and the heating velocity did not show any obvious effect on annealing twin formation during recrystallization.
- The recrystallization front tortuosity, as measured at the mesoscale in EBSD maps, is shown to be positively correlated with the annealing twin density at the end of recrystallization, consistents with the effect of grain boundary curvature proposed in chapter 2. The latter point should be further confirmed by applying the proposed method to larger datasets (2D and 3D, and more thermomechanical conditions).

Résumé en français

Le chapitre 3 vise à étudier les influences de différents facteurs thermomécaniques sur la formation de macles thermiques au cours de la recristallisation. Deux séries d'expériences ont été réalisées sur du nickel pur pour analyser d'une part l'influence du niveau de déformation et de la température de recuit et d'autre part l'influence de la vitesse de montée en température. Les échantillons ont d'abord été déformés par compression à température ambiante puis ont été recuits dans une gamme de température allant de 350°C à 550°C. La déformation a un effet de promotion sur la formation des macles thermiques durant la recristallisation ce qui ne semble pas être le cas de la température de recuit ainsi que de la vitesse de chauffage.

NUMERICAL PART

INTRODUCTION

In this second main part of the present thesis, the numerical part of the PhD project will be presented. In the first part, different annealing twin evolution mechanisms were described from the experimental data. The numerical part aims thus at developing numerical tools to simulate these mechanisms. Two types of numerical approaches i.e. mean field and full field models have been used.

Annealing twin evolution during recrystallization is influenced by different microstructural factors, e.g. possibly the recrystallization front morphology. The consideration of such topological factors requires the development of full field models to simulate local mechanisms and assess their sensitivity to the involved physical parameters. On the other hand, mean field models could be suitable to predict the overall amount of twins as a function of the applied thermomechanical parameters, which would be helpful for developing GBE routes.

For the sake of simplification, we focused at first on the simulation of annealing twin evolution during grain growth, but the derived formulations are also suitable for taking into consideration the effect of an additional driving force related to the presence of stored energy in the annealed microstructure.

First, a mean field model was developed to predict the twin density evolution during grain growth based on the classical Hillert's grain growth model [Hillert, 1965]. This model, which offers new perpestives for twin density prediction, is proven to be consistent with the twin density evolution in the Inconel 718 data. It is presented in chapter 4.

Full field modelling of twin evolution is more challenging. As presented previously, annealing twin boundaries, especially coherent twin boundaries, have very low interfacial energy compared to regular high angle boundaries [Olmsted, 2009]. Typically the energy of a coherent twin boundary is 20 times smaller than the one general high misorientation angle boundaries. Therefore, a strong anisotropy in grain boundary energy has to be taken into account in the full field simulations, which is a challenge. In addition, the twin boundary morphology also needs to be explicitly described. Two implicit methods i.e. phase field and level set method are applied; the theoretical bases of both are presented in chapter 5. In chapter 6, their numerical performances in anisotropic grain growth simulation are compared in a finite element (FE) context. We show evidence that the level set method is more accurate

and efficient in the present numerical context with strong anisotropy in grain boundary energy. A methodology is thus developed in the level set framework to simulate annealing twin evolution during grain growth.

In chapter 7, two large grain growth simulations with respectively isotropic and anisotropic grain boundary energies are performed with the level set method. The grain growth kinetics obtained from these two simulations is compared with the classical Burke and Turnbull model [Burke, 1952]. A new methodology based on level set method to simulate annealing twin evolution is also presented and the possibility to simulate annealing twin evolution during recrystallization and grain growth is discussed.

4. MEAN FIELD MODELING OF ANNEALING TWIN DENSITY EVOLUTION DURING GRAIN GROWTH

As presented in chapter 2, there are almost no annealing twins formed in the grain growth regime for both pure nickel and for the Inconel 718 superalloy. We developed a new mean-field model to predict average twin density evolution in the overall microstructure during grain growth based on this fact.

In this chapter, the model will be described at first, then it will be tested on the experimental results obtained for Inconel 718 presented in chapter 2, and will be compared with the Pande's model.

4.1 Description of the mean field model

The model aims at modelling average twin density evolution in the overall microstructure during grain growth.

In the model, the material microstructure is represented, based on the same principle applied by [Bernard 2011], by a set of representative grains G_i, defined by two variables: the grain diameter D_i and the twin boundary length L_{tb}^{i}. Representative grains stand for the average state of a number N_i of identical spherical grains coming from different points of the microstructure. At this stage, twins are omitted to define a grain.

In mean curvature driven grain growth with isotropic mobility and grain boundary energy (which can be assumed since twins are not considered to be boundaries of the growing grains), the two-dimensional average grain boundary migration velocity of the grain G_i can be expressed using the Hillert's classical mean field model [Hillert 1965]:

$$\frac{dD_i}{dt} = 2 \cdot M\gamma_g \left(\frac{1}{D} - \frac{1}{D_i} \right), \tag{4-1}$$

where M is the grain boundary mobility and D is the arithmetic mean grain size.

As presented previously, essentially no twins formed during grain growth, thus the twin evolution is mainly controlled by the evolution of the pre-existing twins. More concretely, annealing twin boundaries intersecting grain boundaries are extended or shrink in length as the grain boundary migrates. The basic principle of the model is to describe by how much the twin length in a grain is changing when the grain size either increases or decreases. The real topology of twin boundaries is complex, especially that of incoherent twins which could hardly be classified like coherent ones can be (presented in chapter 1, section 1.1.1.3). It would thus be quite complicated, if not impossible, to derive a proper analytical description of the change in twin boundary length associated with a change in grain size. Thus, instead, we have tested a rough but very simple assumption that is: the change in twin boundary length L_{tb}^{i} is proportional to the change in grain size D_i for each grain family G_i and in each time increment.

In mathematical terms, this assumption of the model becomes:

$$\frac{L_{tb}^{i}(t+\Delta t)-L_{tb}^{i}(t)}{L_{tb}^{i}(t)} = k\,\frac{D_i(t+\Delta t)-D_i(t)}{D_i(t)}, \tag{4-2}$$

In first approximation, k will be assumed to be constant and to be identical for growing grains and shrinking grains, which again are strong hypotheses.

When a representative grain is fully consumed by other grains, the corresponding twin boundary length nullifies, as observed. For idealized circular grains, the proportionality factor k is mainly influenced by two factors, illustrated in Fig. 4.1:

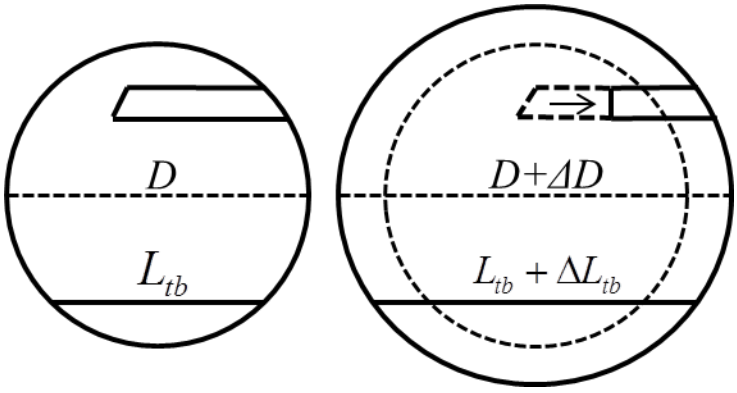

Fig. 4.1. Annealing twin evolution mechanisms during grain growth

- For a coherent twin boundary spanning opposite side of the grain, since $\Delta L_{tb}^{i} \geq \Delta D_i$ (equality occurs when L_{tb}^{i} is a diameter of the considered circular grains) and $L_{tb}^{i} \leq D_i$ we have $\Delta L_{tb}^{i} / L_{tb}^{i} \geq \Delta D_i / D_i$, thus k should in principle be higher than one. However, if there is more than one coherent twin boundary inside the grain, the total twin boundary length is not necessarily smaller than the grain diameter. In this case, the value of k depends also on the initial ratio between the twin boundary length and the grain diameter.
- Incoherent twin boundary segments may migrate inside grains to decrease the total twin boundary length. This may lead to the shortening of the considered twin boundary, even though the GB migration tends to lengthen it, which is another reason for which k might be smaller than 1.

The effect of annealing temperature on incoherent twin boundary migration and the possible material dependency of incoherent twin boundary migration behaviors are implicitly considered in the parameter k.

In the following, the constant k will be identified based on the experimental results presented in section 2.4 (grain growth data of Inconel 718).

4.2 Mean field modelling of twin density evolution during grain growth in Inconel 718

The grain size distribution of the initial microstructure of Inconel 718 (experiments presented in section 2.4) was used as an input. It was discretized into 49 grain size categories (Fig. 4.2a) and the twin density was measured for each category (Fig. 4.2b). The twin density N_L is calculated from the twin boundary length per unit area using Eq. 1-9.

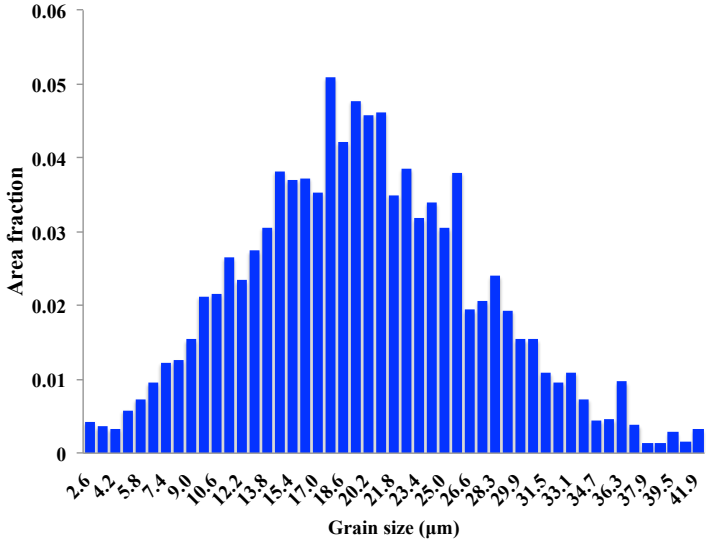

(a) Grain size distribution histogram (mean grain size = 13µm)

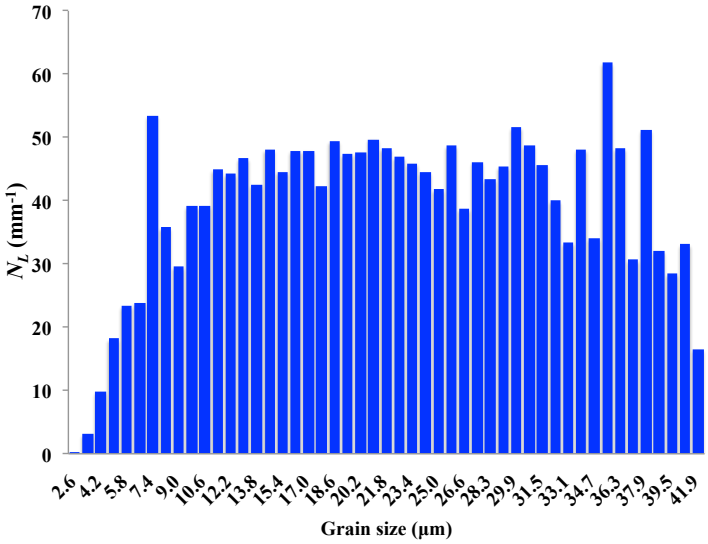

(b) Twin density as a function of grain size

Fig. 4.2. Properties of the initial microstructure (EBSD map shown on Fig. 2.22)

In the initial microstructure, the twin density is quite homogeously distributed over the whole range of grain sizes, except for the small grain families. Meanwhile, the small grains in the 2D observed section could be large grains in 3D. The 2D annealing twin content inside these small grain families could thus deviate from the actual real value in 3D.

For the physical parameters grain boundary mobility M and grain boundary energy γ_{gb}, values were chosen within the range of typical values for metals ($M=1.37\cdot10^{-12}$ $m^4/(J\cdot s)$ and $\gamma_{gb}=0.6$ J/m^2). Those values therefore do not refer to a specific material. Since this model aims at predicting the twin density evolution as a function of grain size, but not as a function of time, it is not necessary to stick to the grain growth kinetics of a particular material. Furthermore,

for a given material, the twin density evolution is not influenced by the grain growth kinetics during grain growth as presented in section 2.2 and 2.4.

The value of 0.9 for k was determined based on the best fit of the experimental data of the grain growth regime on Inconel 718 (originally shown in Fig. 2.24). The average annealing twin density evolution in the overall microstructure modeled by the mean field model with the time step dt=1s is described in Fig. 4.3. With the chosen value of k, the present experimental data can be well described by the mean field model.

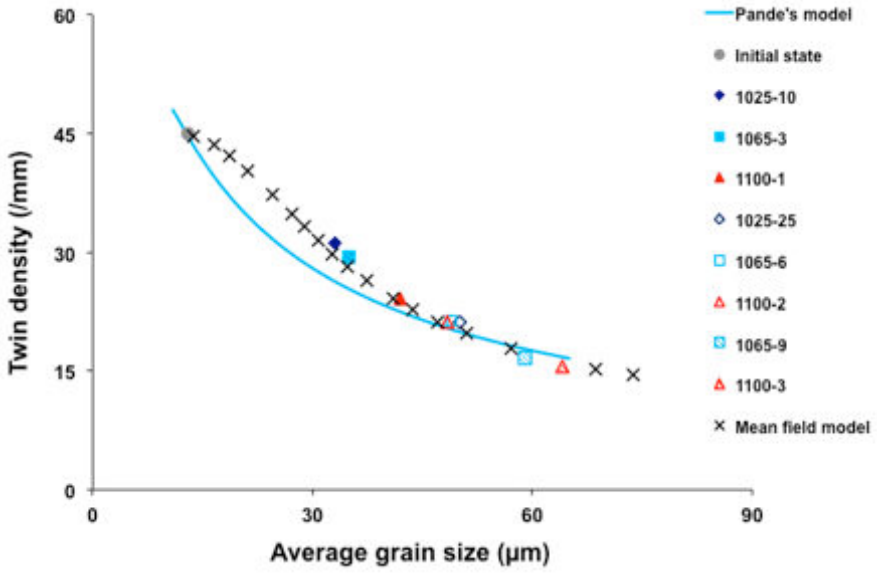

Fig. 4.3. Average twin density evolution compared with Pande's model (best fit to Eq.1-28 with $\gamma_g \approx 1 J \cdot m^{-2}$) and the mean field model.

In addition, for the sake of determining the possible impact of the time step on the modelling results, the evolution of the grain size and twin density distributions at different stages of the mean field modelling using dt=1s and 0.5s are shown in Fig. 4.4. The modelling results using these two time steps are almost identical, which shows the convergence of the calculation.

During the modelling process, small grains are consumed by large grains. The disappearance of small representative grains leads to a decrease in the total number of representative grains, as illustrated by Fig .4.4.

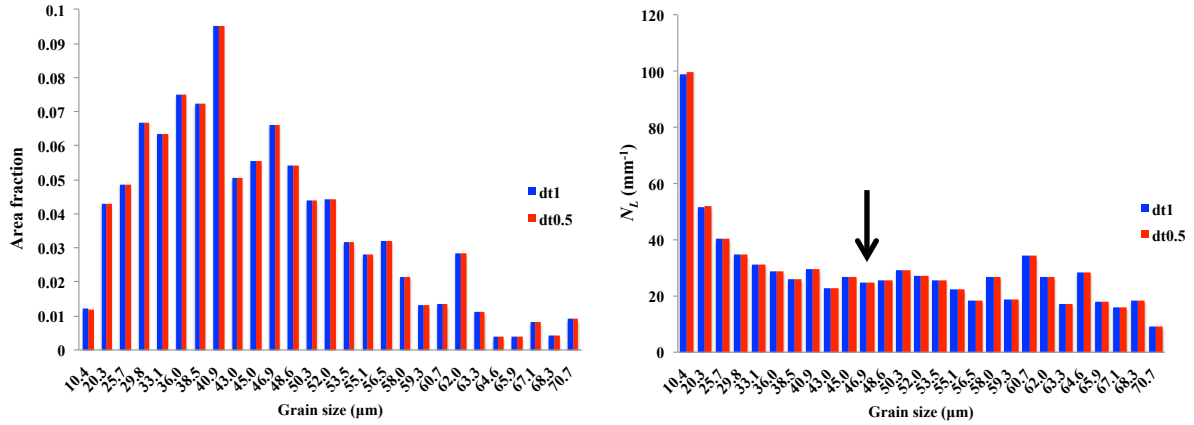

(a-1) Grain size distribution (a-2) Twin density as a function of grain size

(a) Mean field modelling result at t=375s (arithmetic mean grain size = 32.7 μm)

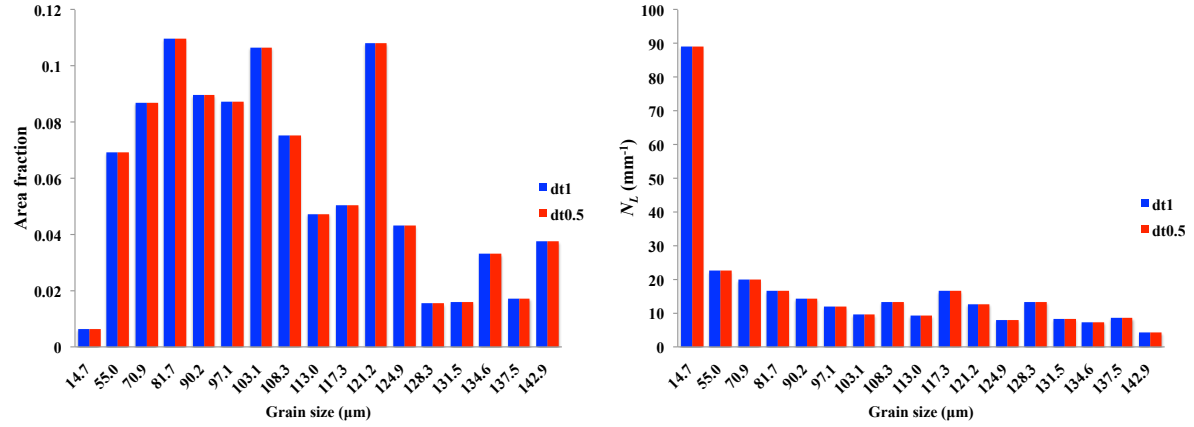

(b-1) Grain size distribution (b-2) Twin density as a function of grain size

(b) Mean field modelling result at t=3150s (arithmetic mean grain size = 73.6 μm)

Fig. 4.4. The evolution of grain size distribution and twin density distribution in the mean field modelling; the grain family at t=375s corresponding to the smallest reprentative grain at t=3150s is pointed by the black in (a-2).

In Fig. 4.4, the twin density related to the large representative grains is quite homogeously distributed over the whole range of grain sizes, as it was in the initial microstructure, and somewhat decreases when increasing grain size. However, the twin density related to the smallest representative grain is much higher. According to Eq. 1-9, the twin density related to G_i can be calculated by the following equation:

$$N_L^i = \frac{2}{\pi} \cdot \frac{L_i}{\pi N_i \left(\frac{D_i}{2}\right)^2} . \tag{4-3}$$

Thus, for each representative grain, the twin density is inversely correlated to the square of the corresponding grain size. At the same time, the change in twin boundary length L_{tb}^i is

proportional to the change in grain size D_i in each time increment as indicated in Eq. 4-2. For the smallest representative grain, consumed by the other grain families, its grain size shrinks a lot compared to its initial grain size. Therefore, the high twin density related to the smallest representative grain is numerically caused by the important shrinkage of its size. For example, in Fig. 4.4, at t=3150s, the grain size of the smallest representative grain is 14.7 μm and the related twin density is about 90 mm^{-1}. At t=375s, the grain size of the corresponding grain family (marked in Fig. 4.4(a)) is about 47 μm, and the related twin density is about 26 mm^{-1}.

4.3 Discussion and conclusion

The model proposed here accounts for the observed mechanism of annealing twin evolution during grain growth: basically no new twins are formed but only the pre-existing ones evolve (expanding or shortening while the related grain boundary moves, or shortening if an end incoherent segment migrates). Despite the rough assumption made in the model for the dependence of the twin length in a grain on the size of that grain (simple proportionality), the experimental data (grain growth in Inconel 718) could be well decribed by the model. The most remarkable point is that there is only one parameter to be identified, contrary to the other existing models, which have at least two parameters.

For the sake of comparison, the Pande's model has wrong assumptions with regards to the underlying phyiscal mechansims, it has two paremeters to be identified, and cannot fit the experimental data as well as the mean field model (as illustrated in Fig. 4.3). The values used for the parameters in the Pande's model are the same as in section 2.4 ($K \approx 0.3 m^3 \cdot J^{-1}$ and $D_0 \approx 2 \mu m$).

The model proposed here appears then to be promising, even though it needs to be further validated by comparison with more experimental data, which could not be done here by lack of time.

Furthermore a 3D extension of the present mean field could be considered, but would require 3D data as an input. The two-dimensional grain size distribution can be reasonably converted to an approached three-dimensional distribution [Saltykov 1967]. However, the two-dimensional annealing twin boundary content cannot easily be converted to three-dimensional data.

Résumé en français

Comme présenté dans le chapitre 2 pour le nickel pure et l'Inconel 718, la formation des macles thermiques semblent être très limitée en régime de croissance de grains. Basé sur cette observation, un nouveau modèle de type champ moyen est proposé afin de modéliser l'évolution de la densité de macles moyenne dans la microstructure en régime de croissance de grains. Le modèle est détaillé, testé sur les données expérimentales obtenues pour l'Inconel 718 et comparé aux prédictions du modèle de Pande.

5. THEORETICAL BASIS – IMPLICIT FULL FIELD MODELING IN ANISOTROPIC GRAIN GROWTH SIMULATION

Over the last two decades, lots of progress has been made in full field modeling of microstructure evolution during recrystallization and grain growth. The most famous and still widely used full field grain growth modelling technique is the probabilistic Monte-Carlo method (MC). This method is based on two main points: first, the use of a pixilated or voxelated description of the granular microstructure and, secondly, the construction of probabilistic evolution rules [Rollet 2001]. Meanwhile, the absence of time scale in the model complicates any comparison with experimental data [Rollet 1997]. The cellular automaton (CA) approach is another probabilistic method [Rollett 1997] [Rollett 2001] [Madej 2013]. Several physical rules are used to locally determine the cell propagation in relation to the neighboring cells and all the cells can be updated at the same time. As in the MC approach, the stochastic nature can lead to the same problem of representativity. In the standard CA method, the state of all cells is simultaneously updated, which provides efficiency. However a precise calculation of the mean curvature, which is necessary for grain boundary migration by capillarity [Rollett 2001] remains difficult. A comparison between MC and CA in static recrystallization modelling is performed in [Sieradzki 2013].

Different from probabilistic models, implicit full field models can describe more precisely the morphological evolution of microstructures. Two implicit full field models exist in the literature: the phase field (PF) method and the level set (LS) method. The phase field method

consists in describing an arbitrary polycrystalline microstructure by a set of continuous field variables. Each field variable represents a grain orientation. Across the grain boundaries between a grain and its neighbor grains, the value of the corresponding field variables varies smoothly from one to zero (or one to minus one) [Collins 1985]. The arbitrary microstructure evolves in the direction to minimize the total free energy expressed as a function of the field variables. Two different phase-field approaches are mainly applied in the literature, namely the continuum-field model originated from the work of Fan and Chen [Fan 1997] and the multi-phase-field model originated from Garcke et al [Garcke 1999]. Both approaches are used in the literature to model the anisotropic grain growth phenomenon, e.g. the continuum-field model in the work of [Moelans 2008 PRB] [Chang 2014] and the multi-phase-field model in the work of [Steinbach 1999] [Hirouchi 2011]. The two approaches were compared in details in terms of formulation and numerical performance, in the context of uniform grids with a finite difference formulation in a paper by [Moelans 2009]. The LS method has many common points with the PF method, e.g. they both avoid tracking interfaces [Bernacki, 2008]. The use of the LS approach is rather recent in the context of grain boundary migration. It was already used to model recrystallization [Bernacki 2008] [Logé 2008] [Bernacki 2009] [Resk 2009] [Agnoli 2014] [Hallberg 2013] (with or without nucleation and with or without capillarity effects), crystal plasticity finite element method [Logé 2008] [Bernacki 2009] [Resk 2009], pure isotropic grain growth [Elsey 2009] [Bernacki 2011] [Fabiano 2014], and large-scale anisotropic pure grain growth in the context of uniform grids with a finite difference formulation [Elsey 2013]. Although these two approaches are therefore now widely used for modeling anisotropic grain growth, their formulations are extremely different and comparing their numerical performances is not straightforward.

As already mentioned, since the numerical part of the present PhD work aims at modelling annealing twin evolution during grain growth, the implicit models that are able to provide precise prediction of morphological evolution of microstructures are more suitable. In this chapter, a literature review is performed to analyse and compare the theoretical bases of phase field and level set methods. Firstly, the two phase-field approaches as well as their comparison in the literature will be presented. Secondly, the considered LS framework will be introduced.

5.1 Continuum field model

5.1.1 Equations of motion for the Phase Fields

If a system is unstable to a change that is infinitesimal in degree but large in extent, its initial state or phase will transform to a more stable one. Gibbs formulated the general conditions necessary for this kind of instability. Specifically he showed that a necessary condition for the stability of a fluid phase to such a fluctuation is that the chemical potential of each component increases with increasing the concentration of the system in that component. However, the initial phase is needed to be unstable to a kinetic fluctuation in order to transform to a more stable phase. For example, a numerical microstructure generated by phase field functions will change to a 'thermodynamically' more stable state by sustaining the fluctuation of the phase field functions.

If we consider an isotropic solid solution free of imperfections, the total Helmholz free energy can be written as [Cahn 1961]:

$$F = \int_V f(c)\,dV, \text{ with } f(c) = f_0(c) + \frac{k}{2}\|\nabla c\|^2, \tag{5-1}$$

where $f_0(c)$ is the Helmholz free energy of a unit volume of the homogeneous material with the composition c, and $\frac{k}{2}\|\nabla c\|^2$ is the first term of an expansion representing the increase in free energy due to introducing a gradient of composition, with k the so-called gradient energy coefficient. The evolution of the composition c will be in the direction ensuring a decrease of the total free energy as shown by the following formula, which is consistent with the Ginzburg-Landau equation:

$$\frac{\partial c}{\partial t} = -L\frac{\delta F}{\delta c}, \tag{5-2}$$

where $\frac{\delta F}{\delta c}$ is the variational derivative and L is the relaxation coefficient. Then,

$$\frac{\delta F}{\delta c} = \frac{\partial f(c)}{\partial c} - \nabla \cdot \frac{\partial f(c)}{\partial \nabla c} \quad . \tag{5-3}$$

M. Allen [Allen 1978] replaced the composition c by a long-range order parameter η. Then the equation (5-3) becomes

$$\frac{\delta F}{\delta \eta} = \frac{\partial f(\eta)}{\partial \eta} - \nabla \cdot \frac{\partial f(\eta)}{\partial \nabla \eta} = \frac{\partial f_0(\eta)}{\partial \eta} - k\Delta\eta \,. \tag{5-4}$$

In the continuum field model, an arbitrary polycrystalline microstructure is described by a set of continuous field variables,

$$\eta_1(t,x),\ \eta_2(t,x),\ \ldots,\ \eta_{N_G}(t,x), \tag{5-5}$$

where $\eta_i(t,x)$ $(i=1,\ldots,N_G)$ are called orientation field variables for distinguishing different orientations of grains and N_G is the number of grains. Inside the grain described by $\eta_0(t,x)$, the value of $\eta_0(t,x)$ is 1 while all other $\eta_{i\neq 0}(t,x)$ are equal to zero. And across the grain boundaries between the grain $\eta_i(t,x)$ and its neighbour grains, the value of $\eta_i(t,x)$ changes continuously from 1 to 0 as illustrated in Fig. 5.1.

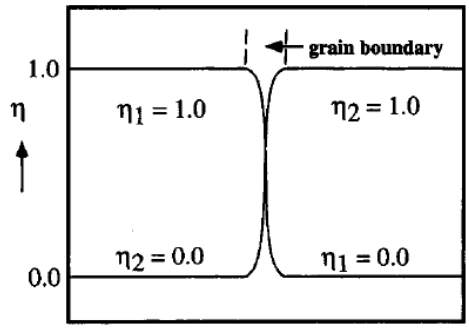

Fig.5.1. Schematic profiles of two orientation variables across a flat grain boundary.

Analogous to the diffuse interface theory of Allen and Cahn [Allen 1978], the total grain boundary energy of a microstructure is expressed by the field variables $\eta_1(x),\ \eta_2(x),\ \ldots,\ \eta_{N_G}(x),$ and their gradients [Fan 1997]:

$$F(t) = \int_V [\tau f_0\left(\eta_1(t,x),\ \ldots,\ \eta_{N_G}(t,x)\right) + \frac{k}{2}\sum_{i=1}^{N_G}\left\|\nabla\eta_i(t,x)\right\|^2]dV \tag{5-6}$$

As previously, f_0 is the local free energy density that is a function of field variables η_i (τ is a model parameter) and k is the gradient energy coefficient. The only requirement for f_0 is to respect N_G minima with equal depth located in the bulk part of each grain i.e. at $\left(\eta_1,\ \eta_2,\ \ldots,\ \eta_{N_G}\right) = \left(1,\ 0,\ \ldots,0\right),\ \left(0,\ 1,\ \ldots,0\right),\ \ldots,\ \left(0,\ 0,\ \ldots,1\right)$. We must pay attention that, originally, Allen [Allen 1978] proved that the migration velocity is then independent of the chosen mathematical function f_0 only for gently curved interfaces. However, Fan and Chen [Fan 1997] have contestably generalised this conclusion to all kind of boundaries.

As presented above, the local evolution rates of field variables are also governed by Ginzburg-Landau equations:

$$\frac{\partial \eta_i}{\partial t}(t,x) = -L\frac{\delta F}{\delta \eta_i(t,x)},\ i = 1,\ 2,\ \ldots,\ N_G \tag{5-7}$$

In order to resolve equations (5-7), an expression of the local free energy density must be proposed.

As explained, the requirement for f_0 is that it provides potential wells with equal well depth located in the bulk part of each grain. Fan and Chen [Fan 1997] proposed a simple function that satisfies this requirement:

$$f_0\left(\eta_1(t,x),\ \eta_2(t,x),\ \ldots,\ \eta_{N_G}(t,x)\right) = \sum_{i=1}^{N_G}\left(-\frac{1}{2}\eta_i^2(t,x) + \frac{1}{4}\eta_i^4(t,x)\right) + \alpha\sum_{i=1}^{N_G}\sum_{j\neq i}^{N_G}\eta_i^2(t,x)\eta_j^2(t,x), \tag{5-8}$$

where α is a positive parameter.

Using the expression for f_0 given in equation (5-8), and then substituting the total free energy F into equation (5-7), we obtain the kinetic equations,

$$\frac{\partial \eta_i}{\partial t}(t,x) = -L\left(\tau\left(-\eta_i(t,x) + \eta_i^3(t,x) + 2\alpha\eta_i(t,x)\sum_{j\neq i}^{N_G}\eta_j^2(t,x)\right) - k\Delta\eta_i(t,x)\right),\ \ i = 1,\ 2,\ \ldots,\ N_G \tag{5-9}$$

Here, the expression of f_0 is constructed by considering the capillarity forces as the only grain boundary migration driving force. It is worth mentioning that in the framework of the continuum phase field model, to simulate microstructure evolution during recrystallization, it is necessary to introduce the driving force due to the different in stored energy level. Phase field variables can be used to describe the subgrain structure inside the deformed matrix. The recrystallization front migration can be thus simulated by the interaction between the phase field varibles representing the recrystallized grains and the ones representing the subgrains inside the deformed matrix [Suwa 2007].

5.1.2 Parameter determination

There are four model parameters i.e. L, α, k and τ in the motion equation (Eq.5-9). Thanks to the work of Moelans et al [Moelans 2008 PRB], these parameters were linked to real physical parameters including the grain boundary energy (γ_{gb}), the grain boundary mobility (m_{gb}) and the grain boundary thickness (l_{gb}):

$$\begin{cases} k = \gamma_{gb} l_{gb} \dfrac{\sqrt{f_{0,\mathrm{int}erf}(\alpha)}}{g(\alpha)} \\ L = \dfrac{m_{gb}}{l_{gb}} \dfrac{g(\alpha)}{\sqrt{f_{0,\mathrm{int}erf}(\alpha)}} \\ \tau = \dfrac{\gamma_{gb}}{l_{gb}} \dfrac{1}{g(\alpha) f_{0,\mathrm{int}erf}(\alpha)} \end{cases}, \tag{5-10}$$

where $f_{0,\mathrm{int}erf}(\alpha)$ refers to the value of f_0 at the middle of the diffuse region and $g(\alpha)$is a function of α, that has to be evaluated numerically. For isotropic grain growth, the phase field variables have symmetrical profiles at grain boundaries i.e. $\eta_i = 1 - \eta_j$ at the interface between only two neighbouring phases *i* and *j*. In this case, α is proven to be necessarily equal to 1.5 [Moelans 2008 PRB]. Accordingly, the three relationships in Eq.5-10 can be used to determine the three other parameters. However, for anisotropic grain growth (misorientation dependent grain boundary energy/mobility), the phase field variables have arbitrary profiles at grain boundaries and the value of α is *a priori* unknown. Therefore, an iterative procedure needs to be applied to calculate the values of the four parameters based on Eq.5-10. A list of discrete values $\gamma_{gb,ij}$ and $m_{gb,ij}$ for each grain boundary Γ_{ij} and the desired grain boundary width l_{gb} are required for the procedure. As output, the discrete values of L_{ij}, k_{ij}, α_{ij} and τ will be obtained. We refer to [Moelans 2008 PRB] for more details of this procedure.

Therefore, for misorientation dependent anisotropic grain growth, the parameters of the motion equation Eq.5-9 can be rewritten as follows:

$$A(t,x) = \frac{\sum_{i=1}^{N_G} \sum_{j>i}^{N_G} A_{ij} \eta_i^2(t,x) \eta_j^2(t,x)}{\sum_{i=1}^{N_G} \sum_{j>i}^{N_G} \eta_i^2(t,x) \eta_j^2(x,t)}, \quad \text{for } A = L,\ \alpha,\ k. \tag{5-11}$$

A_{ij} represent the values of L_{ij}, k_{ij}, α_{ij}. It is worth mentioning that since the grain boundary inclination of Γ_{ij} can be explicitly expressed by phase field variable:

$$\Phi_{i,j}(t,x) = \frac{\nabla\eta_i(t,x) - \nabla\eta_j(t,x)}{\left\| \nabla\eta_i(t,x) - \nabla\eta_j(t,x) \right\|}, \tag{5-12}$$

the inclination dependent anisotropy can also be considered by continuum field model.

The continuum field model is proven to be able to simulate anisotropic grain growth [Chang 2014]. However, two major drawbacks of the model should be underlined:

1. the model was only validated for low anisotropy of grain boundary energy i.e. when the ratio between the highest grain boundary energy and the lowest one is not greater than 3 [Moelans 2008 PRL] [Moelans 2008 PRB] [Chang 2014]. This limit implies that the model is *a priori* not suitable to simulate annealing twin evolution.
2. The parameters in the model cannot be directly associated with real physical parameters. For misorientation dependant anisotropic grain growth, an iterative procedure should be applied to determine the discrete values of grain boundary energy and mobility. This determination procedure will be complicated for large grain growth simulations.

5.2 Multi-phase-field model

Besides the continuum field model, another phase-field approach, originating from the work of Steinbach et al [Steinbach 1996] is referred to as the multi-phase-field model in the literature. Same as for the continuum field model, the polycrystalline microstructure is represented by a set of non-conserved phase fields. The major difference between these two approaches is in the interpretation of the phase-fields. In the continuum field model, the phase field variables, treated independently, change monotonously between values at diffuse grain boundaries without any constraint. Meanwhile, in the multi-phase-field model, the phase fields are interpreted as volume fractions, which are subject to the constraint that the summation of the phase fields must equal to one at each position in the system. Moreover, as presented before, the free energy in the continuum field model has multiple minima. On the contrary, the free energy of the multi-phase-field model has only one single minimum for all phase fields that is equal to zero. In this section, the theoretical basis of the multi-phase-field model is described.

5.2.1 Multiphase free energy density

In the multi-phase-field model, the free energy function is dependent on the local phase field variables η_i and their spatial derivatives $\nabla\eta_i$,

$$F\left\{\eta_1,\ \ldots,\ \eta_{N_G},\ \nabla\eta_1,\ \ldots,\nabla\eta_{N_G}\right\} = \int_V f\left(\eta_1,\ \ldots,\ \eta_{N_G},\ \nabla\eta_1,\ \ldots,\nabla\eta_{N_G}\right)dV\ . \qquad (5\text{-}13)$$

The local free energy density f was expanded following Eq. 5-14 :

$$f = f^{(0)} + \sum_{i=1}^{N_G} f_i^{(1)} + \sum_{i<j}^{N_G} f_{ij}^{(2)} + \sum_{i<j<k}^{N_G} f_{ijk}^{(3)} \quad . \tag{5-14}$$

f^0 contains energy independent of the phase state; f_i^1 is the energy difference between bulk phases; $f_{ij}^{(2)}$ is the energy of the grain boundary between phases i and j ; $f_{ijk}^{(3)}$ corresponds to the energy of triple junctions. We can notice here that different from the continuum phase field model, in which the free energy expression is constructed numerically, the local free energy density f in the multi-phase-field model is expanded into several components associated with real physical meanings. Therefore, in the multi-phase-field model, the consideration of different types of grain boundary driving force, e.g. the stored energy [Takaki 2009], is more straightforward. In the present work, we will concentrate on the application of this method for misorientation dependent anisotropic grain growth simulation.

Different expressions of the local free energy density can be found in the literature. The one given be Steinbach in 1998 is commonly used for anisotropic grain growth simulation [Steinbach 1999] [Debashis 2012] [Guo 2011]. It can be summarized as follows :

I. Steinbach 1999 [Steinbach 1999]

1. $f^{(0)}$ was neglected.
2. $f_i^{(1)}$ was neglected.
3. $f_{ij}^{(2)} = f_{ij}^{pot} + f_{ij}^{kin}$,

$$f_{ij}^{pot}(t,x) = w_{ij}\eta_i(t,x)\eta_j(t,x) \quad , \tag{5-15}$$

$$f_{ij}^{kin}(t,x) = -\frac{1}{2}\varepsilon_{ij}\nabla\eta_i(t,x)\cdot\nabla\eta_j(t,x) \quad . \tag{5-16}$$

4. $f_{ijk}^{(3)}$ was also considered negligible.

As it can be seen in Eq. 5-15 and 5-16, the energy $f_{ij}^{kin}(x,t)$ and $f_{ij}^{pot}\left(x,t\right)$ are not trivial at grain boundaries. More precisely, the term $f_{ij}^{kin}(x,t)$ tends to increase the interface width (to reduce gradients) whereas the potential energy $f_{ij}^{pot}\left(x,t\right)$ tends to decrease it.

In these expressions, w_{ij} and ε_{ij} are model parameters that can be directly linked to real physical parameters which are the grain boundary energy density $\hat{\sigma}_{ij}$ and the average grain boundary thickness λ [Ma 2006] [Guo 2011] by the following equations:

$$\varepsilon_{ij} = \hat{\sigma}_{ij}\frac{8\lambda}{\pi^2},\ w_{ij} = \hat{\sigma}_{ij}\frac{4}{\lambda}. \tag{5-17}$$

It is worth mentioning here that λ is a purely numerical coefficient inherent to the model. Its relationship with l_{gb} will be given in the next chapter (6). The corresponding motion equation derived from this energy expression will be given in the following section.

5.2.2 Equations of motion for the Phase Fields

For the sake of reducing the numerical cost, a new variable – the number of locally present phases $\tilde{N}_G(x,t)$ – was introduced by Steinbach et al [Steinbach 1999] :

$$\tilde{N}_G(t,x) = \sum_{i=1}^{N_G}\chi_i(t,x),\ \text{with}\ \forall j \in \{1,\ldots,N_G\}\ \chi_j(t,x) = 1 \text{ if } \eta_j(t,x) > 0 \text{ and } 0 \text{ otherwise.} \tag{5-18}$$

For example, $\tilde{N}_G(t,x)$ equals 2 on dual interfaces, 3 on triple junctions...

Same as in the continuum field model, the motion of the field variables $\eta_i(t,x)$ is obtained thanks to the minimization of the total free energy F :

$$\frac{\partial \eta_i}{\partial t}(t,x) = -\mu\frac{\delta F}{\delta \eta_i} = \mu\left(\nabla\cdot\frac{\partial}{\partial\nabla\eta_i} - \frac{\partial}{\partial\eta_i}\right)f\ . \tag{5-19}$$

where μ is the kinetics parameter [Guo 2011]. It is worth mentioning that same as L in Eq. 5-9, μ can also be related to real physical parameters, which will be detailed in the next chapter. But the field variables are now connected by the following constraints:

$$\sum_{i=1}^{N_G}\eta_i = 1 \text{ or } \sum_{i=1}^{N_G}\frac{\partial\eta_i}{\partial t} = 0\,. \tag{5-20}$$

This constraint can be implemented into the kinetics equation by using a Lagrange multiplier λ_L,

$$\frac{\partial \eta_i}{\partial t}(t,x) = \mu\left(\nabla\cdot\frac{\partial}{\partial\nabla\eta_i} - \frac{\partial}{\partial\eta_i}\right)\left\{f + \lambda_L\left(\sum_{i=1}^{N_G}\eta_i - 1\right)\right\} = \mu\left(\left(\nabla\cdot\frac{\partial}{\partial\nabla\eta_i} - \frac{\partial}{\partial\eta_i}\right)f - \lambda_L\right). \tag{5-21}$$

By using the number of locally present phases $\tilde{N}_G(t,x)$, Eq (5-20) can be rewritten as

$$\sum_{i=1}^{\tilde{N}_G}\eta_i = 1 \text{ or } \sum_{i=1}^{\tilde{N}_G}\frac{\partial\eta_i}{\partial t} = 0\,. \tag{5-22}$$

The Lagrange multiplier λ_L can then be eliminated with the following mathematical transformations:

$$\frac{\partial \eta_i}{\partial t}(t,x) = -\mu\left(\frac{\delta F}{\delta \eta_i} + \lambda_L\right),$$

$$\lambda_L = \frac{1}{\tilde{N}_G}\sum_{j=1}^{\tilde{N}_G}\left(-\frac{1}{\mu}\frac{\partial \eta_j}{\partial t} - \frac{\delta F}{\delta \eta_j}\right) \overset{\sum_{j=1}^{\tilde{N}_G}\frac{\partial \eta_j}{\partial t}=0}{\Rightarrow} \lambda_L = -\frac{1}{\tilde{N}_G}\sum_{j=1}^{\tilde{N}_G}\left(\frac{\delta F}{\delta \eta_j}\right),$$

$$\frac{\partial \eta_i}{\partial t}(t,x) = \mu\left(-\frac{\delta F}{\delta \eta_i} + \frac{1}{\tilde{N}_G}\sum_{j=1}^{\tilde{N}_G}\left(\frac{\delta F}{\delta \eta_j}\right)\right) = \mu\left(-\frac{\tilde{N}_G - 1}{\tilde{N}_G}\frac{\delta F}{\delta \eta_i} + \frac{1}{\tilde{N}_G}\sum_{j\neq i}^{\tilde{N}_G}\left(\frac{\delta F}{\delta \eta_j}\right)\right) = -\frac{\mu}{\tilde{N}_G}\sum_{j\neq i}^{\tilde{N}_G}\left(\frac{\delta}{\delta \eta_i} - \frac{\delta}{\delta \eta_j}\right)F.$$

Thus,

$$\frac{\partial \eta_i}{\partial t}(t,x) = -\frac{\mu}{\tilde{N}_G}\sum_{j=1}^{\tilde{N}_G}\left(\frac{\delta}{\delta \eta_i} - \frac{\delta}{\delta \eta_j}\right)F = -\frac{\mu}{\tilde{N}_G}\sum_{j=1}^{N_G}\left(\frac{\delta}{\delta \eta_i} - \frac{\delta}{\delta \eta_j}\right)F. \tag{5-23}$$

In equation (5-23), the constraint (5-22) was implemented implicitly into the kinetics equation. Using the free energy expression given by Eq.5-15 and Eq.5-16, the change in phase field variables with time can be derived as follow:

$$\frac{\partial \eta_i}{\partial t}(t,x) = \frac{\mu}{\tilde{N}_G}\sum_{j\neq i}\left(\frac{\delta F}{\delta \eta_i} - \frac{\delta F}{\delta \eta_j}\right) = \frac{\mu}{\tilde{N}_G}\sum_{j\neq i}\left\{\left[\sum_{k\neq i}\left(-\frac{\varepsilon_{ik}}{2}\Delta\eta_k - w_{ik}\eta_k\right) - \sum_{k\neq j}\left(-\frac{\varepsilon_{jk}}{2}\Delta\eta_k - w_{jk}\eta_k\right)\right]\right\}. \tag{5-24}$$

For example, at the interface between grain i and grain j, the motion equation for phase field variable $\eta_i(t,x)$ is then given by:

$$\frac{\partial \eta_i}{\partial t}(t,x) = \mu\frac{\varepsilon_{ij}}{4}\Delta\eta_i + \frac{\mu}{2}\left[w_{ij}\eta_i - \left(\frac{\varepsilon_{ij}}{2}\Delta\eta_j + w_{ij}\eta_j\right)\right], \tag{5-25}$$

whereas at the triple junction between grain i, grain j and grain k, the motion equation for phase field variable η_i can be expressed as:

$$\frac{\partial \eta_i}{\partial t}(t,x) = \frac{\mu}{3}\left(\frac{\varepsilon_{ij}}{2} + \frac{\varepsilon_{ik}}{2}\right)\Delta\eta_i + \frac{\mu}{3}\left\{\begin{array}{l}\left(w_{ij} + w_{ik}\right)\eta_i + \left(\frac{\varepsilon_{jk}}{2} - \varepsilon_{ij}\right)\Delta\eta_j + \left(\frac{\varepsilon_{jk}}{2} - \varepsilon_{ik}\right)\Delta\eta_k + \\ \left(w_{jk} - w_{ij}\right)\eta_j + \left(w_{jk} - w_{ik}\right)\eta_k\end{array}\right\}. \tag{5-26}$$

The multi-phase-field model was compared with the continuum field model in the literature [Moelans 2009]. Both models are shown to be suitable to simulate anisotropic grain growth. The differences between these two models are in the dynamics for vanishing grains in multi-grain structures, especially when the simulation starts from a structure with triple junction dihedral angles far from their thermodynamic equilibrium values. This is due to the different form of the free energy functional used in both approaches. The simulated structures however match quickly once the triple junction angles are close to those required for thermodynamic equilibrium. As explained previously, in the continuum field model, the determination of the model parameters requires an iterative procedure if anisotropic grain boundary properties are considered. Meanwhile, the parameters of the multi-phase-field model can be directly linked to real physical parameters. Therefore, the multi-phase-field model is more suitable for large anisotropic grain growth simulation and it will be applied in the present study.

5.3 Level Set method

The level set method has many common points with the phase field method, the first one being that they both avoid tracking interfaces. The level set method is commonly used to track propagating fronts and is intensively applied to simulate different microstructure evolution phenomena including isotropic grain growth [Bernacki 2011] [Fabiano 2014], static recrystallization [Bernacki 2008][Bernacki 2009][Logé 2008], Smith-Zener pinning [Agnoli 2014]. Recently, it was extended to model large-scale anisotropic grain growth [Elsey 2013] in the context of uniform grids and finite difference formulation. In this section, the formulations of the level set method for isotropic and anisotropic grain growth will be presented.

5.3.1 Formulation for isotropic grain growth

In our formalism, a level set function, defined in a domain Ω, initially corresponds to the distance d to the interface Γ of a sub-domain G belonging to Ω; and this holds at any integration point of the considered FE mesh of Ω [Agnoli 2014]:

$$\begin{cases} \phi(x) = \left(\chi_G(x) - \chi_{\bar{G}}(x)\right) d(x,\Gamma), x \in \Omega \\ \Gamma = \left\{x \in \Omega, \phi(x) = 0\right\} \end{cases} . \tag{5-27}$$

where χ_G and $\chi_{\overline{G}}$ are, respectively the characteristic functions of G and of the complement of G. The form of Eq.5-27 undermines that we assume $\phi \geq 0$ inside G and $\phi \leq 0$ outside. Supposing the domain Ω contains N_G grains, we consider $\{\phi_i, 1 \leq i \leq N_G\}$. By denoting again Γ_{ij} the boundary between G_i and G_j, the total interfacial energy E could be expressed by [Zhao 1996]:

$$E = \sum_{i<j} \gamma_{ij} \operatorname{length}(\Gamma_{ij}), \tag{5-28}$$

where γ_{ij} is the interfacial energy of Γ_{ij}. In 3D, the grain boundary length should be accordling replaced by the grain boundary area. In the present work, we consider the grain boundary mobility to be constant. The migration velocity of the interface Γ_{ij} driven by capillarity forces can be approximately described by Eq. 5-29 [Bernacki 2011]:

$$\vec{v}_{ij} = -m\gamma_{ij}K_{ij}\vec{n}_{ij}, \tag{5-29}$$

where $K_{ij}(t,x)$ is the mean curvature of Γ_{ij} (curvature in 2D or summation of the main curvatures in 3D), m is the grain boundary mobility and $\vec{n}_{ij}(t,x)$ is the outside normal unit vector of the grain boundary (from G_i to G_j). Then the evolution of the LS function ϕ_i can be described by a convection equation:

$$\begin{cases} \dfrac{\partial \phi_i}{\partial t}(t,x) - m\gamma_{ij}K_{ij}(t,x)\vec{n}_{ij}(t,x)\cdot\nabla\phi_i(t,x) = 0 \\ \phi_i(t=0,x) = \phi_i^0(x) \end{cases}, \tag{5-30}$$

where $\phi_i^0(x)$ is the initially imposed distance function of each grain. If $\phi_i(t,x)$ is a distance function such that ($\|\nabla\phi_i(t,x)\| = 1, \forall x$) and if this property is conserved, then the grain boundary curvature convection problem described by Eq.5-30 can be solved thanks to a diffusive formulation [Bernacki 2011] [Fabiano 2014] [Agnoli 2014]. Indeed, in this context:

$$K_{ij} = -\nabla\cdot\vec{n}_{ij} = -\nabla\cdot\left(\frac{\nabla\phi_i}{\|\nabla\phi_i\|}\right) \xrightarrow{\|\nabla\phi_i\|=1} \begin{cases} K_{ij} = -\Delta\phi_i \\ \vec{n}_{ij}\cdot\vec{\nabla}\phi_i = -\|\nabla\phi_i\| = -1 \end{cases}. \tag{5-31}$$

And so Eq.5-30 can be reformulated as :

$$\begin{cases} \dfrac{\partial \phi_i}{\partial t}(t,x) - m\gamma_{ij}\Delta\phi_i(t,x) = 0 \\ \phi_i\left(t=0,x\right) = \phi_i^0\left(x\right) \end{cases}, \ \forall i \in \left\{1,\ldots,N_G\right\}. \tag{5-32}$$

For grain growth simulation with isotropic grain boundary energy, the evolution of the overall microstructure, which is composed by N_G grains, can be represented by the following set of equations,

$$\begin{cases} \dfrac{\partial \phi_i}{\partial t}(t,x) - m\gamma\Delta\phi_i(t,x) = 0 \\ \phi_i\left(t=0,x\right) = \phi_i^0\left(x\right), \ \forall i \in \left\{1,\ldots,N_G\right\} \end{cases}. \tag{5-33}$$

A reinitialization procedure is necessary for LS functions after each resolution of Eq. 5-33 in order to guarantee the conservation of its metrics property ($\left\|\nabla\phi_i\left(t,x\right)\right\| = 1, \forall x$). The methodology developed in [Bernacki 2009], which consists in solving Eq. 5-34 for all LS functions thanks to a convective formulation, is used here:

$$\begin{cases} \dfrac{\partial \phi_i}{\partial t}(t,x) - s_i\left(\left\|\nabla\phi_i(t,x)\right\| - 1\right) = 0 \\ \phi_i\left(t=0,x\right) = \phi_i^0\left(x\right), \ \forall i \in \left\{1,\ldots,N_G\right\} \end{cases}, \tag{5-34}$$

where s_i is the sign of the level set function ϕ_i [Bernacki 2009]. In LS method, a grain disappears when the corresponding LS function becomes negative over the entire simulation domain. Then all the calculations of this function are stopped and this function becomes 'inactive'.

Compatibility problems (i.e. vacuum or overlapping regions) can occur due to the diffusion of the level set functions [Merriman 1994]. A multiple junction treatment is thus performed after solving Eq. 5-33 at each time step. The treatment consists to remove all incompabilities by modifying all the level set functions as follows:

$$\phi_i(t,x) = \frac{1}{2}\left(\phi_i(t,x) - \max_{j\neq i}\phi_j(t,x)\right), \forall i \in \left\{1,\ldots,N_G\right\} \ . \tag{5-35}$$

It is worth highlighting that this treatment is only performed in a thin layer around the zero isovalues before the re-initialisation of the level set function (since it modifies the metric properties of the distance functions).

5.3.2 Formulation for anisotropic grain growth

The numerical treatment indicated by Eq.5-35 does not allow removing the vacuum at triple junctions when the grain boundary energy is anisotropic. An alternative was initially developed by Zhao [Zhao 1996] and then improved by Elsey [Elsey 2013].

Firstly, in [Zhao 1996] the interfacial energy γ_{ij} is rewritten as,

$$\gamma_{ij} = \gamma_i + \gamma_j \ , \tag{5-36}$$

where $\gamma_i \left(i \in \{0,\ldots,N_G\}\right)$ are N_G arbitrarily chosen non-negative weights corresponding to N_G grains in the overall microstructure. It is worth noticing that the relationship 5-36 is not always a bijection between $\{\gamma_i\}$ and $\{\gamma_{ij}\}$, since the number of grain boundaries is not equal to the number of grains, except for simple test cases with only few grains [Atkinson 1988]. This point will be further discussed afterwards. The total interfacial energy E expressed initially by Eq.5-28 can be written as,

$$E = \sum_{i}^{N_G} \oint_{\partial\Omega_i} \gamma_i \, dl \ . \tag{5-37}$$

Zhao [Zhao 1996] proved that minimization of E in Ω satisfies:

$$\begin{cases} \delta(\phi_i)\left(m\gamma_i \nabla \cdot \left(\dfrac{\nabla\phi_i}{\|\nabla\phi_i\|}\right)\right) = 0 \\ \text{Boundary conditions: } \dfrac{\delta(\phi_i)}{\|\nabla\phi_i\|}\dfrac{\partial\phi_i}{\partial\vec{n}} = 0 \text{ on } \partial\Omega, \ \forall i \in \{1,\ldots,N_G\} \end{cases} , \tag{5-38}$$

where $\vec{n}$ is the normal to the border of Ω and $\delta(x)$ is the Dirac delta function.

Using the gradient projection method of Rosen [Rosen 1961] and replacing $\delta(\phi_i)$ by $\nabla\phi_i$, the following non-linear equation is obtained [Zhao 1996]:

$$\begin{cases} \dfrac{\partial \phi_i}{\partial t}(t,x) - m\gamma_i \Delta \phi_i(t,x) = 0 \\ \dfrac{\partial \phi_i}{\partial \vec{n}}(t,x) = 0, \text{ on } \partial\Omega \\ \phi_i\left(t=0,x\right) = \phi_i^0\left(x\right), \ \forall i \in \left\{1,\ldots,N_G\right\} \end{cases} . \tag{5-39}$$

The numerical treatment indicated by Eq.5-35 is applicable in this approach. This methodology is proven to lead to the correct equilibrium at triple junctions, since the time recalling that replaces $\delta(\phi_i)$ by $\nabla\phi_i$ does not affect the steady state solution [Zhao 1996]. However, two drawbacks remain: firstly, at the interface Γ_{ij}, since different diffusion coefficients (γ_i and γ_j) are used, the evolutions in a time step of ϕ_i and ϕ_j, controlled by Eq.5-39, are different. Thus, an overlap or vacuum region can be created at Γ_{ij} due to this difference. The overlap or vacuum region can be removed by the numerical treatment indicated by Eq.5-35. However, the resulted transport velocity $\vec{v}_{ij}$ of Γ_{ij} in the time increment is then given by:

$$\vec{v}_{ij} = -m\frac{\left(\gamma_i + \gamma_j\right)}{2} K_{ij}\vec{n}_{ij} = -m\frac{\gamma_{ij}}{2} K_{ij}\vec{n}_{ij}, \tag{5-40}$$

which is not consistent with the transport velocity indicated by Eq. 5-29. Accordingly, Elsey et al [Elsey 2013] modified Eq. 5-36 into:

$$\gamma_{ij} = \frac{\gamma_i + \gamma_j}{2}, \tag{5-41}$$

in order to correct this deviation. By using Eq.5-41, $\delta(\phi_i)$ in Eq.5-38 should be considered equal to $2\cdot\nabla(\phi_i)$.

The second drawback of the methodology developed by Zhao et al [Zhao 1996] concerns the calculation of the arbitrary weights $\gamma_i\left(i \in \left\{0,\ldots,N_G\right\}\right)$. According to Eq.5-41, $\gamma_i\left(i \in \left\{0,\ldots,N_G\right\}\right)$ are determined thanks to the grain boundary energies γ_{ij}. However, as explained previously, Eq.5-41 can be a bijection between γ_{ij} and $\gamma_i\left(i \in \left\{0,\ldots,N_G\right\}\right)$ only if the grain boundary number equals to the grain number N_G (which is of course false in general [Atkinson 1988]).

In the Elsey et al's approach [Elsey 2013], instead of being a constant for the whole sub-domain G_i, γ_i is considered as a P1 variable $\gamma_i(t,x)$. By using the following notations $\Gamma_i^\varepsilon = \{x \in \Omega, \|\phi_i(t,x)\| \le \varepsilon\}$, $\Gamma_{ij}^\varepsilon = \Gamma_i^\varepsilon \bigcap \Gamma_j^\varepsilon$, and $\Gamma_{ijk}^\varepsilon = \Gamma_i^\varepsilon \bigcap \Gamma_j^\varepsilon \bigcap \Gamma_k^\varepsilon$, with ε a positive fixed parameter, the algorithm proposed by Elsey et al [Elsey 2013] to define $\gamma_i(t,x)$ is summarized below:

if $x \notin \Gamma_i^\varepsilon$, then, $\gamma_i(t,x) = 0$,

else if $\exists j \neq i \ / \ x \in \Gamma_{ij}^\varepsilon$, and $\forall m \in \{1,\ldots,N_G\} \setminus \{i,j\}$, $x \notin \Gamma_m^\varepsilon$, $\gamma_i(t,x) = \gamma_{ij}$

else if $\exists j \neq i$ and $k \notin \{i,j\} \ / \ x \in \Gamma_{ijk}^\varepsilon$, and $\forall m \in \{1,\ldots,N_G\} \setminus \{i,j,k\}$, $x \notin \Gamma_m^\varepsilon$,
$\gamma_i(t,x) = \gamma_{ij} + \gamma_{ik} - \gamma_{jk}$.

else (which undermines at least a quadruple junction) then $R = \{j \in \{1,\ldots N_G\}, j \neq i / x \in \Gamma_{ij}^\varepsilon\}$;
pick randomly $j,k \in R \setminus \{j\}$, and $\gamma_i(t,x) = \gamma_{ij} + \gamma_{ik} - \gamma_{jk}$. (5-42)

In addition, to reduce the computational complexity, Elsey et al proposed in [Elsey 2013] to replace $\gamma_i(t,x)$ by $\gamma_{\max}(t)$ $\left(\gamma_{\max}(t) = \max_i \max_\Omega (\gamma_i(t,x))\right)$. With this modification, a uniform diffusion equation is solved for all the LS functions. Consequently, Eq.5-39 becomes :

$$\begin{cases} \dfrac{\partial \phi_i}{\partial t}(t,x) - m\gamma_{\max}(t)\Delta\phi_i(t,x) = 0 \\ \dfrac{\partial \phi_i}{\partial \vec{n}}(t,x) = 0, \text{ on } \partial\Omega \\ \phi_i(t=0,x) = \phi_i^0(x), \ \forall i \in \{1,\ldots,N_G\} \end{cases} . \quad (5\text{-}43)$$

After the resolution of Eq.5-43 at each time increment, a numerical treatment [Elsey 2013] should be applied on all the active level set functions to take into account the anisotropic grain boundary properties. If $\phi_i^*(t+\Delta t,x)$ denotes the solution of Eq.5-43 at instance $t+\Delta t$, the treatment can be expressed as:

$$\phi_i(t+\Delta t,x) = \frac{\gamma_i(t,x)}{\gamma_{\max}(t)}\phi_i^*(x,t+\Delta t) + \left(1 - \frac{\gamma_i(t,x)}{\gamma_{\max}(t)}\right)\phi_i(t,x). \quad (5\text{-}44)$$

This treatment, and the use of $\gamma_{\max}(t)$, were validated numerically by Elsey et al [Elsey 2013] by resolving the so-called Garcke problem. However, the difference between the Eq. 5-39 and the combination of Eq. 5-43 and Eq. 5-44 in terms of resulting grain boundary kinetics has not been clarified.

In the considered level set framework, it is worth noticing that real physical parameters are used, which facilitate its application on anisotropic grain growth simulation.

5.4 Conclusion

The theoretical bases of the two major implicit methods i.e. phase field and level set for anisotropic grain growth modeling has been presented in this chapter. Two phase field approaches i.e. the continuum field and multi-phase-field model has been introduced. The parameters of the multi-phase-field model can be directly linked to real physical parameters e.g. grain boundary energy and mobility. Meanwhile, in the continuum field model, the determination of the model parameters in the context of anisotropic grain boundary properties is complicated. This complexity leads to the fact that the continuum field model is not suitable for large-scale anisotropic grain growth simulation. On the contrary, within the LS framework, the real physical properties are used to evolve the level set functions. Therefore, in the present study, the multi-phase-field model and the level set method will be used in the following chapters for anisotropic grain growth simulation.

In addition, the majority of the anisotropic grain growth simulations which are reported in the literature were performed in the context of uniform grids and finite difference formulation [Garcke 1999] [Moelans 2008 PRB][Moelans 2009][Chang 2014][Elsey 2013]. In the present work, we will consider the two models in the context of finite element modelling on unstructured finite element mesh, which was, to our knowledge, never be performed.

Résumé en français

Deux modèles de type champ complet existent dans la littérature: la méthode champ de phase et la méthode level-set. Les deux modèles ont déjà été largement utilisés afin de modéliser la croissance de grains dans un contexte anisotrope. Cependant une comparaison croisée de leurs bases théoriques et de leur efficacité n'est pas chose aisée. Cela est proposé dans ce chapitre.

6. COMPARATIVE STUDY OF MULTI-PHASE-FIELD AND LEVEL SET METHOD FOR ANISOTROPIC GRAIN GROWTH SIMULATION

The grain boundary network evolution, notably the development of the so-called special boundaries [Brandon 1966] during grain growth, is tightly linked to macroscopic material properties such as intergranular stress corrosion cracking [Palumbo 1988][Palumbo 1990] [Lin 1995]. The special boundaries have different grain boundary energy from the normal high angle grains boundaries. For this reason, high anisotropic grain boundary properties are essential to be considered in mesoscale grain growth simulations.

In this work, we have considered the multi-phase-field model (MPF) and the level set method (LS) in the context of two-dimensional finite element (FE) modeling on unstructured finite element mesh (FEM). Numerical performances of the two methods in anisotropic grain growth simulations are compared in this chapter for the same configurations. We derived the relationships between the parameters in both models by comparing the model formulations. Three so-called 'Grim Reaper' problems defined initially by Garcke [Garcke 1999], with different steady state solutions, were solved by both models using equivalent parameter values. It must be underlined that local isotropic meshing and remeshing adaptation was introduced in order to limit the computational cost of the FE simulations. The impact of the isotropic mesh size near the grain boundaries (h) and time step (dt) on simulation accuracy was studied in the first problem. Then the combination of h and dt, with which the most

accurate simulation results were obtained, was applied in the two others problems. We show evidence that with appropriate combinations of h and dt there is no obvious deviation between the simulation results obtained for both methods with low anisotropy for grain boundary energy, which means that the ratio between the highest interfacial energy and the lowest one is smaller than 2. In the context of strong anisotropy, conclusions are more complex and MPF approach seems less accurate than the LS one in the present numerical context.

6.1 Algorithm of finite element modelling

The formulations of MPF and LS presented in chapter 5 are implemented into a finite element code to simulate grain growth. The algorithms of the 2D finite element modelling using these two methods are given in this section.

6.1.1 Level set method

- Isotropic grain growth

At the beginning, all the LS functions are considered as active. The finite element modeling of isotropic grain growth includes all the following steps at each time increment of finite element modeling [Bernacki 2011]:

ISOLS1. Resolve Eq. 5-33 for all the active LS functions using a finite element method based on the C++ library 'CIMLIB' with a stabilized diffusion P1 (RFB) solver [Bernacki 2009] [Hachem 2012].

ISOLS2. Numerical treatment to remove the vacuum regions at multiple junctions for all the active LS functions: $\phi_i = \frac{1}{2}\left(\phi_i - \underset{j\neq i}{\text{Max}}\,\phi_j\right)$ [Bernacki 2011].

ISOLS3. Reinitialize all the active LS functions by solving Eq. 5-34 with a convective formulation [Bernacki 2009].

ISOLS4. Update the set of active LS functions: a LS function ϕ_i remains active if it exists at least one integration point (node of the FE mesh in the considered P1 formalism) for which the LS function is positive (equivalent to $\max_{\Omega}(\phi_i(t^{incr},x)) \geq 0$ and the fact that the corresponding grain has not disappeared).

- Anisotropic grain growth

At the beginning, all the LS functions are considered as active. We use the following algorithm at each time increment for our 2D anisotropic grain growth simulation:

ANISOLS1. Resolve Eq. 5-43 for all the active LS functions using a stabilized diffusion P1 (RFB) solver [Bernacki 2009] [Hachem 2012].

ANISOLS2. Perform anisotropic treatment defined by Eq. 5-44 for all the active LS functions.

ANISOLS3. Remove the vacuum regions at triple junctions for all the active LS functions (same as ISOLS2).

ANISOLS4. Reinitialization for all the active LS functions (same as ISOLS3).

ANISOLS5. Update the set of active LS functions (same as ISOLS4).

As explained, local meshing and remeshing adaptation is also considered in order to describe precisely the grain boundaries without dealing with global fine FE mesh. In all considered simulations, local (near the grain boundaries) isotropic meshing refinement is used. In fact, these CIMLIB meshing/remeshing capabilities for polycrystalline microstructures have already been intensively detailed in the literature [Bernacki 2008] [Bernacki 2009] [Bernacki 2011] [Resk 2009] [Hitti 2012][Logé 2008]. Thus, these tools will not be more detailed in this document. It must be underlined that anisotropic meshing capabilities of CIMLIB was not used in this work in order to simplify the discussions concerning comparisons of PF and LS approaches.

Finally it is worth mentioning that, if in a simulation, periodical remeshing operations are needed to guarantee a refined mesh around the interfaces during their migration, these operations are always performed after the reinitialization step.

6.1.2 Multi-phase-field model

In practice, Eq. 5-24 is transformed to the following form for a P1 finite element calculation:

$$\begin{cases} \dfrac{\partial \eta_i}{\partial t} = D_i \Delta \eta_i + SourceTerm_i \\ D_i = \dfrac{\mu}{\tilde{N}_G} \sum_{j \neq i} \dfrac{\varepsilon_{ij}}{2} \\ SourceTerm_i = \dfrac{\mu}{\tilde{N}_G} \sum_{j \neq i} \left[\sum_{k \neq i} \left(-\dfrac{\varepsilon_{ik}}{2} \Delta \eta_k - w_{ik} \eta_k \right) - \sum_{k \neq j} \left(-\dfrac{\varepsilon_{jk}}{2} \Delta \eta_k - w_{jk} \eta_k \right) - \dfrac{\varepsilon_{ij}}{2} \Delta \eta_i \right] \end{cases} \quad . (6\text{-}1)$$

At the beginning, all the PF variables are considered as active. We use the following algorithm at each time increment for the 2D anisotropic grain growth simulation with MPF:

ANISOMPF1. Calculate the corresponding source terms for all the active PF variables.

ANISOMPF2. Resolve Eq.6-1 for all the active PF variables using a stabilized diffusion P1 (RFB) solver [Bernacki 2009] [Hachem 2012].

ANISOMPF3. PF variables are replaced by $\eta_i^* = \dfrac{\eta_i}{\sum_{j=1}^{\tilde{N}_G} \eta_j}$ to satisfy Eq. 5-22 [Takaki 2009].

ANISOMPF4. Update the set of active PF variables: a PF variable η_i remains active if it exists at least one integration point (node of the FE mesh in the considered P1 formalism) for which the PF variable is strictly positive (equivalent to $\max_{\Omega}(\eta_i(t^{incr}, x)) > 0$ and the fact that the corresponding grain has not disappeared).

Same as for the ISOLS or ANISOLS algorithms, the remeshing operation can be performed after ANISOMPF3.

6.2 Three-grain structure

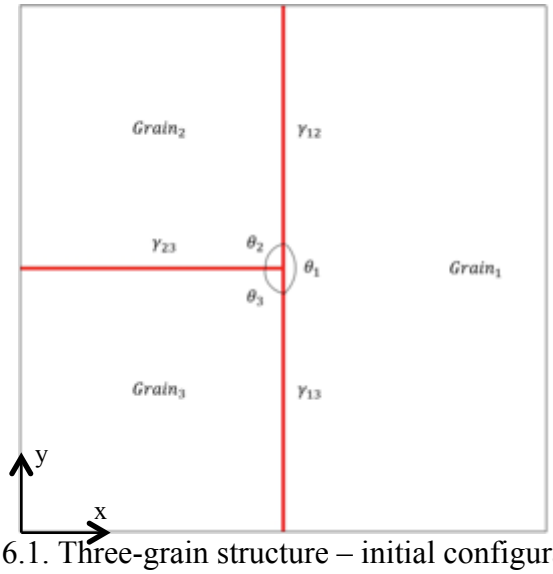

Fig. 6.1. Three-grain structure – initial configuration.

The simulations of the two models for a three-grain structure in 2D are compared in this section. The three-grain structure is illustrated in Fig. 6.1. In the axisymmetric case where γ_{12} equals to γ_{13} and for a migration due to capillarity, Garcke gave the exact analytical solution of this configuration with Neumann boundary conditions [Garcke 1999]. Indeed, according to Garcke [Garcke 1999], on a $[0,a]\times[0,a]$ simulation domain, the equilibrium angle at the steady state of the three-grain structure can be calculated thanks to the following equation:

$$\theta_1 = 2\left(\frac{\pi}{2} - \arctan\sqrt{\frac{\gamma_{23}^2}{4\gamma_{12}^2 - \gamma_{23}^2}}\right). \tag{6-2}$$

And the interface transport velocity C at the steady state is defined as

$$C = m\gamma_{12}\cdot(\pi - \theta_1)\cdot a. \tag{6-3}$$

As the interfacial energy γ_{ij} is explicitly used in LS formulation, Eq.6-2 and Eq.6-3 can be directly verified for LS simulations. However, the parameters used in MPF formulation need to be associated with the real physical parameters m and γ_{ij}. Comparatively with the free energy expression used by Steinbach et al [Steinbach 1999] (indicated by Eq. 5-15, 5-16), in the expression used by Garcke [Garcke 1999] and Moelans [Moelans 2009], the real interfacial energy γ_{ij} is used in the expression of the total free energy, which is illustrated by the following equations:

$$\begin{aligned}
&\overline{F} = \int \left(\overline{f}^{kin} + \overline{f}^{pot} \right) dV, \\
&\overline{f}^{kin} = \sum_{i=1}^{N_G} \sum_{j=i+1}^{N_G} l_{gb} \gamma_{ij} \left(\eta_j \nabla \eta_i - \eta_i \nabla \eta_j \right) \cdot \left(\eta_j \nabla \eta_i - \eta_i \nabla \eta_j \right), \\
&\overline{f}^{pot} = \sum_{i=1}^{N_G} \sum_{j=i+1}^{N_G} \frac{16}{\pi^2} \frac{\gamma_{ij}}{l_{gb}} \eta_i \eta_j,
\end{aligned} \tag{6-4}$$

where l_{gb} is defined as 'the width of the diffuse interface' . The difference between l_{gb} and λ (Eq. 5-17) will be detailed afterwards. At the interface Γ_{ij}, the constraint $\sum_{i}^{\tilde{N}_G} \eta_i = 1$ in MPF method gives $\eta_i + \eta_j = 1$ and $\nabla \eta_i = -\nabla \eta_j$. Thus, $\overline{f}^{kin}$ can be written as:

$$\overline{f}^{kin} = -\sum_{i=1}^{N_G} \sum_{j=i+1}^{N_G} l_{gb} \gamma_{ij} \nabla \eta_i \nabla \eta_j \, . \tag{6-5}$$

The corresponding evolution equation for the phase field variable η_i is:

$$l_{gb} \frac{\partial \eta_i}{\partial t} = \frac{m}{\tilde{N}_G} \sum_{j \neq i} \left(\frac{\delta \overline{F}}{\delta \eta_i} - \frac{\delta \overline{F}}{\delta \eta_j} \right), \tag{6-6}$$

where m is the grain boundary mobility [Moelans 2009].

Comparing Eq. 6-6 with Eq. 5-23, we find:

$$\begin{cases}
m\gamma_{ij} = \mu \dfrac{\varepsilon_{ij}}{2} = \mu \hat{\sigma}_{ij} \dfrac{4\lambda}{\pi^2} \\
\dfrac{16}{\pi^2} \dfrac{m\gamma_{ij}}{l_{gb}^2} = \mu w_{ij} = \mu \hat{\sigma}_{ij} \dfrac{4}{\lambda}
\end{cases} \tag{6-7}$$

From Eq.6-7, we can deduce that:

$$l_{gb} = \frac{4\lambda}{\pi^2} \, . \tag{6-8}$$

Accordingly in MPF used in the present study, the equilibrium angle and the transport velocity of this three-grain structure at the steady state can be written as:

$$\theta_1 = 2 \left(\frac{\pi}{2} - \arctan \sqrt{\frac{\hat{\sigma}_{23}^2}{4\hat{\sigma}_{12}^2 - \hat{\sigma}_{23}^2}} \right), \tag{6-9}$$

$$C = \frac{\mu \varepsilon_{12}}{2} \cdot \left(\pi - \theta_1 \right) a \, . \tag{6-10}$$

6.3 Comparison between MPF and LS methods

6.3.1 Resolution by MPF and LS methods

All the length dimensions in this section are expressed in mm and the velocities are in mm/s. We choose three sets of interfacial energy γ_{ij} (in J/mm^2) for the resolution of this three-grain problem:

$$\{\gamma_{12},\gamma_{13},\gamma_{23}\} = \{7\times10^{-9},7\times10^{-9},3.3\times10^{-9}\},\ \{2.45\times10^{-9},2.45\times10^{-9},3.3\times10^{-9}\},\ \{7\times10^{-9},7\times10^{-9},1.1\times10^{-9}\}.$$

The grain boundary mobility, which is considered as a constant in the present work, equals to $10^{-4}mm^2s/kg$. The values of these parameters do not refer to a specific material but are within the range of typical values for metals. The third set of interfacial energy was chosen to analyze the numerical performance of the two methods in a high anisotropic condition, as the ratio between the highest energy and the lowest energy in the present case is much higher than the value commonly used in the context of phase field simulations [Chang 2014] [Meolans 2009].

All the simulations presented in this section were performed using CIMLIB on a $[0,1]\times[0,1]$ domain with unstructured FE mesh. We will present the simulation results of the first set of interfacial energy obtained by MPF and LS in section 6.3.2 and the results of the second set and the third set in section 6.3.3.

6.3.2 Comparison between MPF and LS for the first set of interfacial energy

In this subsection, to analyze the numerical performance of the two methods, simulations are performed using different values of *h* and *dt*. The finite element mesh is initially refined isotropically in the zone close to the initial position of the grain boundaries. In the following, we will note h_{fine} the chosen mesh size near the grain interfaces and h_{coarse} the mesh size far from the grain interfaces. No remeshing opertation is performed during the simulations in order to avoid the possible influence of remeshing adaptation on simulation results. This choice explains the important thickness (called *E*) of the refined mesh zone (see Fig. 6.2(d)), which was initially fixed to $0.22\ mm$ in order to keep the grain interfaces inside the refined

zone at the end of the simulation. The simulation results of LS and MPF on the same finite element mesh ($h_{fine} = 2\times10^{-3} mm$ and $h_{coarse} = 4\times10^{-2} mm$) are illustrated respectively in Fig. 6.2 and Fig. 6.3. LS results are described thanks to the zero isovalues of ϕ_i, $i \in \{1,2,3\}$, whereas the MPF results are described thanks to the isovalue lines defined by $\eta_i = 0.5$, $i \in \{1,2,3\}$ with a certain width (only for visualization). In both cases, the grain boundary profiles at the steady state are close to the analytical solution.

The simulation results of MPF and LS approaches at $t = 33\,\mathrm{h}20\,\mathrm{min}$ for different combinations of h_{fine} and *dt* are illustrated respectively in Fig. 6.4 and Fig. 6.5. h_{coarse} remains constant and fixed to $4\times10^{-2} mm$. It is worth mentioning that the finite element mesh size h_{fine} remains smaller than one fifth of the interface thickness to guarantee the accuracy of the MPF simulations [Debashis 2012]. The L^2 errors concerning the front velocity of the interface are listed in Table 6.1. The transport velocity (v) is calculated for three values on the y-axis, and the L^2 error $Error$ is calculated based on the errors on these considered y-axis values,

$$Error = \frac{\sqrt{\left(v_{y=0.5} - v_{analytical}\right)^2 + \left(v_{y=0.4} - v_{analytical}\right)^2 + \left(v_{y=0.3} - v_{analytical}\right)^2}}{\sqrt{3v_{analytical}^2}}. \qquad (6\text{-}11)$$

In the present case, the interface transport velocity v varies from $3.4\times10^{-7} mm/s$ to $8\times10^{-7} mm/s$. As mentioned previously, unstructured FE mesh was used in the present case for the phase field simulations. For the considered *dt* and h_{fine} in MPF simulations the magnitude of the ratio $\frac{vdt}{h_{fine}}$ for the average transport velocity is around 1×10^{-3}, which is similar to the magnitude of the ratio used in the literature with uniform grids [Moelans 2009] [Fan 1997]. For LS approach, the magnitude of this ratio is around 0.02.

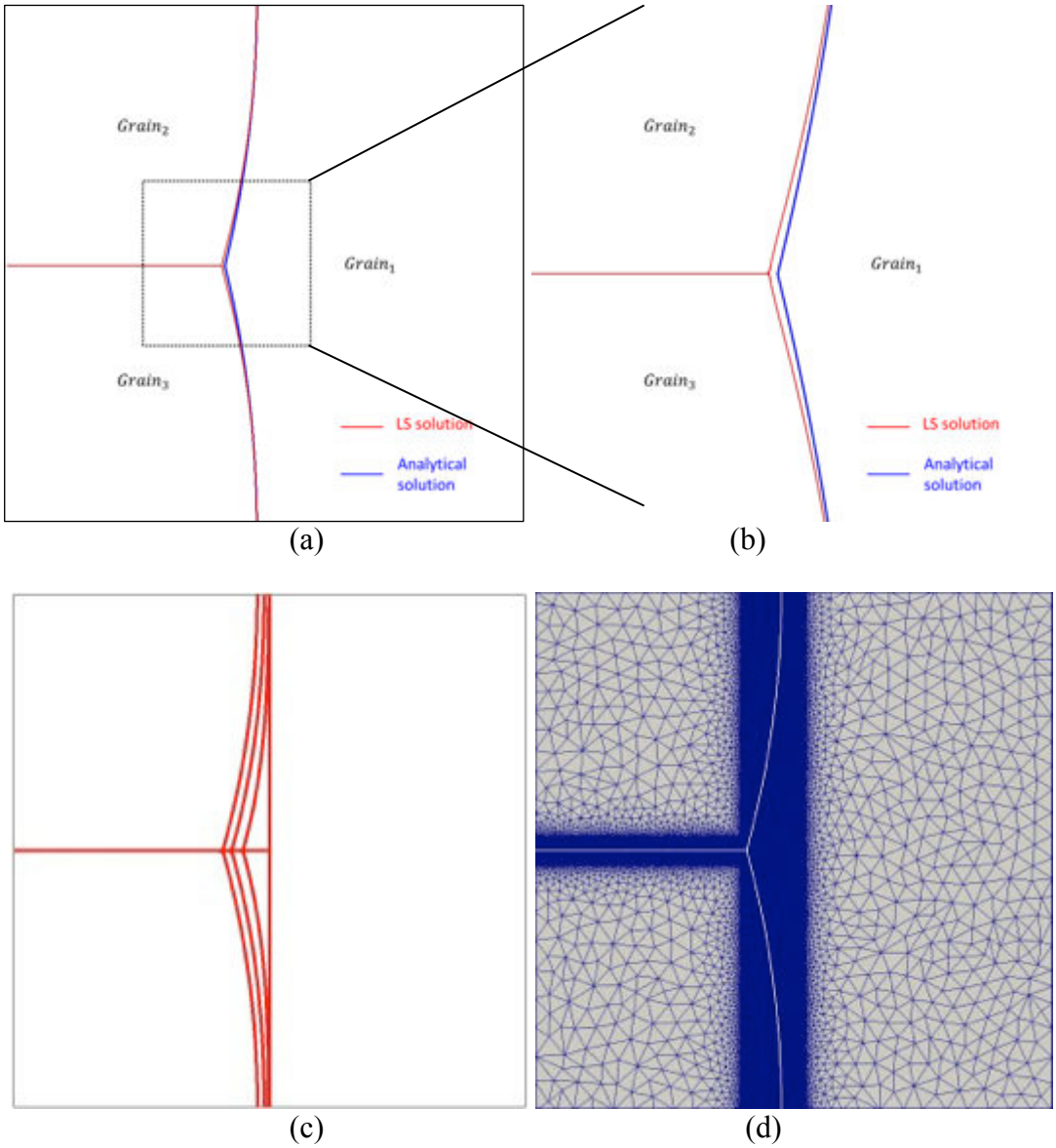

Fig. 6.2. First γ-set: solution of the three-grain problem obtained thanks to the LS approach. System parameters: $dt = 40s$. (a) LS solution (at $t = 33\,\text{h}20\,\text{min}$) compared with the analytical solution. (b) Zoom of (a) at the triple junction. (c) Evolution of the simulated structure at $t = 16\text{h}40\text{min}, 25\text{h}$, and $33\,\text{h}20\,\text{min}$. (d) Snapshot of the used FE mesh (fixed with $h_{fine} = 2\times10^{-3}mm$, $h_{coarse} = 4\times10^{-2}mm$, E= 0.22 mm), the profile corresponds to the simulate structure at t=33h20min.

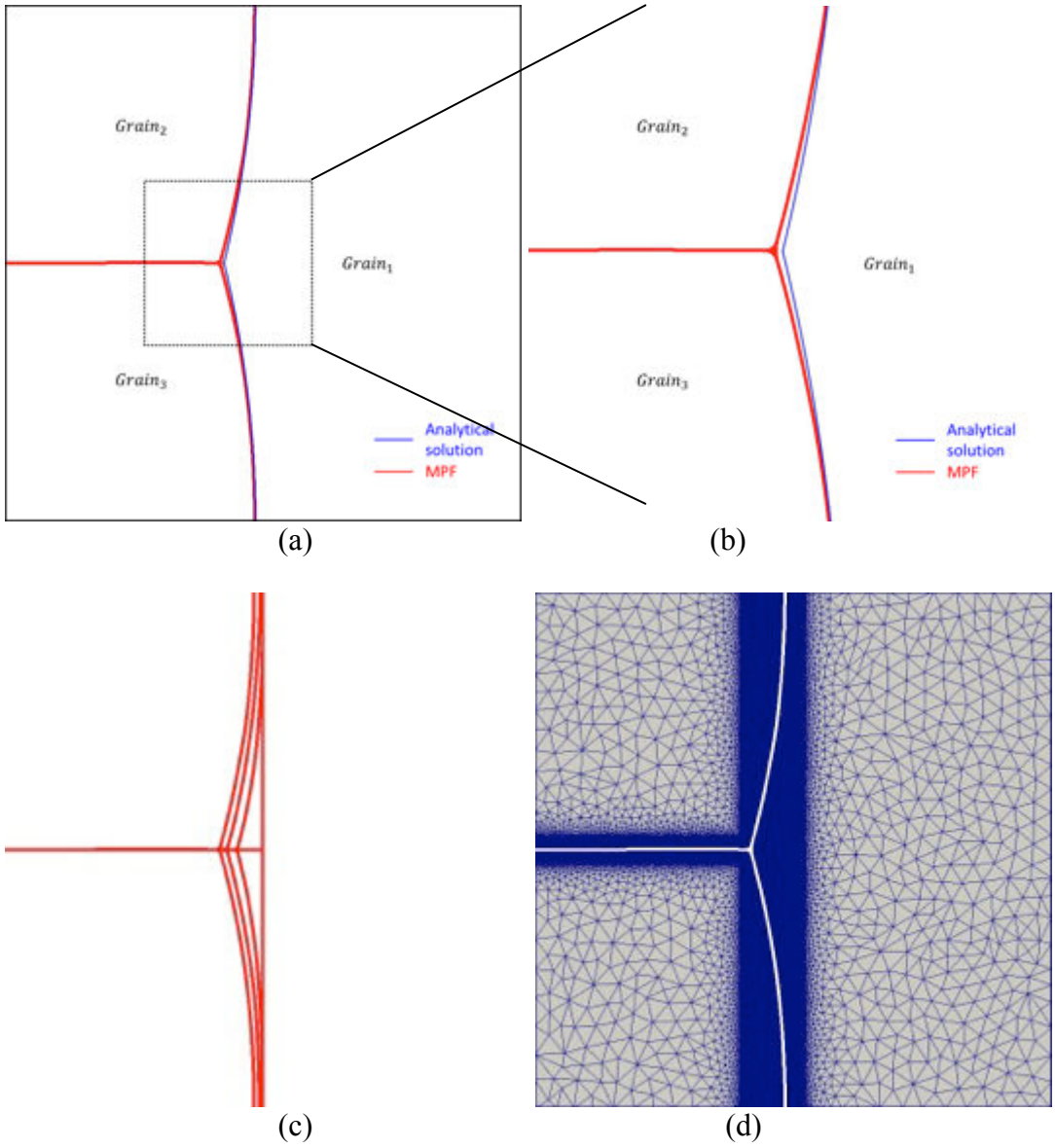

Fig. 6.3. First γ-set: solution of the three-grain problem obtained by the MPF approach. System parameters: $\lambda = 2\times10^{-2}\,mm, dt = 3s$. (a) MPF solution (at $t = 33\,\text{h}20\,\text{min}$) compared with the analytical solution. (b) Zoom of (a) at the triple junction. (c) Evolution of the simulated structure at $t = 16\text{h}40\text{min}, 25\text{h}$, and $33\ \text{h}20\,\text{min}$. (d) Snapshot of the used FE mesh (fixed with $h_{fine} = 2\times10^{-3}\,mm$, $h_{coarse} = 4\times10^{-2}\,mm$, E= 0.22 mm), the profile corresponds to the simulate structure at t=33h20min.

In Fig. 6.6, we overlapped the simulation results of LS and MPF with the lowest L^2 error. For the first set of interfacial energy, the steady state is close to the initial state of the configuration. Thus, the transition from the initial state to the steady state is short. In this case, the evolutions of the configuration obtained by both methods overlap at different instances, which illustrates that these two methods can lead to the same simulation result not only at the

steady state but also during the transition phase. Additionally, for different values on the y-axis, the convergence of the calculated migration velocities of the interface by MPF to the analytical solution is illustrated in Fig. 6.7. As the simulation results obtained by the two methods cannot be distinguished, the calculated migration velocity obtained thanks to the LS approach is not shown here.

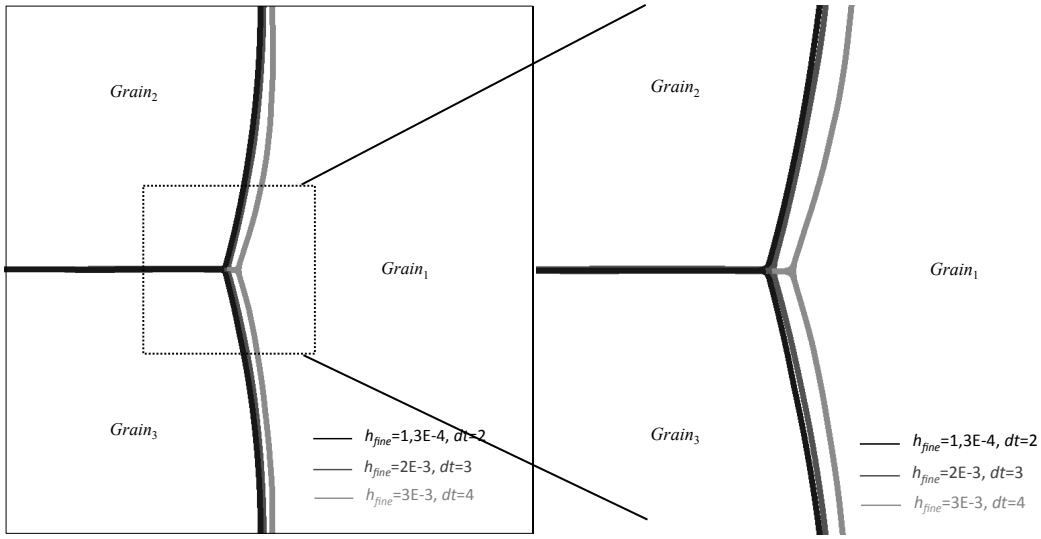

(a) (b)

Fig. 6.4. First γ-set: (a) simulation results at $t = 33\,\mathrm{h}\,20\,\mathrm{min}$ obtained by MPF for different combination of dt (s) and h_{fine} (mm); (b) Zoom of (a) at the triple junction.

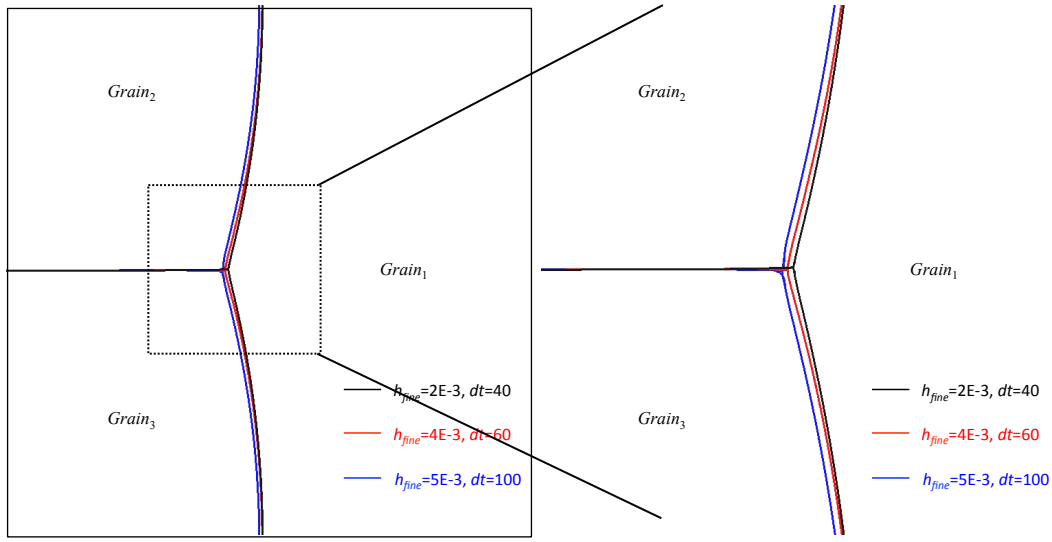

(a) (b)

Fig. 6.5. First γ-set: (a) simulation results at $t = 33\,\mathrm{h}\,20\,\mathrm{min}$ obtained by LS for different combination of dt (s) and h_{fine} (mm); (b) Zoom of (a) at the triple junction.

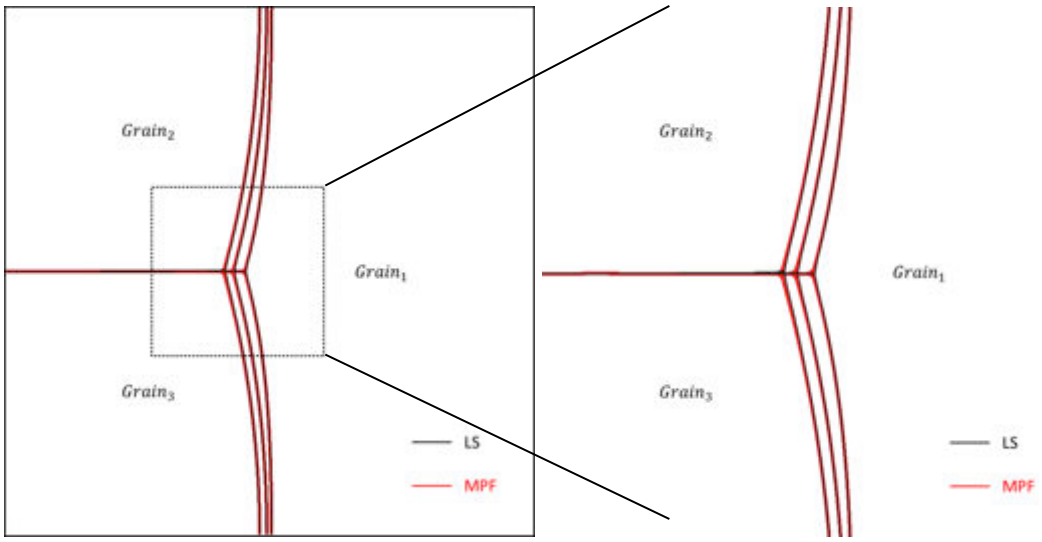

(a) (b)

Fig. 6.6. First γ-set: (a) comparison between the simulation results obtained by the LS approach ($h_{fine}=2\times10^{-3}mm$, dt=40s) and the MPF approach ($h_{fine}=1.3\times10^{-3}mm$, dt=2s) at $t=16\text{h}40\text{min}, 25\text{h}$, and $33\ \text{h}20\,\text{min}$; (b) Zoom of (a) at the triple junction.

Method	$h_{fine}(mm)$	$dt(s)$	L^2 error in transport velocity
LS	2×10^{-3}	40	12.8%
LS	4×10^{-3}	60	19.1%
LS	5×10^{-3}	100	24.2%
MPF	1.3×10^{-3}	2	12.8%
MPF	2×10^{-3}	3	21.6%
MPF	3×10^{-3}	4	38.8%

Table 6.1. First γ-set: errors obtained in transport velocity (Eq.6.11) at $t=33\,\text{h}20\,\text{min}$ as of a function of the fixed parameters h_{fine} and dt for the LS and MPF formalisms.

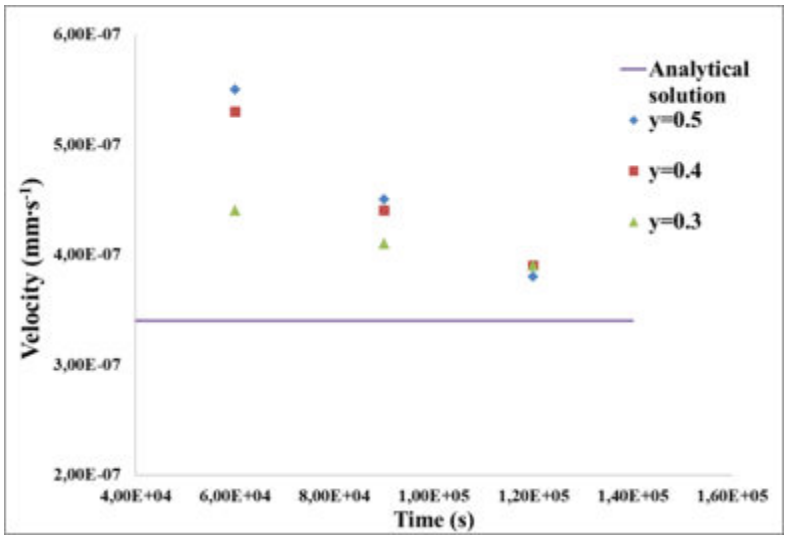

(a)

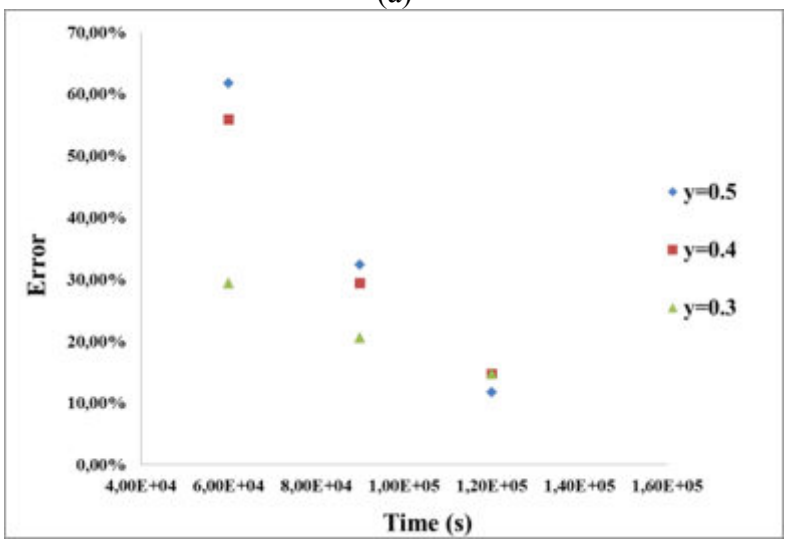

(b)

Fig. 6.7. First γ-set: transport velocities at different points on the y-axis obtained thanks to the MPF approach ($h_{fine}=1.3\times10^{-3}mm$, dt=2s) compared to the velocity of the constantly transported solution of the three-grain problem. (a) Absolute transport velocity; (b) relative error.

As indicated in Table 6.1 and illustrated in Fig. 6.4 and Fig. 6.5, for both LS and MPF models, using bigger mesh size and bigger time steps, the simulation accuracy in terms of grain boundary profile and transport velocity degrades. As shown in Fig. 6.6, with LS and MPF models, same simulation accuracy can be reached with different combinations of h_{fine} and dt. It is worth emphasizing that the analytical solution of the transport velocity (Eq. 6-3) is the constant velocity at the steady state. As illustrated in Fig. 6.7, at the beginning of the simulation, the curvature of the interfaces Γ_{12} and Γ_{13} is more important than the value at the steady state, which leads to higher transport velocity. As the configuration evolves towards

the steady state, the transport velocity tends to the analytical solution equal to the constant transport velocity at the steady state.

As indicated in the algorithm ANISOMPF, a source term, which depends on the phase field variables, needs to be explicitly calculated at each time increment. Therefore, for the sake of convergence of the simulation, instead of using the same value as in LS context, smaller step sizes were used for MPF.

To summarize, for the first set of interfacial energy, LS and MPF can provide simulation results with similar accuracy in transport velocity at the steady with different combinations of h_{fine} and dt.

6.3.3 Comparison between MPF and LS for the second and third set of interfacial energy

For the second set of interfacial energy, as the steady state is reached far from the initial configuration, to avoid requiring a fine isotropic mesh size in an important part of the domain, we have adapted the finite element mesh in an isotropic way in the area close to the interfaces during the simulation (E=0.04mm) by performing a remeshing operation at the end of each time increment for both methods. The influence of parameters h_{fine} and dt on the two methods has been analysed for the first set of interfacial energy. Accordingly here, we keep the identified optimized combinations of dt and h_{fine} ($=2\times10^{-3}mm$, dt=40s for LS approach and $h_{fine}=1.3\times10^{-3}mm$, dt=2s for MPF approach). h_{coarse} is fixed at $0.1mm$ for the two approaches. The simulation results obtained by the LS and MPF approaches are illustrated respectively in Fig. 6.8 and Fig. 6.9 and these results are compared in Fig. 6.10. In the current case, the simulation results obtained by both methods are very close to the analytical solution in terms of both grain boundary profile and transport velocity at the steady state (see Fig. 6.11). However, in this case, since the steady state is reached far away from the initial configuration, the simulation results obtained by the two methods are not perfectly overlapped during the transition phase.

As mentioned at the beginning of this section, the third set of grain boundary energy was used to analyze the performance of the two methods with strong anisotropy for grain boundary energy. The ratio between the highest interfacial energy and the lowest one is close to 7, which is significantly larger as compared to the values commonly used in the literature for full field anisotropic grain growth simulations (for example, this ratio equals to 3 in the work

of Chang et al [Chang 2014] and equals to 1.5 in the work of Moelans et al [Moelans 2009, Moelans 2008 PRB]). For this third set, the steady state is closer to the initial state of the configuration than for the first set of interfacial energy. Thus, no remeshing adaptation was performed in the simulations of both methods (*E=0.1mm)*. The values of *dt*, h_{fine} and h_{coarse} are identical to the ones used for the second set.

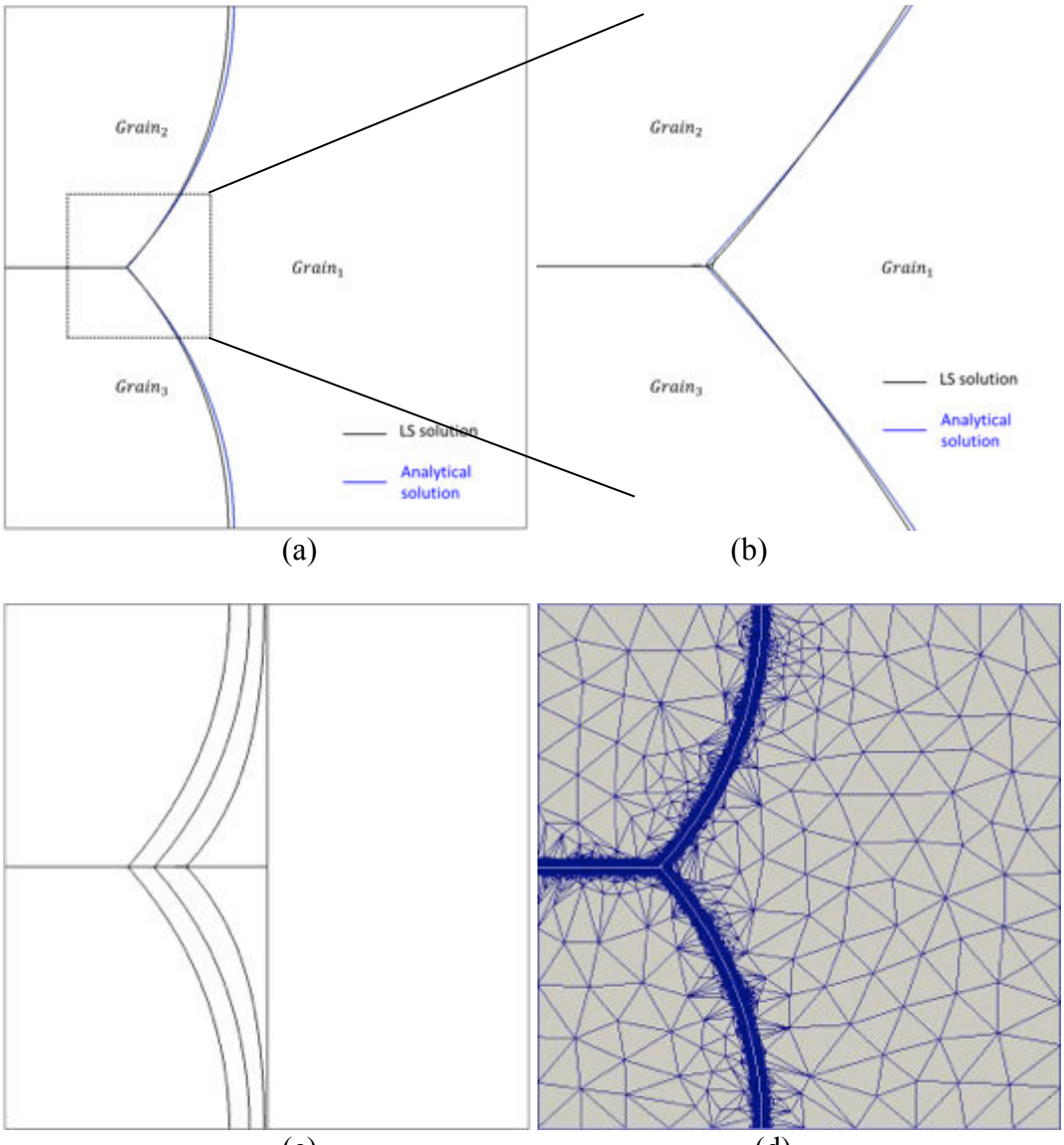

Fig. 6.8. Second γ-set: solution of the three-grain problem by the LS approach at $t = 100\,\mathrm{h}$. System parameters: $dt = 40s$, $h_{fine} = 2\times10^{-3}mm$. (a) LS solution compared with the analytical solution. (b) Zoom of (a) at the triple junction. (c) Evolution of the LS simulated structure at $t = 33\,\mathrm{h}20\,\mathrm{min}$, 66h40min and 100h. (d) Final profiles shown in the final finite element mesh configuration (*E=0.04mm*).

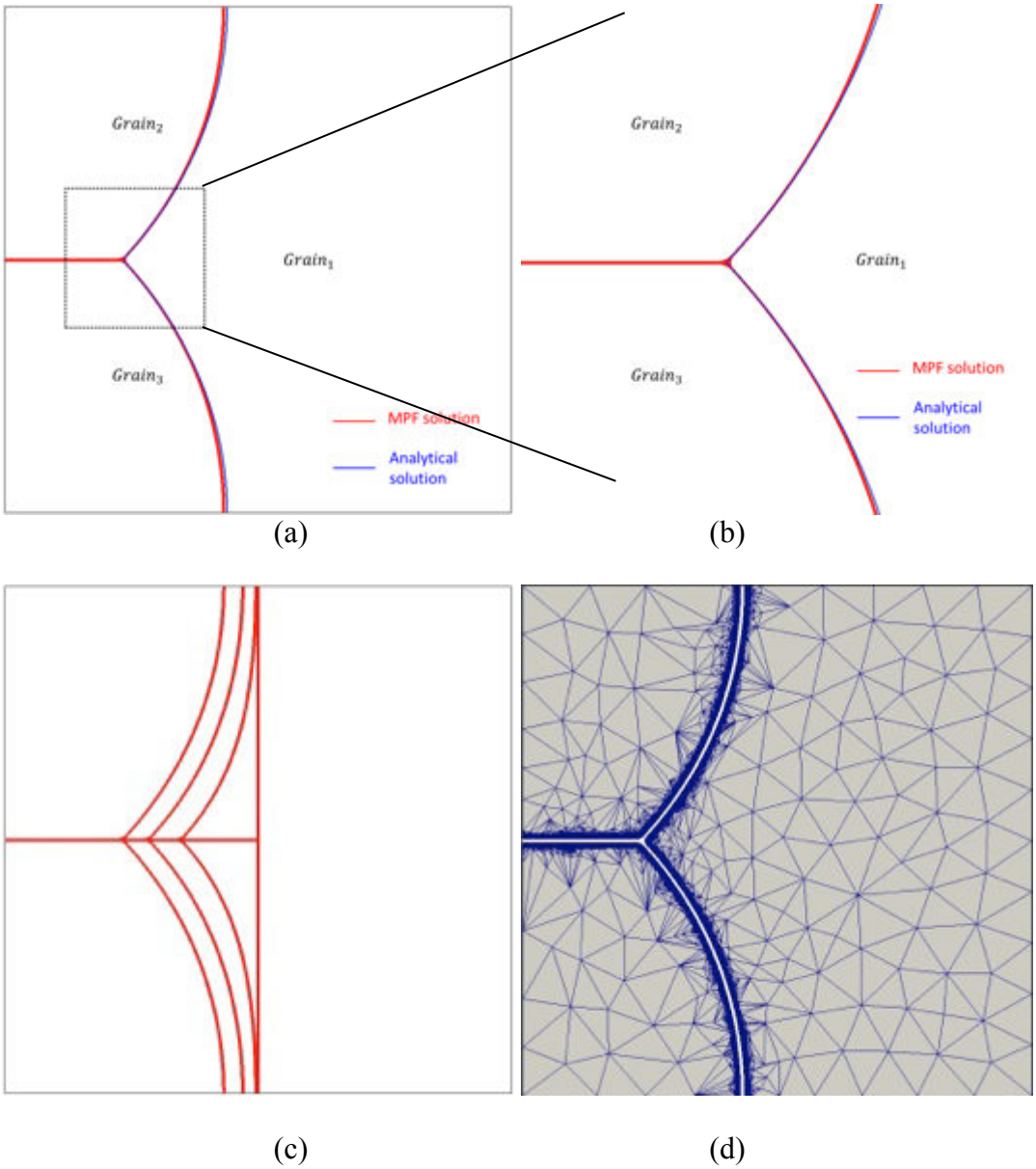

Fig. 6.9. Second γ-set: solution of the three-grain problem by the MPF approach at $t = 100\,\mathrm{h}$. System parameters: $\lambda = 2\times10^{-2}\,mm$, $dt = 2s$, $h_{fine} = 1.3\times10^{-3}\,mm$. (a) MPF solution compared with the analytical solution. (b) Zoom of (a) at the triple junction. (c) Evolution of the MPF simulated structure at $t = 33\,\mathrm{h}20\,\mathrm{min}$, 66h40min and 100h. (d) Final profiles shown in the final finite element mesh configuration (*E=0.04mm*).

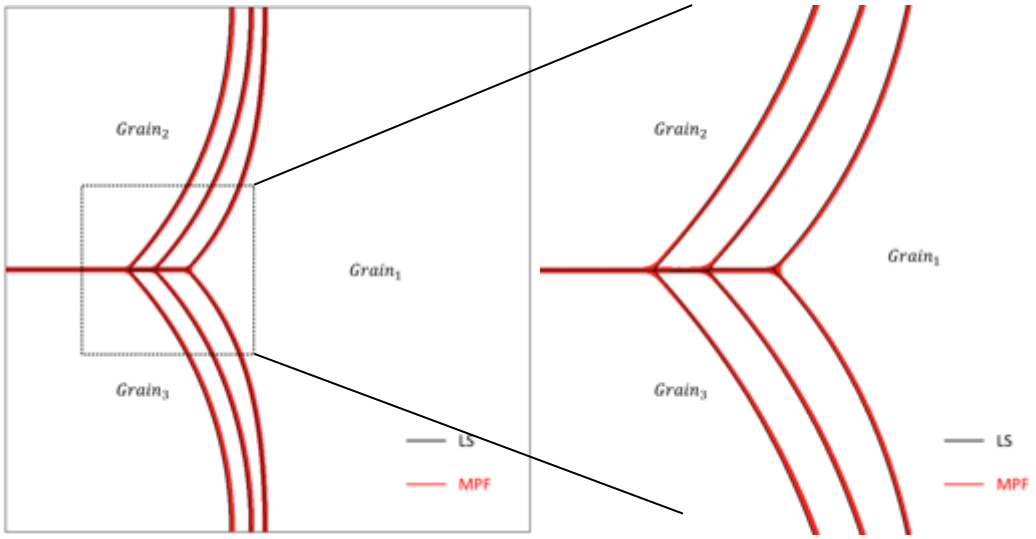

(a) (b)

Fig. 6.10. Second γ-set: (a) comparison between the simulation results of the LS and MPF at $t = 33\,\text{h}20\,\text{min},\ 66\text{h}40\text{min}$ and 100h; (b) Zoom of (a) at the triple junction.

.

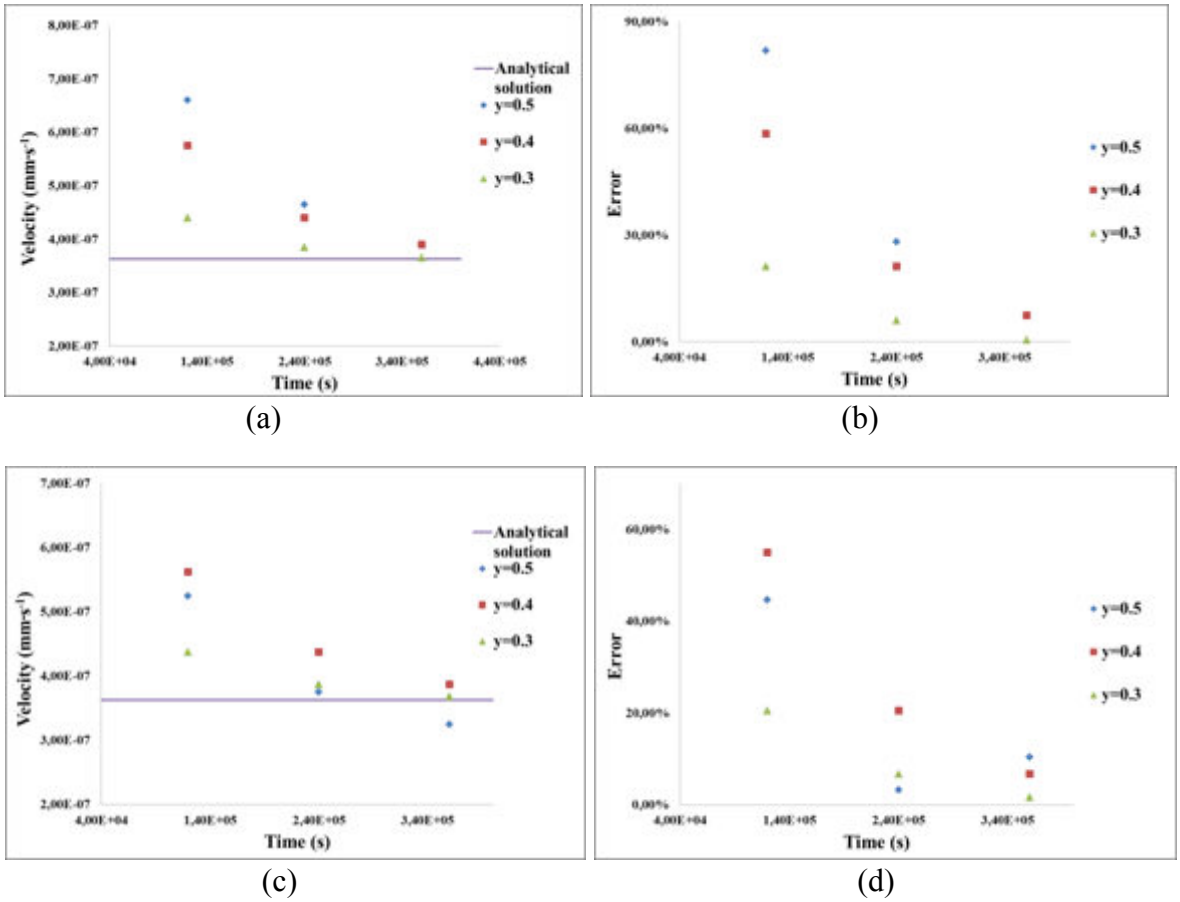

(a) (b)

(c) (d)

Fig. 6.11. Second γ-set: transport velocities at different points on the y-axis obtain by the MPF approach (a, b) and the LS approach (c, d) compared to the velocity of the steady-state constantly transported solution of the three-grain problem.

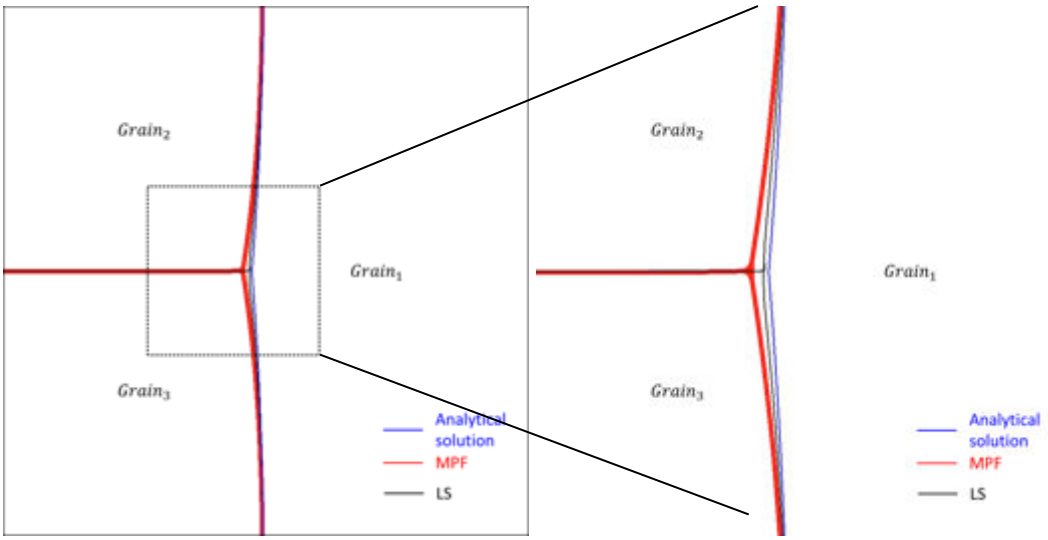

(a) (b)

Fig. 6.12. Third γ-set: (a) comparison between the simulation results obtained thanks to the LS and MPF approaches at $t = 33\,\mathrm{h}20\,\mathrm{min}$; (b) Zoom of (a) at the triple junction. System parameters: $\lambda = 2\times10^{-2}\,mm$, $dt = 2s$ and $h_{fine} = 1.3\times10^{-3}\,mm$.

Method	$h(mm)$	$dt(s)$	L^2 error in transport velocity
LS	2×10^{-3}	40	14.2%
MPF	1.3×10^{-3}	2	68.7%

Table 6.2.Third γ-set: errors obtained in transport velocity (Eq.6.11) at $t = 33\,\mathrm{h}20\,\mathrm{min}$ for the LS and MPF formalisms.

The simulation results obtained by the two methods are compared with the analytical solution in Fig. 6.12 and the L^2 errors in grain boundary migration velocity of the two methods at $t = 33h20\,\mathrm{min}$ are summarized in Table 6.2. The accuracy of the LS simulation is comparable with the ones obtained for the first two sets. However, the simulation accuracy of MPF degrades with high anisotropic interfacial energies. The better performance of LS with high anisotropic interfacial energies could be partially attributed to the numerical treatment expressed by Eq. 5-44. Indeed, in Eq. 5-44, in the extreme case that a grain boundary has a zero interfacial energy ($\sigma_i = 0$), $\phi_i(x, t+\Delta t)$ is imposed equal to $\phi_i(x,t)$, which means that the fact that the grain boundary cannot migrate is strongly imposed. In addition, different from the MPF in which the diffusion coefficient is a P1 variable (see Eq. 6-1), in LS framework, the diffusion coefficient is a P0C constant (see Eq. 5-43). This difference could

also contribute to the different numerical performance of these two methods. Therefore, as mentioned in Chapter 5, it should be interesting to investigate the possible difference between the Eq. 5-39 and the combination of Eq. 5-43 and Eq. 5-44 in terms of resulting grain boundary kinetics.

To summarize, with the present numerical conditions, there is no obvious deviation between the simulation results obtained with LS and with MPF for relatively low anisotropy for interfacial energy (ratio between the highest interfacial energy and the lowest one smaller than 2). However, with the numerical parameters i.e. dt and h_{fine} calibrated to obtain high simulation accuracy in the low anisotropy cases, LS offered better simulation accuracy than MPF for high anisotropy cases.

6.4 Conclusion

Nowadays, two deterministic implicit full field models exist in the literature for grain growth simulation: the PF method and the LS method. We compared in detail their formulation and their application for anisotropic grain growth simulations in the context of a FE formulation on unstructured mesh. Three three-grain problems (so-called 'Grim Reaper' problem) were solved by the two approaches with equivalent model parameter values and the simulation results were compared with the analytical solution. In the present finite element context, both methods can give accurate simulation results with a L^2 error around 10% in transport velocity after having reached a steady state for low anisotropy for grain boundary energy. With the numerical parameters i.e. dt and h_{fine} calibrated in order to obtain high simulation accuracy in the low anisotropy cases, the simulation accuracy with high anisotropy for interfacial energy obtained by LS is acceptable with a L^2 error around 15%; meanwhile, the L^2 error of the MPF simulation increases sharply to about 70%. We deduce thus that in the present numerical context, LS is more suitable for grain growth simulations with strong anisotropy for interfacial energy.

Meanwhile, there are still several points that need to be clarified in this comparison. First of all, as explained, the reason for the different numerical performances of LS and MPF in the high anisotropic condition is not completely clear. A more detailed comparison between these two approaches in this case should be performed by varying the values of h_{fine} and dt. Besides, as mentioned, the difference between the Eq. 5-39 and the combination of Eq. 5-43 and Eq. 5-44 in terms of resulted grain boundary kinetics should be clarified as well.

The present study was conducted in a two-dimensional context using isotropic FE mesh (with or without mesh adaptation), and only a simple three-grain structure is considered. In the future, this study should be extended firstly to 2D multiple-grains structures and then to three-dimensional structures. The application of anisotropic FEM will also be necessary especially for the purpose to reduce the additional numerical cost especially induced by three-dimensional calculations.

In the present PhD work, since in the present numerical context, LS is more suitable to simulate grain growth with strong anisotropy for interfacial energy, LS will be used in the large anisotropic grain growth simulations that will be presented in the next chapter.

Résumé en français

Dans ce chapitre, deux méthodes de type champ complet i.e. la méthode Multi-Phase-Field (MPF) et la méthode level-set (LS) ont été appliquées dans un contexte éléments finis P1 sur maillage non structuré. Les performances numériques de ces deux méthodes ont été comparées pour des configurations identiques. Trois problèmes académiques de type Garcke [Garcke 1999] ont été résolus avec les deux approches en utilisant des paramètres numériques équivalents. La différence entre les résultats de simulations obtenus par ces deux approches pour une anisotropie d'énergie interfaciale faible est négligeable tant qu'une combinaison "taille de maille/pas de temps" optimale est utilisée pour chaque méthode. Néanmoins, pour une anisotropie forte, la conclusion est moins évidente. Il est mis en évidence que dans le contexte numérique proposé, l'approche LS, à coût numérique fixé, semble plus robuste.

CHAPTER 6 COMPARATIVE STUDY OF MULTIPHASE FIELD AND LEVEL SET METHOD FOR ANISOTROPIC GRAIN GROWTH SIMULATION

7. FULL FIELD MODELLING OF 2D LARGE-SCALE ANISOTROPIC GRAIN GROWTH

In the previous chapter, we compared two main implicit full field models i.e. MPF and LS in a simple three-grain structure. We show evidence that the proposed LS numerical context can provide more precise numerical performance especially with strong anisotropy for grain boundary energy. In this chapter, LS is applied to perform 2D large grain growth simulations. Different 2D large grain growth simulations using implicit full-field models were recently reported in the literature. Elsey et al [Elsey 2013] and Chang et al [Chang 2014] studied the effect of microstructure texture on grain growth kinetics using repectively LS and PF approaches with finite difference formulations. Besides, large isotropic 2D grain growth simulations were performed in a finite element context in the work of [Fabiano 2014]. The result grain growth kinetics was compared with the classical mean field models.

In the first part, two 2D large-scale grain growth simulations with about 10000 grains were performed using level set method with respectively anisotropic and isotropic grain boundary energy in a finite element context. The simulation results are compared with the classical Burke and Turnbull model. In addition to the level set framework, other numerical techniques are applied to increase the simulation performance. Two among them i.e. Laguerre Voronoï tessellation method and graph coloring will be highlighted in this chapter. Laguerre Voronoï tessellation method allows to generate digital polycrystalline microstructure by respecting a given grain size distribution [Hitti 2012]. With the graph coloring technique, we can reduce the number of required level set functions that are used to describe the overall microstructure.

Even though large 2D grain growth simulations are largely reported in the literature as listed above, annealing twins have never been taken into account in such simulations. In the first part of this document, we have presented that almost no annealing twin boundaries are formed during grain growth. Thus, annealing twin nucleation can be dispensed in grain growth simulation. Nevertheless, for the sake of simulating microstructure evolution with annealing twin boundaries, three main problems need to be solved. Firstly, considering their special morphologies, annealing twin boundaries cannot be directly generated by a Voronoï or a Laguerre-Voronoï type synthetic geometry. Therefore, the first barrier is how to insert annealing twins into a synthetic microstructure. Secondly, once inserted into the initial synthetic microstructure, the special physical properties i.e. low interfacial energy of annealing twin boundaries should be respected in grain growth simulation (this topic was discussed in the chapter 6). Finally, due to different boundary plane inclinations, twin boundaries have different interfacial energies depending on their coherent or incoherent characters. Therefore, in order to correctly simulate the evolution of different kind of twin boundaries, in addition to misorientation dependent anisotropy, we also need to consider the inclination dependent anisotropy.

In the second part of this chapter, we propose a methodology to simulate two-dimensional annealing twin boundary evolutions during grain growth with LS method. LS framework for misorientation dependent anisotropic grain growth simulation was described in the previous chapter. Thus, in the present chapter, we proposed a new methodology concerning the twin insertion method and the treatment of inclination dependent anisotropy.

7.1 Large anisotropic grain growth simulation

7.1.1 Numerical techniques for large grain growth simulations

7.1.1.1 Voronoï and Laguerre Voronoï tessellations

The Voronoï tessellation method is widely used for synthetic microstructure generation [Rollett 2004]. The Voronoï tessellation is described by a set of N_G Voronoï sites $\{s_i\}$, $i \in \{1,\ldots,N_G\}$. Each site s_i defines a Voronoï cell V_i, which consists of all points closer to s_i than to any other sites:

$$V_i = \left\{ x \in R^d,\ d(x,s_i) = \min_{1 \le j \le N_G} d(x,s_j) \right\}, \tag{7-1}$$

Despite its wide spread use, the classical Voronoï method does not allow to respect a given grain size distribution. In fact, only the average grain size can be respected [Xu 2009], [Hitti 2012]. Therefore, an improved method i.e. Laguerre-Voronoï method is proposed [Aurenhammer 1987] [Imai 1985]. This method consists in using a distribution of non-intersected spherical particles that serves as a basis of the microstructure construction. We refer to [Hitti 2012] [Fabiano 2014] [Agnoli 2014] for more details of the Laguerre-Voronoï method. A 3D Laguerre-Voronoï tessellation is illustrated in Fig. 7.1.

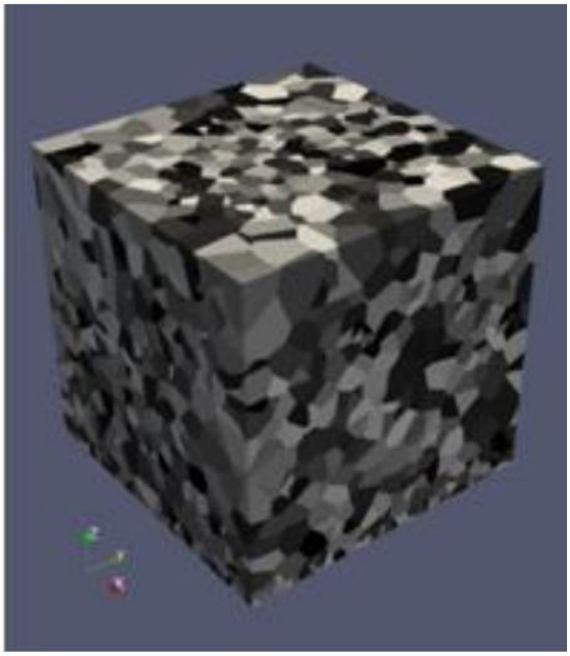

Fig. 7.1. a 3D Laguerre-Voronoï tessellation

7.1.1.2 Container level set functions

In order to limit the number of required level-set functions needed in our simulations, a classical technique of graph coloring [Kubale 2004] is used. The idea is to color the vertices of a graph such that no two adjacent vertices share the same color with a minimal number of colors. The most famous result from the graph coloring field of research is the four-color theorem [Kubale 2004]. Here we use the algorithm implemented by Hitti [Hitti 2012]. In this method, several non-neighbouring grains are grouped in only one level set function (called container level set function). As a consequence, the whole microstructure can be represented by a few level set functions corresponding to a set of strictly disjoint grains. The above technique however presents the limitation that two grains belonging to the same container level set function coalesce when they start touching each other. In this work, in order to delay the onset of grains coalescence, a constraint is introduced in the graph coloring such that only n^{th} ($n = 2,3,4\ldots$) nearest neighbour can belong to the same level set function. The simulation is then stopped as soon as two grains begin to coalesce. The choice of n value depends on how long we want to simulate the phenomenon before coalescence appears. Current improvements of the method (not discussed in this work) consist to perform coloration at each time increment in order to avoid coalescence phenomena.

7.1.2 Large scale simulation

In this section, two 2D large-scale grain growth simulations are performed. The first one is defined with anisotropic grain boundary energies dependent on a grain boundary misorientation angle distribution (Fig. 7.2 (b)) in a 304L stainless steel sample. The EBSD map of the corresponding sample is given in Fig. 7.3. The second simulation is performed by considering an isotropic grain boundary energy calculated by the average misorientation angle.

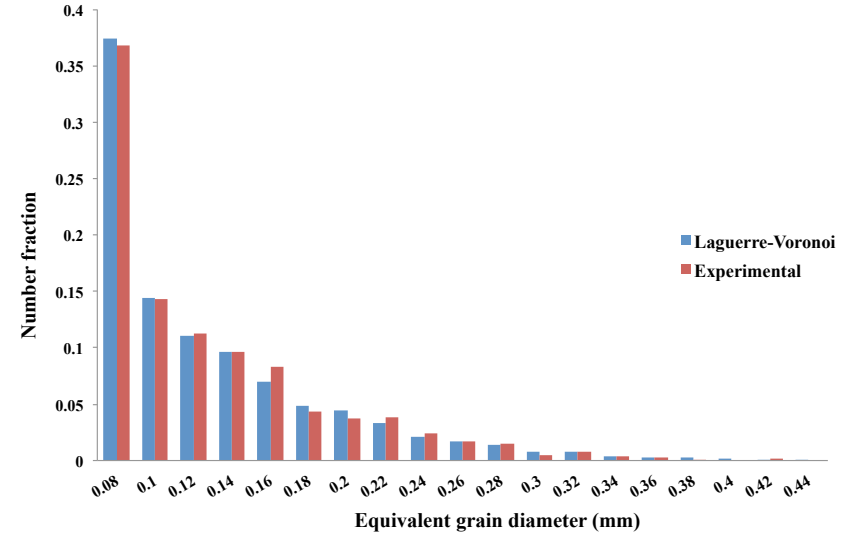

(a)

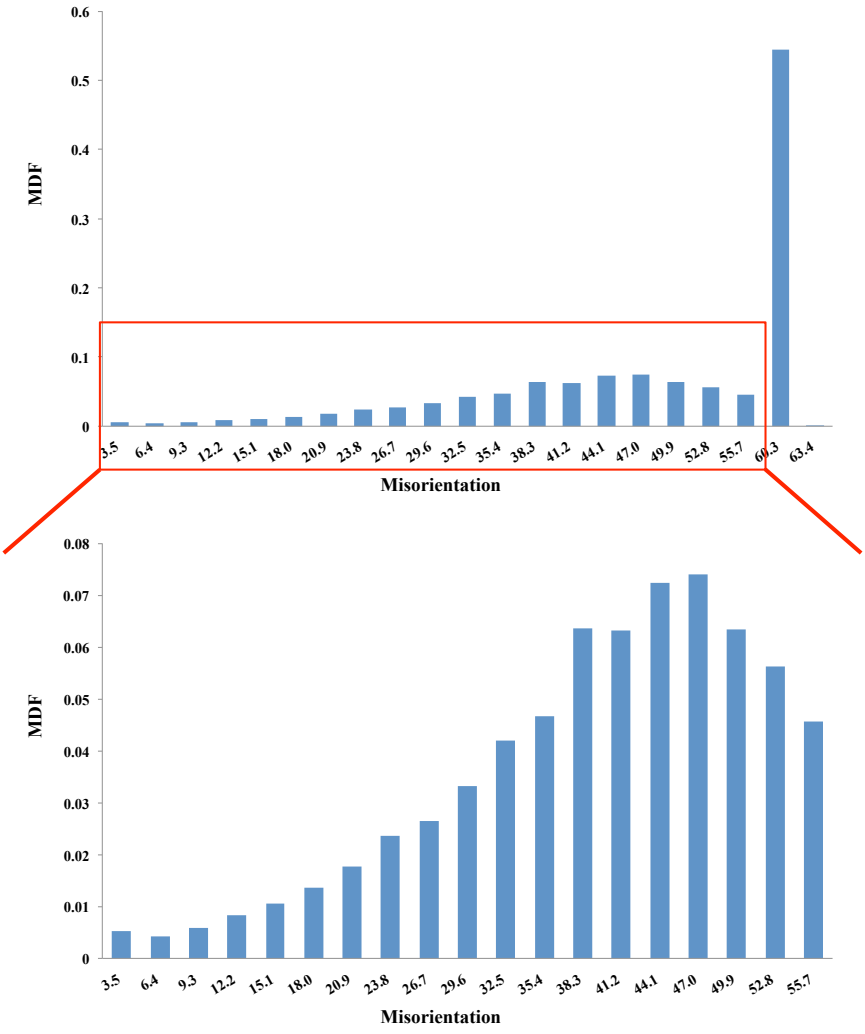

(b)

Fig. 7.2. (a) The experimental grain size distribution of the 304L sample compared with the distribution of the digital microstructure generated by our Laguerre-Voronoi algorithm. (b) The experimental misorientation distribution of the 304L sample (the distribution excluding the misorientation corresponding to twin boundaries is detailed).

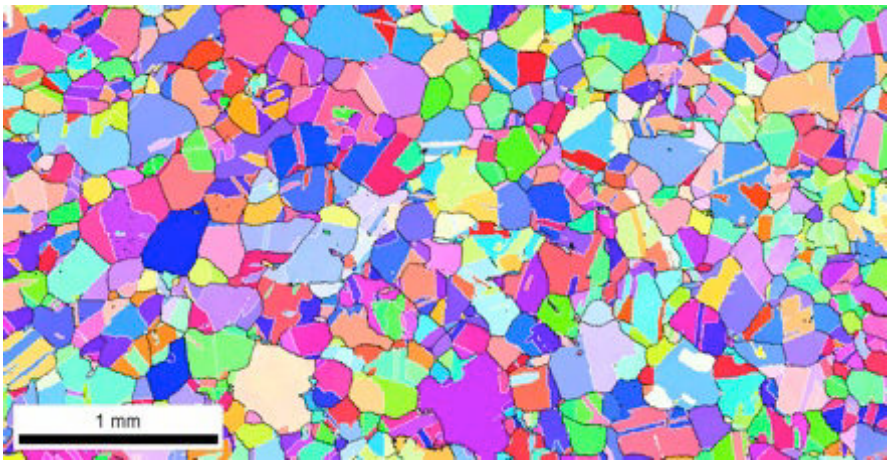

Fig. 7.3. Microstructure of the applied 304L stainless steel sample (same color code as Fig. 2.14); white lines denote annealing twin boundaries.

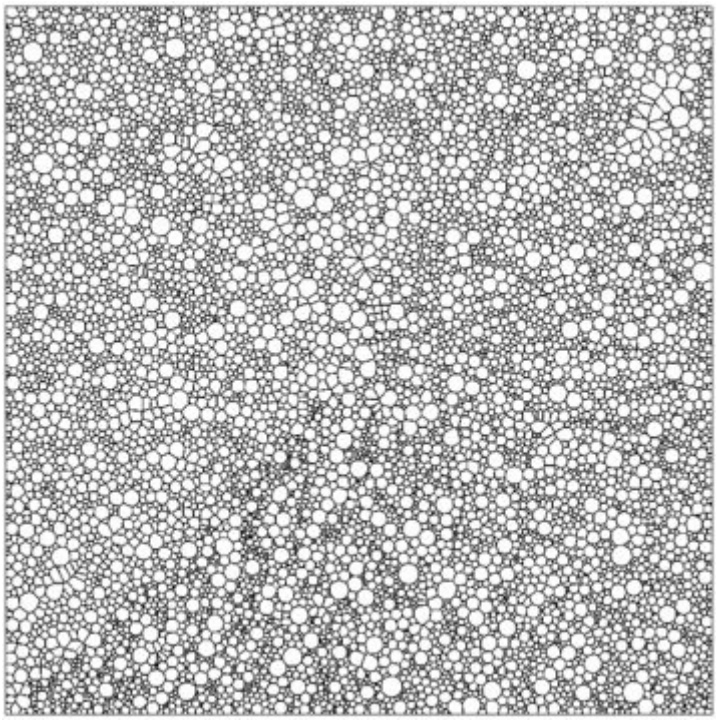

Fig. 7.4. Initial configuration of the ten thousand 2D grain growth simulation.

A digital microstructure containing approximately ten thousand grains (Fig. 7.4) is generated using the Laguerre-Voronoi technique [Hitti 2012] based on the grain size distribution (Fig. 7.2(a)) of the same 304L stainless steel sample. An isothermal heat treatment at 1050°C is simulated. An isotropic and unstructured finite element mesh is applied for both simulations. The mesh size equals to $10^{-2} mm$ leading to around 8000000 elements in a $13mm \times 13mm$ simulation domain. A coloration technique is used to reduce the total number of level set functions required [Fabiano 2014]. Thus, imposing that only the 3rd nearest neighbor can share the same level set function the microstructure is described by around 20 level set

functions. The values used for the grain boundary mobility $M = 1.37 \times 10^{-6} mm^4 J^{-1} s^{-1}$, which comes from previous expermiental work performed in CEMEF [Huang 2011]. In anisotropic context, the annealing twin boundary misorientation is excluded from the misorientation distribution. Accordingly the corresponding bin is cutted from the misorientation distribution (Fig. 7.2(b)). A misorientation angle based on the related probability defined by the misorientation distribution is fixed at each grain boundary. The grain boundary energy γ_{ij} is calculated based on this misorientation angle thanks to the following modified Read-Shockley relationship [Read 1950]:

$$\begin{cases} \gamma_{ij} = \gamma_{\min} + (1 - \gamma_{\min}) \dfrac{|\theta_{ij}|}{\theta_{\max}} \left[1 - \log \left(\dfrac{|\theta_{ij}|}{\theta_{\max}} \right) \right], & \theta_{ij} \le \theta_{\max} \\ \gamma_{ij} = 1 \cdot 10^{-6} Jmm^{-2}, & \theta_{ij} \ge \theta_{\max} \end{cases}, \tag{7-2}$$

where $\gamma_{\min} = 1 \cdot 10^{-7} Jmm^{-2}$ and $\theta_{\max}$ is set to be 30° [Elsey 2013] [Gruber 2009] [Holm 2001]. In the average misorientation angle calculation for isotropic grain growth simulation, all the angles bigger than 30° are considered as equal to 30° and all the angles smaller than 10° are considered as equal to 10°. The corresponding average grain boundary misorientation angle is 27°. The resulted isotropic grain boundary calculated by Eq. 7-2 ($9.47 \cdot 10^{-7}\ Jmm^{-2}$) is close to the interfacial energy of high-angle boundaries ($\theta \ge 30°$). Considering the low quantity of low-angle boundaries, in the isotropic grain growth simulation, the microstructure evolution could be seen as dominated by the evolution of high-angle boundaries.

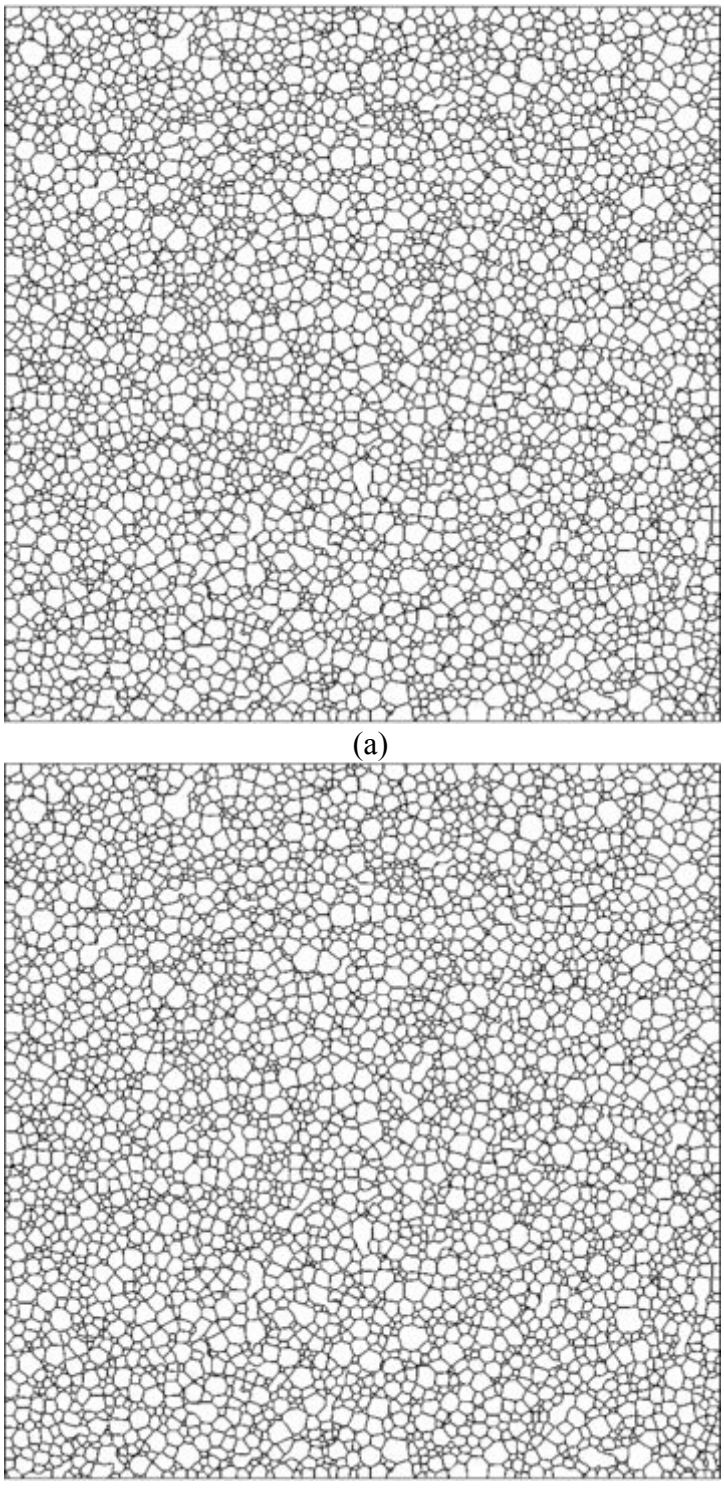

(a)

(b)

Fig. 7.5. Simulation results at $t = 1\text{h}40\,\text{min}$ with anisotropic grain boundary energy (a) and isotropic grain boundary energy (b).

The ANISOLS algorithm is used for the anisotropic grain growth simulation and the ISOLS one for the isotropic simulation. The simulation results at $t = 1\,\text{h}40\,\text{min}$ for both cases are described in Fig. 7.5. Excluding border grains, the anisotropic and isotropic simulations lead

to a similar final grain size distribution (Fig. 7.6). Additionally, the grain size and the grain number in both simulations evolve nearly identically (Fig. 7.7).

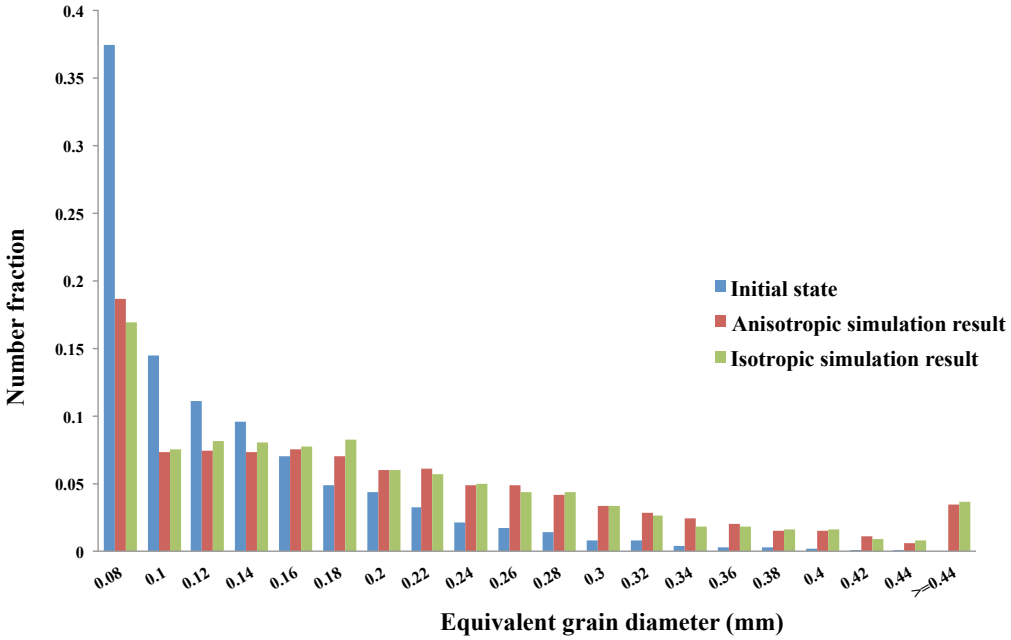

Fig. 7.6. Grain size distributions obtained by anisotropic and isotropic grain growth simulations at $t = 1\,\mathrm{h}40\,\mathrm{min}$.

	Slope (n)	α	Final grain number at t=1h40min
Anisotropic grain growth	1.23	0.52	3282
Isotropic grain growth	1.08	0.48	3187

Table.7.1. Burke and Turnbull model analysis comparing with the simulation results.

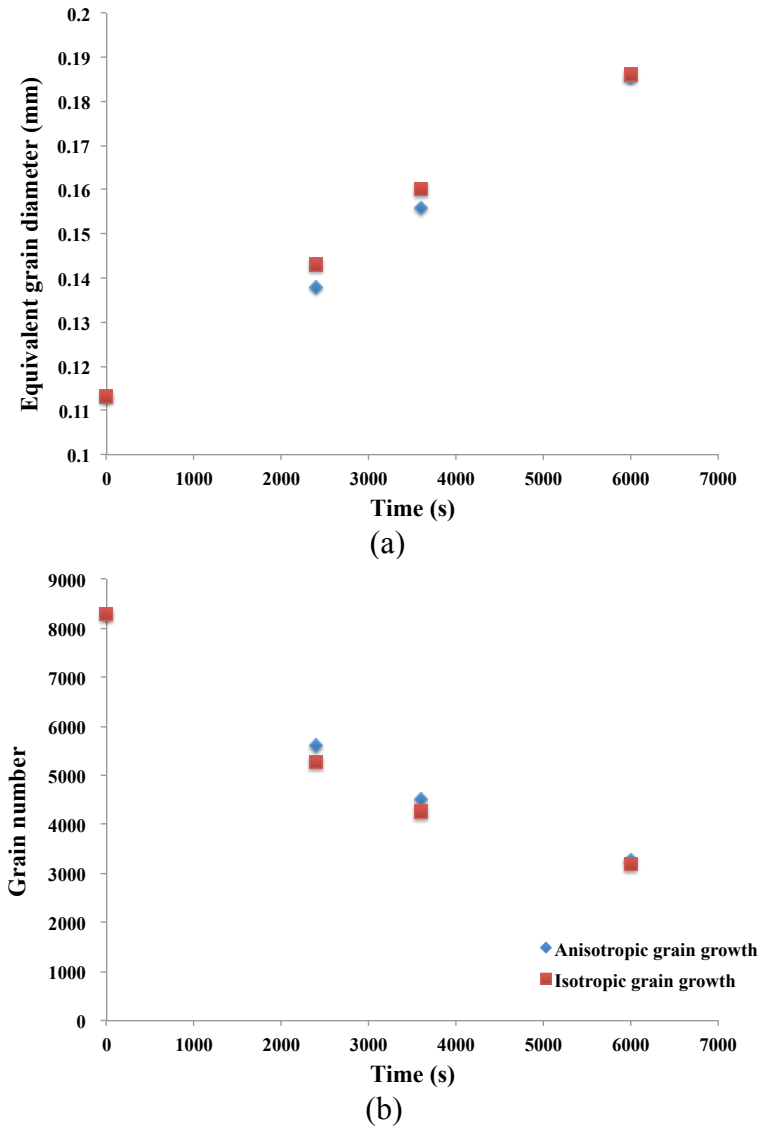

Fig. 7.7. Average grain size (a) and grain number (b) evolution in anisotropic and isotropic grain growth simulations.

The simulation results are compared with the Burke and Turnbull model [Burke 1952] expressed by the following equation,

$$\overline{R}^2 - \overline{R}_0^2 = \alpha m \gamma t^n, \tag{7-3}$$

where $\overline{R}$ (resp. $\overline{R}_0$) corresponds to the average grain radius at time t (resp. t=0) and $\alpha = 0.5, n = 1$. In order to simplify the comparison, the $\log\left(\overline{R}^2 - \overline{R}_0^2\right)$ curve was plotted for both simulations as a function of $\log(t)$ in Fig. 7.8. The two simulations exhibit different trends in this plot. As indicated in Tab.7.1, the isotropic grain growth is closer to the Burke and Turnbull model (the tangent is closer to 1), which is based on uniform grain boundary property hypothesis [Burke 1952]. Meanwhile, this difference is small in comparison with the

difference, which can be caused by the variation of the initial grain size distribution [Fabiano 2014].

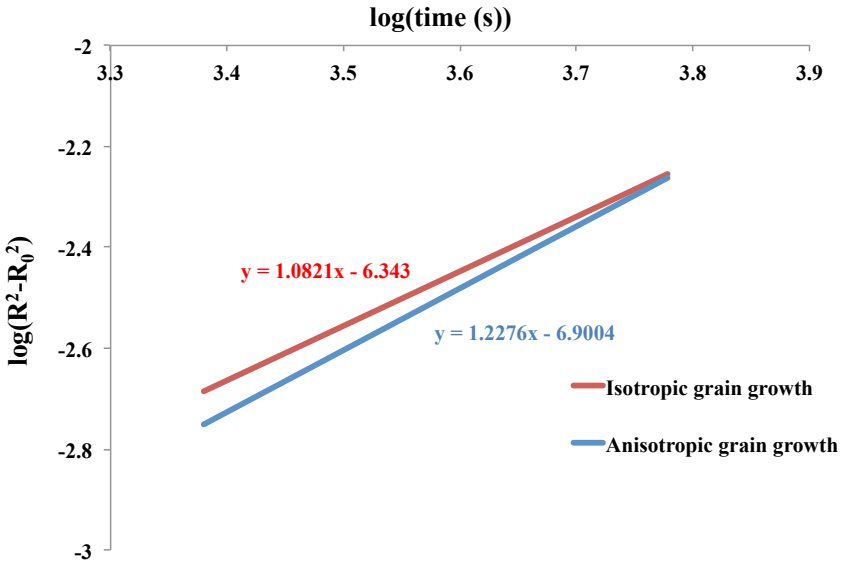

Fig. 7.8. Computed grain size evolutions in anisotropic and isotropic grain growth simualtions; linear approximations are used to be compared with the Burke and Turnbull model.

In conclusion, in the present case where the initial microstructure is not strongly textured, the difference in the grain size evolution computed with anisotropic or isotropic grain boundary energy is small.

7.2. Towards finite element simulation of annealing twin boundary evolution during grain growth in level set framework

7.2.1. Theoretical bases

7.2.1.1 Twin boundary insertion into a Voronoï or a Laguerre-Voronoï geometry

LS functions, which represent the microstructure, are constructed based on the Voronoï sites s_i [Bernacki 2009][Hitti 2012] as follows:

$$\begin{cases} \alpha_{ij}(x) = \dfrac{1}{2}\left\|\overrightarrow{s_i s_j}\right\| - \dfrac{\overrightarrow{s_i s_j} \cdot \overrightarrow{s_i x}}{\left\|\overrightarrow{s_i s_j}\right\|}, 1 \le i, j \le N_G, j \ne i \\ \phi_i(x) = \min\limits_{\substack{1 \le j \le N_G \\ j \ne i}} \left(\alpha_{ij}(x)\right) \end{cases}, \tag{7-4}$$

where $\alpha_{ij}(x)$ correspond to the signed distance of x to the bisector of the segment $\left[s_i, s_j\right]$. One can define a global unsigned distance function ($\phi_{glob}(x)$) as

$$\phi_{glob}(x) = \min_{\substack{1 \le j \le N_G \\ j \ne i}} \left(\alpha_{ij}(x)\right). \tag{7-5}$$

A 3D 200-grain microstructure, the corresponding Voronoï sites and $\phi_{glob}(x)$ function within the finite element mesh, is described in Fig. 7.9.

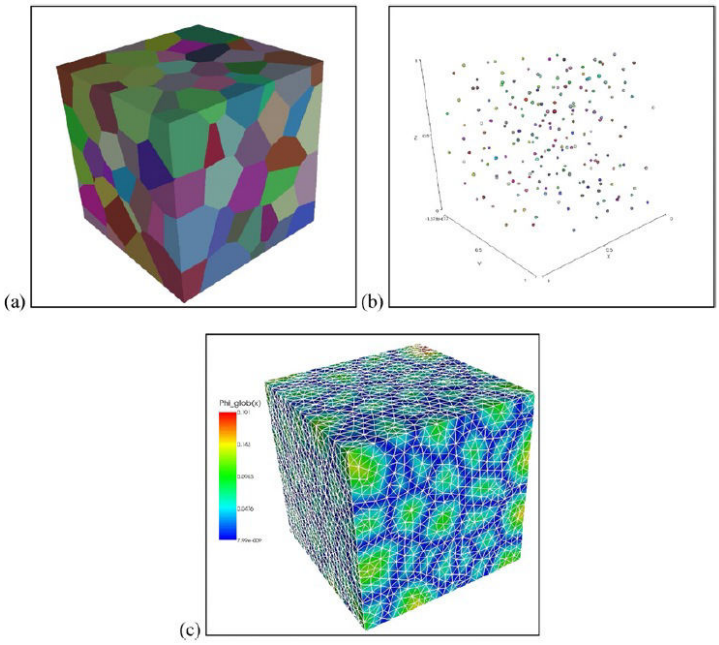

Fig. 7.9. (a) A 200 grains synthetic microstructure (colored by grain id), (b) the corresponding Voronoï sites and (c) the corresponding $\phi_{glob}(x)$ function with the considered finite element mesh in white (figures reproduced from reference [Bernacki 2009]).

Therefore, for inserting an annealing twin into a Voronoï geometry, a new site must be added in a way that the twin boundary morphology can be respected. In a two-grain microstructure, a third grain can be created by adding a new site very close to the site of one of the former grains (G_2 in the example of Fig 7.10). In this case, the angle at the triple junction 123 corresponding to the boundary between G_2 and G_3 is very close to 180°. Thus, the boundary Γ_{23} respects the morphology of a coherent twin boundary. Moreover, the direction of the boundary Γ_{23} can be reoriented by adjusting the coordinates of the third site as shown in Fig. 7.10 (c).

(a) (b) (c)

Fig. 7.10. Twin boundary insertion into 2D Voronoï geometry with the numbers inside brakets indicate the coordinates of the Voronoï sites $\varepsilon << 1$

It is worth mentioning that this strategy can be easily extended to Laguerre-Voronoï geometries. The Laguerre-Voronoï tessellation is described by a set of N_G sites and weights $\{(s_i, r_i)\}$, $i \in \{1,\ldots,N_G\}$. Accordingly, the LS functions are constructed based on the following relationships [Hitti 2012]:

$$\begin{cases} \alpha_{ij}(x) = \dfrac{1}{2}\left(\left\|\overrightarrow{s_i s_j}\right\| + \dfrac{r_i^2 - r_j^2}{\left\|\overrightarrow{s_i s_j}\right\|}\right) - \dfrac{\overrightarrow{s_i s_j} \cdot \overrightarrow{s_i x}}{\left\|\overrightarrow{s_i s_j}\right\|}, 1 \le i, j \le N_G, j \ne i \\ \phi_i(x) = \min\limits_{\substack{1 \le j \le N_G \\ j \ne i}} \left(\alpha_{ij}(x)\right) \end{cases} . \quad (7\text{-}6)$$

Therefore, to insert a twin, a new site $\left(s_i^T, r_i^T\right)$ needs to be inserted so that s_i^T is very close to s_i and r_i^T equals to r_i.

In the previous section, the misorientation distribution is used to attribute grain boundary energies. In this section, to facilitate the construction of twin boundaries, each grain in the synthetic microstructure is defined thanks to a crystallographic orientation. The grain

boundary energies are determined based on the disorientation calculated by the orientations of the corresponding adjacent grains. Therefore, the orientation of the inserted twin grain can be calculated by the orientation of the 'parent grain'. In addition, if we deal with a coherent twin, the direction of the boundary plane can also be determined by the orientation of the 'parent grain'. For example, if the disorientation between the 'parent grain' and the inserted twin is 60° around the [111] axis, then the orientation of the twin and the direction of the coherent twin boundary ($\vec{n}$) can be calculated by the following formulation:

$$[T]=\begin{bmatrix} \frac{2}{3} & \frac{2}{3} & -\frac{1}{3} \\ -\frac{1}{3} & \frac{2}{3} & \frac{2}{3} \\ \frac{2}{3} & -\frac{1}{3} & \frac{2}{3} \end{bmatrix}\cdot[M],\ \vec{n}=[T]\cdot\begin{bmatrix}1\\1\\1\end{bmatrix}=\begin{bmatrix} T_{11}+T_{12}+T_{13} \\ T_{21}+T_{22}+T_{23} \\ T_{31}+T_{32}+T_{33} \end{bmatrix}, \tag{7-7}$$

where $[T]$ and $[M]$ are respectively the orientation matrix of the twin and of the 'parent grain' with Bunge Euler angles. Bunge Euler angles are used to be able to apply directly the orientations in the real EBSD maps (in the OIM software from TSL).

To summarize, with this twin insertion methodology, we can easily add coherent or incoherent twin boundaries into a Voronoï or a Laguerre-Voronoï tessellation. The methodology is described by the following procedure:

TINSERT1. Construct a Voronoï tessellation with N_G sites $S=\{s_i,\ 1\le i\le N_G\}$ or a Laguerre-Voronoï tessellation with $S=\{(s_i,r_i)\},\ i\in\{1,\ldots,N_G\}$.

TINSERT2. Find randomly *n* different sites for twin insertion $S^n=\{s_{i_1},\ldots,s_{i_n}$, with $\{i_1,\ldots,i_n\}\in[1,N_G]$, and $i_k\neq i_l,\ \forall k\neq l\}$; in the case of a Laguerre-Voronoï geometry $S^n=\{(s_{i_1},r_{i_1}),\ldots,(s_{i_n},r_{i_n})$, with $\{i_1,\ldots,i_n\}\in[1,N_G]$, and $i_k\neq i_l,\ \forall k\neq l\}$.

TINSERT3. $\forall s_{i_k}\in S^n$, add a point $s_{i_k}^T$ close to s_{i_k} (in the case of a Laguerre-Voronoï geometry, $r_{i_k}^T=r_{i_k}$). If a coherent twin boundary is inserted, then the direction $\overrightarrow{s_{i_k}s_{i_k}^T}$ is chosen as perpendicular to a {111} plane of G_{i_k}, otherwise, the direction $\overrightarrow{s_is_i^T}$ is fixed randomly. In case of Voronoï tessellation, we note $S^T=\{s_{i_k}^T,\ i_k\in\{i_1,\ldots,i_n\}\}$ and in the case of a Laguerre-

Voronoï tessellation $S^T = \left\{\left(s_{i_k}^T, r_{i_k}^T\right), i_k \in \{i_1, \ldots, i_n\}\right\}$. Finally $G_{i_k}^T$ will denote the grain associated with $s_{i_k}^T$.

TINSERT4. The orientation of $G_{i_k}^T$ is fixed by the corresponding twin orientation calculated thanks to the orientation of G_{i_k}

TINSERT5. A new Voronoï or Laguerre-Voronoï tessellation based on $S^{New} = S \bigcup S^T$ is generated.

In this methodology, *n* twin boundaries will be inserted into *n* different grains and a synthetic microstructure with in average no more than one twin boundary per grain can be obtained. To insert more than one twin boundary per grain, the previous algorithm needs to be extended. However, due to complexity of the twin-chain morphology [Lin 2014], in the present study this extension will not be treated.

As presented in the previous chapter, in order to reduce computational cost, classical technique of graph coloring is applied in large grain growth simulations. Applying this technique, several non-neighboring grains are represented by one level set function. The inserted twins should be represented by a different level set function from its parent grain and the total number of the level set functions used to represent inserted twins should be limited. In that case, a complementary procedure needs to be applied to color both original grains and inserted twins.

TINSERTCOLOR1. Describe $\{G_i,\ 1 \le i \le N_G\}$ by N_{color} colors, which correspond to N_{color} container LS functions $\Phi = \{\bar{\phi}_i,\ 1 \le i \le N_{color}\}$;

TINSERTCOLOR2. $\forall s_{i_k} \in S^n$, Color $\left\{G_{i_k}^T, i_k \in [i_1, i_n]\right\}$ by N_{color}^T colors in the following way:

If the parent grains G_{i_k} and G_{i_l} are represented by the same color, then new color will be used for both $G_{i_k}^T$ and $G_{i_l}^T$;

TINSERTCOLOR3. $\left\{G_i^{new},\ 1 \le i \le N_G + n\right\}$ is represented by $N_{color}^{new} = N_{color} + N_{color}^T$ colors.

$\{G_i,\ 1 \le i \le N_G\}$, $\left\{G_{i_k}^T, i_k \in \{i_1, \ldots i_n\}\right\}$ and $\left\{G_i^{new},\ 1 \le i \le N_G + n\right\}$ are respectively the set of grains in S, S^T and S^{new}. In this procedure, if two parent grains G_{i_k} and G_{i_l} are described by the same color, then $G_{i_k}^T$ and $G_{i_l}^T$ will be represented by another color.

7.2.1.2 Twin boundary inclination represented by level set functions

The properties of an annealing twin boundary differ according to its coherent or incoherent character. Coherent twin boundaries have very low grain boundary energy and mobility. Meanwhile, incoherent twin boundaries have higher interfacial energy, as illustrated in Fig. 1.5. The difference between coherent and incoherent twin boundaries is the twin boundary inclination. Therefore, despite the weak dependence on boundary inclination of regular high-angle boundaries [Humphreys 2004], the consideration of twin boundary inclination is essential for the simulation of twin boundary evolution.

In the literature, the inclination dependent anisotropy is only considered in the phase field framework as presented in chapter 5 of the present thesis. In the present study, we consider twin boundary inclination but in our LS framework.

In 2D phase field framework, the inclination angle can be expressed as a function of the phase field functions. This idea also holds for the LS method. As already presented, the outward unit normal to any isovalue of ϕ_i is given by the normalized gradient of ϕ_i [Bernacki 2009]. Therefore, the normal of the grain boundary plane can be described explicitly thanks to the LS functions ϕ_i. In the case of an annealing twin boundary, the comparison between the calculated twin boundary normal and the theoretical coherent twin boundary normal can indicate if the twin boundary is coherent or incoherent. To summarize, coherent and incoherent twin boundaries can be distinguished by the following algorithm:

For each integration point near the twin boundary Γ_{ij} between G_i and G_j

TWININC1. Calculate the four possible coherent twin boundary normal $\left(\vec{n}_i^j\right)_{1\le j\le 4}$ based on the orientations of G_i and G_j. It is worth mentioning that in 2D, the 2D traces of the {111} planes that are calculated. The fact that different {111} planes could share the same 2D trace is ignored here.

TWININC2. Calculate the actual 2D twin boundary normal $\vec{n}$ ($\vec{n} = \dfrac{\nabla\phi_i}{\left\|\nabla\phi_i\right\|}$).

TWININC3. **If** $\exists j \in \{1,\ldots,4\} / \left\|\vec{n} - \vec{n}_i^j\right\| \le \varepsilon$,

the properties of a coherent twin boundary will be attributed to this integration point,

Else

the properties of an incoherent twin boundary will be attributed to this integration point,

where ε is a critical value. ε can be considered as physically related to the maximum admitted angular deviation from the coherency plane. It is worth mentioning that this methodology can be extended to treat the inclination dependent anisotropy of all grain boundaries. However, since the properties of regular high-angle boundaries are not very sensitive to grain boundary inclination compared to twin boundaries [Humphreys 2004], this method is only applied for twin boundaries in the present study.

7.2.2. Simulation of annealing twin boundary evolution during grain growth

Finally, to simulate annealing twin boundary evolution during grain growth, the original algorithm for anisotropic grain growth simulation needs to be modified as follow:

1. Insert twin boundaries into the initial synthetic microstructure using the algorithm TINSERT.
2. If the graph coloring technique is used, the algorithm TINSERTCOLOR should be applied after TINSERT.
3. For the sake of determination of grain boundary energies, a first test is performed in order to verify if the boundary is a twin boundary based on the orientations of the two adjacent grains. Then, the algorithm TWININC is used to differentiate coherent and incoherent twin boundary. The corresponding interfacial energy is then attributed to the boundary.
4. Perform the ANISOLS algorithm.

All the simulations presented in this section were performed on a $[0mm,1mm]\times[0mm,1mm]$ domain. The grain boundary mobility, which is considered as a constant, equals to $10^{-4} mm^2 \cdot s \cdot kg^{-1}$. It is worth mentioning that in reality, the grain boundary mobility is also an anisotropic parameter depending on grain boundary crystallography, which has five degrees of freedom. Coherent twin boundaries are nearly immobile. Meanwhile, incoherent twin boundaries, which have the same misorientation with coherent ones, are even more mobile than regular grain boundaries [Olmsted 2009]. In the present study, the product of the grain boundary energy and the mobility is considered as an ensemble. Therefore, we did not consider separately the anisotropy of grain boundary mobility.

7.2.2.1 Theoretical tests

In this section, two three-grain problems with Neumann boundary condition are solved to validate our methodology. In the first case "3G_1T_1" (resp. the second one "3G_1T_2"), a coherent (resp. an incoherent) twin boundary is inserted into an initial two-grains configuration as illustrated in Fig. 7.11. In 3G_1T_1, the interfacial energy of the inserted coherent twin boundary is fixed as null, and the two high-angle boundaries have the same interfacial energy equal to $1.1 \cdot 10^{-6} J \cdot mm^{-2}$. In 3G_1T_2, the interfacial energies of the regular high angle boundaries are determined by the corresponding misorientation calculated

thanks to the grain orientations indicated in Fig. 7.11 using the Read-shockley relationship (see Eq.7-3), where the maximal misorientation $\theta_{\max}$ is fixed as 30°. As explained, incoherent twin boundaries have low interfacial energy but high mobility. Here, we roughly give the incoherent twin boundary in 3G_1T_2 an intermediate interfacial energy ($5.94 \cdot 10^{-7} J \cdot mm^{-2}$) to illustrate its difference from regular boundaries and coherent twin boundaries.

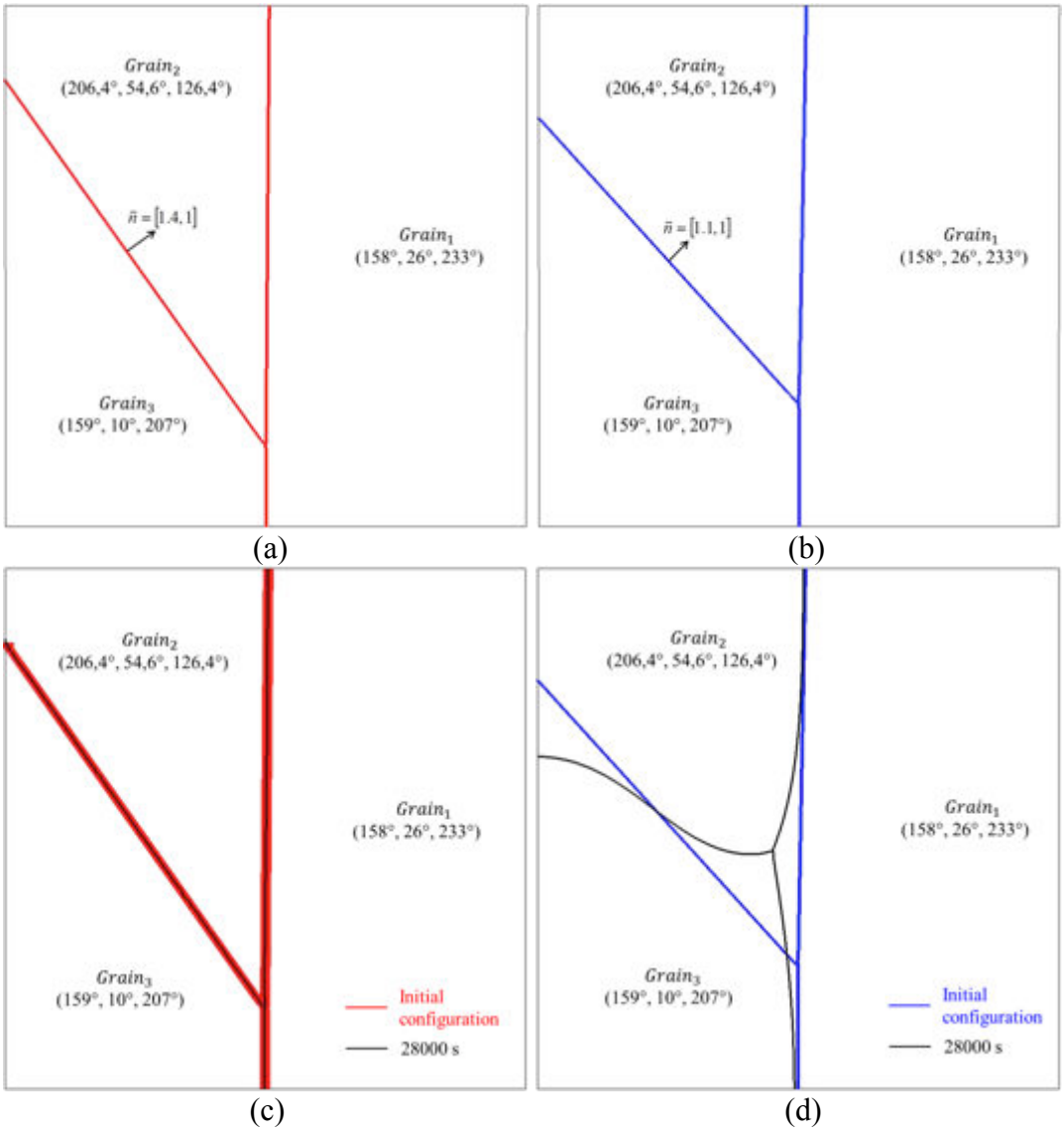

Fig. 7.11 Theoretical test of twin boundary evolution in three-grain structures: (a) initial configuration of 3G_1T_1 containing a coherent twin boundary; (b) initial configuration of 3G_1T_2 containing an incoherent twin boundary; (c) simulation result after 28000s for 3G_1T_1; (d) simulation result after 28000s for 3G_1T_2.

The optimal FE parameters identified for the LS simulation of the three-grain problem presented in chapter 6 are used ($h_{fine} = 2\mu m$, $dt = 40s$, $h_{coarse} = 0.04mm$, E=$0.04mm$). In the

case of the incoherent twin boundary, an isotropic remeshing operation is performed at the end of each time increment. The simulation results after 28000 seconds in both cases are described in Fig.7.11. In the case 3G_1T_1, where a coherent twin boundary is inserted, since the interfacial energy associated with the twin boundary is zero, the initial configuration is at the equilibrium state and was kept during the simulation. In the case, 3G_1T_2 the incoherent twin boundary is treated as a grain boundary with a low interfacial energy. Therefore, the configuration tends to reach the equilibrium state at the triple junction and the boundary condition is respected at the frontiers of the simulation domain.

The evolution of the twin boundary length is described in Fig. 7.12.

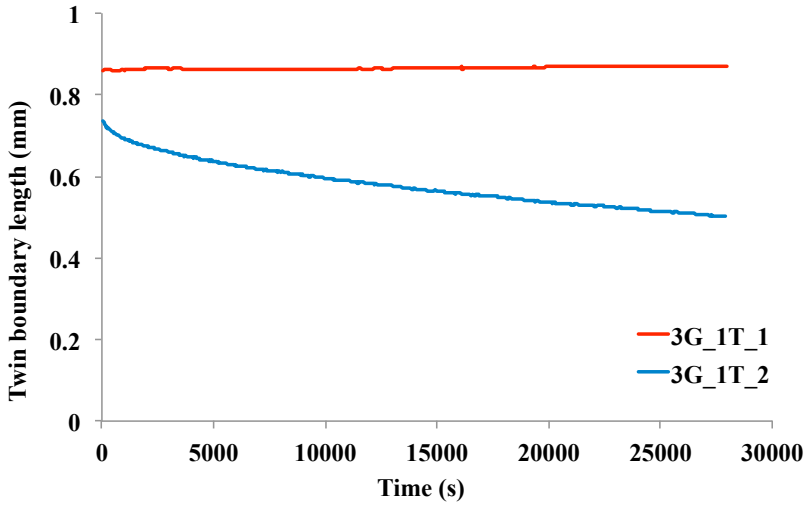

Fig. 7.12 Simulation results of 3G_1T_1 and 3G_1T_2 : twin boundary length evolution.

For these two simple three-grains problems, the twin boundary evolutions exhibited in the simulation results are consistent with the experimental ones. The coherent twin boundaries are immobile during microstructural evolution due to their low interfacial energy and mobility. Meanwhile the incoherent twin boundaries can migrate inside grains to reduce the total interfacial energy.

7.2.2.2. Annealing twin evolution in polycrystalline structures

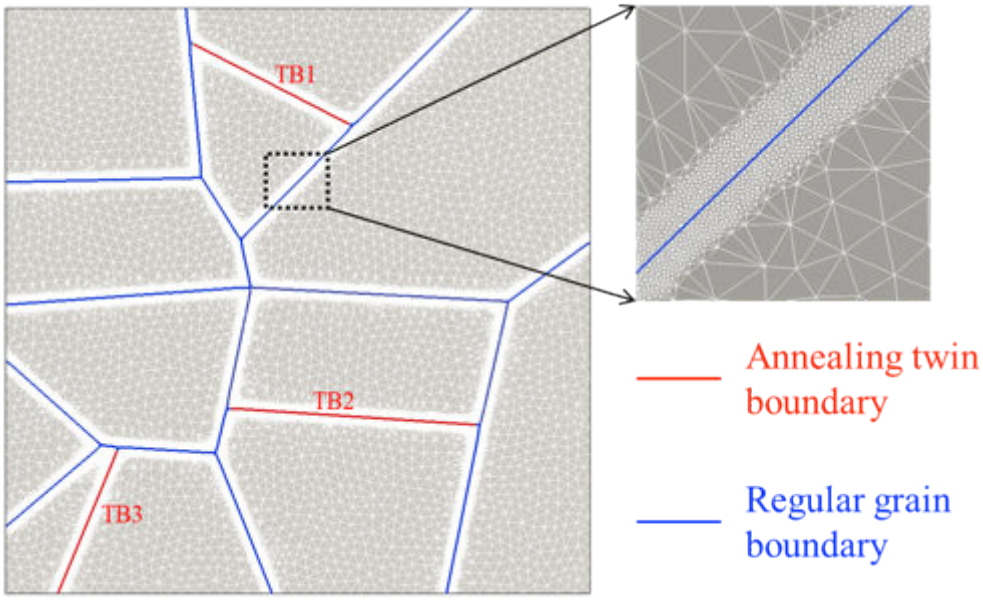

Fig. 7.13. Simulation 12G_3T: initial configuration and zoom describing the refined isotropic FE mesh around grain boundaries.

New configurations are proposed in order to test annealing twin evolution behaviors during the grain growth simulation in polycrystalline cases. In the configuration referred to as "12G_3T", an initial synthetic microstructure made of 12 grains including three twins was built (Fig. 7.13). Three coherent twin boundaries were inserted into an initial nine-grain microstructure. The FE mesh used for the simulation was refined in an isotropic way around the grain boundaries. Same as in the previous simulations, the mesh size (h_{fine}) inside the refined zone equals to $2\mu m$. Since the average grain boundary migration kinetics is more important than in the three-grain structure, the time step (dt) is accordingly adjusted to $30s$. An isotropic remeshing is performed at the end of each time increment.

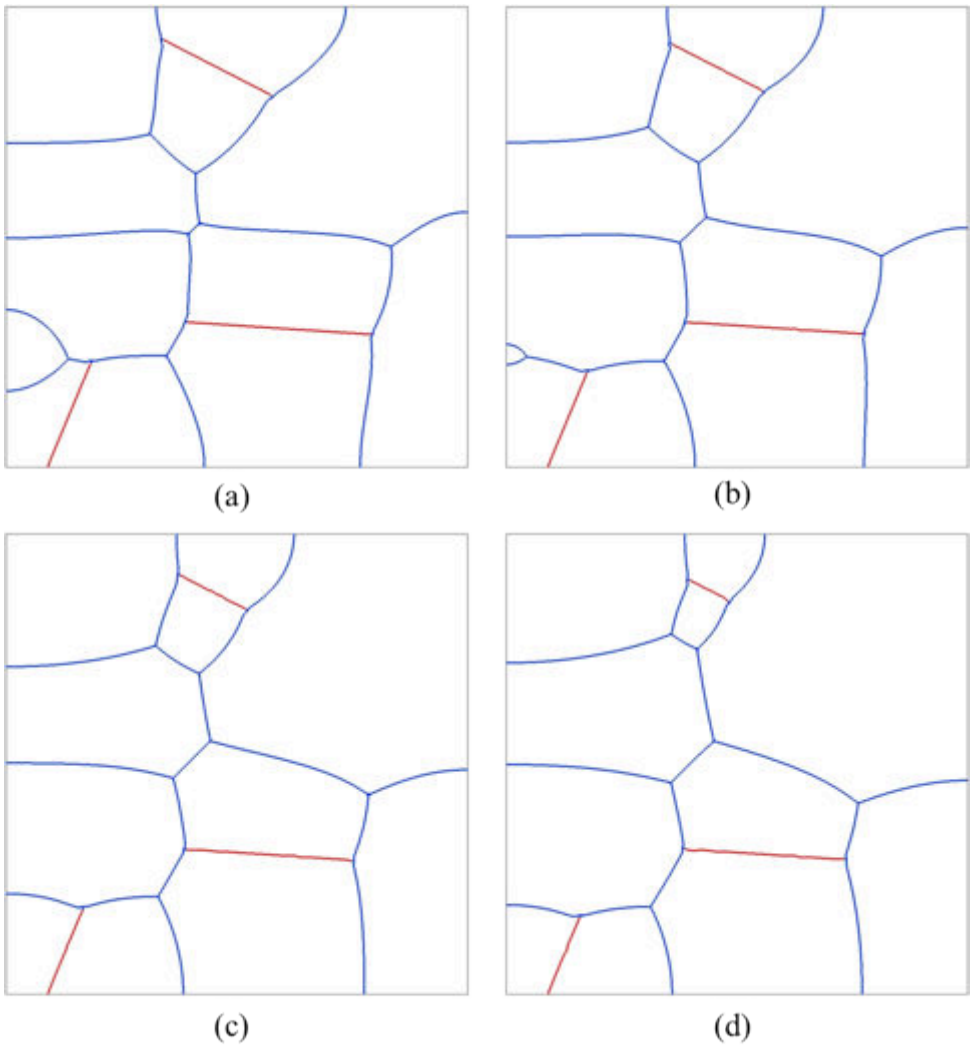

Fig. 7.14. 12G_3T case: simulation results; (a) after 50 min, (b) 150min, (c) 300min, and (d) 450min.

In this simulation, the inserted coherent twin boundaries are given zero interfacial energy. All the other regular boundaries are considered having a uniform grain boundary energy equals to $1.1 \cdot 10^{-6} J \cdot mm^{-2}$. The simulation results are illustrated in Fig. 7.14. In the simulation, the twin boundaries shrink driven by the migration of the grain boundaries. The total twin boundary length decreases during the simulation (see Fig. 7.15), which is consistent with the annealing twin density evolution trend revealed by the experimental data (e.g. Fig. 2.24). The simulation result at 450 minutes is compared with the initial configuration in Fig. 7.16. In this comparison, we can see that the extreme equilibrium angle at the triple junctions intercepted by the coherent twin boundaries i.e. 180 degrees was respected around the triple junctions. In addition, due the zero interfacial energy, all the coherent twin boundaries were immobile during the simulation.

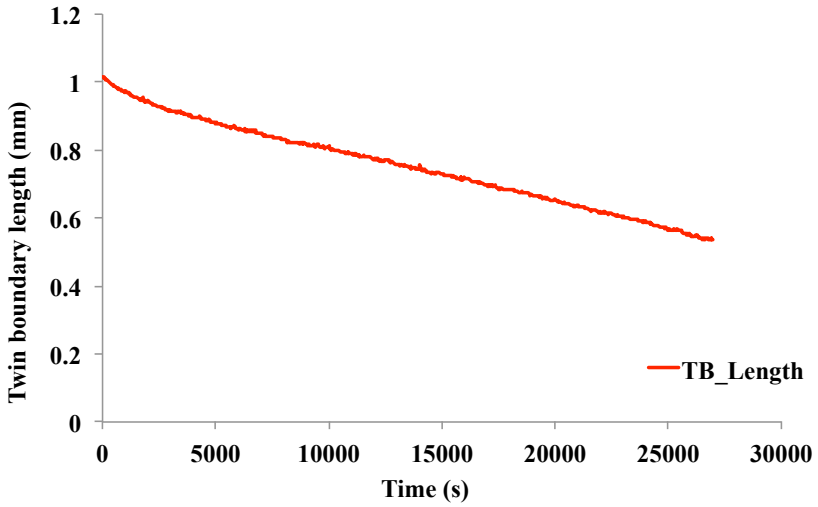

Fig. 7.15. Twin boundary length evolution for the case 12G_3T

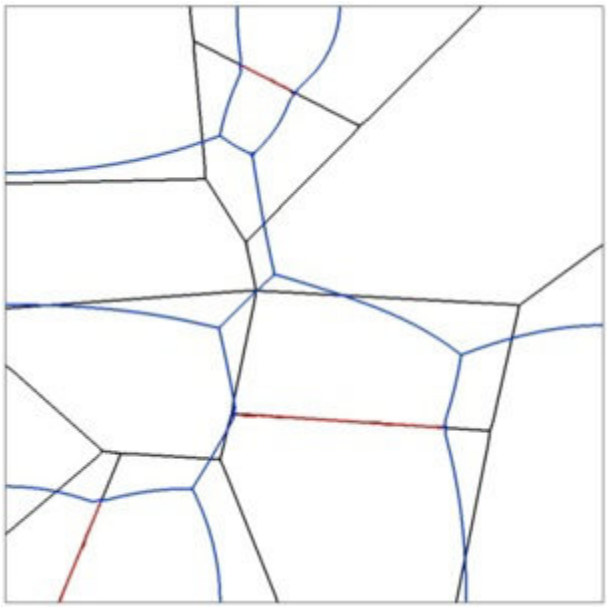

Fig. 7.16. 12G_3T case: comparison between the simulation result after 450min (blue lines for regular grain boundaries and red lines for annealing twin boundaries) and the initial configuration described by black lines.

A larger grain growth simulation "200G_80T_1" involving 280 grains was performed. 80 coherent twin boundaries are inserted into a 200-grains initial synthetic microstructure (Fig. 7.17). The FE mesh is refined again in an isotropic way around grain boundaries ($h_{fine} = 2\mu m$). About 40000 elements are used for the initial mesh generation. Since more grains are considered in a constant simulation domain, the average grain growth kinetics is faster than for the previous simulations. Accordingly, the time step is reduced to 5s to guarantee the simulation accuracy. Isotropic remeshing adaptation is performed at the end of each time increment. The technique of graph coloring was used for this simulation. The 200 initial

grains are described by 22 LS functions. By applying the algorithm TINSERTCOLOR, the 80 inserted twins are represented by 21 LS functions. Therefore, 43 LS functions are used in total to describe the microstructure.

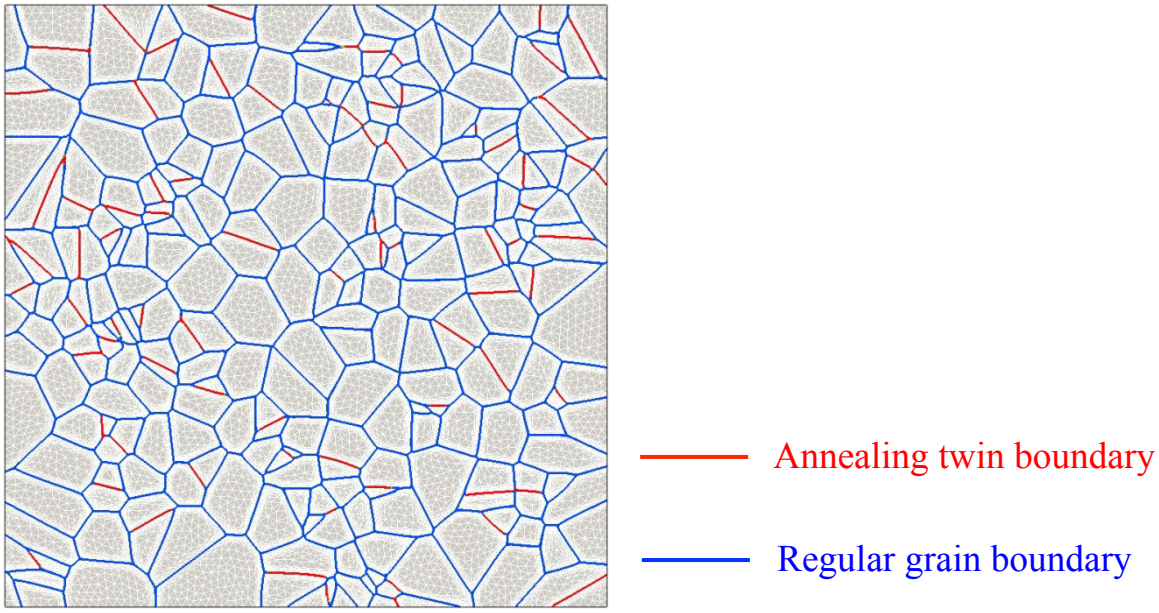

Fig. 7.17 200G_80T_1 case: initial configuration of the large grain growth simulation with 80 inserted twin boundaries.

In this simulation, grain boundary evolution becomes more complex. We observed that in growing grains the twin boundaries differed from the initial coherent twin boundary plane driven by the migration of the intercepted regular high angle boundaries (see Fig. 7.18). The deviated parts become thus incoherent. This transformation is also revealed in the experimental data of the present study and in the literature, as illustrated in Fig. 7.19 (blue square). Meanwhile, another transformation is also observed in the experimental data. Once a twin boundary differs from the original coherent plan, instead of transforming into an incoherent twin boundary, coherent steps formed to adjust incrementally the twin boundary direction as shown in Fig. 7.19 (black square). However, due the discontinuity in grain boundary normal, this type of step-like morphology cannot be described easily in the considered LS framework.

It is worth mentioning that static EBSD maps cannot reveal annealing twin morphology transformations. Accordingly, an *in situ* observation should be performed in order to further confirm this transformation.

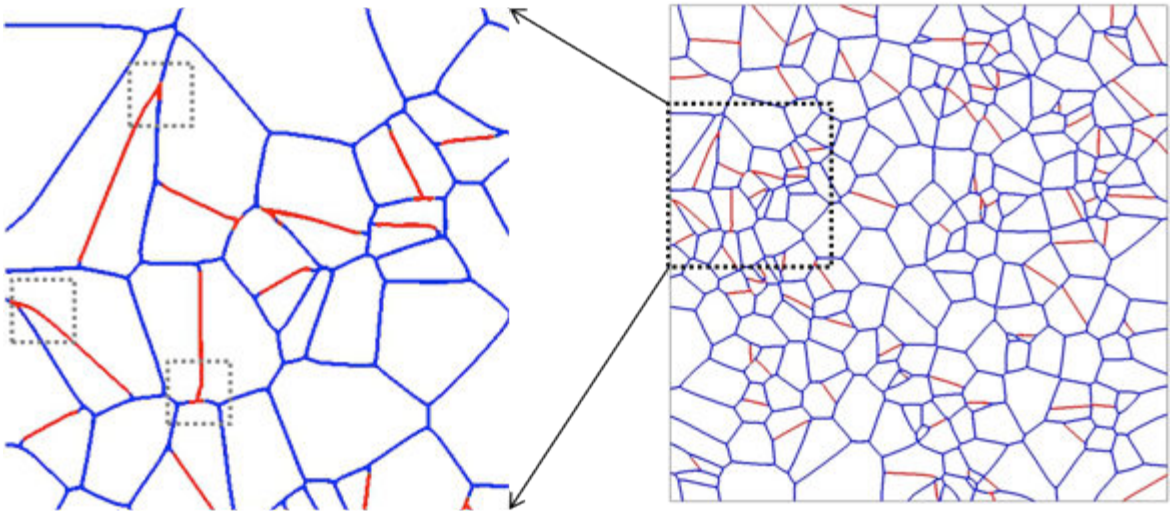

Fig. 7.18. 200G_80T_1: coherent twin boundary evolution behaviors during the grain growth simulation (simulation result after 50s).

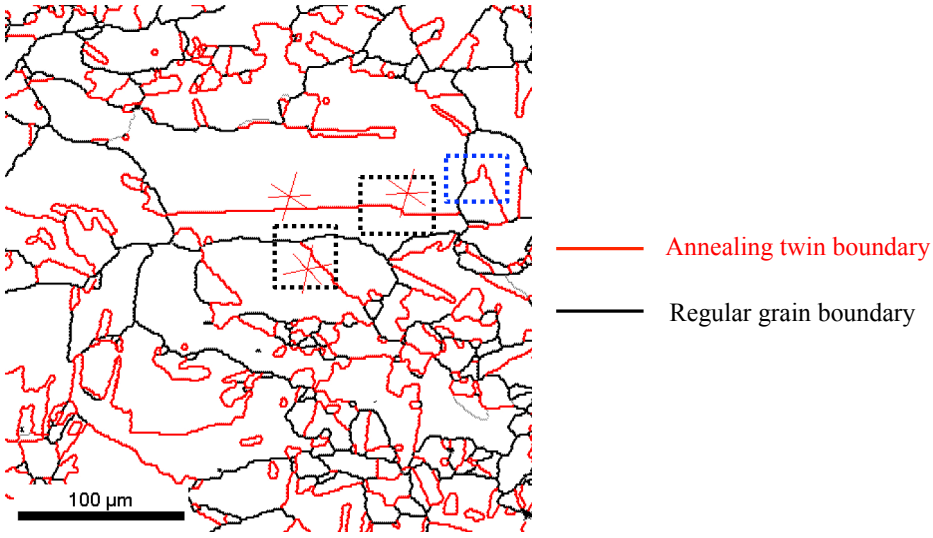

(a)

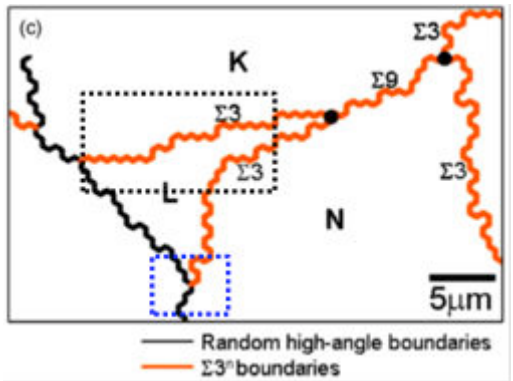

(b)

Fig. 7.19. Annealing twin boundary morphology in fully recrystallized microstructures; (a) microstructure from the experiment presented in the third chapter (the trace of the {111} planes of the highlighted grains are indicated in the map). (b) Microstructure of a deformed and subsequently annealed Pb-base alloy sample (figure reproduced from reference [Song 2007]).

In reality, when the twin boundary plane differs from the theoretical coherent plane, this twin boundary is not coherent any more and it should accordingly have an interfacial energy different from zero. Therefore, two extra simulations, called 200G_80T_2 and 200G_80T_3, were performed using the same initial microstructure and simulation parameters (h_{fine}, h_{coarse}, dt, E) that for the 200G_80T_1 case. In these simulations the algorithm TWININC was applied to follow the evolution of the twin boundary inclination. The tolerance angle for coherent twin boundary detection (ε) is fixed to 2°. As mentioned, in the initial microstructure, all the twin boundaries are coherent. During the simulation, if a part of the twin boundary differs from the theoretical coherent twin boundary plan, then this part will be treated as an incoherent twin boundary (which was not considered in the 200G_80T_1 case), as illustrated in Fig. 7.20. The two simulations differ by the energy attributed to the incoherent twin boundaries, as indicated in Table.7.2.

Ref	γ_{HAB}	γ_{ICTB}	γ_{CTB}
200G_80T_2	$1.1\cdot10^{-6} J\cdot mm^{-2}$	$1.94\cdot10^{-7} J\cdot mm^{-2}$	$0 J\cdot mm^{-2}$
200G_80T_3	$1.1\cdot10^{-6} J\cdot mm^{-2}$	$4.1\cdot10^{-7} J\cdot mm^{-2}$	$0 J\cdot mm^{-2}$

Table 7.2. Interfacial energy of grain boundaries and twin boundaries used for the cases 200G_80T_2 and 200G_80T_3.

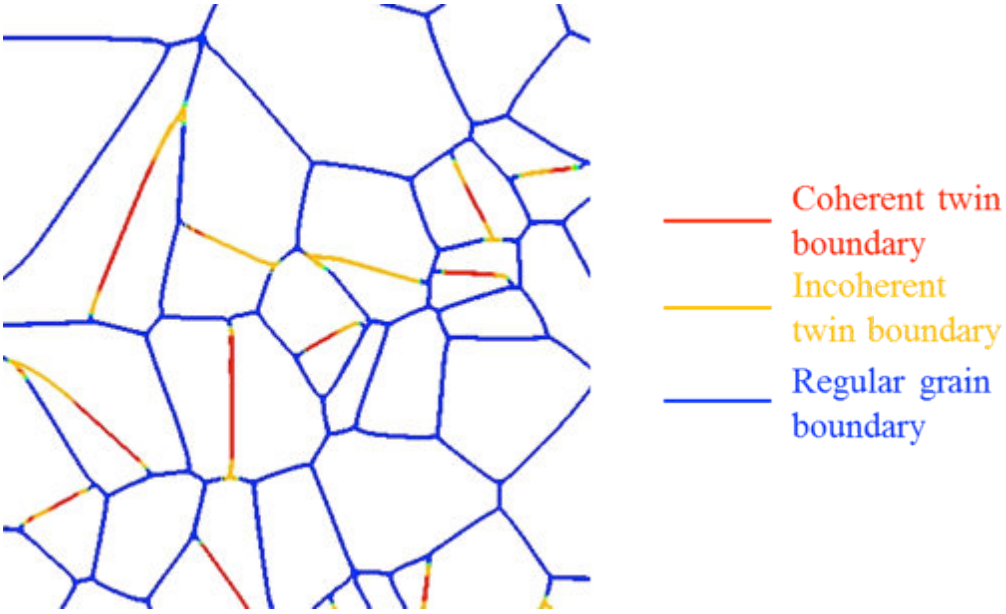

Fig. 7.20 200G_80T_2 case: twin boundary evolution in the simulation after 50s.

The simulation results of cases 200G_80T_2 and 200G_80T_3 are described in Figures 7.21, 7.22 and 7.23. The twin density (calculated by Eq. 1-9), proportional to the twin boundary

length, decreases during grain growth (see Fig. 7.21(a)), which is consistent with the annealing twin evolution trend in the experimental data. However, this decrease in the simulation in 200G_80T_3 is faster than in 200G_80T_2. This difference can consistently be related with the interfacial energy given to the incoherent part of the twin boundaries.

The grain growth kinetics is illustrated in Fig. 7.21(b). The number-weighted mean grain size was calculated without considering twins as grains. The grain growth kinetics is slower in 200G_80T_2 than in 200G_80T_3, especially at the end of the simulation. This difference can be explained by the different incoherent twin boundary energies used in the two simulations. For a shrinking grain with an incoherent twin boundary inside, higher twin boundary energy accelerate the shrinkage of the grain highlighted by black squares in Fig. 7.22. Therefore, there are fewer grains in total left at the end of the simulation for 200G_80T_3, which leads to a bigger average grain size.

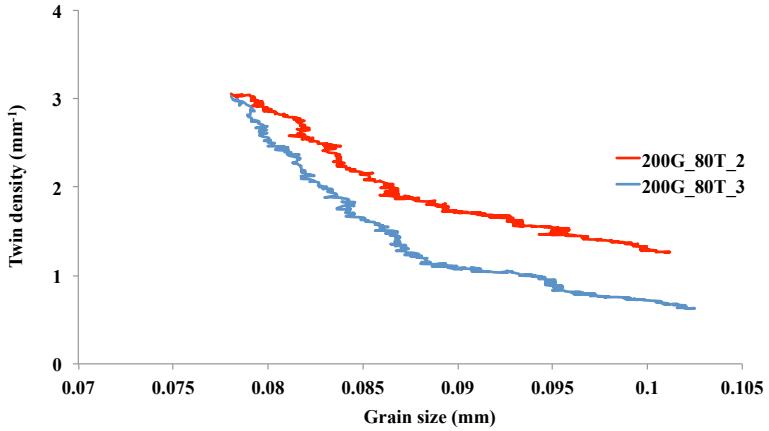

(a)

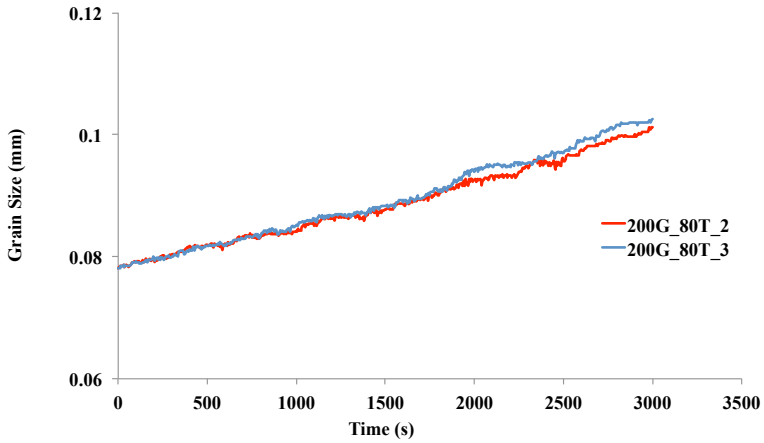

(b)

Fig. 7.21. 200G_80T_2 and 200G_80T_3 cases: twin density evolution during grain growth simulations; (b) grain growth kinetics.

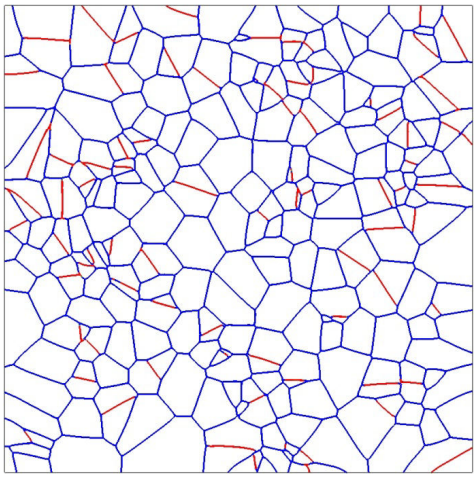

(50-2)

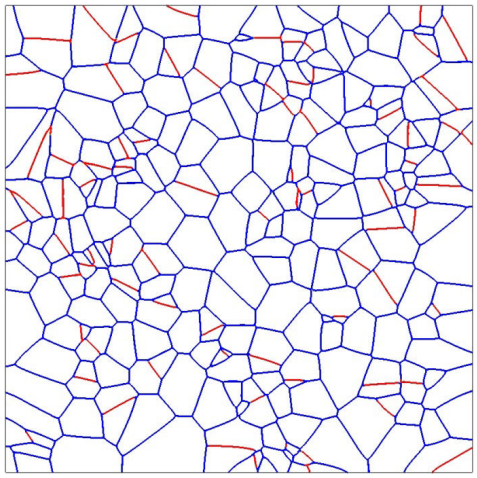

(50-3)

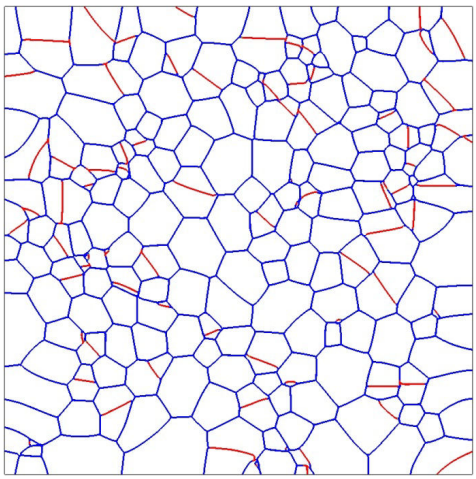

(450-2)

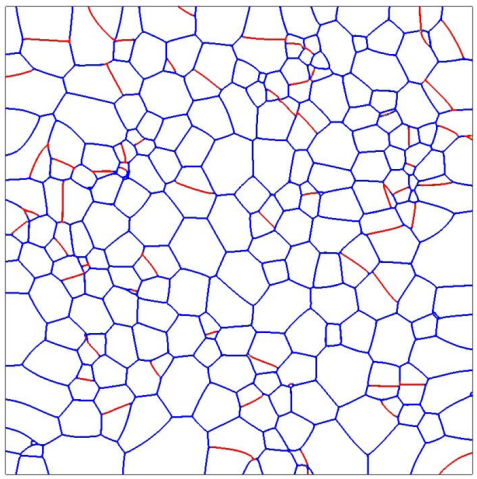

(450-3)

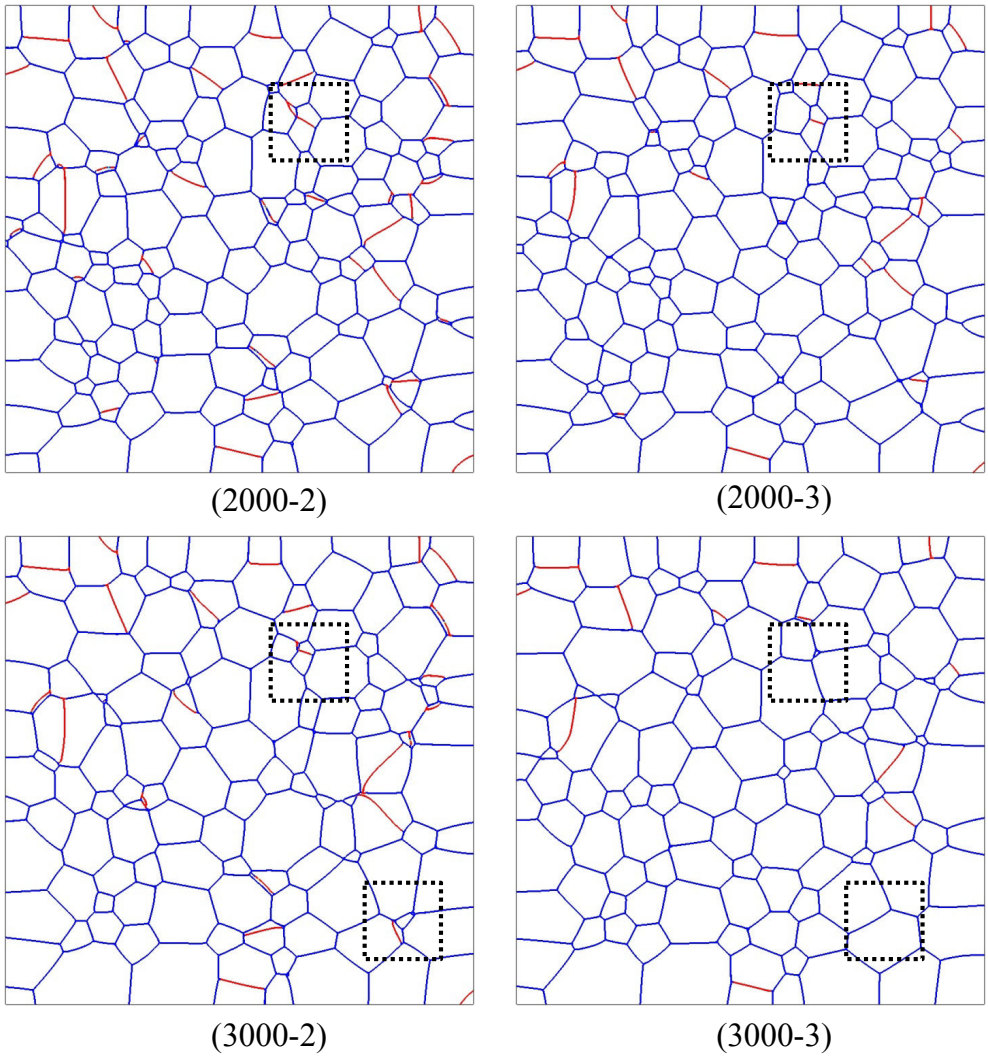

Fig. 7.22. 200G_80T_2 (left side) and 200G_80T_3 (right side) cases: microstructure evolution (the cumulative simulation time is indicated below each result).

In addition to the overall twin evolution trend, several local twin evolution mechanisms revealed by the simulation results are worth to be highlighted (Fig. 7.23). Firstly, as in the experimental data, twin boundaries propagate in growing grains or shrink in shrinking grains (marked by black squares). Secondly, as mentioned previously, driven by regular grain boundary migration, twin boundaries can differ from the coherent plane and become incoherent twin boundaries. Given a certain interfacial energy, incoherent twin boundaries are mobile. Some of them go back to the coherent plane in the simulation (marked by a black circle). This transformation, which is energetically favorable, has also been observed in a molecular dynamic simulation in the literature [Wang 2011].

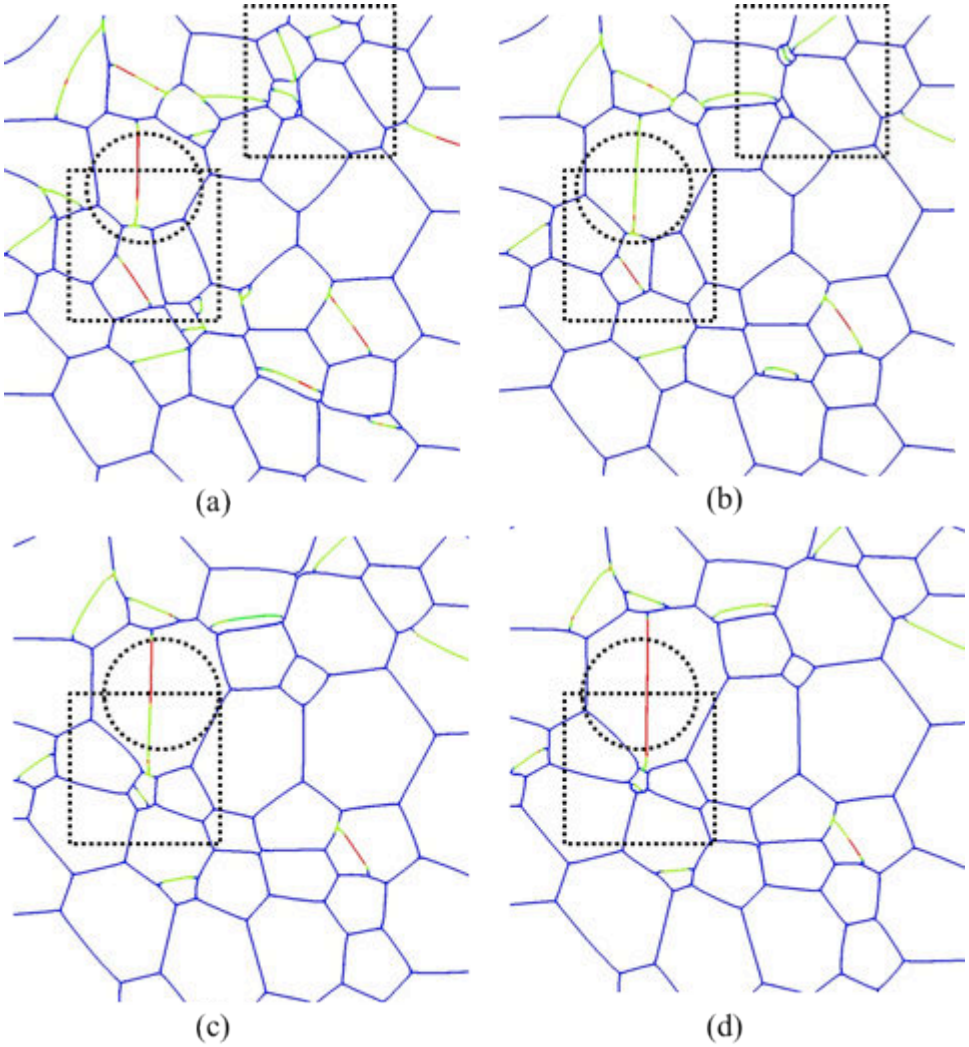

Fig. 7.23. Zoom on the 200G_80T_2 case: twin boundary evolution after (a) 450s, (b) 1000s, (c) 1500s, (d) 1700s. The color code for the grain boundaries is the same as in Fig. 7.20.

7.2.3. Towards the simulation of real annealing twin evolution during grain growth and recrystallization

We have detailed a numerical methodology counting the strong anisotropy in interfacial energy induced by twin boundaries. However, we are not able to simulate with this methodology all the twin evolution mechanisms revealed by the experimental data. It cannot be done completely for the grain growth regime, and even less for the recrystallization regime. In this section, the possibility to full field model real annealing twin evolution will be discussed.

7.2.3.1 Grain growth

As presented in the first part of the present thesis, there is almost no twin formed during grain growth. This fact facilitates the simulation of twin evolution during grain growth. In this chapter, several grain growth simulations are performed with the presence of twin boundaries. A difficulty observed in these simulations is the step-like morphology of real twin boundaries. Thanks to this kind of morphology, the twin boundary can keep its low overall mobility even after a deviation from the coherent plane. Since the morphology is mathematically discontinuous at the polycristalline scale, it cannot be well described by the considered LS framework at the considered mesoscopic scale.

In the present work, we developed a method to insert straight twin boundaries into Voronoï or Laguerre-Voronoï geometries. We plan to complete this method in the future to construct synthetic microstructures that are closer to the reality, especially by inserting more than one twin boundary per grain considering both cases of parallel twin boundaries and intersected twin boundaries. As shown in the first part of the thesis, at the end of recrystallization, the number of twin boundaries per grain generally is not homogeously distributed in the grains with different sizes. Therefore, the insertion of twin boundaries should follow the relationship between the number of twin boundaries per grain and the grain size.

With a more realistic initial microstructure, we could compare the simulation results with the twin density evolution during grain growth in the experimental data and obtained by the mean field model. Nevertheless, some 2D twin morphologies cannot be inserted by this method due to the limitations of tessellation cells e.g. type C and D in Fig. 1-1(c). The microstructures evolving by grain growth are those resulting from recrystallization and include, at least at the beginning, a significant proportion of incoherent boundaries. It also sounds unlikely that it

would be possible to account for that property, unless experimental micrographs would be meshed and used as an input microstructure.

The annealing twin simulation for the grain growth regime should also be extended to three-dimension. Nevertheless, the complicated twin morphologies in 3D [Lin 2014] could be a barrier for this extenstion. However, meshing the initial 3D microstructure and constructing a synthetic microstructure based on the mesh will be a very costly alternative. Thus, to work on this topic in a statistical way seems to be an important perspective.

7.2.3.2 Recrystallization

As presented in the experimental part of the present thesis, annealing twins are formed during recrystallization. Therefore, how to insert annealing twins during recrystallization simulation following a given criterion e.g. when the velocity of a recrystallization front exceeds a critical value is a crucial problem to be solved in order to simulate annealing twin evolution during recrystallization. In addition, as explained in the experimental part, annealing twins are more likely to form behind a convex recrystallization front, and when the tortuosity of the recrystallization front is higher. These results probably need further confirmation, but, then, accordingly the recrystallization front curvature would need to be calculated in the simulation, and the algorithm of dynamic twin generation would have to be implemented in the considered LS context. In addition, to account for the tortuosity issue, crystal plasticity should be used to predict subgrain deformation structures, or again experimental accurate data for the deformed starting state should be used as an input.

To summarize, compared with the grain growth regime, main difficulties keep being to evercome to simulate twin formation and evolution during recrystallization. Same as the simulation of the grain growth regime, the simulation of annealing twin development during recrystallization should also be extended to three-dimension.

7.3. Conclusion

In this chapter, at first two 2D large grain growth simulations with about 10000 grains were performed respectively with anisotropic and isotropic grain boundary energy using the level set method, in a finite element context. The simulation result of isotropic grain growth is consistent with the Burke-Turnbull model. The difference in grain size evolution between these two simulations is small but the considered grain boundary energy anisotropy was not very strong. It is worth mentioning that it is the first time that such simulations are performed in a finite element context with unstructured FE mesh.

In addition, a new methodology, including twin initial insertion, detection of coherent or incoherent character of twin boundaries and twin boundary quantification, was proposed to simulate annealing twin evolution during grain growth within the LS framework. Grain growth simulations with inserted twin boundaries were performed. The new methodology is proved to be able to take into account the high anisotropy in interfacial energy induced especially by coherent twin boundaries and to follow the twin boundary length evolution during the simulations. We found that coherent twin boundaries could differ from the coherent plane driven by regular grain boundary migration. Two grain growth simulations with 200 grains and 80 inserted twin boundaries were performed, in which we distinguish coherent and incoherent twin boundaries. We show evidence that higher incoherent twin boundary energy can accelerate the average grain growth kinetics.

Résumé en français

Dans ce chapitre, deux grandes simulations level-set 2D, l'une avec une énergie interfaciale isotrope et l'autre avec une énergie interfaciale anisotrope ont été réalisées Les résultats de simulations ont été comparés avec le modèle de Burke and Turnbull. Une nouvelle méthodologie pour simuler dans un cadre level-set l’évolution des macles thermiques durant la croissance de grains en deux dimensions a été proposée. La méthode d'insertion des joints de macles dans nos microstructures immergées est détaillée. De plus, la dépendance à l'inclinaison du joint de grain est également prise en compte.

CONCLUSION AND FUTURE WORK

Despite the amount of work dedicated to the subject, the understanding of annealing twin formation mechanism is not complete in the literature. In the present PhD work, we have tried to obtain a deeper understanding of this phenomenon, which is essential to physical metallurgy and especially to grain boundary engineering. For this purpose, different F.C.C. materials including the 304L stainless steel, commercially pure nickel and the nickel based superalloy Inconel 718 were investigated.

Thanks to an *in situ* experiment performed on commercially pure nickel, we found that the annealing twin density and the number of twin boundaries per grain increase in both individual grains and the overall microstructure during recrystallization. Meanwhile, during grain growth, the average twin density of the overall microstructure decreases. Furthermore, the number of twin boundaries per grain in the biggest grains, which control microstructure evolution, did not increase with the corresponding average grain size. Consistently, we found in the *in situ* observations that there were almost no twins generated in the grain growth regime. Incoherent twin boundaries may migrate in the direction to reduce the total interfacial energy, this was clearly observed in 304L and somewhat in pure Nickel. That phenomenon seems to be material and/or temperature dependent. The scarce formation of new twins and the possible migration of incoherent segments are two main factors that make the average annealing twin density decrease. Thus we unambiguously confirmed that annealing twins are mainly formed in the recrystallization regime, especially driven by the migration of recrystallization front into deformed regions. Therefore, curvature driven grain boundary migration by itself is not sufficient to generate significant number of annealing twins. Accordingly the influence of the curvature direction of the migrating boundary was proposed as a new explanation for the revealed annealing twin development mechanisms.

The effects of different thermo-mechanical factors including prior deformation amount, initial grain size, annealing temperature and heating velocity on annealing twin formation during recrystallization were determined. The prior deformation amount and the initial grain size influence annealing twin formation during recrystallization. More precisely, for a given initial grain size, annealing twin density in the overall microstructure after the completion of recrystallization appears to be primarily promoted by the deformation level. For a given strain level, smaller initial grain size leads to higher twin density. Meanwhile the effects of the

annealing temperature and the heating velocity on annealing twin formation are not obvious in the present ranges (rather narrow range, 100°C, for temperature, but wide range, two decades, for heating rate). Based on the experimental observations, we have provided new perspectives to explain twin formation by considering the role of the recrystallization front roughness. The recrystallization front tortuosity, as measured at the mesoscale in EBSD maps, appears to be positively correlated with the annealing twin density at the end of recrystallization. However, this correlation, which is consistent with the proposed effect of grain boundary curvature, needs to be further validated on larger 2D and 3D datasets, and for other thermo-mechanical conditions.

Two mathematical models from the literature for annealing twin density prediction during grain growth i.e. Gleiter's and Pande's models are reviewed. The Gleiter's model, due to its temperature dependency, is shown to not be consistent with the experimental data reported in the literature and with our experimental results. The Pande's model, on the other hand, does not account for the annealing twin evolution mechanisms revealed by the experimental observations that there are almost no twins generated in the grain growth regime. Accordingly, we have proposed the basis of a new mean field model better consistent with the experimental observations. Experimental data (grain growth in Inconel 718) could be well described by the proposed model, which has the great advantage of having only one parameter to be identified. However, this model needs to be further validated by comparison with more experimental data. 3D extension of the model could also be considered in the future, but then the knowledge of the twin boundary area in each grain size category will be required as an input, which is far from being trivial.

Mean field models can actually be used to predict twin density evolution but not the evolution of grain boundary network. Full field modelling is thus necessary to simulate the overall microstructure evolution during recrystallization and grain growth in order to better understand the observed phenomena and confirm the postulated annealing twin formation mechanisms. Full field modelling of twin evolution is challenging notably because annealing twin boundaries, especially coherent twin boundaries, have a very low interfacial energy as compared to regular high angle boundaries (about twenty times lower). Accordingly, the indent of the full field modelling of anisotropic grain growth in the present study is the consideration of the strong anisotropy in grain boundary energy induced by the presence of twin boundaries. In addition, the twin boundary morphology also needs to be explicitly

described. Two implicit methods i.e. phase field (more precisely multi phase field, MPF) and level set (LS) method were applied. Their numerical performances in anisotropic grain growth simulation were compared in a finite element (FE) context, using equivalent numerical parameters. It seems that, in the considered numerical context (high boundary energy anisotropy, FE formulation, unstructured FE mesh), the LS method is more accurate that the MPF approach. Thus, a new LS methodology has been proposed to simulate annealing twin evolution during grain growth. In this methodology, twin boundaries can be inserted into synthetic microstructures and annealing twin boundaries can be distinguished in terms of their coherent or incoherent characters. Grain growth simulations with inserted twin boundaries were performed. This methodology is proved to be able to take into account the high anisotropy in interfacial energy introduced by coherent twin boundaries and to retrieve the experimental twin density evolution trend during the simulations. We found that coherent twin boundary could be driven out of the coherent plane by regular grain boundary migration. Two grain growth simulations with 200 grains and 80 inserted twin boundaries were performed, in which coherent and incoherent twin boundaries were distinguished. These simulations show evidence that higher incoherent twin boundary energy can accelerate the average grain growth kinetics. In the future, more realistic synthetic microstructure will be built by inserting more than one twin boundary per grain in order to compare the simulated annealing twin density evolution during grain growth with the experimentally assessed behaviour of real microstructures. Meanwhile, how to simulate annealing twin development during recrystallization is still a challenging issue. It would probably require designing nucleation criteria based on the local curvature of the recrystallization front (itself highly dependent on the quality of the description of the initial deformed state), and on the proximity of a {111} plane. On the other hand the idea that the velocity of the recrystallization front migration could be an important factor in the control of the twin formation frequency is not obvious from our results. Full field modelling would also be a great tool to validate or invalidate such hypothesis.

The present study was performed in a two dimensional context. The extension to 3D, both experimentally and numerically is essential to have a better understanding of annealing twin formation mechanisms. As mentioned in the first chapter, by analyzing a 3D-nf-HEDM dataset of a fully recrystallized pure nickel sample, the complexity of real annealing twin morphologies was recently confirmed [Lin 2014]. Near Field High Energy Diffraction Microscopy (nf-HEDM), which has already been used to follow 3D microstructural evolution

in a non-destructive way in different F.C.C. materials (nickel [Hefferan 2010], aluminium [Hefferan 2012]), would be the best technique to investigate twinning during recrystallization. Such a 3D *in situ* observation of microstructural evolution during recrystallization can indeed certainly provide valuable insights in annealing twin formation mechanisms, notably with regards to our new hypothesis that the recrystallization front roughness would play an outmost important role.

Besides, as explained in the third chapter, annealing twin formation should be linked to atomic movement inside migrating grain boundaries. Despite the amount of work dedicated to annealing twin formation mechanisms, a more detailed and targeted study, which can reveal the relationship between annealing twin formation and grain boundary migration, appears as a necessity. Limited by the suitable experimental techniques, this study would have to be performed numerically thanks to multiscale approaches linking for example molecular dynamics simulations with a mesoscopic numerical method (LS for example).

REFERENCES

[Alvi 2008] M.H. Alvi, S.W. Cheong, J.P. Suni, H. Weiland, A.D. Rollett, 'Cube texture in hot-rolled aluminum alloy 1050 (AA1050) - nucleation and growth behavior', Acta Mater. 56, 3098-3108 (2008)

[Agnoli 2014] A. Agnoli, N. Bozzolo, R. Logé, JM. Franchet, J. Laigo, M. Bernacki, 'Development of a level set methodology to simulate grain growth in the presence of real secondary phase particles and stored energy - Application to a nickel-base superalloy', Comput. Mater. Sci. 89, 233-241 (2014)

[Allen 1978] S.M. Allen, J.W. Cahn, 'A microscopic theory for antiphase boundary motion and its application to antiphase domain coarsening', Acta Metall. 27, 1085-1095 (1978)

[Atkinson 1988] H.V. Atkinson, 'Theories of normal grain growth in pure single phase systems', Acta Metall, 36, 469-491 (1988)

[Aurenhammer 1987] F. Aurenhammer, 'Power diagrams: properties, algorithms and applications', SIAM Journal on Computing, 16, 78-96 (1987)

[Bair 2014] J.L. Bair, S.L. Hatch, D.P. Field, 'Formation of annealing twin boundaries in nickel', Scripta Mater. 81, 52-55 (2014)

[Bernacki 2008] M. Bernacki, Y. Chastel, T. Coupez, R.E. Logé, 'Level set framework for the numerical modelling of primary recrystallization in polycrystalline materials', Scripta Mater. 58, 1129-1132 (2008)

[Bernacki 2009] M. Bernacki, H. Resk, T. Coupez, R.E. Logé, 'Finite element model of primary recrystallization in polycrystalline aggregates using a level set frameworki', Model. And Simu. In Mater. Sci. And Eng. 17, 064006 (2009)

[Bernacki 2011] M. Bernacki, R.E. Logé, T. Coupez, 'Level set framework for the finite-element modelling of recrystallization and grain growth in polycrystalline materials', Scripta Mater. 64, 525-528 (2011)

[Bernard 2011] P. Bernard, S. Bag, K. Huang, R.E. Logé, 'A two-site mean field model of discoutinuous dynamic recrystallization', Mater.Sci.Eng. A 528, 7357-7367 (2011)

[Bollman 1970] W. Bollman, Crystal Defects and Crystalline Interfaces (Springer-Verlag, New York 143-149) (1970)

[Bozzolo 2012] N. Bozzlo, N. Souai, R.E. Logé, 'Evolution of microstructure and twin density during thermomechanical processing in a γ-γ' nickel-based superally', Acta Mater. 50, 5056-5066 (2012)

[Bozzolo 2012] N. Bozzolo, S. Jacomet, R.E. Logé, 'Fast in-situ annealing stage coupled with EBSD: A suitable tool to observe quick recrystallization mechanisms', Mater. Character. 70, 28-32 (2012)

[Brandon 1969] D.G. Brandon, ‘The structure of high-angle grain boundaries’, Acta Metall. 14, 1479-1484 (1969)

[Brons 2013] J.G. Brons, G.B. Thompson, ‘A comparison of grain boundary evolution during grain growth in fcc metals’, Acta Mater. 61, 3936-3944 (2013)

[Burgers 1946] W.G. Burgers, ‘Simulation Crystals and Twin-formation in Recrystallized Aluminum’, Nature, 157, 76-77 (1946)

[Burgers 1949] W.G. Burgers, ‘Cystal growth in the solid state (Recrystallization)’, Physica, 15, 92-106 (1949)

[Burke 1950] E. Burke, ‘The formation of annealing twins’, Trans. Am. Inst. Min. Engrs 188, 1324-1328 (1950)

[Burke 1952] J.E. Burke, D. Turnbull, 'Recrystallization and grain growth', Progress in Metal Phys. 3, 220-292 (1952)

[Bystrzycki 1993] J. Bystrzycki, W. Przetakiewicz, K.J. Kurzydlowski, 'Study of annealing twins and island grains in F.C.C. alloy', Acta Metall. 41, 2639-2649 (1993)

[Cahn 1961] J.W. Cahn, ‘On spinodal decomposition’, Acta Metall. 9 (1961)

[Cahoon 2009] J.R. Cahoon, Q. Li, N.L. Richards, 'Microstructural and processing factors influencing the formation of annealing twins', Mater.Sci.Eng. A 526, 56-61 (2009)

[Carpenter 1926] H. Carpenter, S. Tamura, ‘The formation of twinned metallic crystals’, Proc.R.Soc. A113, 161 (1926)

[Chang 2014] K. Chang, N. Moelans, 'Effect of grain boundary energy anisotropy on highly textured grain structures studied by phase-field simulations', Acta Mater. 64, 443-454 (2014)

[Charnock 1967] W. Charnock, J. Nutting, ‘The factors determining the frequency of occurence of annealing twins’, Met. Sci. J. 78-83 (1967)

[Collins 1985] J.B. Collins, H. Levine, 'Diffuse interface model of diffusion-limited crystal growth', Phys.Rev.B 31, 6119-6122, (1985)

[Dash 1963] S. Dash, N. Brown, ‘An investigation of the origin and growth of annealing twins’, Acta Metall. 11, 1067-1075 (1963)

[Debashis 2012] K. Debashis, 'Correlating grain boundary properties to distributions during anisotropic grain growth - an interface field study in two and three dimensions', PhD thesis, Carnegie Mellon University (2012)

[Don 1986] J. Don, S. Majumdar, 'Creep cavitation and grain boundary structure in type 304 stainless steel', Acta Metall. 34, 961-967 (1986)

[Edwards 1924] G.A. Edwards, L.B. Pfeil, ‘The production of large crystals by annealing strained iron’, J. Iron Steel Inst., (1924)

[Elsey 2009] M. Elsey, S. Esedoglu and P. Smereka, ‘Diffusion generated motion for grain growth in two and three dimensions’, J. of Comput. Phys. 228, 8015-8033 (2009)

[Elsey 2013] M. Elsey, S. Esedoglu, P. Smereka, 'Simulations of anisotropic grain growth: Efficient algorithms and misorientation distributions', Acta Mater. 64, 2033-2043 (2013)

[Epstein 1989] N. Epstein, ‘On tortuosity and the tortuosity factor in flow and diffusion through porous media’, Chem. Eng. Sci. 44, 777-779 (1989)

[Fabiano 2014] A.L. Cruz-Fabiano, R. Logé, M. Bernacki, 'Assessment of simplified 2D grain growth models from numerical experiments based on a level set framework', Comput. Mater. Sci., 92, 305-312 (2014)

[Fan 1997] D. Fan, L.Q. Chen, 'Computer simulation of grain growth using a continuum field model', Acta Metall. 45, 611-622 (1997)

[Field 2007] D.P. Field, L.T. Bradford, M.M. Nowell, T.M. Lillo, 'The role of annealing twins during recrystallization of Cu', Acta Mater. 55, 4233-4241 (2007)

[Fullman 1951] R. L. Fullman And J. C. Fisher, ‘Formation of annealing twins during grain growth’, J. appl. Phys. 22, 1350-1355 (1951)

[Garcke 1999] H. Garcke, B. Nestler, B. Stoth, 'A multiphase field concept: numerical simulations of moving phase boundaries and multiple junctions', SIAM Journal on Applied Math. 1-23 (1999)

[Gertsman 1994] V.Y. Gertwman, K. Tangri, R.Z. Valiev, 'On the grain boundary statistics in metals and alloys susceptible to annealing twinning', Acta Metall. 42, 1785-1804 (1994)

[Gleiter 1969] H. Gleiter, ‘The formation of annealing twins’, Acta Metall. 17, 1421-1428 (1969)

[Goodhew 1979] P.J. Goodhew, ‘Annealing twin formation by boundary dissociation’, Metal Sci. 13, 108-112 (1979)

[Gruber 2009] J. Gruber, H.M. Miller, T.D. Hoffmann, G.S. Rohrer, A.D. Rollett, 'Misorientation texture development during grain growth. Part I: Simulation and experiment', Acta Mater. 57, 6102-6112 (2009)

[Guo 2011] W. Guo, R. Spartschek, I. Steinbach, 'An analytical study of the static state of multi-junctions in a multiphase field model', Physica D, 240, 382-388 (2011)

[Hachem 2012] E. Hachem, H. Digonnet, E. Massoni, T. Coupez, ‘Immersed volume method for solving natural convection, conduction and radiation of a hat-shaped disk inside a 3D enclosure’, International Journal of numerical methods for heat & fluid flow, 22, 6 (2012)

[Hallberg 2013] H. Hallberg, ‘A modified level set approach to 2D modeling of dynamic recrystallization’, Model. Simu. Mater. Sci. And Eng. 21, 085012 (2013)

[Hefferan 2010] C.M. Hefferan, S.F. Li, J. Lind, U. Lienert, A.D. Rollett, P. Wynblatt, R.M. Suter, 'Statistics of high purity nickel microstructure from high energy X-ray diffraction microscopy', Computers, Materials, & Continua, 14, 209-220 (2010)

[Hefferan 2012] C. M. Hefferan, J. Lind, S.F. Li, U. Lienert, A.D. Rollett, R.M. Suter, 'Observation of recovery and recrystallization in high-purity aluminum measured with forward modeling analysis of high-energy diffraction microscopy'. Acta Materialia, 60, 4311-4318 (2012)

[Hillert 1965] M. Hillert, 'On the theory of normal and abnormal grain growth', Acta Metall. 13, 227-238 (1965)

[Hirouchi 2012] T. Hirouchi, T. Tsuru, Y, Shibutani, 'Grain growth prediction with inclination dependence of <110> tilt grain boundary using multi-phase-field model with penalty for multiple junctions', Comput. Mater. Sci. 53, 474-482 (2012)

[Hitti 2012] K. Hitti, P. Laure, T. Coupez, L. Silva, M. Bernacki, 'Precise generation of complex statistical Representative Volume Elements (RVEs) in a finite element context', Comput. Mater. Sci. 61, 224-238, (2012)

[Holm 2001] E. Holm, G. Hassold, M. Miodownik, 'On misorientation distribution evolution during anisotropic grain growth', Acta Mater. 49, 2981-2991 (2001)

[Holm 2011] E.A. Holm, G.S. Rohrer, S.M. Foils, A.D. Rollett, H.M. Miller, D.L. Olmsted, 'Validating computed grain boundary energies in fcc metals using the grain boundary character distribution', Acta Mater. 59, 5250-5256 (2011)

[Hu 1956] H. Hu, C.S. Smith, 'The formation of low-energy interfaces during grain growth in alpha and alpha-beta brasses', Acta Metall. 4 (1956)

[Huang 2011] K. Huang, 'Towards the modeling of recrystallization phenomena in multi-pass conditions – Application to 304L steel', PhD thesis, Mines-ParisTech (2011)

[Humphreys 1996] F.J. Humphreys, 'Qunatitative metallography by electron backscattered diffraction', J. of Microscopy, 195, 170-185 (1999)

[Humphreys 2004] F.J. Humphreys, 'Recrystallization and related annealing phenomena', M. Hatherly, Elsevier, Amsterdam (2004)

[Imai 1985] H. Imai, M. Iri, K. Murota, 'Voronoi diagram in the Laguerre geometry and its applications', SIAM Journal on Computing, 14, 93-105 (1985)

[Jin 2013] Y. Jin, M. Bernacki, G.S. Rohrer, A.D. Rollett, B. Lin, N. Bozzolo, 'Formation of annealing twins during recrystallization and grain growth in 304L austenitic stainless steel', Mater. Sci. Forum 753, 113-116 (2013)

[Jin 2014] Y. Jin, B. Lin, M. Bernacki, G.S. Rohrer, A.D. Rollett, N. Bozzolo, 'Annealing twin development during recrystallization and grain growth in pure Nickel', Mater.Sci.Eng. A 597, 295-303 (2014)

[Kerisit 2013] C. Kerisit, R.E. Logé, S. Jacomet, V. Llorca, N. Bozzolo, ‘EBSD coupled to SEM in situ annealing for assessing recrystallization and grain growth mechanisms in pure tantalum’, 250, 189-199 (2013)

[Kubale 2004] M. Kubale, 'Graph coloring', American Mathematical Society, Providence, Rhode Island (2004)

[Kumar 2000] M. Kumar, W.E. King, A.J. Schwartz, ‘Modifications to the microstructural topology in F.C.C. materials through thermomechanical processing’, Act Mater. 48, 2081-2091 (2000)

[Kumar 2005] M. Kumar, W.E. King, 'Universal features of grain boundary networks in FCC materials', J. of Mater. Sci. 40, 847-852 (2005)

[Lee 2003] S.B. Lee, ‘Correlation between grain boundary faceting-defaceting transition and change of grain boundary properties with temperature’, Mater. Letters, 57, 3779-3783 (2003)

[Lehockey 1998] E.M. Lehockey, G. Palumbo, K.T. Aust et al., 'On the role of intercrystalline defects in polycrystal plasticity', Scripta Mat. 39, 341-346 (1998)

[Li 2006] Q. Li, J.R. Cahoon, N.L. Richards, 'On the calculation of annealing twin density', Scripta Mater. 55, 1155-1158 (2006)

[Li 2009] Q. Li, J.R. Cahoon, N.L. Richards, ‘Effects of thermo-mechanical processing parameters on the special boundary configurations of commercially pure nickel’, Mat. Sci. Eng. A 527, 263-271 (2009)

[Li 2014] B. Li, S. Tin, ‘The role of deformation temperature and strain on grain boundary engineering of Inconel 600’, Mater. Sci. Eng. A, 603, 104-113 (2014)

[Lim 1990] L.C. Lim and T. Watanabe, 'Fracture-Toughness and Brittle-Ductile Transition Controlled by Grain-Boundary Character Distribution (GBCD) in Polycrystals', Acta Met. 38, 2507-2516 (1990)

[Lin 1995] P. Lin, G. Palumbo, U. Erb et al., 'Influence of Grain Boundary Character Distribution on Sensitization and Intergranular Corrosion of Alloy 600', Scripta Metall. 33, 1387-1392 (1995)

[Lin 2014] B. Lin, Y. Jin, C.M. Hefferan, R. Suter, M. Bernacki, N. Bozzolo, A.D. Rollett, G.S. Rohrer, ‘Annealing twin grain shape evolution as observed in 3D HEDM’, in progress

[Logé 2008] R. Logé, M. Bernacki, H. Resk, L. Delannay, H. Digonnet, Y. Chastel, T. Coupez, 'Linking plastic deformation to recrystallization in metals using digital microstructures', Philo. Mag. 88, 3691-3712 (2008)

[Ma 2006] N. Ma, Q. Chen, Y. Wang, ‘Implementation of high interfacial energy anisotropy in phase field simulations’, Scripta Mat. 54(11), 1919-1924 (2006)

[Madej 2013] L. Madej, L. Sieradzki, M. Sitko, K. Perzynski, K. Radwanski, R. Kuziak, ‘Multi scale cellular automata and finite element based model for cold deformation and

annealing of a ferrite-pearlitic microstructure', Comput. Mater. Sci. 77, 172-181 (2013)

[Mahajan 1997] S. Mahajan, C.S. Pande, M.A. Imam, B.B. Rath, 'Formation of annealing twins in F.C.C. crystals', Acta Mater. 45, 2633-2638 (1997)

[Maksimova 1989] E.L. Maksimova, E.I. Robkin, L.S. Shvindleman, B.B. Straumal, 'Phase transitions at grain boundaries in the presence of impurities', Acta Metal. 37, 1995-1998 (1989)

[Mandal 2014] S. Mandal, K.G. Pradeep, S. Zaefferer, D. Raabe, 'A novel approach to measure grain boundary segregation in bulk polycrystalline materials in dependence of the boundaries five rotational degrees of freedom', Scripta Mat. 81, 16-19 (2014)

[Martorano 2006] M.A. Martorano, M.A. Fortes, A.F. Padilha, 'The growth of protrusion at the boundary of a recrystallized grain', Acta Mater. 54, 2769-2776 (2006)

[Merriman 1994] B. Merriman, J.K. Bence, S. Osher, Journal of Comput. Physics, 112, 334-363 (1994)

[Meyers 1978] M.A. Meyers, L.E. Murr, 'A model for the formation of annealing twins in F.C.C. metals and alloys', Acta Metall. 26, 951-962 (1978)

[Meyers 1984] M. A. Meyers and Christian McCowan, 'The formation of annealing twins: overview and new thoughts', Metals/Materials Technology Series, American Society for Metals (1984)

[Moelans 2008] N. Moelans, B. Blanpain, P. Wollants, 'Quantitative Phase-Field Approach for Simulating Grain Growth in Anisotropic Systems with Arbitrary Inclination and Misorientation Dependence', Phy. Rev. Let. 101.025502 (2008)

[Moelans 2008] N. Moelans, B. Blanpain, P. Wollants, 'Quantitative analysis of grain boundary properties in a generalized phase field model for grain growth in anisotropic systems', Phys. Rev. B, 78(2), 024113 (2008)

[Moelans 2009] N. Moelans, F. Wendler, B. Nestler, 'Comparative study of twin phase-field models for grain growth', Comp. Mat. Sci. 46, 479-490 (2009)

[Murr 1972] L.E. Murr, 'Temperature coefficient of twin-boundary energy: The determination of stacking fault energy from the coherent twin-boundary energy in pure F.C.C. metals', Scripta Metall. 6, 203-208 (1972)

[Nielsen 1967] J.P. Nielsen, 'The origin of annealing twins', Acta Metall. 15, 1083-1085 (1967)

[Olmsted 2009] D.L. Olmsted, S.M. Foiles, E.A. Holm, 'Survey of computed grain boundary properties in face-centered cubic metals: I. Grain boundary energy', Acta Mater. 57, 36943703 (2009)

[Palumbo 1988] G. Palumbo, K.T. Aust, 'Localized Corrosion at Grain-Boundary Intersections in High Purity Nickel', Scripta Metall. 22, 847-852 (1988)

[Palumbo 1990] G. Palumbo, K.T. Aust, 'Structure-Dependence of Intergranular Corrosion in High Purity Nickel', Acta Metall. 38, 2343-2352 (1990)

[Palumbo 1998] G. Palumbo, E.M. Lehockey, P. Lin, 'Applications for grain boundary engineered materials', JOM, 40-43 (1998)

[Pande 1990] C.S. Pande, M.A. Imam, B.B. Rath, ‘Study of annealing twins in FCC metals and alloys’, Metall. Trans. A 21, 2891-2896 (1990)

[Porter 1981] D.A. Porter, K.E. Easterling, ‘Phase transformations in metals and alloys’, CRC Press (1981)

[Randle 2002] V. Randle, 'Sigma-Boundary Statistics by Length and Numbder', Interface Sci. 10, 271-277 (2002)

[Randle 2008] V. Randle, P.R. Rios, Y. Hu, ‘Grain growth and twinning in nickel’, Scripta Mater. 58, 130-133 (2008)

[Read 1950] W.T. Read, W. Shockley, ‘Dislocation models of crystal grain boundaries’, Phys. Rev. 78, 275 (1950)

[Resk 2009] H. Resk, L. Delannay, M. Bernacki, T. Coupez, R. Logé, ‘Adaptive mesh refinement and automatic remeshing in crystal plasticity finite element simulations’, Model. Simu. Mater. Sci. And Eng. 17, 075012 (2009)

[Rohrer 2004] G.S. Rohrer, D.M. Saylor, B. El Dasher, B.L. Adams, A.D. Rollett, P. Wynblatt, 'The distribution of internal interfaces in polycrystals', Z. Metallk., 94, 197-214 (2004)

[Rollett 1997] A.D. Rollett, ‘Overview of modeling and simulation of recrystallization’, Progress in Mater. Sci. 79-99 (1997)

[Rollett 2001] A.D. Rollett, D. Raabe, 'A hybrid model for mesoscopic simulation of recrystallization', Comput. Mater. Sci. 21, 69-78 (2001)

[Rollett 2004] A.D. Rollett et al, 'Modelling polycrystalline microstructures in 3D', Roc. Conf. Numiform, Columbus, 71-77 (2004)

[Rosen 1961] J.G. Rosen, 'The Gradient Projection Method for Non- linear Programming', Journal SIAM 9, 514 (1961)

[Saltykov 1967] S.A. Saltykov, ' The determination of the size distribution of particles in an opaque material from a measurement of the size distribution of their sections', Proc. Second Int. Cong. For Stereology, 163 (1967)

[Sieradzki 2013] L. Sieradzki, L. Madej, ‘A perceptive comparison of the cellular automata and Monte Carlo techniques in application to static recrystallization modeling in polycrystalline materials’, Comput. Mater. Sci. 67, 156-173 (2013)

[Song 2007] K.H. Song, Y.B. Chun, S.K. Hwang, 'Direct observation of annealing twin formation in a Pb-base alloy', Mater.Sci.Eng. A 454-455, 629-636 (2007)

[Steinbach 1996] I. Steinbach, F. Pezzolla, B. Nestler, M. Seebelberg, R. Prieler, G.J. Schmitz, J.L.L. Rezende, 'A phase field concept for multiphase systems', Physica D, 94, 135-147 (1996)

[Steinbach 1999] I. Steinbach, F. Pezzolla, 'A generalized field method for multiphase transformation using interface fields', Physica D, 134, 385-393 (1999)

[Surholt 1997] T. Surholt, C. Herzig, 'Grain boundary self-diffusion in Cu polycrystals of different purity', Acta Mater. 45, 3817-3823 (1997)

[Suwa 2007] Y. Suwa, Y. Saito, H. Onodera, 'Phase field simulation of stored energy driven interface migration at a recrystallization front', Mater. Sci. Eng. A, 457, 132-138 (2007)

[Takaki 2009] T. Takaki, Y. Hisakuni, T. Hirouchi, A. Yamanaka, Y. Tomita, 'Multi-phase-field simulations for dynamic recrystallization', Comput. Mater. Sci. 45, 881-888 (2009)

[Thaveeprungsriporn 1997] V. Thaveeprungsriporn, G.S. Was, 'The role of coincidence-site-lattice boundaries in creep of Ni-16Cr-9Fe at 360°C', Met. Trans. A 28A, 2101-2112 (1997)

[Tucker 2012] J.C. Tucker, L.H. Chan, G.S. Rohrer, M.A. Groeber, A.D. Rollett, 'Comparison of grain size distributions in a Ni-based superalloy in three and two dimensions using the Saltykov method', Scripta Mater. 66, 554-557 (2012)

[Underwood 1970] E.E. Underwood, 'Quantitative stereology', Addison-Wesley publishing company (1970)

[Wang 2011] W. Wang, Y. Dai, J. Li, B. Liu, 'An Atomic-Level Mechanism of Annealing Twinning in Copper Observed by Molecular Dynamics Simulation', Crystal Growth & Design, 11, 2928-2934 (2011)

[Wang 2014] W. Wang, F. Brisset, A.L. Helbert, D. Solas, I. Drouelle, M.H. Mathon, T. Baudin, 'Influence of stored energy on twin formation during primary recrystallization', Mater.Sci.Eng. 1 589, 112-118 (2014)

[Wantanabe 1984] T. Wantanabe, 'Grain boundary design and control', Res.Mech. 11, 47-84 (1984)

[Xu 2009] T. Xu, M. Li, 'Topological and statistical properties of a constrained Voronoi tessellation', Philo. Mag. 89, 349-374 (2009)

[Yan 2010] X. Yan, H. Zhang, 'On the atomistic mechanisms of grain boundary migration in [001] twist boundaries: Molecular dynamics simulations', Comput. Mater. Sci. 48, 773-782 (2010)

[Zhang 2006] H. Zhang, D.J. Srolovitz, 'Characterization of atomic motion governing grain boundary migration', Phys. Rev. B, 74, 115404 (2006)

[Zhang 2009] H. Zhang, D.J. Srolovitz, J.F. Douglas, J.A. Warren, 'Grain boundaries exhibit the dynamics of glass-forming liquids', PNAS, 106, 7735-7740 (2009)

[Zhao 1996] HK. Zhao, T. Chan, B. Merriman, S. Osher, 'A variational level set approach to multiphase motion', Journal of Comput. Physics, 127, 179-195 (1996)

Mécanismes de formation des macles thermiques

RESUME : Le maclage thermique est un défaut cristallographique largement discuté dans les métaux de type CFC à faible énergie de faute d'empilement. Malgré une importante littérature scientifique dédiée à ce sujet, les mécanismes expliquant précisément la formation de ces macles thermiques ne sont pas totalement élucidés à ce jour. Dans ce travail, nous avons cherché à améliorer notre compréhension de ce phénomène fondamental en métallurgie physique. Différents matériaux de type CFC (acier inoxydable 304L, nickel pur et Inconel 718) ont été considérés. Nous avons confirmé, grâce à des expériences de traitement thermique *in situ* couplées à des cartographies d'orientation, que la majorité des macles thermiques sont générées durant la recristallisation. De la même manière, par une expérience réalisée sur l'Inconel 718, nous avons mis en évidence que la croissance de grains pure n'était pas source de joints de macle. Par conséquent, il semble évident que les phénomènes de recristallisation et de croissance de grains ont des régimes totalement distincts associés à des mécanismes spécifiques du point de vue de la formation des macles thermiques, et doivent donc absolument être étudiés séparément. Nous avons ainsi proposé un nouveau modèle, dans lequel l'effet du signe de la courbure moyenne du front de recristallisation est pris en compte. Les influences de différents facteurs thermomécaniques, y compris le niveau de déformation, la taille de grains initiale, la température de recuit et la vitesse de montée en température, ont été étudiées à travers deux séries d'expériences. Suite à l'effet du signe de la courbure moyenne du joint de grain, nous avons proposé une méthode pour quantifier la tortuosité du front de recristallisation. Dans cette étude, nous montrons que cette quantité est corrélée à la densité de macles post-recristallisation. En sus des analyses expérimentales, des outils numériques de type champ moyen et champ complet ont également été développés dans cette étude afin de modéliser l'évolution des macles thermiques tout en tenant en compte des mécanismes physiques mis en évidence expérimentalement. Les bases d'un nouveau modèle de type champ moyen ont été proposées afin de modéliser l'évolution de la densité de macles moyenne durant le phénomène de croissance de grains. Ce modèle, dans lequel seulement un paramètre doit être identifié par des donnés expérimentales, semble mieux décrire les résultats expérimentaux obtenus pour l'inconel 718 comparé au modèle de Pande, référence en la matière. Deux méthodes implicites i.e. la méthode level-set et la méthode champ de phase ont été comparées au niveau de leurs formulations et de leurs performances numériques pour des simulations de croissance de grains anisotrope. C'est la première fois que ces deux méthodes sont comparées dans le contexte de l'utilisation de maillages éléments finis non stucturés et hétérogènes en terme de taille de maille. Une nouvelle méthodologie a été ainsi proposée dans le cadre de l'approche level-set pour simuler l'évolution de macles thermiques durant le phénomène de croissance de grains. Dans cette nouvelle méthodologie, les joints de macles peuvent être insérés dans des microstructures synthétiques. De plus, les joints de macles peuvent être distingués selon leur nature cohérente ou incohérente. Nous avons montré à travers les différentes simulations réalisées que les propriétés spéciales des joints de macles peuvent être prises en compte avec ce nouveau formalisme.

Mots clés : Macle thermique, Recristallisation, Croissance de grains, EBSD, Modélisation à champ complet

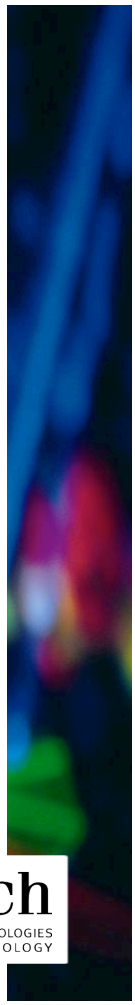

MINES ParisTech

ParisTech
INSTITUT DES SCIENCES ET TECHNOLOGIES
PARIS INSTITUTE OF TECHNOLOGY

Annealing twin formation mechanisms

ABSTRACT : Annealing twin is a crystallographic defect that is largely reported in F.C.C. metals especially those with low stacking fault energy. Despite the amount of work dedicated to the subject, the understanding of annealing twin formation mechansims is not complete in the literature. In the present work, by applying both experimental and numerical tools, we tried to have a more profound understanding of this phenomenon, which is essential to Physical Metallurgy. For this purpose, different F.C.C. Materials including 304L stainless steel, commercially pure nickel and nickel based superalloy Inconel 718 are investigated. We confirmed that annealing twins are mainly formed in the recrystallization regime, especially driven by the migration of recrystallization front into deformed regions by using *in situ* EBSD technique. In addition, we found in the *in situ* observations that there are almost no twins generated in the grain growth regime. This observation is confirmed by another grain growth experiment performed on Inconel 718. Therefore, curvature driven grain boundary migration by itself is not sufficient to generate annealing twins. A new atomistic model to explain annealing twin formation mechanism, in which the effect of migrating boundary curvature is considered, is proposed. The effects of different thermo-mechanical factors, including prior deformation level, initial grain size, annealing temperature and the heating velocity, on annealing twin formation are determined via two experiments performed on commercially pure nickel. Based on the idea of grain boundary curvature, we proposed a method to quantify recrsytallization front tortuosity. In the present study, we show evidence that this quantity is positively correlated with the twin density at the end of the recrystallization regime. In addition to experimental studies, numerical tools including both mean field and full field approaches are applied to model annealing twin evolution during grain growth by taking into account the revealed mechanisms. A basis of a new mean field model is proposed to model annealing twin density evolution during grain growth. This model, which has only one parameter to be identified, provides a better consistency with the experimental data of Inconel 718 compared to the Pande's model. Besides, full field approaches are also applied to simulate the overall microstructure evolution during grain growth. Two implicit methods i.e. the level set and the multi-phase-field methods are compared in terms of their formulations and their numerical performance in anisotropic grain growth simulations. It is the first time that these two methods are compared in the finite element context with non-structural mesh. In the present numerical context, the level set method is more suitable to describe strong anisotropy in grain boundary energy. A new methodology is thus developed in the level set framework to simulate annealing twin evolution during grain growth. This methodology, in which we can insert annealing twin boundaries into synthetic microstructures and distinguish coherent and incoherent twin boundaries, is proven to be able to counting for the strong anisotropy introduced by coherent annealing twin boundaries.

Keywords: Annealing twin, Recrystallization, Grain growth, EBSD, Full field modeling